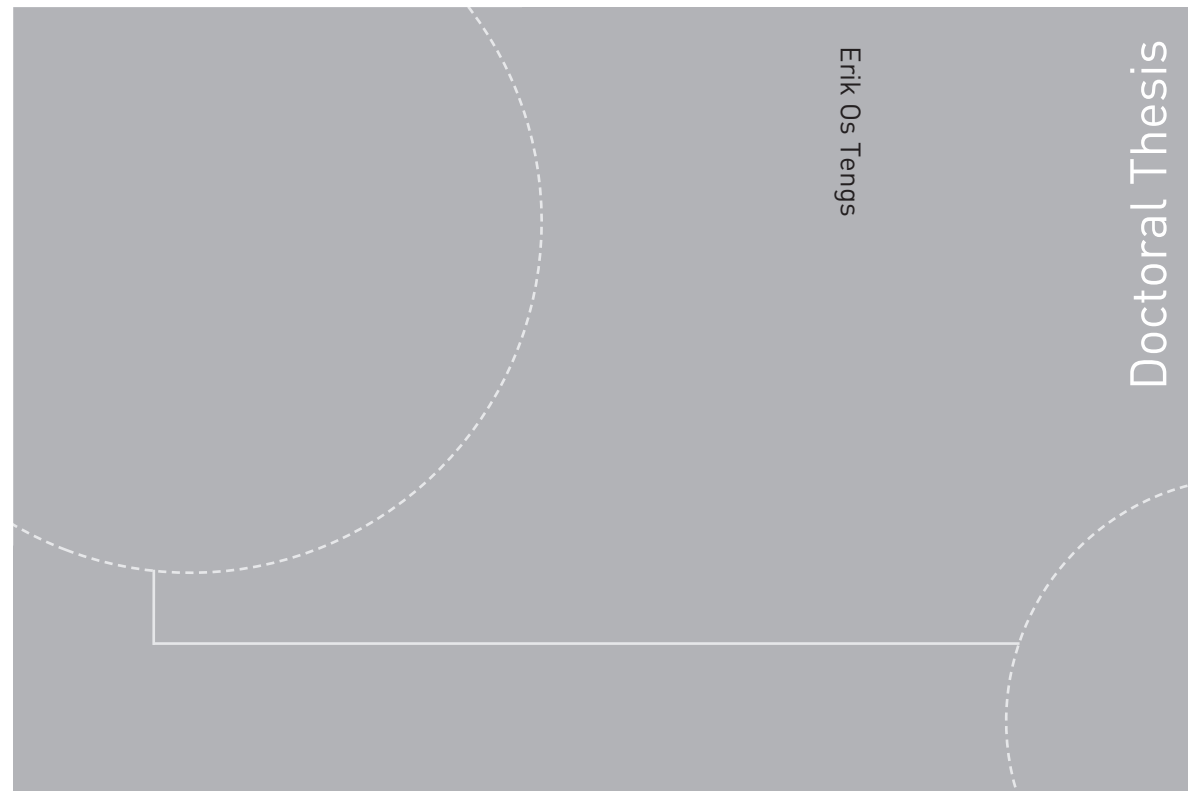


ISBN 978-82-326-4054-6 (printed version)
ISBN 978-82-326-4055-3 (electronic version)
ISSN 1503-8181



Erik Os Tengs

Numerical simulation of Fluid- Structure Interaction in high head Francis turbines

Erik Os Tengs

Numerical simulation of Fluid- Structure Interaction in high head Francis turbines

Thesis for the degree of Philosophiae Doctor

Trondheim, October 2019

Norwegian University of Science and Technology
Faculty of Engineering
Department of Energy and Process Engineering



Norwegian University of
Science and Technology

NTNU

Norwegian University of Science and Technology

Thesis for the degree of Philosophiae Doctor

Faculty of Engineering

Department of Energy and Process Engineering

© Erik Os Tengs

ISBN 978-82-326-4054-6 (printed version)

ISBN 978-82-326-4055-3 (electronic version)

ISSN 1503-8181

Doctoral theses at NTNU, 2019:229



Printed by Skipnes Kommunikasjon as

*Successful engineering is all about
understanding how things break or fail.*

- Henry Petroski

Preface

This work has been conducted at EDR&Medeso AS and the Waterpower Laboratory, Department of Energy and Process Engineering at the Norwegian University of Science and Technology. The thesis is presented as a collection of scientific papers written during the period 2016-2019. The work is part of the HiFrancis research project, funded by The Research Council of Norway.

Abstract

Renewable energy sources are becoming an integral part of the global energy mix. As hydropower can be used to stabilize the new energy market, this calls for increased demands from Francis turbines. Accurate calculation of the dynamic loads, as well as estimation of the deflection and stresses in the turbine materials, is essential for safe and reliable operation of modern turbines.

The primary objective of this work has been to investigate the phenomenon of resonance in Francis turbines. A procedure for numerically simulating this is presented, a three-step procedure consisting of calculating a fluid pressure, a damping ratio, and finally performing a coupled structural-acoustic simulation. The pressure in the runner channel is shown to be the sum of the viscous and acoustic pressure contributions, and this corresponds well with experiments.

Included in structural- acoustic simulations is the effect of added mass. This effect will lower the natural frequency of the turbine runner from the frequency of free-vibration in a vacuum. Added mass is crucial to include, as one of the critical points in a design process is to ensure that the load frequency is not equal to the natural frequency of the runner.

Obtaining accurate viscous load from CFD was shown to be straightforward. Both full turbine models and reduced geometry models predicted pressure fluctuations within a couple of percent of experimental results. The damping ratio can be obtained by a modal work approach, a one-way CFD simulation using the mode shape and frequency of the structure as input. On a simplified blade cascade this was shown to be a very successful procedure, and easy to apply to turbine-like structures as well. Another interesting finding was a nearly linear relationship between the damping and a reduced velocity parameter. This relation could be used as a rough estimate for damping if CFD analysis is not performed.

As the computational expense of performing accurate fluid and mechanical simulations are high, several model order reduction procedures have been tested. Depending on the physical domain, and solver method, different methods are used. In fluid simulations, it is seen that the most efficient way of reducing simulation time is to solve in the frequency domain. These methods are under development; however, there exist similar strategies today that can be used to reduce the geometrical domain as well.

In the structural domain, the goal is to reduce the coefficient matrices in the governing second order equations. This is done in two different ways, using a modal decomposition method, and Krylov vectors as vector space. The modal decomposition method provides a way of solving a quasi-two-way coupled fluid-structure simulation. Here an interesting added stiffness effect was observed when the flow across a hydrofoil was increased. The Krylov vector approach was shown to provide almost identical results as solving the full structural model.

Keywords: Francis turbine, Computational Fluid Dynamics, Vibration analysis, Rotor-Stator Interaction, Fluid-Structure Interaction, Model Order Reduction

Acknowledgements

I want to express my great appreciation to my supervisor, Pål-Tore Storli, and my co-supervisors Ole-Gunnar Dahlhaug and Chirag Trivedi. Their support, suggestions, and vast knowledge have guided me through the last three years. I would also like to thank all my other friends and colleagues at the Waterpower laboratory at NTNU. Rarely will you find such a pleasant working environment, both socially and professionally, something that significantly enhances the research output.

I am very grateful to all the help, guidance, and support given by my mentor Martin A. Holst at EDR&Medeso. He and the rest of my colleagues at EDR&Medeso have taught me everything I know about numerical simulations, and this work would not have been possible without their help and expertise. For that, I am truly grateful.

I had the honor of doing research with several people from different companies and institutions throughout these years. I thank you all for the interesting work and discussions and hope to collaborate further in the future.

Last but not least, I would like to thank my friends and family. Even though I am terrible at sharing what I work with, you have all been a constant support in this period. You have helped me think about other things than my research, and sometimes that is the most valuable help you can give.

Contents

Contents	ix
List of Tables	xiii
List of Figures	xvi
List of Symbols	xvii
 I	 1
1 Introduction	3
1.1 Motivation	4
1.2 Objectives	4
1.3 Outline	6
 2 Theory	 9
2.1 The Francis turbine	9
2.2 Structural failure	12
2.3 Governing equations	13

2.4	Numerical simulations	18
2.5	Fluid - Structure Interaction	20
2.6	Model Order Reduction	21
3	Summary of papers	25
4	Discussion and Further Work	37
5	Conclusion	41
	References	43
II	Selected Papers	47
Paper 1		
	<i>Francis-99: Coupled simulation of the resonance effects in runner channels</i>	
	Tengs, E., Fevåg, L.S. , Storli, P. T.	
	<i>Journal of Physics: Conference Series,</i>	
	1296 012005, 2019	49
Paper 2		
	<i>Effects of passage modelling in high head Francis turbines</i>	
	Tengs, E. , Storli, P. T. , Holst, M. A.	
	<i>Hydropower and Dams,</i>	
	E-Proceedings Hydro 2017	67
Paper 3		
	<i>Numerical simulation of the hydrodynamic damping of a vibrating hydrofoil</i>	
	Tengs, E., Bergan, C.W. , Jakobsen, KR. , Storli, P. T.	
	<i>IOP Conference Series: Earth and Environmental Science,</i>	
	240 062002, 2019	77

Paper 4***Model Order Reduction Technique Applied on Harmonic Analysis of a Submerged Vibrating Blade***

Tengs, E., Charrassier, F., Holst, M., Storli, P. T.

International Journal of Applied Mechanics and Engineering,

24.1 (2019): 131-142

89**Paper 5*****Two-way coupled simulation of the Francis-99 hydrofoil using model order reduction***

Tengs, E., Einzinger, J. , Storli, P. T.

Journal of Physics: Conference Series,

1296 012001, 2019

103**III Additional Papers****117****Paper 6*****Numerical Generation of Hill-Diagrams; Validation on the Francis99 Model Turbine***

Tengs, E. , Storli, P. T. , Holst, M. A.

International Journal of Fluid Machinery and Systems,

11.3 (2018): 294-303.

119**Paper 7*****Optimization procedure for variable speed turbine design***

Tengs, E., Storli, P. T. , Holst, M. A.

Engineering Applications of Computational Fluid Mechanics,

12.1 (2018): 652-661

131**Paper 8*****Reducing computational effort of high head Francis turbines***

Jakobsen, KR., Tengs, E., Holst, M. A.

IOP Conference Series: Earth and Environmental Science,

240 072001, 2019

143

Paper 9***High Efficiency CFD Simulations of High Head Francis Turbines***

Jakobsen, K.R., Tengs, E., Holst, M. A.

International Journal of Fluid Machinery and Systems,

Accepted for publication, 2019

155**Paper 10*****An Experimental Investigation of the Hydrodynamic Damping of Vibrating Hydrofoils***

Bergan, C. W., Tengs, E. O., Solemslie, B. W., Dahlhaug, O. G.

*IOP Conference Series: Earth and Environmental Science,***240** 062008, 2019**167****Paper 11*****Damping Measurements on a Multi-Blade Cascade with Multiple Degrees of Freedom***

Bergan, C. W., Tengs, E. O., Østby, P.T., Solemslie, B. W., Dahlhaug, O. G.

*Journal of Physics: Conference Series,***1296** 012003, 2019**179**

List of Tables

4.1 Time savings 39

List of Figures

1.1	Time versus accuracy	5
1.2	Overview of papers in thesis, and the different themes covered . .	7
2.1	A typical Francis turbine and its main components [11]	10
2.2	Onboard pressure probes in the Francis-99 runner [17]	11
2.3	The Francis-99 hydrofoil used for damping experiments [18] . . .	11
2.4	Using an S-N curve to estimate lifetime of a component	12
2.5	Damped and undamped vibration	16
2.6	First mode shape of Francis-99 hydrofoil. Deformation is exaggerated compared to true deformation in experiments. Taken from paper 5	17
2.7	Example of mesh in a structural analysis. Taken from paper 1 . . .	19
2.8	Different FSI coupling strategies	20
2.9	The concept of using a mode decomposition to express structural deformation. For illustration only, mode shapes are not real. . . .	22
2.10	Reducing the size of a structural coefficient matrix	23
3.1	Workflow for identification of resonance	26
3.2	Conceptual resonance conditions. Taken from paper 1	26

3.3	Numerical and experimental pressure in the runner channels. Viscous and acoustic pressure combined. Taken from paper 1	27
3.4	Pressure decomposition in the runner channels. Comparison with experiments . Taken from paper 1	28
3.5	Frequency spectrum of pressure from incompressible CFD. Taken from paper 2	29
3.6	Error in hydraulic efficiency at different operating conditions. Taken from paper 6	30
3.7	Change in Hill diagram after optimizing blade leading edge. Taken from paper 7	31
3.8	Damping sensitivity on pressure amplitudes. Taken from paper 1 .	32
3.9	Experimental and numerical damping on the Francis-99 hydrofoil. Taken from paper 3	33
3.10	Damping versus reduced velocity. Taken from paper 11	34
3.11	Harmonic sweep of Francis-99 hydrofoil using ANSYS and Krylov Model Order Reduction technique. Taken from paper 4	35
3.12	Two-way simulation of added stiffness effect of flowing water. Taken from paper 5	36
4.1	Dynamic Amplification Factor on Francis-99 hydrofoil. Taken from paper 4	38

List of Symbols

Latin Symbols

A	Eigenproblem square matrix [$1/s^2$]
A_x	Fourier coefficients [-]
B_x	Fourier coefficients [-]
C	Damping matrix [kg/s]
c	Speed of sound [m/s]
F	Force [N]
f	Frequency [1/s]
f_n	Natural frequency [1/s]
i	Imaginary unit [-]
K	Stiffness matrix [N/m]
M	Mass matrix [kg]
p	Pressure [Pa]
t	Time [s]
u	Deformation [m]
v	Velocity components [m/s]

v^{**} Reduced velocity [m]

w Eigenvector [m]

Greek Symbols

α Rayleigh damping coefficient [1/s]

β Rayleigh damping coefficient [s]

λ Eigenvalue [$1/s^2$]

μ Dynamic viscosity [m^2/s]

ν Kinematic viscosity [$Pa \cdot s$]

ω Angular frequency, $2\pi f$ [rad/s]

ω_n Natural angular frequency, $2\pi f_n$ [rad/s]

Φ Mode shape [m]

ϕ Phase shift [$^\circ$]

ρ Density [kg/m^3]

σ Stress [MPa]

ξ Damping ratio [-]

Abbreviations

CFD Computational Fluid Dynamics

DAF Dynamic Amplification Factor

FEM Finite Element Method

FSI Fluid Structure Interaction

HHF High Head Francis turbines

MOR Model Order Reduction

ND Nodal Diameter

NTNU Norwegian University of Science and Technology

RANS Reynolds Averaged Navier-Stokes

RSI Rotor Stator Interaction

SST Shear Stress Transport

Indices

a Acoustic

fs Fluid-structure

gv Guide vane

n Natural

r Runner

red Reduced

s Structure

Part I

Chapter I

Introduction

Rapid and widespread industrialization has caused global energy consumption to rise steadily during the last decades. At the time of writing, this global energy mix is heavily dependent on fossil fuels, with market shares in the range of $\approx 80\%$ [1]. Due to the recent focus on climate changes, this ratio is rapidly changing, and some estimates predict that renewables will be the largest energy source already by the year 2040 [2]. Most of the renewable energy sources, solar and wind, in particular, are intermittent energy sources. This means that the energy is not continuously available, as local variations in weather occur. This is usually not an issue in hydropower, due to the option of storing water in reservoirs. Hydropower is, therefore, a possible stabilizer in a future energy mix, consumed when the intermittent sources are unavailable.

Hydropower is one of the oldest renewable energy sources we have. The first documented use of water wheels dates back to the 4th century BC in India [3]. Throughout modern history, water wheels have primarily been used for agricultural purposes, and from the 19th century in the production of electricity. Amazingly, James B. Francis, the inventor of the Francis turbine, obtained a hydraulic efficiency of 90% all the way back in 1848 [4]. The efficiency has gradually improved over the years, with the introduction of numerical tools and modern production methods driving the innovation today.

In the future energy system, the following trends might be a reality;

- To stabilize the energy market, hydropower could be operated less at design conditions, and have more frequency load changes and start/stop cycles.
- To optimize hydraulic efficiency, turbine blades are made thinner, by the help of modern production methods.

The two are a potentially dangerous combination, as off-design operation using thin blades increases the demand of the turbine design, especially from a structural point of view [5]. A turbine with optimized hydraulic performance may not display optimal structural integrity.

1.1 Motivation

In recent decades, several High Head Francis turbines (HHF) have experienced failures, with blade cracks as one of the main culprits [6]. Data from a major turbine manufacturer in Norway indicates that this is not a new problem [7], it is, however, worrying that it keeps on happening with all the modern tools available today. From field measurements, it is also known in the industry that the primary fluctuating pressure component in an HHF originates in a phenomenon called Rotor-Stator Interaction (RSI), formally defined later [8].

To investigate this problem, the HiFrancis research project was started, under which this thesis is a part [9]. The HiFrancis research project, funded by the Norwegian Research Council, is a collaborative project in the Norwegian hydropower industry, where the goal is to understand the physics behind the RSI and resonance effects better and to validate the numerical methods available today.

1.2 Objectives

The overall objective is to understand the underlying physics behind resonance in turbine runners and to be able to simulate the phenomenon accurately. This goal can be broken down into the following objectives;

- Accurate calculation of the fluid loads in the runner
- Accurate calculation of the hydrodynamic damping

Accurate prediction of the fluid loads is, of course, necessary to obtain a proper estimation of the material stresses. In addition, the hydrodynamic damping is a critical input to any structural simulation. These two objectives and the coupling between them are the main focus of the research. Additionally, as the project has an industrial interest, an effort will be put into reducing simulation time wherever possible, ideally without compromising much on the accuracy.

To achieve the above objectives, the following specific activities are performed.

- The Francis-99 model runner at the Waterpower Laboratory in Trondheim has several pressure sensors both in the volute, distributor and draft tube, as well as onboard the runner. The pressure values, and importantly, the amplitude of the fluctuating pressure, will be used throughout the thesis as validation data for different numerical procedures.
- It is important to understand the physics behind the hydrodynamic damping phenomenon to perform accurate structural simulations. The hydrofoil test rig at the Waterpower Laboratory in Trondheim has been used to investigate this. Data from experiments will be used to validate the numerical methods used and to understand the different phenomena observed.
- Different methods for model order reduction will be used to speed up simulations.

Limitations. It should be stated explicitly that the overall goal is to obtain acceptable accuracy in an industrial time-frame, rather than perfect results if this implies excessive computational cost. Conceptually, in figure 1.1, t_1 will be preferred to t_2 if the accuracy is of the same order.

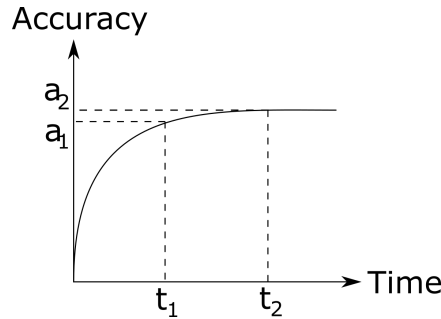


Figure 1.1: Time versus accuracy

This implies certain limitations concerning the simulations performed. Specifically, the turbulence models are limited to RANS models, and incompressible flow is assumed in all fluid simulations. Another limitation in this work is that the damping simulations, and preceding experiments, have been done on simplified geometries, not a turbine runner.

1.3 Outline

This thesis is presented as a collection of scientific papers. The main research material in this thesis is therefore found in the papers in Part II. The material is, however, presented and intended to be read as one connected work, where all the papers support the overall goal of the research. The thesis will have the following outline;

Chapter 2 will present basic theory and governing equations for the different topics covered. This section is not intended to be a comprehensive review of all theory, rather an introduction of the different themes. More information on the research methodology can be found in the attached papers.

Chapter 3 will present the key findings in the papers, link the different papers together, and present a proposed workflow for simulating the resonance phenomenon.

Chapter 4 will present a general discussion, and bring forward some interesting topics for future work.

Chapter 5 will present conclusions from the work.

Part II contains the scientific papers. The papers are divided into *selected* papers and *additional* papers. The selected papers cover the key components of the thesis, whereas the additional papers are various in-depth numerical analyses into the different topics covered, as well as experimental work. Figure 1.2 shows an overview of the papers in this thesis; details will be presented in chapter 3. The arrows indicate how the papers from different topics are linked together.

The suggested approach for the reader is not to read all the papers without context, instead use the summary and discussion chapters as an introduction to the results, and read the papers that catch the readers interest for further information.

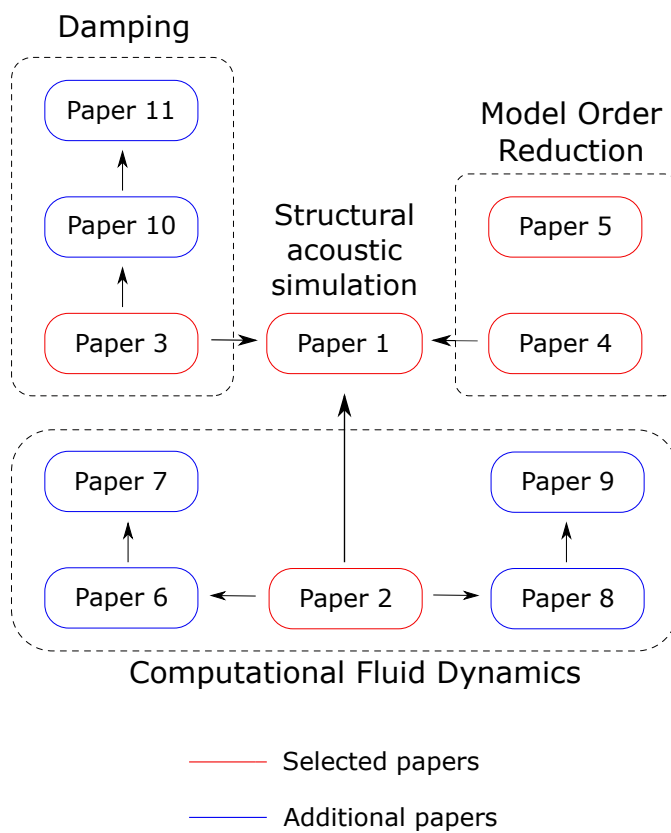


Figure 1.2: Overview of papers in thesis, and the different themes covered

Chapter II

Theory

- ◇ This chapter presents the basic theory and equations needed to follow the discussion.
-

2.1 The Francis turbine

A hydraulic turbine is a machine designed to convert kinetic and/or potential energy in water flow into rotational mechanical energy. Many different turbine types exist today, the main types being Francis, Kaplan, and Pelton turbines, their usage is dependent on the flow rate and the available water head at the individual site. In this thesis, only Francis turbines will be considered. The Francis turbine is the most used turbine type in the world, operating in a large range of water heads [10]. The high head Francis turbine ($H > 300\text{m}$) is of special interest, as several turbines of that type have had failures lately. Figure 2.1 shows a typical Francis turbine, with its key components [11]. The spiral casing, stay vanes and guide vanes direct high-pressure water into the turbine runner. The runner extracts energy from the water, onto the rotating shaft connected to a generator. Several types of pressure pulsations can be found in a Francis turbine, ranging from draft tube swirl to vortex shedding oscillations [12]. In High Head Francis turbines, however, it has been found that the dominating pressure component originates in Rotor-Stator Interaction (RSI) [8].

Rotor Stator Interaction. RSI is a phenomenon occurring in most rotating machinery. Every time a rotating component (runner blade) passes a stationary com-

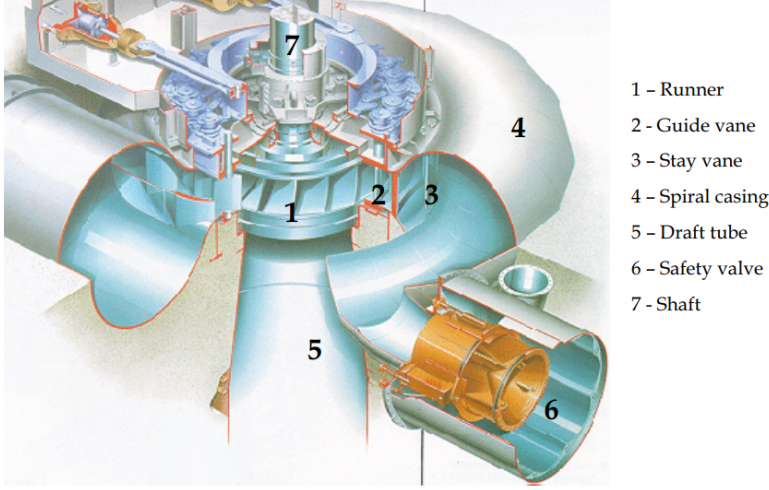


Figure 2.1: A typical Francis turbine and its main components [11]

ponent (guide vane), a pressure pulse is created due to the acceleration of the surrounding fluid. As this phenomenon has been shown to be dominating in High Head Francis turbines, RSI will be the sole focus of this thesis. Depending on the runner speed f_{runner} , the number of guide vanes Z_{gv} , and the number of runner blades Z_r , one can calculate the dominating load frequencies f_{RSI} as well as the spatial distribution of the load, referred to as the Nodal Diameter, ND [13, 14].

$$f_{RSI} = n \cdot f_{runner} \cdot Z_{gv}, \quad n = 1, 2, \dots, \quad (2.1)$$

$$ND = mZ_r \pm nZ_{gv}, \quad m, n = 1, 2, \dots, \quad (2.2)$$

n, m are integers denoting the higher harmonics, but usually, only the first couple are relevant as the high-frequency modes are damped out.

The Francis-99 turbine. At the Norwegian University of Science and Technology (NTNU), a model turbine geometry and experimental data have been made available to the public. The turbine, named the Francis-99 turbine, has been the focus of extensive experimental and numerical research, e.g., in the Francis-99 workshops for numerical engineers [15, 16].

The Francis-99 runner is a high head Francis turbine with a specific speed of 0.27 and consists of 15 main and 15 splitter blades. The model has on-board pressure probes that can measure the pressure fluctuations inside the runner. Figure 2.2 shows the placement of the pressure probes along one runner channel. The experimental results from these probes are the basis for the validation of the numerical methods used in this work.

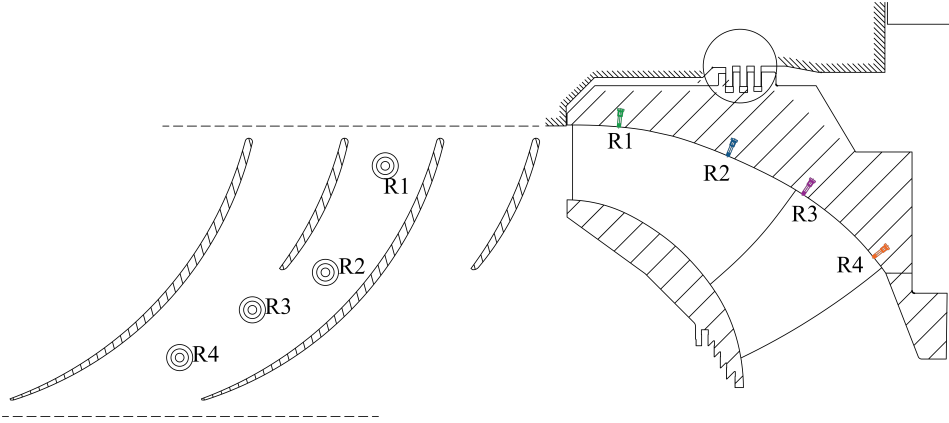


Figure 2.2: Onboard pressure probes in the Francis-99 runner [17]

Additionally, in order to study the phenomenon of damping, several hydrofoils have been tested in the Waterpower Laboratory at NTNU. Figure 2.3 shows the design of one of the foils, henceforth referred to as the **Francis-99 hydrofoil**. The results from these experiments have been used as validation in the numerical simulation of damping. Damping is a crucial parameter in structural simulations, and understanding this mechanism can help to prevent structural failure.

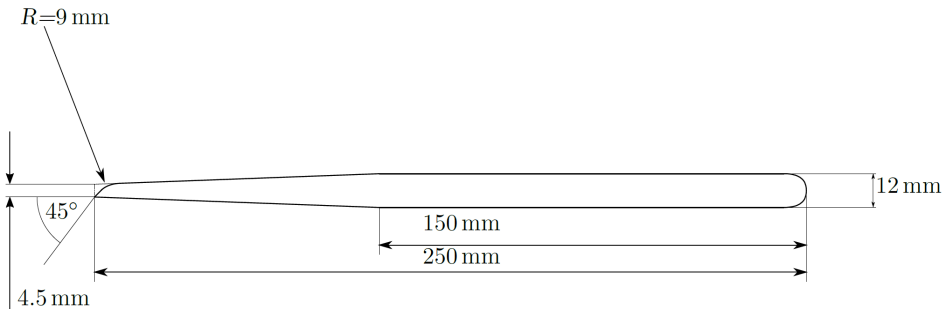


Figure 2.3: The Francis-99 hydrofoil used for damping experiments [18]

2.2 Structural failure

As mentioned in the previous sections, several types of pressure loads can be found in a turbine, potentially causing material failure. Structural failure can broadly speaking be divided into failures due to static loads and dynamic loads [19]. A static load exceeding the yield strength of the material will cause failure; however, this phenomenon is rare in turbines and will not be discussed. The second failure mode, dynamic loading, and **fatigue** is highly relevant.

Fatigue. Fatigue is material failure due to repeated, cyclic loads [20]. The stress levels in the material are usually low, as opposed to plastic deformation under high stresses.

The integrated fluctuating pressure in the runner will create corresponding cyclic stresses in the material (see figure 2.4 left). An S-N curve can be used to estimate how many cycles a material can withstand at a specific stress level [20], see figure 2.4 right.

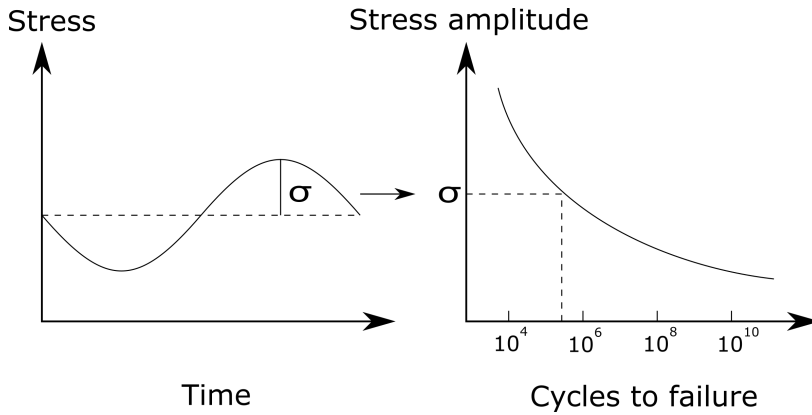


Figure 2.4: Using an S-N curve to estimate lifetime of a component

If a structure is subjected to several different stress conditions, the accumulated damage can be estimated by e.g., the Miner-Palmgren rule, eq. 2.3 [21],

$$\sum_{i=1}^k \frac{n_i}{N_i} = C \quad (2.3)$$

where n_i is the number of stress cycles at load i , and N_i is the number of stress

cycles to failure at load i . When $C = 1$ one assumes that the material is at the end of its lifetime, although there are significant uncertainties related to the S-N curves used to extract the above parameters. Actual fatigue calculation is not in the scope of this work, the focus is instead on the correct calculation of the loads in the runner, and prediction of the resonance phenomenon.

Resonance. To correctly calculate the loads in the runner, the phenomenon of resonance has to be considered. Resonance is probably one of the most well-known phenomena in structural mechanics. It occurs when two conditions are fulfilled; the frequency of a structural load is equal or in the vicinity of the structural natural frequency, and the spatial distribution of the load matches the structural eigenmode [19]. In such cases, even small forces can cause catastrophic structural failures. Even though resonance is a well-known issue, avoiding it may not be straightforward. It is dependent on the correct calculation of the loads as well as the natural frequencies and eigenmodes of the structure. In a turbine, a phenomenon called **added mass** complicates this calculation.

Added mass. When a submerged object is accelerating, the surrounding fluid has to be displaced. Fluid forces will, in such cases, oppose the motion of the object, and the resulting effect can be modelled as if the object mass is larger. This is referred to as the added mass effect [22]. The reason why the added mass effect is important is that the natural frequency of an object is inversely proportional to the square root of its mass. Therefore, objects submerged in water will have a lower natural frequency than when tested in air, which can complicate the resonance calculations.

Summarizing the phenomena described above, the fluid pressure in the runner, combined with the runner vibrational characteristics (eigenmodes and eigenfrequencies) will determine whether resonance is likely and determine the stresses and strains in the material. Indications of resonance were found experimentally in the Francis-99 runner, in the second harmonic of the RSI pressure. This makes the model ideal for validation of numerical procedures.

2.3 Governing equations

The preceding sections present some fundamental phenomena in fluid and structural mechanics. Fluid loads, structural eigenfrequencies, added mass effects, and more are all critical inputs for calculating the actual structural response. The following sections present the governing equations in the various physical domains.

Fluid Mechanics. The governing equations of fluid flow are the well-known Navier-Stokes equations, in this case, limited to the iso-thermal, incompressible case. The continuity and momentum equations can be written as follows [22];

$$\frac{\partial v_j}{\partial x_j} = 0 \quad (2.4)$$

$$\frac{\partial v_i}{\partial t} + v_j \frac{\partial v_i}{\partial x_j} = -\frac{1}{\rho} \frac{\partial p}{\partial x_i} + \nu \frac{\partial^2 v_i}{\partial x_j \partial x_j} \quad (2.5)$$

where v_i denotes the velocity components, p the pressure, ρ the density and ν the kinematic viscosity of the fluid. Body forces are omitted, and Einstein notation is used.

In many engineering applications, the flow may exhibit chaotic or *random* fluctuations on top of the bulk motion of the fluid. This phenomenon is called **Turbulence** and is one of the oldest unsolved problems in physics [23]. In this work, turbulence has not been studied in detail; a brief overview follows. A dimensionless quantity called the Reynolds number can be used to classify a flow as either laminar or turbulent [22];

$$Re = \frac{vL}{\nu} \quad (2.6)$$

where v is the flow velocity, L a characteristic length and ν the kinematic viscosity. Depending on the type of flow, different limits can be defined; in this thesis, the flow is assumed to be turbulent. The reason why turbulent flow appears random is that the flow is very sensitive to changes in initial and boundary conditions [24]. The practical way of dealing with turbulence is to use the *Reynolds Averaged Navier-Stokes* (RANS) equations. Let the flow at a given time be decomposed into a mean component and a fluctuating component,

$$v_i = \bar{v} + v' \quad (2.7)$$

where overbar notation denotes the mean, and prime notation denotes fluctuation. If eq. 2.7 is inserted into the Navier-Stokes equations, and averaged, we get the RANS equations:

$$\frac{\partial \overline{v_j}}{\partial x_j} = 0 \quad (2.8)$$

$$\frac{\partial \overline{v_i}}{\partial t} + \overline{v_j} \frac{\partial \overline{v_i}}{\partial x_j} = -\frac{1}{\rho} \frac{\partial p}{\partial x_i} + \nu \frac{\partial^2 \overline{v_i}}{\partial x_j \partial x_j} - \frac{\partial}{\partial x_i} \overline{v'_i v'_j} \quad (2.9)$$

where the difference from equation 2.5 is the last term in the momentum equations, the Reynold Stresses. In the RANS equations, there are more unknowns than equations, and therefore, the Reynolds stresses have to be modelled. Different models frequently used in engineering problems include the $k - \epsilon$ and the $k - \omega$ model as well as the *SST* model [25, 26, 27], all with strengths and weaknesses in different areas of the flow. The industry standard *SST* model is used throughout this work. Further details regarding turbulence are beyond the scope of this thesis; more information can be found in the book by Pope [24].

Structural Mechanics. On the structural side, this thesis primarily covers vibration and harmonic motion. The governing equation for such phenomena is as follows [19]:

$$M\ddot{u} + C\dot{u} + Ku = F \quad (2.10)$$

where M, C, K, F is the mass, damping, stiffness and force coefficient matrices. In the case of harmonic motion, $u = u_0 e^{st}$, with s being a complex number, eq 2.10 can be re-written to:

$$(s^2 M + sC + K)u_0 = F_0 e^{i\phi} \quad (2.11)$$

where u_0 and F_0 are in general complex, and ϕ is a potential phase shift between the load and the deflection. Assume zero external forces, and s can be solved for:

$$s = -\omega_n \xi \pm i\omega_n \sqrt{1 - \xi^2} \quad (2.12)$$

where $\omega_n^2 = K/M$ is the natural angular frequency and $\xi = C/(2M\omega_n)$ is the damping ratio. For undamped vibration, $\xi = 0$, the response is pure harmonic motion:

$$u = u_0 e^{i\omega_n t} \quad (2.13)$$

and for damped vibration, $0 < \xi < 1$, the response becomes [28]:

$$u = u_0 e^{-\omega_n \xi t} \pm i \omega_n t \sqrt{1 - \xi^2} \quad (2.14)$$

The latter is harmonic motion enveloped by a decaying exponential function, see figure 2.5 for the different vibration types. Overdamped vibration, $\xi > 1$, will not be considered.

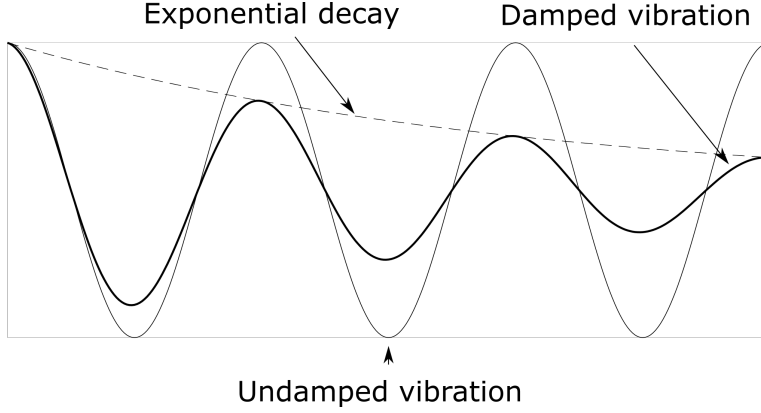


Figure 2.5: Damped and undamped vibration

For modal analysis, the unforced, undamped version of eq. 2.10 is used:

$$K u_0 = \omega_n^2 M u_0 \quad (2.15)$$

Which can be linked to the standard eigenvalue problem,

$$A w = \lambda w \quad (2.16)$$

where λ are the eigenvalues and w the eigenvectors of the system. The square matrix A represents the system characteristics, in this case the mass and stiffness matrices. In structural mechanics, it is customary to refer to eigen/natural frequencies ω_n , rather than eigenvalues. The relation is simple, $\lambda = \omega_n^2$, as can be

seen from equation 2.15. The physical interpretation of an eigenvector is the mode shape of a structure. A mode shape Φ is the spatial distribution of the deformation during harmonic motion, see figure 2.6 for the first bending mode of the Francis-99 hydrofoil. Note that the mode shapes from a modal analysis are of arbitrary length. This implies that a mode shape may look non-physical, but this is purely a mathematical artifact from the definition of eigenvalues and eigenvectors. One important property with mode shapes is that they are all linearly independent [28].

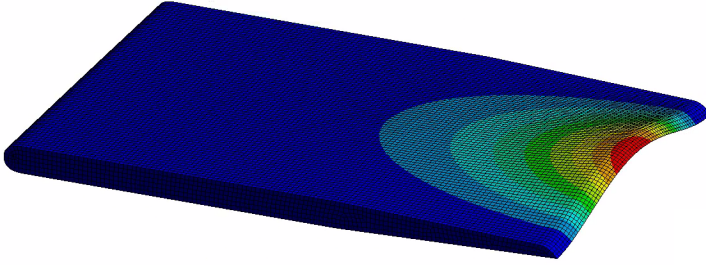


Figure 2.6: First mode shape of Francis-99 hydrofoil. Deformation is exaggerated compared to true deformation in experiments. Taken from paper 5

Damping. The damping matrix in equation 2.10 is hard to determine a priori. A typical way of thinking of damping is the fact that it is an energy dissipative process. If one were to calculate the work over one vibrational period of the motion of equation 2.10, $W = \int F dx$, assuming harmonic motion and where x is the vibrational distance, only the damping term would provide a non-zero result [29]. This fact, coupled with the definition of the damping ratio, $\xi = C/(2M\omega_n)$ will provide an estimate for the damping, given that the work, W , on the structure can be calculated, and the maximum deflection, u_0 , is known:

$$\xi = \frac{W}{2\pi M\omega_n^2 u_0^2} \quad (2.17)$$

This procedure, a *modal work* or *flutter* approach, will be used to obtain an estimate of the damping ratio numerically.

Another way of assessing the damping is to use the general representation of damped oscillating motion:

$$u = u_0 e^{-\omega \xi t} \cos(\omega t) \quad (2.18)$$

and extract the damping from the decaying exponential function, see also figure 2.5.

Acoustics. In fluids where the interesting variable is not the advective, bulk motion of the fluid, but the propagation of waves, acoustic theory can be used. The wave equation models how information spreads through a medium [30]:

$$\nabla^2 p' - \frac{1}{c^2} \frac{d^2 p'}{dt^2} + \nabla \cdot \left[\frac{4\mu}{3} \nabla (\nabla \cdot v') \right] = 0 \quad (2.19)$$

where p', v' is a pressure and velocity fluctuation respectively, c is the speed of sound, and μ is the dynamic viscosity. The above equation can be written in matrix form and coupled with the standard second order structural equation, eq 2.10, to the Eulerian displacement formulation below [31]:

$$\left(-\omega^2 \begin{bmatrix} M_s & 0 \\ M_{fs} & M_a \end{bmatrix} + i\omega \begin{bmatrix} C_s & 0 \\ 0 & C_a \end{bmatrix} + \begin{bmatrix} K_s & K_{fs} \\ 0 & K_a \end{bmatrix} \right) \begin{Bmatrix} u \\ p \end{Bmatrix} = \begin{Bmatrix} F_s \\ F_a \end{Bmatrix} \quad (2.20)$$

The Eulerian displacement equation solves for the acoustic pressure propagation in the acoustic domain, the structural deformation, and the interaction between the domains, i.e., the added mass effect.

2.4 Numerical simulations

The governing equations presented in the previous section cannot be solved analytically for anything other than trivial problems. In most real-life cases, the equations have to be discretized in time and space and be solved using either direct or iterative solver methods, depending on the problem. See figure 2.7 for a typical spatial discretization (mesh) in a structural analysis. There exists a vast amount of literature on the numerical implementation of the above equations, most of which are beyond the scope of this thesis. Some principles will be presented briefly.

Computational Fluid Dynamics. Computational Fluid Dynamics (CFD) is becoming the third pillar of fluid mechanical research, alongside analytical approaches and experimental work. In CFD, the governing equations of fluid flow are solved

numerically by discretizing in time and space and solved usually with an iterative approach. Interested readers will find a great introduction to CFD in the book by Ferziger and Peric [32].

The commercial CFD software ANSYS® CFX® is used throughout this thesis. A hybrid finite-element/finite-volume approach is used to discretize the Navier-Stokes equations 2.5. Control volumes are created around the mesh vertices, providing the conservation properties of the Finite Volume Method. The use of Finite-Element shape functions approximates the variation within each volume.

CFX uses a fully coupled pressure-velocity solver strategy. This means that the usual pressure correction procedure is not used, and the momentum equations are solved with the pressure equation in the same matrix. This procedure is computationally more expensive per iteration, but will usually converge fast, as only the non-linearities need to converge. The specific implementation in CFX is an industry secret and not available to the author.

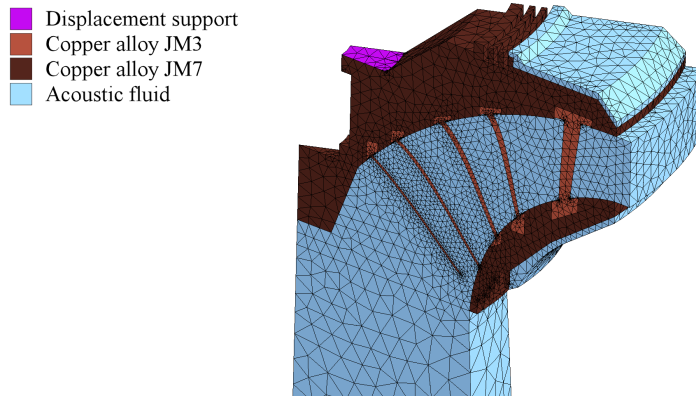


Figure 2.7: Example of mesh in a structural analysis. Taken from paper 1

Finite Element Method. Finite Element Method (FEM) is the equivalent to CFD in the structural domain. The famous FEM book by Zienkiewicz is highly recommended for interested readers [28].

The commercial FEM software ANSYS® Mechanical® is used throughout this thesis. A FEM method usually creates a set of algebraic equations by discretizing the domain and expressing the governing equations using an energy minimization technique. The global set of equations from the FEM procedure can be solved with either a direct solver or an iterative solver.

2.5 Fluid - Structure Interaction

Fluid-Structure Interaction (FSI) is a quite broad term, including everything from simple fluid pressure load on structures, to bio-medical simulations of organs. To separate the different procedures, the following grouping is proposed, see [33] for more:

- One-way coupling: Using two solvers, e.g., a CFD code and a FEM code, one domain is solved first, then information is passed to the second domain and solved. There is no feedback to the first system. See figure 2.8 a).
- Two-way coupling: Using two solvers, e.g., a CFD code and a FEM code, one domain is solved first, then information is passed to the second domain and solved. There is feedback to the second system, and usually, an iterative loop to converge the information transfer. See figure 2.8 b).
- Fully coupled: The domains are modelled using a common set of equations, and equal discretization. The equations are solved simultaneously. See figure 2.8 c).

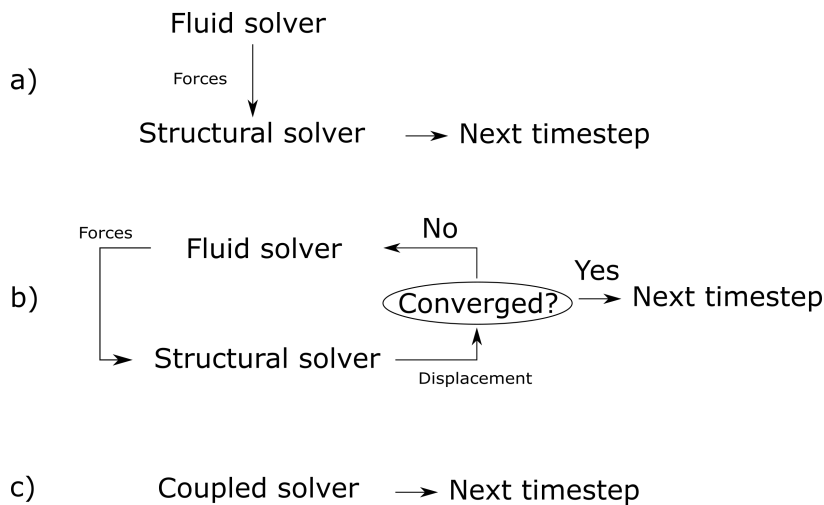


Figure 2.8: Different FSI coupling strategies

In commercial software, the first procedure is widely used, e.g., to map pressure loads onto a structure. The second procedure is rarely used due to excessive

computational demands. The third is primarily used for non-viscous flow, i.e., acoustic-structural simulations. All methods will be investigated in this thesis.

2.6 Model Order Reduction

Model Order Reduction (MOR) in this thesis will be defined as a method of reducing the complexity of a simulation. Metamodels, surrogate modeling, and other methods based on input/output relations are not covered. The methods used are different based on what physical domain it is applied to, see a brief introduction below.

Fourier Series. A Fourier series is one of the most common ways of expressing a periodic signal [34]. The idea is that a repeating signal can be decomposed into a weighted sum of harmonic (sinusoidal) functions:

$$f(t) = A_0 + \sum_{n=1}^{\infty} A_n \cos(n\omega t) + B_n \sin(n\omega t) \quad (2.21)$$

where the coefficients A_0, A_n, B_n are defined as follows,

$$A_0 = \frac{1}{T} \int_t^{t+T} f(t) dt \quad (2.22)$$

$$A_n = \frac{2}{T} \int_t^{t+T} f(t) \cos(n\omega t) dt \quad (2.23)$$

$$B_n = \frac{2}{T} \int_t^{t+T} f(t) \sin(n\omega t) dt \quad (2.24)$$

In rotationally symmetric geometries like a turbine runner, this becomes a great tool for reducing the computational domain. Let us assume that the pressure field in a domain is periodic in time, $p(r, \rho, z, t) = p(r, \rho, z, t + T)$ and in space, $p(r, \rho, z, t) = p(r, \rho + \Delta\rho, z, t)$. If only a section of the runner is modeled, the periodic boundaries could then be expressed using Fourier series. Alternatively, in a more sophisticated manner, the conservation variables in eq. 2.5 can be rewritten as a Fourier series to remove the time dependency. The set of equations can then be solved in the frequency domain; a method referred to as Harmonic Balance Method [35, 36].

Modal Decomposition. In a modal decomposition, the structural motion is assumed to be a linear combination of its mode shapes [28]:

$$u(t) = \sum_n^N q_n(t) \Phi_n \quad (2.25)$$

where u is the deflection, q is the modal amplitude, and Φ is the mode shape obtained from a modal analysis. Visually, using a fixed beam, it can be illustrated as in figure 2.9.

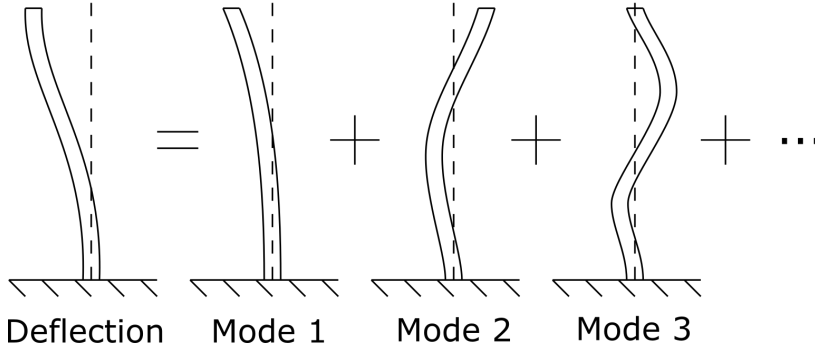


Figure 2.9: The concept of using a mode decomposition to express structural deformation. For illustration only, mode shapes are not real.

By inserting eq. 2.25 in eq. 2.10 and pre-multiplying with the mode shapes, the equation can be re-written as:

$$m_i \ddot{q} + c_i \dot{q} + k_i q = \overline{f}_i \quad (2.26)$$

where $m_i = \Phi_i^T M \Phi_i$ and so on. The orthogonality of the modes ensures that $\Phi_i^T M \Phi_j = 0$ for $i \neq j$, and makes eq. 2.26 a set of linearly independent equations. The underlying assumptions include linear behaviour and that the Rayleigh damping model is used [37]:

$$C = \alpha M + \beta K \quad (2.27)$$

where α, β are the Rayleigh damping coefficients. Usually, only the low-frequency modes are included in the above approach. Using the Rayleigh damping model, it

is easy to show this. The damping ratio can be written as:

$$\xi = \frac{C}{2M\omega_n} = \frac{1}{2\omega_n}(\alpha + \omega_n^2\beta) \quad (2.28)$$

where we see that the high-frequency modes are damped out.

Krylov Subspaces. While modal decomposition is an intuitive, physical basis for model order reduction, Krylov subspaces are more abstract. The principle is the same; you want to reduce the size of a coefficient matrix by the use of some basis, see figure 2.10;

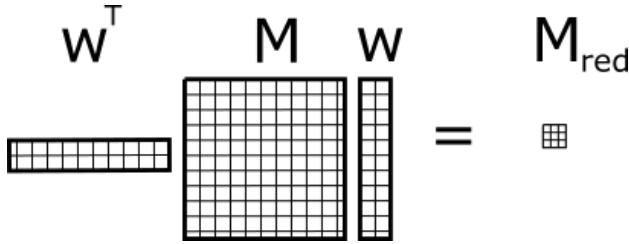


Figure 2.10: Reducing the size of a structural coefficient matrix

or mathematically,

$$w^T M w = M_{red} \quad (2.29)$$

where w is some vector. In a modal decomposition, these vectors are the eigenvectors of the system (recall $m_i = \Phi_i^T M \Phi_i$), here Krylov vectors are used. A Krylov vector is an intelligently created vector that satisfies moment matching conditions of the transfer function of the system. Put simply, if the transfer function of a system were to be expressed using a series expansion (think Taylor or Fourier series), then a Krylov subspace of order m matches the first m terms in the series expansion. The mathematics is outside of the scope of this thesis; interested readers can find more in, e.g., [38, 39].

The resulting reduced coefficient matrices are full, as opposed to the diagonal matrices from the modal decomposition. The matrices are however very small, and the final system, eq. 2.30, can be solved using a direct solver with negligible computational effort.

$$M_{red}\ddot{u} + C_{red}\dot{u} + K_{red}u = F_{red} \quad (2.30)$$

An advantage of using Krylov vectors as a way of reducing the structural system is that arbitrary damping, gyroscopic effects, and more could be included, effects that destroy the symmetry in the original system. This is not allowed using the modal decomposition method.

Chapter III

Summary of papers

- ◇ This chapter summarizes the results from the different papers and shows how the papers are connected. A workflow for assessing the resonance risk is presented.
-

This thesis is paper-based, meaning it consists of a series of scientific papers. The author has been involved in research into a variety of topics, and this chapter will serve as a summary of the findings in the research, as well as a guide for how the papers are interconnected. The presented research can be divided into three main topics, *CFD*, *Damping* and *Model Order Reduction*. All of these topics have been researched to better understand the key aspects of an *Acoustic Harmonic Simulation*, where potential resonance issues in high head Francis turbines can be quantified. Please refer to figure 1.2 to get an overview of the different papers in this thesis and how they interact. As well as being divided into different topics, the papers in figure 1.2 are also divided into *selected* and *additional* papers. This is to concretize which papers are critical to the main goal of the thesis, resonance issues in turbine runner channels, and which are supporting papers. The additional papers cover in-depth studies into the different topics covered, touches upon new solver methods in CFD, implements conceptual optimization schemes, presents experimental work, and more.

As discussed in chapter 1, the main objective of the research has been to investigate the issue of resonance in high head Francis turbines. Figure 3.1 shows a proposed workflow for assessing this phenomenon.

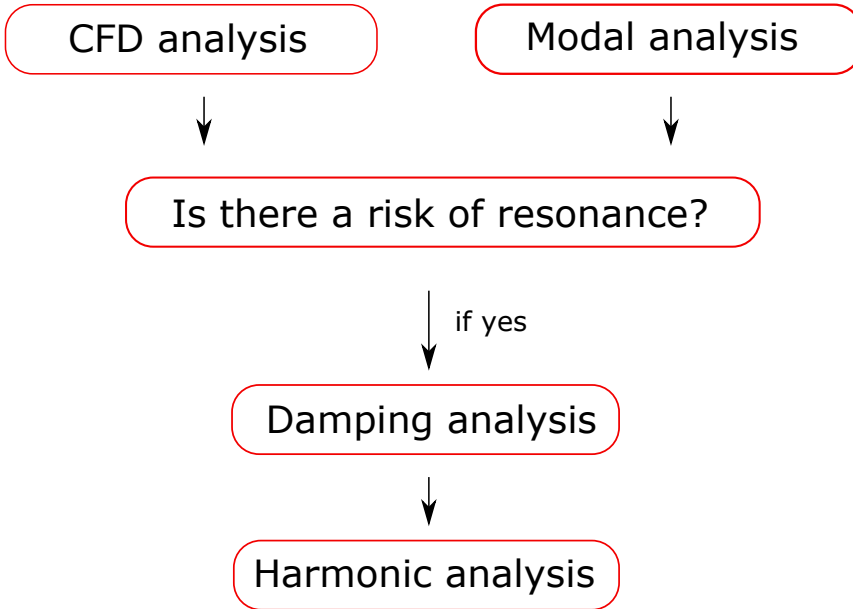


Figure 3.1: Workflow for identification of resonance

In any engineering problem regarding resonance, one has to first get an overview of the fluctuating load and the vibrational characteristics of the structure. In this case, this is done using a CFD analysis and a modal analysis, respectively. The load characteristics can also be calculated analytically by eq. 2.1-2.2. As mentioned in the theory chapter, resonance occurs if the load shape and frequency matches the mode shape and natural frequency. Figure 3.2 shows the conceptual idea, where only load F_1 can excite motion in the structure, even if the frequency of F_2 matches its eigenfrequency.

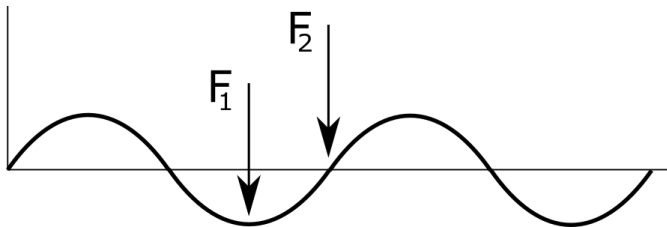


Figure 3.2: Conceptual resonance conditions. Taken from paper 1

To answer the question "Is there a risk of resonance", the load has to be compared with the results from the modal analysis. Rarely will both the frequency and the spatial distribution of the load perfectly match the vibration of the structure. Engineering experience and judgment will therefore be applied and assess whether the dynamic effects are critical for the operation of the turbine. To *quantify* the dynamic effects, the next step is a harmonic analysis where the fluctuating load is applied to the structure, and the proper structural response is calculated.

In **Paper 1**, the resonance phenomenon in runner channels was simulated using a coupled structural-acoustic simulation. A viscous pressure from an incompressible CFD analysis was loaded on the structure as a load, and acoustic elements modelled both the added mass effect and the acoustic pressure propagation in the domain. A harmonic analysis is performed in the frequency domain, meaning no time-stepping procedure. This implies that the load from the CFD analysis had to be expressed as a Fourier Series, which represents a periodic signal as a sum of trigonometric functions, see section 2.6. This representation is frequency based and is loaded onto the structure. The total numerical pressure in the runner channel is therefore the sum of the viscous pressure load and the resulting acoustic pressure from the harmonic analysis. Figure 3.3 shows a comparison with experiments of the second pressure harmonic through the Francis-99 runner.

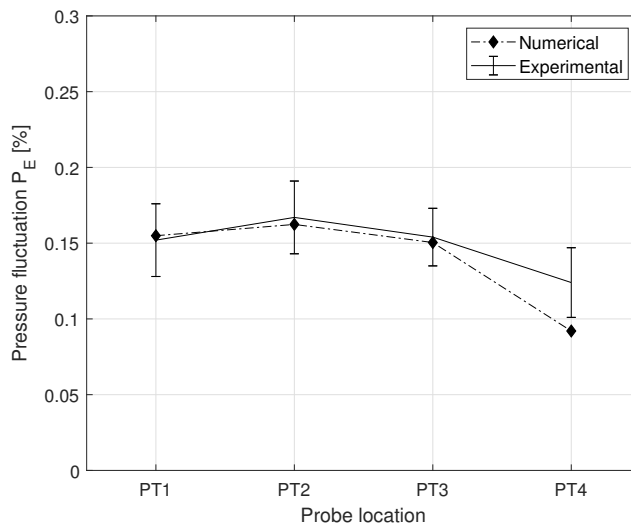


Figure 3.3: Numerical and experimental pressure in the runner channels. Viscous and acoustic pressure combined. Taken from paper 1

Figure 3.4 shows a decomposition of the second pressure harmonic into viscous and acoustic contribution. The viscous pressure is linearly decreasing through the runner channels, while the acoustic pressure is seen to *increase* in some of the pressure probes. Viscous and acoustic pressure of the same order may indicate resonance conditions, as far away from resonance, the contribution from the acoustic pressure would be close to zero. The viscous component from CFD is seen to almost perfectly match the experimental results, while there are some differences in the acoustic pressure, especially at the outlet. Paper 1 is discussing the reason for the discrepancy, and identified the most critical inputs to the simulation; 1) a viscous pressure from a CFD analysis, and 2) the damping ratio. The specific geometry of the Francis-99 runner was also a source of uncertainty. The acoustic pressure amplitudes were found to be linearly dependent on the viscous pressure, and non-linearly dependent on the damping ratio. To investigate these parameters in more detail, we refer to the other papers in the thesis, starting with the CFD analysis.

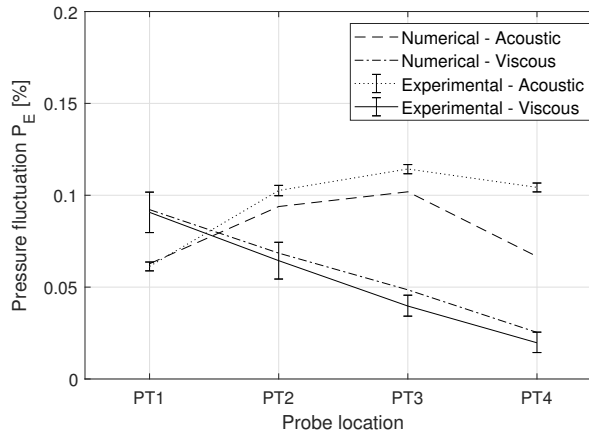


Figure 3.4: Pressure decomposition in the runner channels. Comparison with experiments . Taken from paper 1

Computational Fluid Dynamics. A CFD analysis is the basis for turbine design. Hydraulic efficiency, torque, power, and more are standard outputs from simulations. In terms of fatigue, the oscillating pressure values are also of interest. However, for turbines close to resonance conditions, a CFD analysis alone will underpredict the pressure fluctuations. Figure 3.5 is taken from **Paper 2**, where the experimental pressure fluctuation inside the runner channels was compared

with numerical models. Both full turbine and passage models were tested, with a passage model being a simulation where only a few of the runner passages are simulated to speed up simulation time. This method is using a Fourier Series representation on the periodic boundaries to allow for variations in the circumferential direction.

Figure 3.5 is very telling. Firstly we see how well the first harmonic of the pressure is predicted, both in full turbine simulations (360 simulation), and passage models (FG Fourier Inlet). Secondly, we see how *bad* the second harmonic is predicted. Later, in paper 1, we learned that the "missing" pressure component in the second harmonic is the acoustic contribution of the surrounding water. Figure 3.5 is therefore an indication of resonance in the runner channels, and illustrates the background of the whole project; *an incompressible CFD analysis alone will fail to predict correct pressure load*. The fact that the first pressure harmonic is so well predicted, however, validates the CFD simulations to the point that we trust the viscous pressure to be correct. This assumption was later validated, see e.g., figure 3.4 where the viscous pressure corresponds well with the experimental data even at the second pressure harmonic, the harmony where a resonance phenomenon is observed.

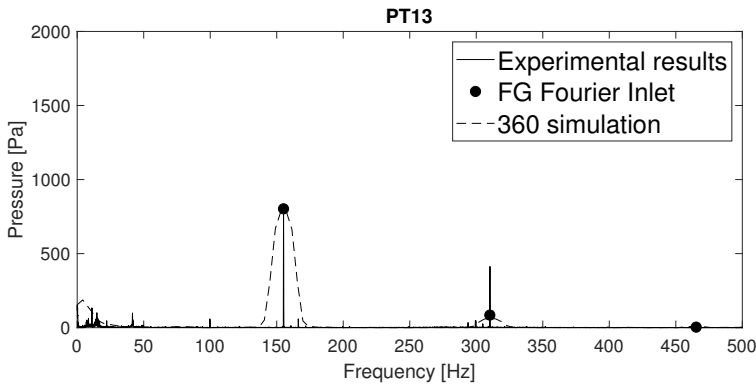


Figure 3.5: Frequency spectrum of pressure from incompressible CFD. Taken from paper 2

From the base case CFD analysis, the CFD work split in two directions. In the first direction, **Paper 6** and **Paper 7** aims to prove that simple CFD analyses are sufficient for optimization of turbine design. The argument is that global parameters like head and torque are relatively easy to predict compared to local phenomena like the shedding of vortices. Paper 6 creates a foundation by valid-

ating the rapid generation of Hill-Diagrams. In this paper, steady CFD analyses were performed to extract the hydraulic efficiency at different operating points. The simulations were compared with experimental results from the Waterpower Laboratory, in terms of a relative error between the simulated hydraulic efficiency and the experimental one, see figure 3.6. There is an overall good match with the experimental results, even though the simulations performed were simplified, with each simulation performed in just minutes.

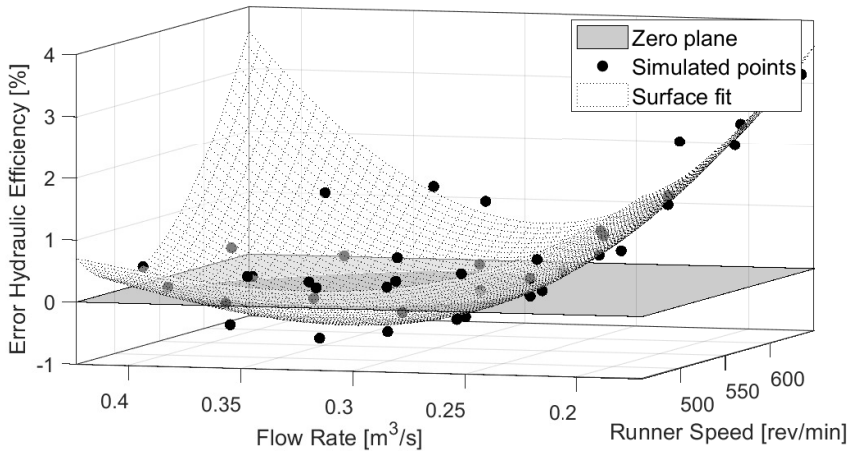


Figure 3.6: Error in hydraulic efficiency at different operating conditions. Taken from paper 6

In paper 7, a design code is coupled to the simulation framework from paper 6 to form an automated optimization loop. The framework ensured automatic turbine design, meshing, and simulation, as well as several different optimization choices. By treating the blade leading edge geometry as a variable, it was shown that it was possible to use this procedure to increase the hydraulic efficiency of the turbine, especially at off-design conditions. See figure 3.7, where the numbers 24 and 5 denotes the design number in the optimization loop. Further research in this direction, the design of variable speed turbines, is ongoing in the research project HydroFlex [40].

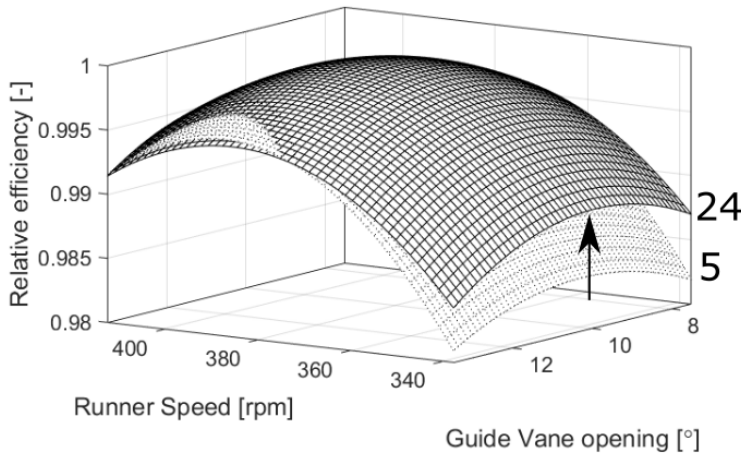


Figure 3.7: Change in Hill diagram after optimizing blade leading edge. Taken from paper 7

The second direction from the initial CFD analysis is **Paper 8** and **Paper 9**. These papers investigate different ways of speeding up simulations and shows, among other things a linear speedup with mesh size, when components like volute and draft-tube are omitted. It also touches upon new solver methods like the Harmonic Balance method, a frequency based solver for periodic flow. This method is briefly explained in section 2.6, and will no doubt be valuable in the future as it provides a dramatic speedup compared to solving in time. As of today, the method is on a development level.

Damping estimation. Going back to the overall objectives, now that the CFD part is assumed to be of reasonable accuracy, we focus on the damping. The reason why the damping is so important is that it is the only term in equation 2.10 that dissipates energy. The deflection amplitude and acoustic pressure amplitudes are also very much dependent on the damping ratio. In fact, with no damping, the response at resonance tends to infinity, a clearly unphysical case. Figure 3.8 shows the acoustic pressure amplitude through the Francis-99 runner using damping ratios in the range $\xi = [1\% - 5\%]$. The sensitivity with respect to damping is large. Looking in detail, we see that for low damping, the contribution from the acoustic pressure can be at least ten times larger than the viscous pressure. This highlights the need for an accurate prediction of the damping ratio.

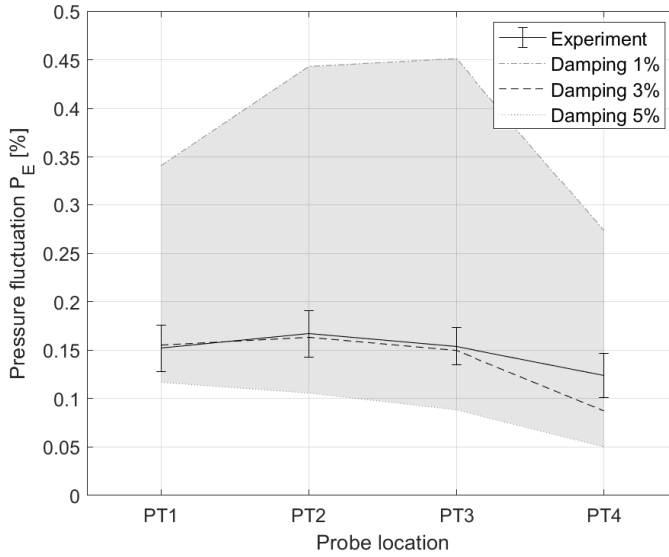


Figure 3.8: Damping sensitivity on pressure amplitudes. Taken from paper 1

Many of the papers in this thesis consider the extraction of the hydrodynamic damping, both numerically and experimentally. In **Paper 3**, a one-way coupled flutter approach was used numerically. The hydrofoil test geometry was used, see section 2.1, as it was easier to perform a controlled experiment of the damping in this test rig. The numerical method used is called the modal work method, where the hydrofoil is moving with a pre-determined mode-shape and frequency, affecting the surrounding water. In such simulations, the water does not affect the hydrofoil other than exerting a fluid pressure. The damping can then be extracted as the normalized work from the water on the blade, see eq. 2.17. This method was shown to give very good results compared with experiments, see figure 3.9. Note a change in the damping characteristics before and after the lock-in region. From a design point of view, it is interesting that the damping is linearly increasing with the flow velocity, as high damping improves the structural integrity. High flow velocities, however, increases viscous losses. In the end, it will always be a trade-off between hydraulic efficiency and structural integrity. **Paper 10** is a mirror of paper 3, explained from the experimental side.

In **Paper 11**, the experiments were repeated, now with three blades in a cascade. This opened up a series of new possibilities, especially with regards to different

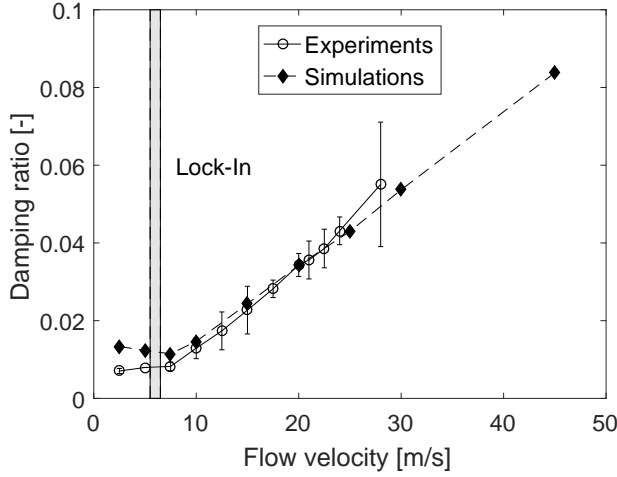


Figure 3.9: Experimental and numerical damping on the Francis-99 hydrofoil. Taken from paper 3

combinations of phases between the blades. Among the most interesting discoveries was the fact that only in- and out of phase motion was possible in the blades (0° or $\pm 180^\circ$). This indicated a strongly coupled system and prevented testing of other phase angles between the blades, something we see in a turbine. Secondly, a reduced velocity, $v^{**} = v/f_n$ was proposed, where f_n is the natural frequency of the blade, and it was seen that if the damping was plotted against this variable, different hydrofoils, experiments, and simulations, all aligned about a common trend, see figure 3.10.

Some of the interesting takeaways from the research on damping:

- One-way coupled numerical simulations are validated and should be used to obtain the damping ratio.
- Only real mode shapes are possible to obtain in the current blade cascade; a rotationally symmetric geometry should be tested to get other phase angles between the blades.
- The relationship between damping and flow velocity may be generalized using the natural frequency of the mode shape.

Especially the last finding is interesting as the relation is close to $\xi/v^{**} \approx 1$, see

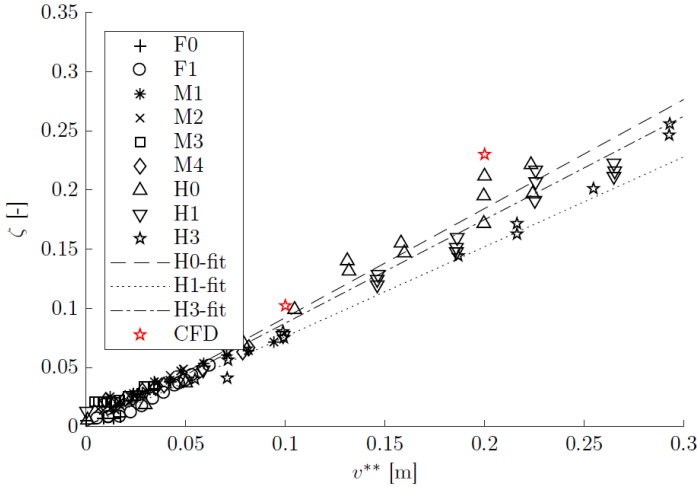


Figure 3.10: Damping versus reduced velocity. Taken from paper 11

figure 3.10. In a design process, this could be a reasonable rule of thumb for the damping, although a proper CFD analysis is always recommended. Note that in paper 11, and figure 3.10, the damping is denoted by ζ , not ξ .

Model Order Reduction. The last group of papers focuses on Model Order Reduction techniques. Numerical simulations, in particular, CFD and harmonic analysis with acoustic elements are computationally expensive. A CFD analysis is CPU intensive, with simulations lasting days, weeks or more, while harmonic analyses often being memory intensive. **Paper 4** presents a model order reduction method based on Krylov subspaces. The method is implemented for acoustic-structural analysis, similar to what was performed in paper 1, but on the hydrofoil geometry. In essence, the method reduces the structural coefficient matrices to full matrices of negligible size and solves them directly. A dramatic speedup of $\mathcal{O}(1 - 2)$ was observed without loss in accuracy, see figure 3.11. In fact, it was observed that the reduction process demanded a computational expense in the same order as a modal analysis. When the model is reduced, however, a harmonic sweep can be performed in seconds, revealing a lot more information than a modal analysis alone. In particular, the acoustic pressure discussed in paper 1 can be obtained over a broad frequency range, rather than at resonance conditions only.

In paper 3,10 and 11, it was shown experimentally that the damping characteristics

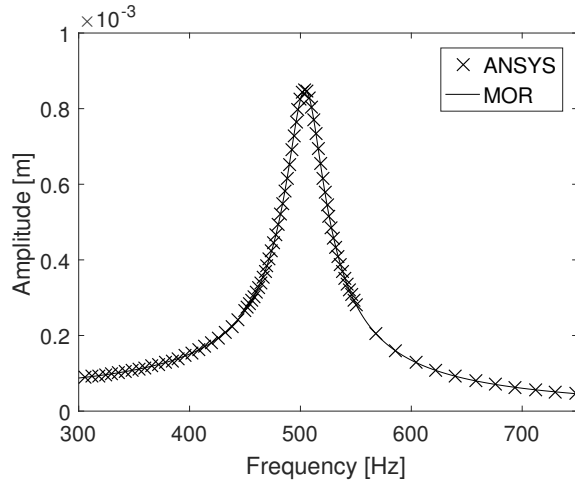


Figure 3.11: Harmonic sweep of Francis-99 hydrofoil using ANSYS and Krylov Model Order Reduction technique. Taken from paper 4

change as the flow velocity passes the lock-in region, see e.g., figure 3.9. The reason for this was not fully understood. A similar trend was observed for the eigenfrequency of the foil, i.e., a stiffening effect as the flow velocity increased. In **paper 5** a quasi-two-way coupled simulation was implemented. This method reduces the structural system using a modal decomposition procedure and solves the structural response inside the fluid solver, contrary to the previously tested one-way approach in paper 3. The final method had a computational expense similar to CFD alone while resolving a lot more of the physics.

The procedure was used on the hydrofoil geometry, and interestingly both the change in damping and the change in eigenfrequency was observed. See figure 3.12 for numerical results of the "added stiffness" effect, where the gray area indicates the lock-in region. This effect was also observed in the experiments but is not possible to show in a one-way configuration. One of the advantages of the two way approach is the fact that the different forcing terms can be tracked during the simulation. This was used to try to explain the different phenomena. There were indications that the increase in damping was caused by a change in the phase between the deformation of the foil and the external pressure force on the foil. The change in eigenfrequency might be explained by a change in the ratio of restoring and inertial forces, $\omega_n^2 = K/M$, when crossing the lock-in region.

To summarize the presented workflow for simulating resonance loads;

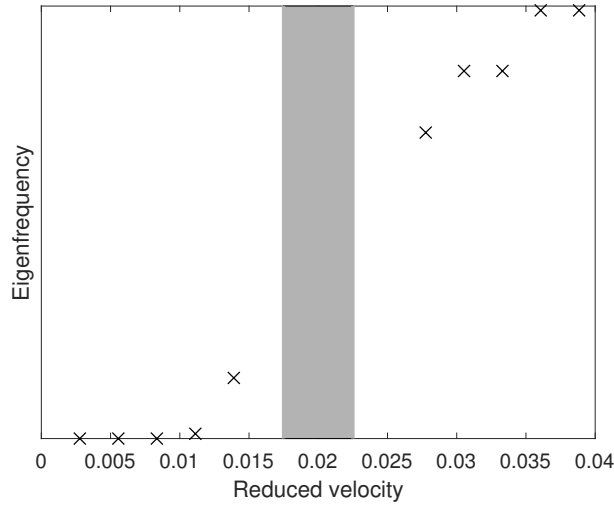


Figure 3.12: Two-way simulation of added stiffness effect of flowing water. Taken from paper 5

- Perform modal analysis to obtain mode shapes and eigenfrequencies of the runner. A similar setup as the one used in paper 1 can be used. Use the Tanaka formulae, eq. 2.1 and 2.2 to evaluate if any of the eigenfrequencies are within critical distance from a loading frequency. If so, continue with further analysis, or consider a redesign.
- Perform a CFD analysis and extract static pressure and the dominating fluctuating pressure components. The methods described in paper 2, 8, and 9 are validated. In the near future, this will most likely be done using a frequency based solver, $\mathcal{O}(1 - 2)$ more efficient than today's time-stepping methods.
- Obtain damping estimate. The modal work method used in paper 3 is validated. The findings from paper 11 can also be used, i.e., $\xi/v^* \approx 1$, if a flutter analysis is too time-consuming.
- Perform a harmonic acoustic-structural analysis with acoustic elements as in paper 1. If acoustic pressure is to be extracted at more than resonance conditions, e.g., to evaluate the sensitivity with respect to the distance between the load and natural-frequency, consider using the Krylov MOR procedure from paper 4 to speed up the calculations.

Chapter IV

Discussion and Further Work

- ◇ This chapter presents a general discussion and possible further work.
-

Risk of resonance. It was previously mentioned that the requirements for perfect resonance are rarely satisfied. Usually, the loading and natural frequencies are not equal. How significant should the separation be for the operation to be considered safe? A Dynamic Amplification Factor (DAF) is often used to quantify the dynamic effects in a system. It can be defined as the response of the dynamic load divided by the same load applied statically [19]. Figure 4.1 shows the DAF of the Francis-99 hydrofoil using a fluid load.

The figure shows that in the worst case, the response due to dynamic effects can be ≈ 75 times higher than static loads. The DAF is very damping dependent, see e.g., figure 3.8, however, the figure can be used to assess the risk or rather, the effect of resonance. We see that 20% separation from the natural frequency results in a dynamic magnification of $\approx 2 - 3$. Using a rule of being outside of $\pm 20\%$ from the natural frequency might therefore be tempting; however, care should be taken. An important effect that should be considered is that numerical simulations tend to overestimate the natural frequency of a structure, meaning that the problem is not symmetric [41]. Using a rule of thumb of, e.g., $\pm 20\%$ could therefore be dangerous. Additionally, in complex structures, several eigenmodes might be close to each other in terms of natural frequencies, something that might complicate the numerical calculations.

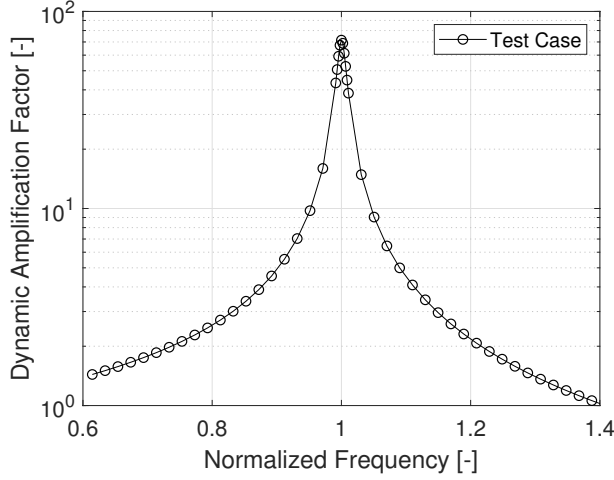


Figure 4.1: Dynamic Amplification Factor on Francis-99 hydrofoil. Taken from paper 4

Compressible CFD. Based on the summary of papers chapter, a valid question can be; why not perform compressible CFD simulations? If the missing component in an incompressible CFD simulation is the acoustic component, could the problem be solved by implementing compressibility? Studies differ in their conclusions. Trivedi [17] performed compressible simulation on the same Francis-99 geometry, and did see slight changes in the pressure amplitudes, however not close to the size of the acoustic component seen in figure 3.4. Yan et al. [42] did show that the addition of compressibility significantly increased the pressure amplitudes, although on a pump-turbine geometry. Additionally, the speed of sound had to be scaled down from prototype to model size. The reason for this may be the differences in time scales. A typical speed of sound in water can be set at $c = 1000m/s$, and a typical flow velocity $v = 40m/s$. Define an *acoustic* and *viscous* Courant number [32];

$$C_{ac} = c \frac{\Delta t}{\Delta x} \quad (4.1)$$

$$C_v = v \frac{\Delta t}{\Delta x} \quad (4.2)$$

and it becomes evident that the required timestep in a compressible simulation has

to be very small compared to an incompressible simulation if a low Courant number is to be satisfied. A similar argument can be made if we create an "acoustic" frequency, $f = c/L$, which is high for small lengths. In essence, the problem becomes numerically stiff. Resolving the fastest transients in such simulations (typically the speed of sound) is rarely done, and if it is, at an enormous computational expense. Additionally, even if a compressible simulation was run with a satisfactory temporal resolution, and the pressure was captured, a CFD would not reveal the structural stresses and deformations. Structural simulations would have to be performed in either case and thus, obtaining the full pressure field with CFD alone becomes of academic interest more than a practical design procedure.

Time Consumption. It is a known problem in the industry that there has to be a compromise between result accuracy and simulation time. In the present work, perfect accuracy has not been the goal, rather *acceptable* results as fast as possible. To investigate ways of reducing simulation time, several different time-saving measures have been implemented in the different papers. Table 4.1 summarizes the speedup factors of the methods.

Table 4.1: Time savings

Method	Domain	Paper	Speedup factor
Mesh reduction	All	8	Linear
Krylov subspace	Structure	4	x10-100
Fourier Transformation	Fluid	2	≈ 5
Harmonic Balance	Fluid	9	≈ 25
Modal Decomposition	Structure	5	∞^*

**Two-way simulation as fast as CFD only*

We see that particularly the Krylov subspace method for the structural domain and the Harmonic Balance method for the fluid domain are very promising. A speedup factor alone, however, is not enough to characterize the actual gain from using a particular method. The absolute time-consumption has to be considered. From experience, we know that a transient CFD analysis is by far the most time-consuming analysis in this thesis. In broad terms, a modal analysis is performed in minutes, a harmonic analysis in hours, and a CFD analysis in days. The most significant gain is therefore obtained in the fluid domain.

Further work. The presented work illuminates several interesting topics that could be investigated further.

- **Model Order Reduction.** In paper 5, a modal decomposition method was used to reduce the structural domain such that structural deformation could be solved inside a commercial CFD solver. This quasi two-way coupling was very successful and provided insight into complex phenomena like increasing damping and eigenfrequency across the lock-in region. In paper 4, another model order reduction method was used, based on Krylov vectors.

An exciting way forward would be to combine the two approaches. Instead of using a modal decomposition method (with its limitations), one could reduce the structural domain using Krylov vectors. This would open up for arbitrary damping, gyroscopic effects, and other limitations related to the symmetry of the original structural system. The drawback is that the reduced system is not diagonal. A direct solver, e.g., Fortran based, would have to be included to invert the full matrices from the reduced system.

Implementing the possibility of complex forces and deflections in the discretization of the structural domain is another possible improvement. Especially in terms of turbines and other rotationally symmetric geometries, would this add a layer of complexity compared to the scheme used here.

- **Damping.** In terms of damping, all experiments and simulations in this thesis have been performed on a hydrofoil, with real mode shapes. Re-doing the experiments on a rotationally symmetric geometry with complex mode shapes would be closer to what is seen in a turbine. The numerical calculation of the damping should not be more complicated than using a real mode; however, a validation of the method would be valuable. Additionally, the opportunity of choosing the inter-blade phase angle would highlight if any combination of guide vanes and runner blades is unfavorable in terms of low damping values.
- **Frequency based solutions.** Modal and harmonic structural analyses are solved in the frequency domain. As the frequency-based Harmonic Balance CFD method continues to evolve, we could end up with a complete workflow without solving any time-stepping simulations. This would simplify the information mapping between the domains as all conservation variables would be expressed as Fourier coefficients. The simulation time would also decrease dramatically, as a transient CFD analysis is by far the most time-consuming part of the outlined workflow.

Chapter V

Conclusion

Modern high head turbines push the limits of structural integrity in order to maximize hydraulic efficiency. During the last decades, many Francis turbines have had severe issues and downtime, and a resonance phenomenon is assumed to be the reason for many of these failures. The research project HiFrancis was started to investigate this phenomenon and this thesis presents some of the results from the numerical work. It turns out that in order to capture both the added mass effects of the surrounding water, as well as the possible resonance issues, a coupled acoustic-structural simulation has to be performed. This thesis presents a proposed workflow for solving acoustic-structural simulations, as well as how to obtain the critical parameters like the viscous load and the damping ratio.

Conventional incompressible CFD is unable to capture acoustic phenomena. Even if compressible effects were accounted for, such a procedure would be too computationally expensive for typical industrial use. Additionally, if the end goal is structural deformation and stresses, then a structural analysis would have to be performed in any case. On the CFD side, it is therefore recommended to perform a conventional simulation to obtain the viscous pressure component. It is shown that this can be obtained with high accuracy, even by using different simplified models. The viscous pressure will act as a load in an acoustic-structural simulation, where the acoustic component of the pressure is calculated. The total pressure in the turbine will be the sum of the two components.

Structural deformation decreases as the damping increases. High damping is therefore positive from a fatigue point of view. The relation, however, is highly non-linear, and obtaining a proper damping estimate is essential if the deformation/stress calculations are to be trusted. From experiments, it was observed that the relation flow velocity/damping behaved differently before and after the lock-in region.

Using a one-way FSI coupling, this damping was obtained numerically with good accuracy. Interestingly, if the damping ratio is plotted against a reduced velocity parameter, many different hydrofoil geometries show the same behavior. This might indicate that it is possible to obtain a general rule of thumb regarding damping, using only the flow velocity and the eigenfrequency of the foil.

Additionally, procedures for speeding up simulations are presented with good results. On the CFD side, the Fourier series based Harmonic Balance method is the most promising, providing speedups of one to two orders of magnitude. It is currently on the development level, but will likely be commonplace in a few years.

On the structural side, the Krylov subspace method showed excellent results, while also providing speedups of one to two orders of magnitude. This procedure creates tiny, full matrices of chosen order that represents the original system in a remarkably good way. The drawback of using this representation is that with it being a purely mathematical construction, it is somewhat decoupled from the original physical system.

A modal decomposition method was shown as a way of performing quasi two-way FSI simulations. Instead of using two software, the structural deformation was solved inside the fluid solver. This procedure managed to replicate the experimental result of positive proportionality between the flow velocity and damping and eigenfrequency. Especially the jump in eigenfrequency is interesting, and it was proposed that it originates in the fact that the ratio of restoring and inertial forces changes as the flow velocity crosses the lock-in region.

References

- [1] REN21 *Renewables Global Status Report, 2018*
- [2] BP Energy *World Energy Outlook, 2019*
- [3] Reynolds T S 1983 *Stronger than a hundred men: a history of the vertical water wheel* vol 7 (JHU Press)
- [4] Francis J B 1968 *Lowell Hydraulic Experiments* (D. Van Nostrand)
- [5] Seidel U, Mende C, Hübner B, Weber W and Otto A 2014 *IOP Conf. Series: Earth and Env. Science* **22** 032054
- [6] Østby P, Billdal J T, Sivertsen K, Haugen B and Dahlhaug O G 2016 *Int. J. Hydropower Dams* **23** 88–92
- [7] Børresen B 2009 Cracks in runners, analysis, prevention and experiences Produksjonsteknisk konferanse 2009 (In norwegian)
- [8] Seidel U, Hübner B, Löfflad J and Faigle P 2012 *IOP Conf. Series: Earth and Env. Science* **15** 052010
- [9] Hifrancis research project <https://www.ntnu.edu/nvks/hifrancis> accessed: 2019-03-12
- [10] Breeze P 2019 *Power generation technologies* (Newnes)
- [11] Kobro E 2010 *Measurement of Pressure Pulsations in Francis Turbines* Ph.D. thesis Norwegian University of Science and Technology (*Preprint* <http://hdl.handle.net/11250/234140>)

- [12] Dorfler P, Sick M and Coutu A 2012 *Flow-induced pulsation and vibration in hydroelectric machinery* (Springer Science & Business Media)
- [13] Tanaka H 2011 *International Journal of Fluid Machinery and Systems* **4** 289–306
- [14] Franke G, Powell C, Fisher R, Seidel U and Koutnik J 2005 *Sound and Vibration* **39** 14–18
- [15] Francis-99 research project <https://www.ntnu.edu/nvks/francis-99> accessed: 2019-03-12
- [16] Trivedi C, Cervantes M and Dahlhaug O 2016 *Energies* **9** 74
- [17] Trivedi C 2018 *Journal of Fluids Engineering* **140** 011101
- [18] Bergan C W, Solemslie B W, Østby P and Dahlhaug O G 2018 *International Journal of Fluid Machinery and Systems* **11** 146–153
- [19] Craig R R and Kurdila A J 2006 *Fundamentals of structural dynamics* (John Wiley & Sons)
- [20] Callister W D, Rethwisch D G *et al.* 2007 *Materials science and engineering: an introduction* vol 7 (John Wiley & Sons New York)
- [21] Miner M *et al.* 1945 *Journal of applied mechanics* **12** A159–A164
- [22] Kundu P K, Cohen I M and Dowling D 2008 *Fluid Mechanics* (Elsevier)
- [23] Nelkin M 1992 *Science* **255** 566–570
- [24] Pope S B 2001 *Turbulent flows* (Cambridge Academic Press)
- [25] Launder B E and Spalding D B 1983 The numerical computation of turbulent flows *Numerical prediction of flow, heat transfer, turbulence and combustion* (Elsevier) pp 96–116
- [26] Wilcox D C 2008 *AIAA journal* **46** 2823–2838
- [27] Menter F R 1994 *AIAA journal* **32** 1598–1605
- [28] Zienkiewicz O C, Taylor R L and Zhu J Z 2005 *The finite element method: its basis and fundamentals* (Elsevier)

-
- [29] Tengs E O, Bergan C W, Jakobsen K R and Storli P T 2019 *IOP Conference Series: Earth and Environmental Science* **240** 062002
- [30] Ansys - acoustic fundamentals https://ansyshelp.ansys.com/account/secured?returnurl=/Views/Secured/corp/v193/ansys_thry/thy_sacoul.html accessed: 2019-03-12
- [31] Everstine G 1997 *Computers & Structures* **65** 307–321
- [32] Ferziger J H and Peric M 2012 *Computational methods for fluid dynamics* (Springer Science & Business Media)
- [33] Benra F K, Dohmen H J, Pei J, Schuster S and Wan B 2011 *Journal of applied mathematics* **2011** 853560
- [34] Tolstov G P 2012 *Fourier series* (Courier Corporation)
- [35] Hall K C, Thomas J P and Clark W S 2002 *AIAA journal* **40** 879–886
- [36] Gopinath A, Van Der Weide E, Alonso J, Jameson A, Ekici K and Hall K 2007 Three-dimensional unsteady multi-stage turbomachinery simulations using the harmonic balance technique *45th AIAA Aerospace Sciences Meeting and Exhibit* p 892
- [37] G radin M and Rixen D J 2014 *Mechanical vibrations: theory and application to structural dynamics* (John Wiley & Sons)
- [38] Rudnyi E B and Korvink J G 2004 Model order reduction for large scale engineering models developed in ansys *International Workshop on Applied Parallel Computing* (Springer) pp 349–356
- [39] Puri R S, Morrey D, Bell A J, Durodola J F, Rudnyi E B and Korvink J G 2009 *Applied Mathematical Modelling* **33** 4097–4119
- [40] Hydroflex research project <https://www.h2020hydroflex.eu> accessed: 2019-06-04
- [41] Liu Y and Glass G 2013 *SAE Technical Paper* 2013–01–1375
- [42] Yan J, Koutnik J, Seidel U and H bner B 2010 *International Journal of Fluid Machinery and Systems* **3** 315–323

Part II

Selected Papers

Paper 1

Francis-99: Coupled simulation of the resonance effects in runner channels

Tengs, E., Fevåg, L.S. , Storli, P. T.

Journal of Physics: Conference Series, **1296** 012005, 2019

Francis-99: Coupled simulation of the resonance effects in runner channels

Erik Tengs^{1,2}, Live Salvesen Fevåg¹, Pål-Tore Storli²

¹ EDR&Medeso, Leif Tronstad Plass 3, 1337 Sandvika, Norway

² Norwegian University of Science and Technology, 7491 Trondheim, Norway

E-mail: erik.tengs@edrmedeso.com

Abstract. A resonance phenomenon is observed experimentally in the runner channels of the Francis-99 model turbine runner. An incompressible CFD simulation is unable to simulate this. Two different coupled physics schemes are therefore presented to investigate if such effects can be replicated through simulations. The first procedure is a fully coupled acoustic-structural simulation, where the surrounding fluid is modelled using acoustic theory. This includes added mass effects and pressure propagation, but not advective and viscous effects. The second procedure is a quasi two-way coupled Fluid-Structure approach based on modal decomposition of the structural domain. In this procedure, the incompressible Navier-Stokes equations are solved along with the structural deformation.

The fully coupled acoustic-structural approach does successfully exhibit a magnification of the pressure through the runner channels, indicating a resonance effect. The exact values of the acoustic pressure amplitudes are highly sensitive to the damping, the blade connection to the shroud close to the trailing edge, and more.

The second procedure manages to simulate the structural deformation with the correct nodal diameters excited by the Rotor Stator Interaction, all inside the fluid solver. The pressure amplitudes however, does not exhibit the desired resonance effect, likely due to the assumption of incompressible fluid.

1. Introduction

Fluid-Structure Interaction (FSI) is a phenomenon that occurs in many physical fields. In general, all phenomena where there is a mutual interaction between a fluid and a structure can be classified as FSI problems, but it usually catches the public interest when catastrophic failures happen. The most famous incident is the Tacoma bridge collapse [1], but it is also seen in many fatal turbine failures in the hydro power industry [2]. The rise of the use of numerical tools have given engineers a better chance of discovering such design flaws early in the process. The tools are not perfect however, and continuous testing, development and validation with experiments are needed to ensure optimal results.

The Francis-99 workshops is a series of three workshops that aims to provide a meeting place for numerical engineers, and provide experimental data for validation of different numerical tools [3]. The open-geometry Francis-99 turbine at the Waterpower Laboratory at NTNU is the basis for discussion, and the different workshops focus on different topics, see i.e. a review of the first workshop regarding CFD [4]. The third workshop discusses FSI, with two test cases made available for the public.



One of the test cases available for the third workshop of the Francis99 research project deals resonance in runner channels. Figure 1 and 2 is taken from [3, 5] and shows the following;

The Francis-99 model runner have been operated in the laboratory at different rotational speeds. As the number of guide vanes and runner blades are constant, this will result in different excitation frequencies in the runner, created by Rotor Stator Interaction (RSI). The turbine has four pressure probes PTR1-4, sequentially placed along the channel, see [5] for more. Figure 1 shows $P_E = p'/gH$, the pressure fluctuation normalized as a percentage of the specific energy in the machine, of the first pressure harmonic. Firstly, we observe that there seems to be a close to constant pressure amplitude for the different rotational speeds, and secondly, the pressure decreases through the channel. This is how we would expect a viscous fluid system to behave. Viscous dissipation dampens the pressure amplitudes through the channel [6]. However, if we turn our attention to figure 2, which shows the amplitude of the *second* pressure harmonic, we see something completely different. Firstly, there is a peak in the pressures around $f \approx 280Hz$, and secondly, at the peak, the pressure is no longer decreasing through the channel. At $f \approx 280Hz$, it is seen that PTR2 and PTR3 have higher pressure amplitudes than PTR1 and PTR4. This may indicate a coupled physics system. The structure is excited by the pressure forces at a frequency close to its natural frequency, and a magnification of the pressure occurs.

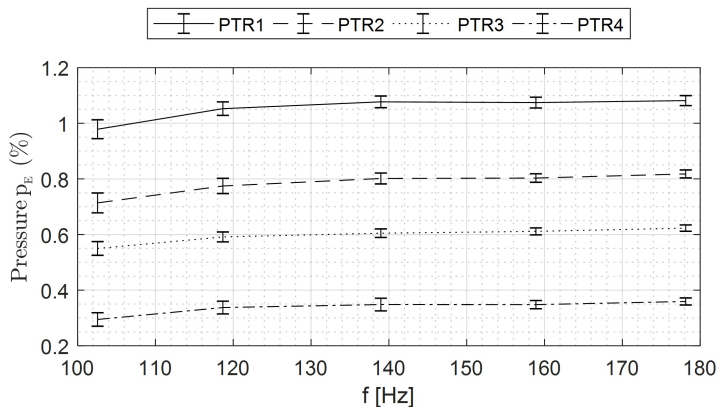


Figure 1. Pressure amplitudes at RSI frequency [3]

In general, for transient, incompressible CFD analysis, the trend showed in figure 1, i.e. a dampening of the pressure amplitudes through the runner, is observed for both the first and the second pressure harmonic. This is shown earlier in the Francis-99 workshops, and also in the HiFrancis research project [7, 8]. Interestingly, the cited references predict the first harmonic of the pressure field very well, but underestimates the second harmonic. This is another indication that there is no resonance at the first pressure harmonic, but there is one at the second. This illustrates the shortcomings of only performing a CFD analysis, and in this article we wish to expand on this and simulate coupled physics, namely include the structural deformation in the simulations. In short, this article wishes to simulate the effect shown in figure 2 by the use of coupled fluid-structure simulations.

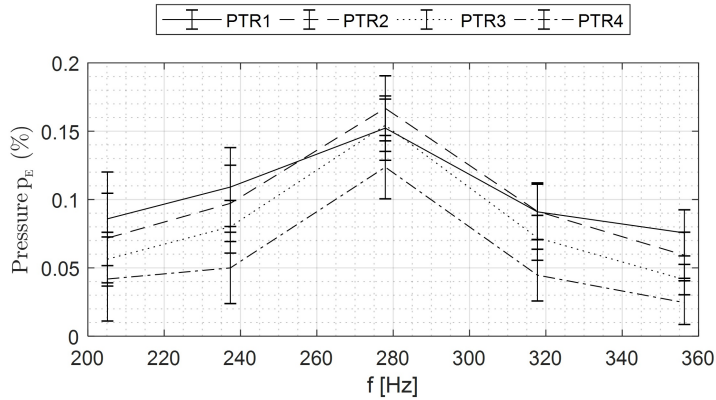


Figure 2. Pressure amplitudes at 2-dRSI frequency [3]

2. Theory and methods

Let us define some key terms regarding Fluid-Structure Interaction (FSI). A step-wise coupled simulation denotes a simulation where information passes from one of the physical domains to the other. The information can go one way, known as a one-way coupled simulation, or it can go both ways, a two-way coupled simulation. An example of a one-way coupled simulation is to perform a steady CFD analysis of a turbine runner, and map the pressure field onto a static structural analysis. If the structural deformation is sent back to the CFD solver to update the fluid domain, it becomes a two-way coupled simulation. See [9] for a thorough comparison between one- and two-way coupled simulations.

A third variant, a *fully coupled*/ monolithic simulation denotes a simulation where the two physical domains are solved for simultaneously, using a single system of equations, common mesh and discretization schemes. This is rarely done in commercial software for viscous flow, however is common practice for structural analysis when the surrounding fluid asserts an added mass effect. It is therefore important to keep in mind that a two-way coupled simulation is *not* a fully coupled simulation. The principle is completely different, as is the usage and availability.

This article will present both a fully coupled simulation and a two-way coupled simulation on the Francis-99 turbine. The following sections will go into more detail on the different approaches, starting with the acoustic-structural simulations.

2.1. Acoustic-Structural simulations

When submerged in water, the dynamic properties and response of a structure is altered by the surrounding heavy fluid. To account for the added mass effects of the fluid, a coupled acoustic-structural simulation can be performed. In ANSYS, this is done by modelling the surrounding fluid using the wave equation [10]. The fluid is primarily defined by its density and speed of sound, such that added mass from the forces on shared surfaces, and pressure propagation in the fluid domain, is considered.

The wave equation can be written on a form similar to the second order structural equation and combined to a *coupled* set of equations. The equation solved for in coupled acoustic-structural equations is referred to as the Eulerian displacement-pressure formulation [10, 11, 12]:

$$\left(-\omega^2 \begin{bmatrix} M_s & 0 \\ M_{fs} & M_a \end{bmatrix} + i\omega \begin{bmatrix} C_s & 0 \\ 0 & C_a \end{bmatrix} + \begin{bmatrix} K_s & K_{fs} \\ 0 & K_a \end{bmatrix} \right) \begin{Bmatrix} u \\ p \end{Bmatrix} = \begin{Bmatrix} F_s \\ F_a \end{Bmatrix} \quad (1)$$

Where M, C, K, F are the mass, damping, stiffness and force matrix respectively. u is the structural displacement, p is the acoustic pressure, and ω is the natural frequency. The subscripts s, a, fs denote structure, acoustic, and fluid-structure respectively. The cross-multiplication matrices (M_{fs}, K_{fs}) are obtained by enforcing boundary conditions on the fluid-structure interface. This ensures that information will cross the domain interfaces in a consistent way. The derivation of eq. 1 can be found in Appendix A.

Nodal Diameters. We want to find evidence of resonance in the runner by performing a coupled acoustic-structural simulation. First a modal analysis can be performed. Given that the dominant load frequencies, f_{RSI} , in the system are known,

$$f_{RSI} = n \cdot f_{runner} \cdot Z_{gv}, \quad n = 1, 2, \dots, \quad (2)$$

a modal analysis will reveal if there are any eigenfrequencies in this range. Z_{gv} denotes the number of guide vanes. Matching loading frequency and eigenfrequency is a *necessary* but not *sufficient* condition to cause resonance. Additionally, the spatial distribution of the load has to match the spatial distribution of the eigenmode. This is illustrated in figure 3, where a eigenmode of a string is shown along with two forces. Even if the frequency of load F_2 is equal to the eigenfrequency of the string, the mode will not be excited as the load is placed at a node. Force F_1 however, will excite the given eigenmode, and resonance will occur if the load- and eigenfrequency matches.

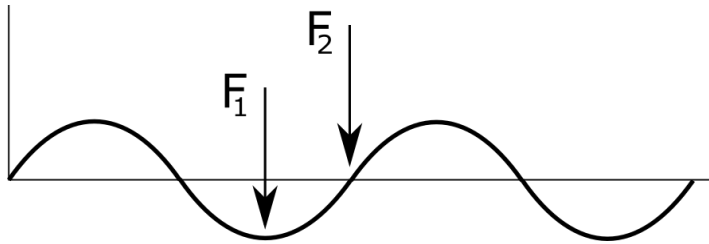


Figure 3. Conceptual resonance conditions

For a disc-like structure like a turbine, this generalizes to the concept of Nodal Diameters (ND). The ND of the symmetric, rotating pressure pattern created by RSI is determined by the number of stationary and rotating components [13, 14];

$$ND = mZ_r \pm nZ_{gv}, \quad m, n = 1, 2, \dots, \quad (3)$$

Where m, n are integers, and Z_r, Z_{gv} is the number of runner and guide vanes respectively. Resonance can occur if the loading frequency matches a runner eigenfrequency with a corresponding mode characterized by the same nodal diameter.

For the Francis-99 runner, we have at design; $Z_r = 30, Z_{gv} = 28, f_{runner} = 333[rpm]$. By using this in eq. 2 and 3, we can sum up the expected critical behavior as follows; The turbine can be excited at ND2 at $f_{RSI1} = 155Hz$, at ND4 at $f_{RSI2} = 310Hz$, for $n = m = [1, 2]$. Higher harmonics are also possible, although the lowest modes are most likely to be excited. As discussed earlier, in the laboratory, the runner was operated in a range of rotational speeds to increase the chance of finding resonance conditions.

A preliminary modal analysis was performed on the Francis-99 turbine. No ND2 modes were found with eigenfrequencies in the range $f = [100 - 180][Hz]$, however an ND4 mode

was found with in the range $f = [200 - 360][Hz]$. This corresponds well with figures 1 and 2. However, as stated in the problem text, the goal of the present work is not to find the exact eigenfrequency, but to find the resonance phenomenon. This means that the applied load in the coming simulations will correspond to the eigenfrequency found in the simulations, rather than matching the one seen in figure 2. The following section will outline the procedure of performing a harmonic analysis of the turbine excited by an ND4 pressure field.

2.1.1. Numerical Procedure. The simulations are performed using ANSYS Mechanical Enterprise Release 19.2. The numerical model is created as perfectly symmetric assembly of 15 sectors. Figure 4 shows the structural parts, with material assignment of copper alloys JM7 and JM3 [15] to the hub/shroud and blades respectively. Instrumentation, holes and more present in the Francis-99 model turbine are omitted. Bolts and bolt holes are not modelled, instead the blades are attached to the hub and shroud by bonded contact, defined on the surfaces that will be press-fit by the bolts, as seen in red in Figure 5. As discussed in the workshop test case description [3], there is some uncertainty with regards to the fixation of the blades to the shroud towards the trailing edge. The edge in question, marked with blue in Figure 5, is kept free to move relative to the shroud. The acoustic domain is shown in Figure 6. Water with default ANSYS values for density and speed of sound is used as fluid.

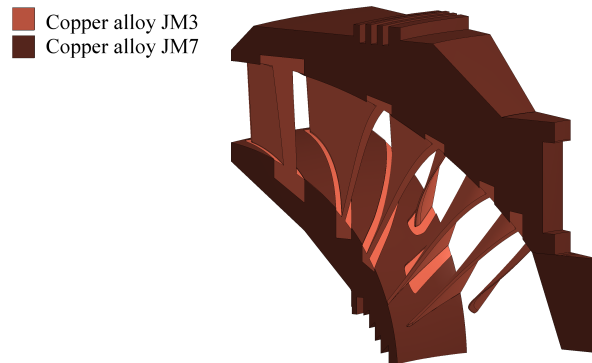


Figure 4. Runner geometry with material assignment. One of 15 identical sectors displayed

For the runner, the element size is limited to 14 mm, with refinement of 4.5 mm assigned to the blades. The total number of nodes is $2 \cdot 10^6$. Table 1 lists the estimated discretization error for selected outputs using the Grid Convergence Index (GCI) [16]. f_n denotes the eigenfrequency, and PT1-4 denotes the pressure amplitudes in the four probes of figure 1. All errors are well below 1%, and the mesh is assumed to produce a converged solution.

The analyses are run as full harmonic analyses using the distributed sparse direct solver. The runner is fixed in space at the hub, replacing the connection to the shaft. Reflective boundaries are specified at all acoustic boundaries. Interaction occurs at the interface between the structural and acoustic domain through shared nodes.

Damping is represented as beta damping, from the concept of proportional or Raleigh damping [17];

$$\beta = \frac{2\xi}{\omega} \quad (4)$$

where β is the frequency dependent, stiffness proportional damping coefficient, and ξ is the

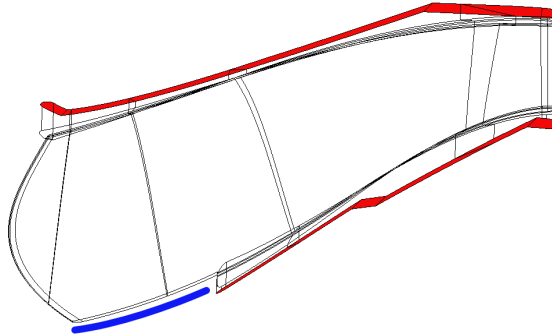


Figure 5. Runner blade. Contact to hub and shroud highlighted

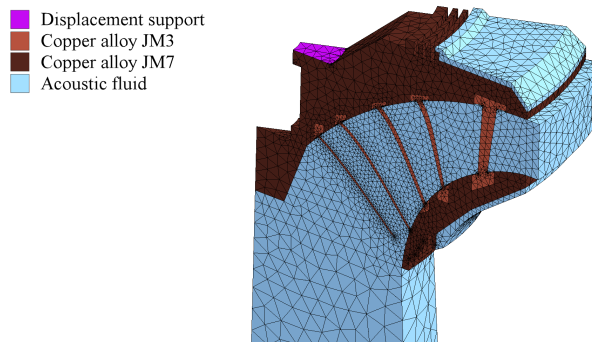


Figure 6. Acoustic and structural elements. One of 15 identical sectors displayed

Table 1. Discretization error

Indicator	GCI error
f_n	0.7 %
PT1	0.0 %
PT2	0.5 %
PT3	0.1 %
PT4	0.1 %

damping ratio. In Agnalt et. al [5], the damping in this experiment was estimated using least squares fitting to be in the range $\xi = [2.5\% - 5.1\%]$.

The load applied in the structural-acoustic simulation is taken from an incompressible CFD simulation, [8]. The load is imported as Fourier coefficients A_i, B_i , with i being 2 for the second pressure harmonic. The Fourier coefficients are applied as a surface load at the runner channel surfaces. This way, the load does not constrain the acoustic pressure degree of freedom in the acoustic domain, instead acts as a load on the structural domain.

The structural response is highly nonlinear with respect to the damping ratio ξ as well as the difference in loading frequency and eigenfrequency, especially close to resonance conditions.

To evaluate the sensitivity of these parameters, simulations are set up with damping values $\xi = [1, 3, 5]\%$ and the load frequency is specified to be within $\pm 7.5\%$ of the eigenfrequency found in the modal analysis. A simulation run at numerical resonance with 3% damping is selected as the reference case.

2.2. Two-way coupled simulation

The traditional way of performing a two-way simulation is to set up both a fluid and a structure simulation separately, and during the execution process pass information from one domain to the other. The usual information flow is as follows; the fluid domain passes on the pressure forces on the fluid-structure interfaces, and the structural domain passes back the structural deformation. The mesh used in the fluid simulation will then deform accordingly and the calculation will continue. Usually this is done in an implicit manner for each time-step, meaning that there is an iterative procedure until a certain convergence criterion is met.

In the procedure chosen in this paper, a quasi two-way approach is used. This procedure applies a modal decomposition to the structural domain, expresses the structural deformation as a set of linearly independent equations, and solves the system inside the iterative fluid solver. This means that there is only need for one solver, in this case ANSYS CFX, a significant speedup. See figure 7 for a simplified flowchart. If the structural domain is discretized using a Crank-Nicolson scheme, the modal deformation and velocity can be described as follows;

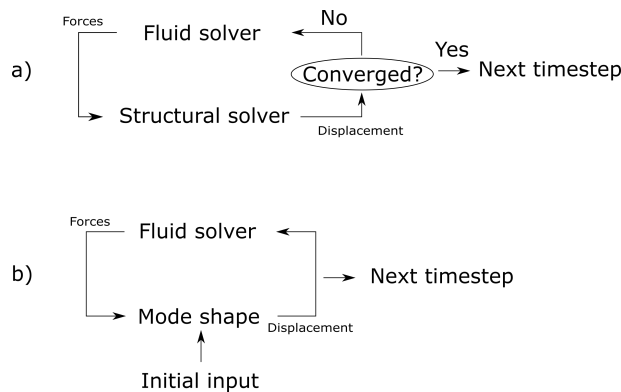


Figure 7. Flow chart describing a) Two-way procedure, b) Quasi two-way procedure

$$q_{i,k+1} = \frac{q_{i,k}(1 + \omega\xi\Delta t - \frac{1}{4}\omega^2\Delta t^2) + \Delta t v_{i,k} + \frac{1}{4}\Delta t^2(f_{i,k+1} + f_{i,k})}{1 + \omega\xi\Delta t + \frac{1}{4}\omega^2\Delta t^2} \quad (5)$$

$$v_{i,k+1} = 2 \frac{q_{i,k+1} - q_{i,k}}{\Delta t} - v_{i,k} \quad (6)$$

where $q_{i,k}, v_{i,k}$ denotes the modal amplitude and velocity of mode i at timestep k . The derivation of the above expressions and the theory behind can be found in [18].

2.2.1. Numerical procedure. The runner mesh was created in ANSYS TurboGrid, as one section consisting of one main and one splitter blade. The final mesh consisted of 15 of this section, to eliminate any error linked to unsymmetrical mesh. Figure 8 shows the mesh on the hub, around the main and splitter blades. The same mesh was used in reference [19], and indicates

that the GCI discretization error is $< 0.5\%$ for global parameters. On the inlet of the runner the total pressure profile from a simulation with spiral casing, guide vanes and full draft tube was prescribed, taken from [8].

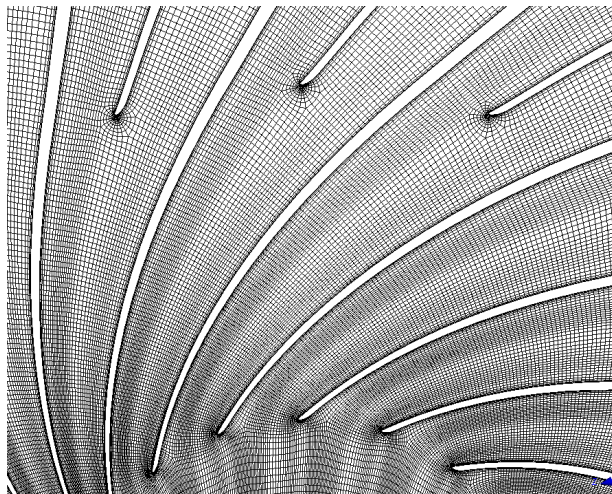


Figure 8. CFD mesh at hub, detailing blade outlet

A modal analysis of the runner will result in a complex mode shape. A complex mode contains a real and complex component, but is easiest understood as a mode where all parts of the structure does not reach its maximum deflection at the same time. A generic representation, $A(x,y)\sin(\omega t)$ is therefore insufficient to describe the whole structure, and a second sinusoid is needed. Due to the real nature of equation 5-6, this mode could not be directly imported into the current setup. Instead, a local (real) blade mode was imported to each blade, and set to be free to move independently of each other. Any complex mode shapes would then be created by the pressure field induced by the RSI effects. This is a simplification, but it works for demonstration purposes.

3. Results and Discussion

3.1. Acoustic-Structural simulations

This section will present the results from the acoustic-structural simulations. Figure 9 shows the total simulated pressure compared with the experimental results provided by the workshop committee. The pressure from the numerical simulations is the sum of the convective pressure from an uncoupled CFD analysis [8] and the acoustic pressure from the reference case using 3% damping at resonance.

There is a very good match with the experiments, especially in the beginning of the channel, where the values are close to identical. The shape of the pressure distribution through the channel also corresponds well, although the pressure amplitude at the outlet, PT4, is underestimated. Reasons for this will be discussed. Figure 10 shows the convective and acoustic components of the pressure for both the numerical and experimental results. The experimental results are taken from the workshop website [3], as well as reconstructed from [5].

Figure 9 shows an overall good agreement between the numerical simulations and the experiments. In figure 10 however, we see that virtually all of the error is in the acoustic

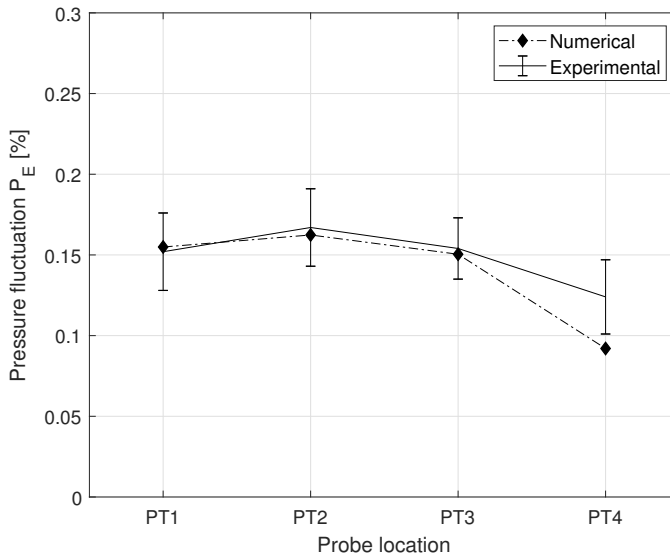


Figure 9. Numerical and experimental pressure amplitudes

part of the pressure, as the convective part is very well predicted. Of several possible reasons, two assumptions have been identified as significant and will be presented below.

Damping. Figure 11 shows the experimental results combined with an uncertainty band indicating the sensitivity to damping. An immediate observation is the strong dependence on the damping, and also the non-linearity of the relation. Increasing the damping from 1% – 3% significantly reduces the response, while increasing from 3% – 5% is not as severe. As mentioned, the damping used here is based on Agnalt et. al [5], who estimated the damping to be in the range $\xi = [2.5\% - 5.1\%]$. If such an estimate is unavailable, a flutter analysis should be performed to obtain a reasonable damping estimate. This has been done previously with good results by i.e [20]. The effect of the load not being equal to the eigenfrequency was also tested. Going by figure 2 and its reference [5] it is estimated that the experiment was performed within a couple of percent from the eigenfrequency. In this range, the effect of different damping ratios is dominating, although a combined effect is seen. I.e. with low damping, the response is more sensitive to how close the load is to the resonance peak. Conversely, high damping makes the resonance peak flatter.

Effect of blade fixation. The bolted geometry of the Francis-99 model turbine makes the numerical simulations especially complex. Replacing the bolts by contacts, as performed in this paper, is an assumption. Additionally, there is some uncertainty with regards to the fixation of the blades to the shroud towards the trailing edge.

To investigate the impact of the connection between blades and shroud, a simulation was performed with a bonded contact at the edge marked blue in figure 5, fully fixating the blade to the shroud.

Figure 12 shows the results from simulations with different fixation of the edge in question. As

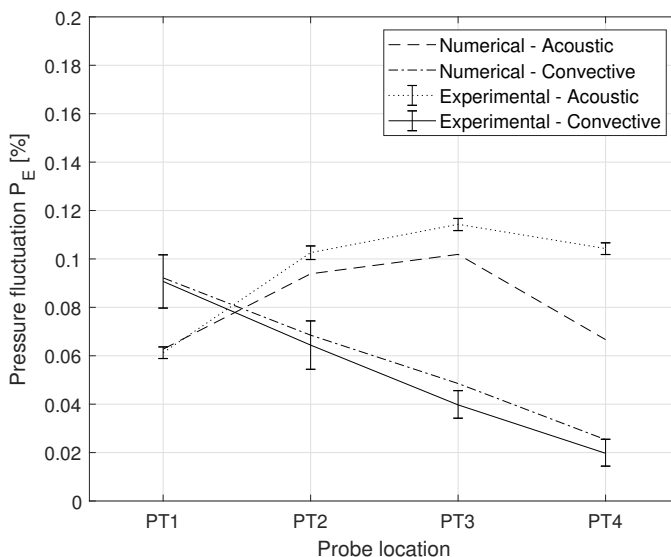


Figure 10. Numerical and experimental pressure decomposed into convective and acoustic components

expected, the second setup results in a stiffer turbine and higher eigenfrequency. Note however, that both harmonic simulations are performed at numerical resonance. The two simulations give different deformation patterns and also different pressure distribution in the runner channels. This leads our case to an increase in the pressure amplitudes in the probes. The two cases presented here are the extreme variations, it is likely that the true trailing edge connection is somewhere in between what is shown in figure 12.

By combining the effects seen in figure 11 and 12 it would be possible to be well within the experimental uncertainty in all pressure probes. This has not been done, but it illustrates the importance of investigating and documenting the sensitivity to the key parameters in the simulations, especially if no experimental results are available for validation.

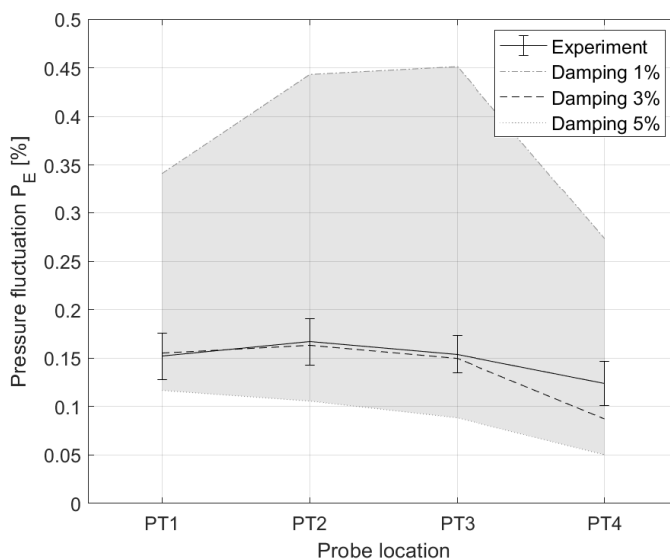


Figure 11. Sensitivity of pressure amplitudes to damping

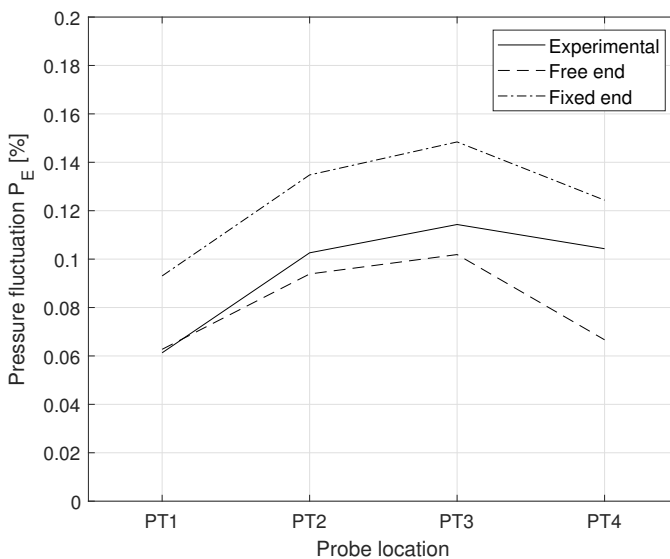


Figure 12. Acoustic pressure with different fixation of the blade to shroud close to the trailing edge

3.2. Two-way coupled simulation

Figure 13 shows the normalized structural deformation resulting from the RSI pressure field. Nodal diameter 2 is observed. A visual inspection of the time-series of the blade deformation, or a Fourier transform of the same signal, reveals that also the ND=4 is present. This is a nice validation of the Tanaka formula, eq. 3, which predicted ND2 and ND4 for the given combination of guide and runner vanes.

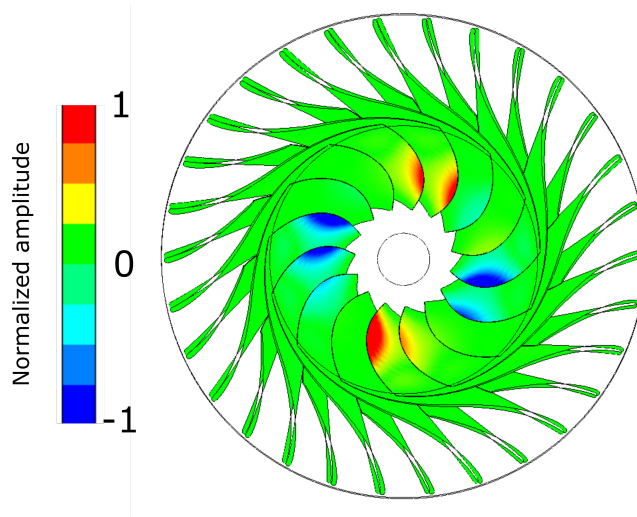


Figure 13. Normalized blade deflection from Two-way simulation, seen from the outlet.

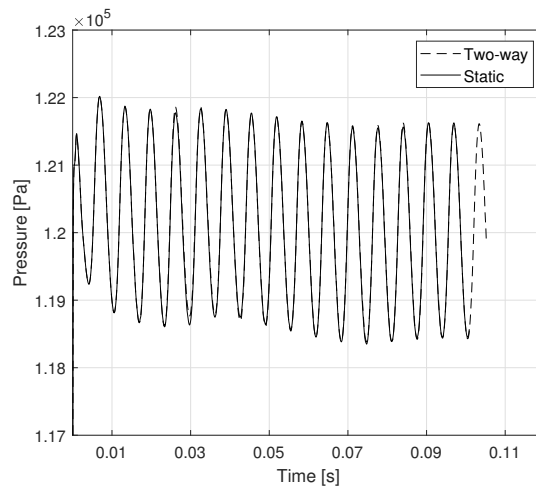


Figure 14. Pressure time series from CFD (static) and Two-way simulation

Figure 14 shows the pressure signal in one pressure probe for two simulations; one with stationary blades, in the other, the blades are allowed to deflect, as shown in figure 13. There is close to no difference in the pressure values.

Taking one step back, we can define the goal from the two-way simulations by the following questions;

- Does the pressure field from the RSI excite the expected Nodal Diameters?
- Does the vibration of the blades change the pressure pulsations in the channels compared to rigid blades?

Figure 13 clearly shows that the first is true. The second question is whether it is a coupling between the structural deflection and the pressure, i.e. if this procedure can be used to capture the resonance phenomena. Figure 14 shows that this is not the case. There is no difference in the pressure through the channel. The magnitude of the deflection is in the same order as the coupled acoustic-structural simulations in section 3.1, indicating that too small deflections is not the cause for the lack of pressure amplification.

The current setup for the FSI - MOR have some clear limitations. The lack of a complex description of the structural decomposition means that only real deformations can be simulated. This was partially circumvented in this paper, but introduces a general uncertainty. Also, the structural model with fixed trailing edge had to be used as the CFD mesh cannot handle relative motion between hub/shroud and blade at the joint. This meant that the imported structural eigenfrequency (or stiffness) was artificially high. Two options are available to mitigate this; firstly, the eigenfrequency can be modified, at the risk of losing the consistency between modal amplitude and stiffness. Another option is to change the rotational speed of the runner along with the head and flow to ensure hydraulically identical conditions. The question then is the predictive value of the simulation as the load frequency is knowingly too high.

The biggest limitation however, in the current setup, is believed to be the lack of compressibility. As was seen in figure 10, the contribution of the acoustic pressure is significant and necessary to predict the true pressure in the channel. Acoustic pressure is impossible to simulate in an incompressible simulation with no speed of sound. The medium (water) is unable to transmit pressure waves described by eqs. A.8.

4. Conclusions

Two different fluid-structural coupling procedures are presented in order to capture the resonance effect in a Francis turbine runner channel. The acoustic-structural coupling is successful in replicating the experimental results to a good degree. Complex bolting and connections in the Francis-99 model turbine creates uncertainties in the numerical simulations, in particular the fixation of the blade close to the trailing edge. Additionally, the amplitude at resonance is very dependent on the damping. If a damping estimate is not available from experiments, a flutter analysis should be performed to obtain a proper input.

The two-way simulation using a reduced order structural model did not produce the resonance phenomena. The reason for this is believed to be the lack of compressibility, which means that the acoustic pressure is not captured. This indicates that the use of the procedure should be limited to cases where the assumption of incompressibility is valid.

Acknowledgement

This work was done in the HiFrancis project, supported by the Norwegian Research Council and the Hydropower industry in Norway.

References

- [1] Billah K Y and Scanlan R H 1991 *American Journal of Physics* **59** 118–124
- [2] Østby P, Billdal J T, Sivertsen K, Haugen B and Dahlhaug O G 2016 *Int. J. Hydropower Dams* **23** 88–92
- [3] Francis-99 research project <https://www.ntnu.edu/nvks/francis-99> accessed: 2019-03-12
- [4] Trivedi C, Cervantes M and Dahlhaug O 2016 *Energies* **9** 74
- [5] Agnalt E, Østby P, Solemslie B W and Dahlhaug O G 2018 *Shock and Vibration* **2018**
- [6] Kundu P K, Cohen I M and Dowling D 2008 *Fluid mechanics* 4th
- [7] Hifranis research project <https://www.ntnu.edu/nvks/hifranis> accessed: 2019-03-12
- [8] Jakobsen K R G, Tengs E and Holst M A 2019 *IOP Conference Series: Earth and Environmental Science* **240** 072001
- [9] Benra F K, Dohmen H J, Pei J, Schuster S and Wan B 2011 *Journal of applied mathematics* **2011**
- [10] Ansys® mechanical apdl, release 19.3, theory reference, acoustics, ansys, inc.
- [11] Everstine G 1997 *Computers & Structures* **65** 307–321
- [12] Puri R S, Morrey D, Bell A J, Durodola J F, Rudnyi E B and Korvink J G 2009 *Applied Mathematical Modelling* **33** 4097–4119
- [13] Tanaka H 2011 *International Journal of Fluid Machinery and Systems* **4** 289–306
- [14] Franke G, Powell C, Fisher R, Seidel U and Koutnik J 2005 *Sound and Vibration* **39** 14–18
- [15] Johnson metall - alloys <http://www.johnson-metall.com/en/product-data-sheets> accessed: 2019-03-12
- [16] Celik I B, Ghia U, Roache P J *et al.* 2008 *Journal of fluids {Engineering-Transactions} of the {ASME}* **130**
- [17] Craig R R and Kurdila A J 2006 *Fundamentals of structural dynamics* (John Wiley & Sons)
- [18] Tengs E and Einzinger J 2019 Two-way coupled simulation of the francis-99 hydrofoil using model order reduction *Journal of Physics: Conference Series* (Accepted for publication)
- [19] Jakobsen K R G and Holst M A 2017 Cfd simulations of transient load change on a high head francis turbine *Journal of Physics: Conference Series* vol 782 (IOP Publishing) p 012002
- [20] Tengs E O, Bergan C W, Jakobsen K R and Storli P T 2019 *IOP Conference Series: Earth and Environmental Science* **240** 062002
- [21] Zienkiewicz O C, Taylor R L and Zhu J Z 2005 *The finite element method: its basis and fundamentals* (Elsevier)

Appendix A. Derivation of the Eulerian displacement-pressure formulation

In the following section, the basic equations for solving acoustic problems will be presented. Most of the derivation can be found in [6], and ANSYS specific implementation can be found in [10]. Starting with the continuity equation;

$$\frac{d\rho}{dt} = -\nabla \cdot (\rho \bar{v}) + Q \quad (\text{A.1})$$

Where ρ is the density, v is the velocity vector, and Q is a mass source. The Navier-Stokes equation can be written as follows;

$$\rho \left[\frac{d\bar{v}}{dt} + v \cdot \nabla v \right] = -\nabla p + \nabla \cdot \tau + \rho \bar{b} \quad (\text{A.2})$$

Where τ is the shear tensor. For simplicity, we assume no body forces \bar{b} , no mass source Q , and no mean velocity from this point on. Also assume small perturbations such that a linearization is possible;

$$\begin{aligned} p &= p_0 + p' \\ \rho &= \rho_0 + \rho' \\ v_i &= 0 + v'_i \end{aligned} \quad (\text{A.3})$$

Where the subscript 0 denotes constant values, and the prime denotes the fluctuating part, small relative to the respective constants. Inserting the above into the continuity and Navier-Stokes equation respectively;

$$\frac{d\rho'}{dt} = -\nabla \cdot (\rho v') \quad (\text{A.4})$$

and,

$$\rho_0 \frac{dv'}{dt} = -\nabla p' + \nabla \cdot \tau \quad (\text{A.5})$$

For newtonian fluids, the stress tensor can be written as a sum of a "shear" part and a compressibility part,

$$\tau = \mu(\nabla v + (\nabla v)^T) + \lambda(\nabla \cdot v)I \quad (\text{A.6})$$

Where μ is the dynamic viscosity, and λ is the "second" or volume viscosity, given as $\lambda = -\frac{2}{3}\mu$ by the Stokes approximation [6]. The above is usually a very convenient split, as only the first term is applicable in incompressible simulations (where $\nabla \cdot v = 0$). Substituting the above into the Navier-Stokes, noting that the flow is irrotational, gives the following [10];

$$\rho_0 \frac{dv'}{dt} = -\nabla p' + \frac{4\mu}{3} \nabla(\nabla \cdot v') \quad (\text{A.7})$$

To obtain the wave equation, subtract the space derivative of the Navier-Stokes equation from the time derivative of the continuity equation:

$$\nabla^2 p' - \frac{1}{c^2} \frac{d^2 p'}{dt^2} + \nabla \cdot \left[\frac{4\mu}{3} \nabla(\nabla \cdot v') \right] = 0 \quad (\text{A.8})$$

Where we have used the isentropic definition of the speed of sound, c [6];

$$c^2 \simeq \frac{p'}{\rho'} \quad (\text{A.9})$$

The known Galerkin method is used to formalize the finite element formulation. Eq. A.8 is multiplied by a testing function w , and integrated over the domain. This procedure is well explained in a number of FEA text books, i.e. [21], and ANSYS' own documentation [10], and yields the following after some manipulation;

$$\iiint_{\Omega} \frac{1}{\rho_0 c^2} w \frac{d^2 p'}{dt^2} dV + \iiint_{\Omega} \nabla w \cdot \left(\frac{4\mu}{3\rho_0^2 c^2} \nabla \frac{dp}{dt} \right) dV + \iiint_{\Omega} \nabla w \cdot \left(\frac{1}{\rho_0} \nabla p' \right) dV + \oint_{\Gamma} w \bar{n} \cdot \frac{d^2 v'}{dt^2} = 0 \quad (\text{A.10})$$

The above representation is rewritten to matrix form using element shape functions;

$$\begin{aligned} p &= N^T p_e \\ u &= N'^T u_e \end{aligned} \quad (\text{A.11})$$

where N, N' are the shape functions for the pressure and displacements respectively. p_e, u_e is the nodal pressure and displacements. Insert the shape function representation into equation A.10, and rewrite on matrix form;

$$M_a \ddot{p}_e + C_a \dot{p}_e + K_a p_e + \rho_0 R^T \ddot{u}_e = 0 \quad (\text{A.12})$$

where the acoustic matrices are defined as follows [10];

$$\begin{aligned} M_a &= \rho_0 \iiint_{\Omega} \frac{1}{\rho_0 c^2} N N^T dV, \quad C_a = \rho_0 \iiint_{\Omega} \frac{4\mu}{3\rho_0^2 c^2} \nabla N^T \nabla N dV \\ K_a &= \rho_0 \iiint_{\Omega} \frac{1}{\rho_0} \nabla N^T \nabla N dV, \quad R^T = \oint_{\Gamma} N \bar{n} (N')^T ds \end{aligned} \quad (\text{A.13})$$

Note that the acoustic wave equation written on a matrix form, eq. A.12 is similar to the known second order structural equation;

$$M \ddot{u} + C \dot{u} + K u = F \quad (\text{A.14})$$

The two equations, A.12 and A.14 can now be combined, rewritten on a harmonic form by assuming that all unknowns behave harmonically, to the Eulerian displacement-pressure formulation [10, 11, 12]:

$$\left(-\omega^2 \begin{bmatrix} M_s & 0 \\ M_{fs} & M_a \end{bmatrix} + i\omega \begin{bmatrix} C_s & 0 \\ 0 & C_a \end{bmatrix} + \begin{bmatrix} K_s & K_{fs} \\ 0 & K_a \end{bmatrix} \right) \begin{Bmatrix} u \\ p \end{Bmatrix} = \begin{Bmatrix} F_s \\ F_a \end{Bmatrix} \quad (\text{A.15})$$

The matrices (M_{fs}, K_{fs}) can be shown to be $(\rho_0 R^T, -R)$ respectively [10].

Paper 2

Effects of passage modelling in high head Francis turbines

Tengs, E. , Storli, P. T. , Holst, M. A.

Hydropower and Dams, E-Proceedings Hydro 2017

Effects of passage modelling in high head Francis turbines

E.Tengs

EDR&Medeso
Leif Tronstads Plass 4
Sandvika
Norway

P.T.Storli

Department of Energy and Process Engineering,
Norwegian University of Science and Technology
Alfred Getz veg 4
Trondheim
Norway

M. Holst

EDR&Medeso
Leif Tronstads Plass 4
Sandvika
Norway

Introduction

The recent trend of a more open power market have led to an increased need for flexible power production. At the same time, many countries, especially in Europe, have committed to reduce the portion on energy from fossil fuel, and focus more on renewables. Most renewables, namely solar and wind power, are intermittent power sources, that is highly dependent on the weather conditions at a given time. This is not the case for hydropower, due to the possibility of storing water in dams. Therefore, hydropower has become a buffer, a battery that can help stabilizing the open power market.

This marked trend has also led to a more irregular operation of hydro turbines. Turbines are designed to operate at a certain configuration, and deviation from this increases the stresses inside the turbine runner. Turbine manufacturers usually design for, and guarantee, 30 years of normal operation, however, several brand new high head turbines have experienced cracks at the outlet in the last decades [1], [2]. The reason is thought to be the complex pressure field created by the rotor-stator interaction (RSI) between the runner and guide vanes. Given the precision of modern production methods, this could indicate that there is a lack of knowledge in the design process of high head turbines. This article will compare different approaches to numerical modelling with comprehensive experimental results. The numerical models will range from full 360 degree models with all components, to different passage models. As some of these methods are intended to be used in a design process, the computational time is a critical aspect. The accuracy of the different methods with respect to time will be investigated. The scope of this article is limited to the RSI pressure field, draft tube phenomena etc. will not be covered.

1 Theory and methods

High head Francis (HHF) turbine runners break down because of fatigue. Fatigue is material failure due to repeated sub-critical loading. A simple way of estimating the fatigue lifetime is using the Miner-Palmgren rule[3];

$$\sum_{i=1}^k \frac{s_i}{S_i} = C \quad (1)$$

where s_i is the number of cycles at load i , and S_i is the number of cycles to failure at load i . Eq (1) sums the contribution from different loadings, and when the sum is equal to unity, the material is assumed to be destroyed. The need for accurate calculation of the loading is obvious; a Francis turbine may experience millions of load cycles during a day, and a small error in the assumed load would dramatically change the expected lifetime. Another critical factor for Francis turbines is the different operating points. Off-design operation and start/stop of the turbine is known to produce large stresses. A complete lifetime analysis will therefore need accurate load prediction at several operating points. In this article, the scope is limited to obtaining accurate loadings at the best operating point, and to investigate if this is obtainable using reduced geometric modelling.

1.1 Rotor Stator Interaction

In high head Francis turbines, Rotor-Stator Interaction(RSI) is the largest source of pressure pulsations [4]. RSI is an unavoidable phenomenon present in all rotating machinery. Every time a rotating component passes a stationary component, a pressure pulse is created, which can propagate through the runner. The pressure field is a function of the number of stationary and rotational components, usually described as a sinusoidal signal, interested readers can find more in [5]–[7]. The most important frequency observed in the runner is the guide vane passing frequency, $\omega = vZ_{gv}$, with v being the runner speed and Z_{gv} is the number of guide vanes. As this is a non-linear system, and the excitation will have a complex shape, harmonics of the guide vane frequency are expected to be present in the flow field. The goal is to compare the RSI pressure signal in the turbine with experimental results from the Norwegian University of Science and Technology.

1.2 Experimental measurements

Experiments have been performed on the Francis99 model turbine at the Waterpower Laboratory at the Norwegian University of Science and Technology (NTNU). The runner consists of 15 main blades, and 15 splitter blades, and there are 28 guide vanes. The model turbine has been the focus point of extensive research, among others, the research project Francis99 [8], which is focusing purely on numerically replicating detailed experimental results from the model, and the HiFrancis project [9], which this work is a part of. The experimental procedure followed the guidelines set in IEC 60193 [10], further information about the experiments can be found in two Master's thesis from NTNU [11], [12]. Figure 1 shows the location of the onboard pressure probes in the runner that will be used for validation in this article.

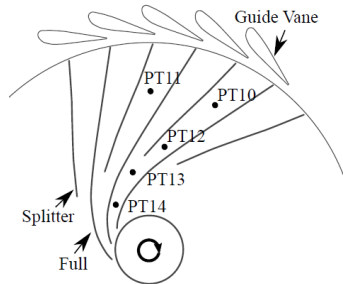


Fig. 1: On-board Pressure Transducers, from[11]

1.3 Numerical Reference

The main goal of this article is to investigate the effects of using passage modelling to reduce computational time. As a numerical reference, simulations have been performed on a complete turbine, that is, complete volute with spiral casing and stay/guide vanes, complete runner with leakage flow, and complete draft tube[13]. Let this simulation be denoted as the 360 simulation. The numerical domain is shown in figure 2, along with the reduced geometrical model. The simulations were performed using ANSYS CFX, the *SST* turbulence model and incompressible flow. Further information can be found in table 1 .

Table 1 – Simulation settings full 360 simulation

Parameters	Description
Software	ANSYS CFX
Analysis type	Transient
Components	Full volute, complete runner, draft tube
Grid	Volute: 10 M (Tet), Runner: 10 M (Hex), Draft: 22 M (Tet)
Interfaces	Transient Rotor Stator (sliding mesh)
Fluid properties	Incompressible water, constant properties
Boundary Conditions	Inlet: Mass flow, Outlet: 0 Pa average static pressure
	No-slip walls
Turbulence model	SST
Time step	64 per blade passing

The runner mesh was created using ANSYS Turbogrid. The mesh consists of 15 passages, rotationally symmetric with node-matching periodic interfaces. The complete volute and draft tube mesh was created separately using ANSYS Meshing. The total number of elements in the converged mesh was 42 M. The Grid Convergence Index (GCI) [14] was used to verify the mesh quality. An example GCI procedure can be found in [15], only the results will be presented here. Table 2 presents the GCI error for the parameters head and torque, and shows that the spatial discretization error on the converged mesh is small. The converged mesh had an average y^+ of 2.8 in the runner. The exact same runner mesh will be used in the reduced models.

Table 2 – Grid convergence index

Parameter	GCI error
Head	0.22%
Torque	0.04%

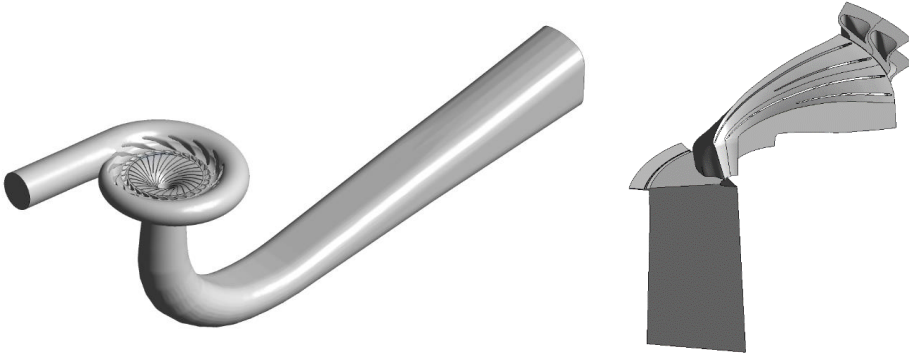


Fig. 2: Complete(left) and reduced(right) numerical domain

1.4 Reduced Computational Models

Many different strategies exist if the goal is to reduce the simulation time. Certain domains may be left out of the simulation, e.g. spiral casing or draft tube, or simplifications in mathematical models, e.g. turbulence. In this article, the focus will be on reducing the geometrical domain, specifically by using the rotational symmetry of the turbine. A general turbine consists of P geometrically identical runner blades, and Q guide vanes. A passage model will use p runner blades and q guide vanes as a reduced geometrical model. Figure 3 shows an example passage model, with $p = q = 2$, from a runner with $P = 19$ and $Q = 24$. This example is chosen to highlight certain problems arising in

passage modelling, mainly how to deal with the rotationally periodic interfaces and the pitch change (unequal angular span).

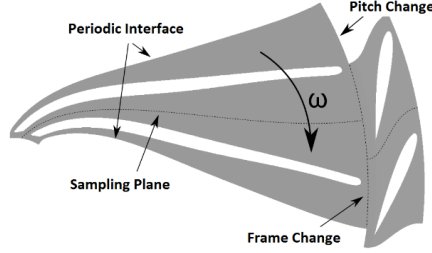


Fig. 3: Example passage, two guide vanes and two runner blades

Conventional periodic interfaces require the assumption that fluxes on one interface equals that of the other. This is not the case in a hydro turbine if $P \neq Q$. What we see however, is *phase-shifted* periodic boundaries. This means that one periodic interface will equal the other at an earlier or later instance in time. This will have to be addressed by the method used. Pitch change, or unequal angular span of the runner and guide vane passages, also occur when $P \neq Q$. In figure 3, the pitch is $\frac{19}{24} = 0.79$. If the pitch is different from unity, some modification will be performed on the information crossing the frame change interface (stationary/rotational). The following sections will describe briefly the methods used in this article, and how they deal with the mentioned challenges.

In all passage models used, the inlet boundary conditions were total pressure and velocity directions taken from a steady simulation. The settings were otherwise as for the 360 degree simulation. The velocity components imposed on the inlet in order to replicate the effect of the guide/stay vanes, was the same as the guide vane/stay vane outlet angle. This approximation is true even if an extended inlet section is included to allow for development of the pressure and velocity field upstream of the blade.

1.4.1 Profile Transformation

The profile transformation method (PT) is the simplest passage model in CFX. The PT method scales the flow from the stator domain, to match the size of the runner domain. Mass and momentum is conserved over the interface. In effect, this method mimics $P = Q$ and does therefore use conventional periodicity in the runner. There is no formal pitch limit for this method, but the error grows as the pitch change increases[16]. Recommended values are in the range $[0.98 - 1.02]$. In the experimental turbine, almost half the turbine would need to be modelled ($\frac{11}{12} * \frac{30}{28} = 1.018$) to meet this criterion. This will not be satisfied in this article, as the full turbine is already simulated. Instead, the PT model will use 4 guide vanes and 2 main + 2 splitter blades. This setup, with pitch ≈ 0.93 , will investigate the effects of violating the recommended pitch ratio, as well as serving as a reference case for the more advanced passage models.

1.4.2 Fourier Transformation Method

The rest of the techniques used in this article are based on a Fourier series decomposition. A brief overview of the theory will follow. Starting with a periodic function $x(t)$. This function can be represented as a sum of trigonometric functions, known as a Fourier series.

$$x(t) = a_0 + \sum_{n=1}^N [a_n \cos(n\omega t) + b_n \sin(n\omega t)] \quad (2)$$

Where N is the truncation order and ω is the fundamental frequency. The Fourier Transformation method (FT) assumes a periodic flow field, and uses a Fourier series decomposition in space and time to express the field variables, $x(t)$, at the interfaces. The Fourier decomposition in time accounts for the phase-shifted boundaries. The method requires that two guide vanes and two runner passages are modelled, let the periodic interfaces be denoted as P_1, P_2 , and the midplane P_{samp} . The data at each timestep is sampled at the sampling plane P_{samp} , and the following phase-shifted periodic boundary conditions are easily derived.

$$x_{P_1}(t) = x_{P_{samp}}(t - \Delta t) \quad (3)$$

$$x_{P_2}(t) = x_{P_{samp}}(t + \Delta t) \quad (4)$$

Where Δt is the phase shift from P_{samp} to the periodic boundary. The time/space Fourier decomposition accounts for information crossing the rotor/stator interface. There are no known limitations in pitch change when using the FT method, as the Fourier series is an analytical function that can be applied directly at the interface. Another advantage is that the storage need is greatly reduced, as only the Fourier coefficients a_n, b_n is retained, and no transient result files are needed. In this case, the FT method reduces the number of grid elements by a factor of 17.

1.4.3 Frozen Gust

A variant of the Fourier Transformation method is to only simulate the runner passage. This method is called the Frozen Gust (FG) method. The periodic boundaries are still handled with a phase shift as explained above, however there is no pitch change as only the runner is simulated. Less than 2 M grid elements are used in the FG simulation, a reduction with a factor of 21.

As only the runner domain is simulated, the inlet boundaries are close to the runner blade. The boundary conditions are total pressure profile and velocity directions taken from a steady simulation, whereas in reality, these parameters are likely to oscillate. The original boundary condition is therefore suspected to be inaccurate. Manual Fourier coefficient sampling was implemented in the 360 simulation in order to extract the true periodic nature at the RSI interface. The profile was then reconstructed at the inlet of the Frozen Gust simulation as a periodic inlet boundary condition. Let this method be denoted as FG Fourier Inlet. Using this approach, the time consumption cannot be compared directly, as a 360 simulation is performed prior to the simulation. However, if this approach is applicable, and if one assumes that an approximation using only one harmonic is sufficient, then a simple sinusoidal expression like below could also be used to express the inlet condition.

$$\gamma = 1 + \Delta\gamma * \sin(\phi) \quad (5)$$

Where γ is the boundary parameter, $\Delta\gamma$ describes the oscillation amplitude in percent of the mean value, and $\phi(x, y)$ sets the fixed spatial distribution (if the boundary is defined in the rotating frame of reference, ϕ will be expanded to include a temporal term). An initial guess was taken to be $\Delta\gamma \approx 9\%$ (twice the steady pressure variation) and ϕ is given as $28 \cdot \tan^{-1}(x/y)$. In the above expression, the values apply to the whole interface, and the accuracy of mapping the Fourier coefficients of all nodes is lost. The above expression can however, be implemented *without* performing a preceding simulation. Let this method be denoted as FG Sine Inlet. Both approaches described above was implemented to assess the sensitivity of the inlet boundary condition for the Frozen Gust configuration.

2 Results

Figure 4 shows the spectral content of the experimental results, and the Frozen Gust methods with different inlet boundary conditions at pressure probe PT10. Please refer to figure 1 for probe locations.

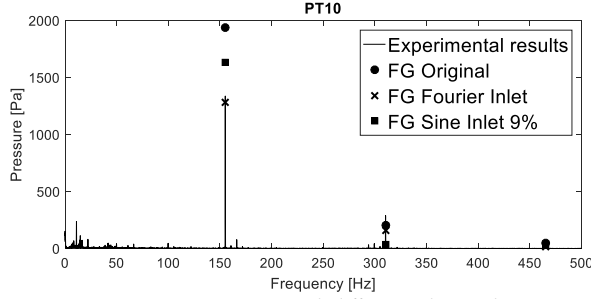


Fig. 4: Frozen Gust with different inlet conditions

As the Fourier inlet performed best, this approach will be implemented from now on. Figure 5 shows the spectral content of pressure probe PT10, PT12, PT13 and PT14, for the experiment, the 360 simulation and the Frozen Gust simulation. The FFT from the 360 simulations results in a wider frequency band than the experiments, as the time series was significantly shorter. The FFT algorithm (based on *pwelch* in Matlab) was shown to give amplitudes independent of the length of the time series, a comparison is therefore trusted. The Frozen Gust amplitudes are reconstructed from the Fourier coefficients obtained in the simulations, and is therefore illustrated as dots. The PT simulation results is only included at PT10 as the results clearly are wrong. The results from the FT simulation diverged, and were deemed too uncertain to be included in this article.

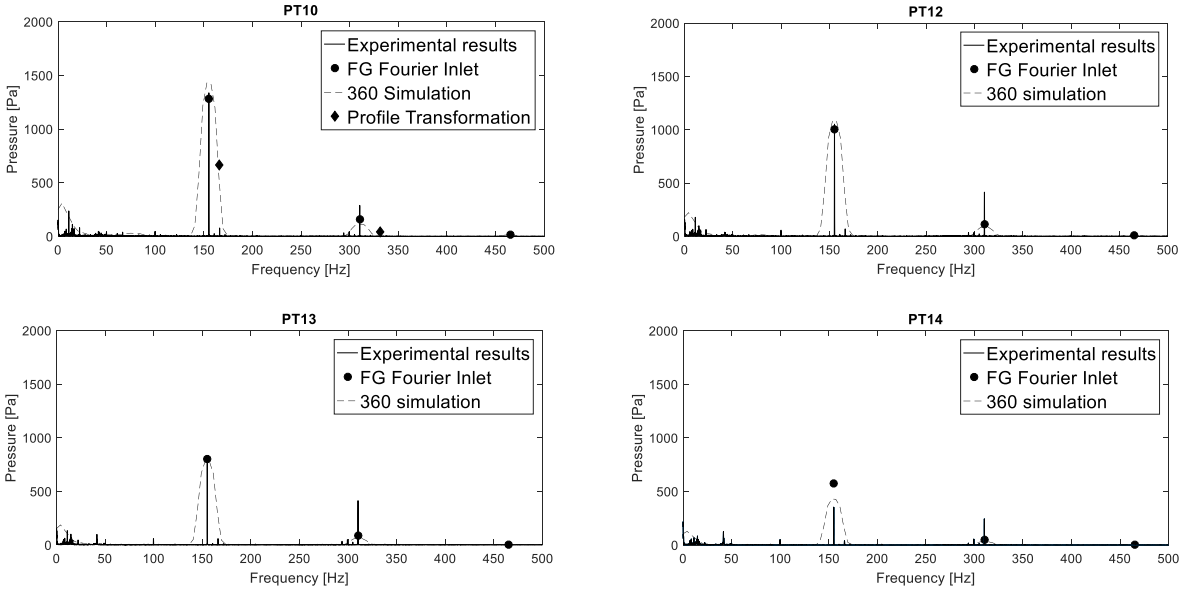


Fig. 5: Spectral comparison at PT10, PT12, PT13 and PT14

The blade passing frequency is very well predicted in all pressure probes. We also observe a dampening of the pressure through the channel, from PT10 to PT14. The second harmonic is consistently underpredicted by 50% or more.

2.1 Computational Effort

Simulations on reduced geometrical domains are performed to reduce the computational effort. This section will compare the computational effort in the different methods. The different simulations have been performed on different number of cores, different number of runner revolutions, and in some cases different time steps. Table 3 shows the time consumption normalized with respect to abovementioned parameters, with the 360 degree simulation as reference (assuming linear scaling).

Table 3 – Simulation time per period

Method	Relative speedup
Full 360	1
FT ¹	3.7
FG	5.5
PT	8.3

¹Diverging results, included for comparison

Interestingly, the speedup of the passage methods is less than the reduction in computational domain should indicate (recall section 1.4.2). This is due to the extra computational effort needed to use these methods. The speedup is still significant, especially when considering the number of periods needed to get a periodic solution, where especially the FG method excels. The PT method is the fastest, but should not be used with large pitch change.

3 Discussion

The Profile Transformation method scales the size of the stator domain, and thus, the frequencies observed in the runner is wrong, see PT10 in figure 5. The error is known in advance, it is scaled by the pitch change. Moreover, we see an underestimation of the pressure amplitudes, and most importantly, the phase is wrong due to the conventional periodic boundaries. All runner channels experience the same exact flow field in this approximation, and any attempt in mapping the pressure to a structural simulation will give wrong results. This method should not be used for anything other than global flow parameters, as long as the pitch is outside of the recommended range.

The FT simulation showed promising signs, however a small, growing mass imbalance in the runner caused the simulation to diverge. This was observed after 5-10 full runner revolutions. Care should therefore be taken when using this method; observe the imbalances, and perform enough revolutions. The method was discarded in this work.

The Frozen Gust simulation converged to a periodic solution after only 5-10 blade passings. As Fourier coefficient sampling is built in to this method, there is no need to extract long time series and perform FFT's. Using a steady profile however, is too strict and causes an overestimation of the first harmonic pressure amplitude. From figure 4 we see that mapping the Fourier coefficients on the inlet works extremely well in reducing the amplitude of the first harmonic. In a design process, this method may not be applicable as the Fourier coefficients at the inlet is not obtainable from a steady simulation. However, it shows the accuracy of the Frozen Gust technique with proper boundary conditions.

The pragmatic method of applying a sinusoidal wave on the inlet did also reduce the first harmonic amplitude as wanted. The parameter in eq. (5) must be chosen in advance, and choosing a value larger than the variation in the steady profile is advisable, however the higher the Δy , the higher the pressure amplitudes. A sensitivity study on Δy have not been performed. Note also the second harmonic in the FG Sine Inlet case; it is close to zero. This is because only one harmonic is prescribed at the boundary. This have to be taken into account if this method is to be used.

From the above, we conclude that the first harmonic is satisfactory predicted through the runner. However, observe the experimental second harmonic in figure 5. It is almost constant from PT10 to PT14, something the simulations do not show at all. In fact, in PT14, the simulated amplitude of the second harmonic is only 13% of the experimental case. If this trend continues to the edge of the blade, and blades are designed too thin because of it, then this might be one of the reasons the blades experiences cracks at the outlet. Compressible flow simulations on the same geometry show the same problem[17]. Future work on simulation of the RSI phenomena should focus on the higher harmonics as it seems that the current state of the art simulations does not capture this behaviour satisfactory. One possible solution may be to use a fully periodic, harmonic balance solution technique similar to Hall et.al [18] to better resolve the nonlinearities in the system.

4 Conclusions

Full 360 degree simulations with all components predict the blade passing frequency very well. The amplitude is overestimated in the order of 5% or less. The second harmonic is underestimated by more than 50%, with the error increasing downstream of the RSI interface. Third, and higher harmonics are barely seen, this is in accordance with experimental results. The default Frozen Gust simulations overestimate the main frequency amplitude in the order of 45%. Introducing a periodic inlet boundary condition in the Frozen Gust simulation softens the main frequency oscillations to a near perfect match with the experimental results. A pragmatic, a priori method is proposed with promising results. In terms of RSI effects, the Frozen Gust is performing similarly to the full 360 simulations, and introduces a speedup of a factor of 5 or more. The Profile Transformation method does not compare with the other methods, and should only be used for global parameters. The second harmonic is underpredicted dramatically in all simulations and should be investigated further.

REFERENCES

- [1] "Resonansproblemer stoppet Svartisen-turbin," *Tu.no*, 26-Mar-2012. [Online]. Norwegian text available: <http://www.tu.no/artikler/resonansproblemer-stoppet-svartisen-turbin/245664>. [Accessed: 22-Dec-2016].
- [2] A. Couto, D. Proulx, S. Coulson, and A. Demers, "Dynamic assessment of hydraulic turbines," *Proc. HydroVision*, pp. 16–20, 2004.
- [3] M. A. Miner, "Cumulative damage in fatigue," *J. Appl. Mech.*, vol. 12, no. 3, pp. 159–164, 1945.
- [4] U. Seidel, B. Hübner, J. Löfflad, and P. Faigle, "Evaluation of RSI-induced stresses in Francis runners," *IOP Conf. Ser. Earth Environ. Sci.*, vol. 15, no. 5, p. 052010, 2012.
- [5] H. Tanaka, "Vibration Behavior and Dynamic Stress of Runners of Very High Head Reversible Pump-turbines," *Int. J. Fluid Mach. Syst.*, vol. 4, no. 2, pp. 289–306, 2011.
- [6] G. Franke, C. Powell, R. Fisher, U. Seidel, and J. Koutnik, "On pressure mode shapes arising from rotor/stator interactions," *Sound Vib.*, vol. 39, no. 3, pp. 14–18, 2005.
- [7] C. G. Rodriguez, E. Egusquiza, and I. F. Santos, "Frequencies in the Vibration Induced by the Rotor Stator Interaction in a Centrifugal Pump Turbine," *J. Fluids Eng.*, vol. 129, no. 11, pp. 1428–1435, May 2007.
- [8] C. Fossen, "Francis-99," [Online]. Available: <https://www.ntnu.edu/nvks/francis-99>. [Accessed: 23-Dec-2016].
- [9] C. Fossen, "HiFrancis - NVKS," [Online]. Available: <https://www.ntnu.edu/nvks/hifrancis>. [Accessed: 22-Dec-2016].
- [10] International Electrotechnical Commission, "IEC 60193: 1999, Hydraulic turbines, storage pumps and pump-turbines - Model acceptance tests," *Geneva Switz.*, 1999.
- [11] E. Agnalt, "Pressure measurements inside a Francis turbine runner," Master Thesis, NTNU 2016. Available: <https://brage.bibsys.no/xmlui/handle/11250/2409954>.
- [12] K. Kloster, "Trykkpulsasjoner inne i et Francis løpehjul," Master Thesis, NTNU 2016. English text available: <https://brage.bibsys.no/xmlui/handle/11250/2409957>.
- [13] K.-R. G. Jakobsen and M. A. Holst, "CFD simulations of transient load change on a high head Francis turbine," in *Journal of Physics: Conference Series*, 2017, vol. 782, p. 012002.
- [14] P. J. Roache, "Perspective: a method for uniform reporting of grid refinement studies," *J. Fluids Eng.*, vol. 116, no. 3, pp. 405–413, 1994.
- [15] I. Celik, U. Ghia, P. Roache, and Christopher, "Procedure for estimation and reporting of uncertainty due to discretization in {CFD} applications," *J. Fluids Eng.-Trans. ASME*, vol. 130, no. 7, Jul. 2008.
- [16] "CFX Best Practices Guide for Turbomachinery - ANSYS," [Online]. Available: <http://www.ansys.com/>. [Accessed: 17-Jul-2017].
- [17] C. Trivedi, "Investigations of compressible turbulent flow in a high head Francis turbine," *J. Fluids Eng.*, Aug. 2017.
- [18] K. C. Hall, J. P. Thomas, and W. S. Clark, "Computation of unsteady nonlinear flows in cascades using a harmonic balance technique," *AIAA J.*, vol. 40, no. 5, pp. 879–886, 2002.

The Authors

Erik Tengs got his master degree in mechanical engineering in 2016 at the Norwegian University of Science and Technology (NTNU) in 2016. After his studies, he started as an Industrial PhD candidate working for EDR&Medeso, a company specializing in engineering simulations. His thesis will look at numerical simulation of fluid structure interaction in high head Francis turbines. This work is part of a larger research project, HiFrancis, where this problem is investigated numerically and experimentally.

Pål-Tore Storli received his PhD from the Norwegian University of Science and Technology (NTNU) in 2010 on the topic Transient Friction. He worked as a postdoctoral research fellow until starting as an Associate Professor at the Waterpower laboratory at NTNU in 2014. His main research areas are dynamic operation of Francis turbines and on fatigue mechanisms for high head Francis runners, and he is teaching fluid mechanics to engineering students in basic undergraduate courses.

Martin Holst got his master degree in mechanical engineering in 2012 at the Norwegian University of Science and Technology. In 2012 he started working in EDR&Medeso providing support and training of ANSYS products additional to consultancy project. He has been involved in several projects concerning multiphase flows, erosion, heat transfer, turbomachinery applications, rigid body simulations and fluid structure interaction. He is currently working as Technical Manager in EDR&Medeso AS.

Paper 3

Numerical simulation of the hydrodynamic damping of a vibrating hydrofoil

Tengs, E., Bergan, C.W. , Jakobsen, K.R. , Storli, P. T.

IOP Conference Series: Earth and Environmental Science, **240** 062002, 2019

Numerical simulation of the hydrodynamic damping of a vibrating hydrofoil

E O Tengs^{1,2}, C W Bergan¹, K-R Jakobsen² and P T Storli¹

¹ Waterpower Laboratory, Norwegian University of Science and Technology, Alfred Getz Vei 4, 7491 Trondheim, Norway

² EDR & Medeso AS, Leif Tronstads Plass 4, 1337 Sandvika, Norway

E-mail: erik.tengs@edrmedeso.com

Abstract. The periodic loads from Rotor-Stator interaction is believed to be the main fatigue contributor in High Head Francis turbines. The calculation of the structural response, and thus fatigue, is heavily reliant on the proper hydrodynamic damping characteristics of the water - structure system. The relationship between the water velocity and the hydrodynamic damping is also of great interest. To investigate this, the hydrodynamic damping characteristics of a submerged hydrofoil is simulated in ANSYS CFX. A one-way coupling is implemented, where the blade is forced to vibrate with the first bending mode at the natural frequency, while the hydrodynamic work is calculated over a vibrational period. The velocity of the flow over the hydrofoil is varied in the range $v = 2.5 - 45$ m/s. Two distinct damping regimes are observed depending on whether the vortex shedding frequency is below or above the lock-in region. The hydrodynamic damping is approximately constant before, and linearly increasing after this region. Experimental data from the Norwegian University of Science and Technology is available for validation, and shows the same trends. The sensitivity with respect to maximum vibrational amplitude is tested, and shows that the hydrodynamic damping is independent of the amplitude as long as the deflections are small.

1. Introduction

Several high head Francis turbines have had failures in the last decades [1, 2]. The reason is thought to be complex fluid-structure interaction in the runner, a resonance issue originating in the pressure field created from the interaction between the stationary and rotating components, known as Rotor-Stator Interaction (RSI) [3]. When designing a turbine, it is desired that the natural frequencies of the structure is far away from the known RSI frequencies. However, the presence of water, a relatively heavy fluid, severely changes structural response under loading. This complicates the calculations of the structural properties. The added mass effects tend to reduce the natural frequencies of the structure, as well as dampening the amplitude of the excitation [4]. In some rare situations, the different vibration modes may even change order [5]. Many have tried to obtain a rule of thumb with regards to the reduction of the natural frequencies, however this has not been found, and may not even be possible [4, 5, 6]. When solving for the frequency response in a submerged Francis turbine, a coupled acoustic-structural simulation is therefore necessary. A crucial input to such simulations is the hydrodynamic damping. As additional complexity, the water in a turbine is not stationary, in a high head Francis turbine, the relative



velocity between blade and water may reach $v > 40$ m/s. The effect of the moving water on the damping is therefore of great interest, and has been studied experimentally earlier [7, 8, 9]. The general trend is that the hydrodynamic damping is increasing as the flow velocity increase. A general recommendation as to the slope is however not obtainable. The maximal flow velocity in the abovementioned experiments was $v \approx 20$ m/s. As far as numerical approximations, Monette et al. [10] provided a mathematical description of the hydrodynamic damping phenomena, and Liaghat et al. [11] performed a two-way fluid-structure coupled simulation on the same geometry. Similar experiments at the Norwegian University of Science and Technology have lately reached $v \approx 30$ m/s over the hydrofoil, and also investigated the effects of the lock in region on the damping [12]. This article will try to replicate these experiments numerically, i.e. obtain the hydrodynamic damping coefficient in a system where water is flowing over a vibrating hydrofoil at different velocities. A one-way coupling of the fluid and structure will be performed to reduce the computational cost. The effects of the lock-in region on the damping will also be investigated.

1.1. Dynamic systems

Second order oscillating systems have the following form;

$$M\ddot{u} + C\dot{u} + Ku = F \quad (1)$$

Where M, C, K is the mass, damping and stiffness matrices respectively, u denotes the structural deflection, and F is the loading. Dot notation denotes a one-time differentiation with respect to time, meaning \dot{u} represents velocity and \ddot{u} represents acceleration. The structural deflection is assumed to be periodic with amplitude $u = u_o$ and frequency ω ; $u = u_o \sin(\omega t)$. A crucial input to the above equation is the damping. There exist several different types of damping, in the normal damping model there is viscous, frequency-dependent damping, but there is also material, frequency-independent damping [13]. In water, the viscous damping has been found to dominate the material damping [14]. The scope of this paper is therefore limited to obtaining the viscous damping ratio.

2. Methods

2.1. Hydrodynamic damping

In order to obtain the viscous damping ratio, we need to derive an expression for the damping effects of the water surrounding a structure. The damping ratio, ξ , of a second order system described by equation (1) is by definition [13]:

$$\xi = C(2M\omega)^{-1} \quad (2)$$

However, obtaining the mass and the damping coefficients is not as easy as in a classical mass – spring – damper system. We need to develop other parameters which can replace the unknowns in equation (2). In the following we show that the hydrodynamic work extracted from a CFD analysis help us doing this.

Assuming linear behaviour, the structural deformation, u, can be decomposed into a superposition of the different structural modes, Φ_i , where a mode is the oscillating shape of a system vibrating at its natural frequency [13].

$$u = \sum_i^k \Phi_i q_i \quad (3)$$

Where q_i is a scaling factor. The second order oscillating structural system, equation (1), can be rewritten using the above definition (using only one mode);

$$\Phi^T M \Phi \ddot{q} + \Phi^T C \Phi \dot{q} + \Phi^T K \Phi q = \Phi^T F \quad (4)$$

Let the coefficients still be denoted M, C, K, F for simplicity. The coefficient of \ddot{q} is usually normalized such that $\Phi^T M \Phi = 1$ [15]. The second order system can now be written as;

$$\ddot{q} + C \dot{q} + K q = F \quad (5)$$

Damping extracts energy from the blade. We are therefore interested in the work, $W = \int F dx$, over a period. The scaling factor will be periodic, $q = q_0 \sin(\omega t)$, as it follows the structural deflection, per equation (3). Integrating the left-hand side of equation (5) shows that only the first order term, $\int C \dot{q} dq$, yields a non-zero result over a vibrational period. The work is therefore as follows;

$$W = \int C \dot{q} dq = \int_0^T C \dot{q}^2 dt = C \int_0^{2\pi/\omega} [q_0 \omega \cos(\omega t)]^2 dt = C \pi \omega q_0^2 \quad (6)$$

Additionally, the hydrodynamic work, the work from the structure to the fluid, can be defined as:

$$W = - \int_0^T \int_A p \cdot \dot{u}_n dA dt \quad (7)$$

Where T is one period, p is the fluid pressure, and \dot{u}_n is the velocity of the surface of the structure in the normal direction. Combining equations (2) and (6) finally leads to the definition of the hydrodynamic damping ratio;

$$\xi = \frac{W}{2\pi M \omega^2 q_0^2} \quad (8)$$

Where W is the hydrodynamic work, equation (7), $M = 1$ [kgm²] is the modal mass, ω is the angular velocity [rad/s], and q_0 the scaling factor [-]. The hydrodynamic work is obtained from a CFD simulation, the other parameters are obtained from a modal analysis.

2.1.1. Flutter. Hydrodynamic flutter denotes the possibility of negative damping, an instable vibrational system. If certain requirements are met, the fluid flow could transfer energy to the hydrofoil, rather than absorb energy. The system vibration would in that case be self - magnifying, and violent failure could occur. Starting with equation (7). The work per cycle from the fluid to the blade is as follows follows:

$$W = \int_0^T \int_A p \cdot \dot{u}_n dA dt \quad (9)$$

For simplicity we rewrite $p \int dA = F$ to obtain

$$W = \int_0^T \dot{u}_n F dt \quad (10)$$

Assuming harmonic motion of the blade, $u = u_0 \sin(\omega t)$ and thus, blade velocity $\dot{u} = \omega u_0 \cos(\omega t)$. Let the force follow a similar harmonic motion, oscillating prior to the displacement with a phase angle $\Delta\phi$, $F = F_0 \sin(\omega t + \Delta\phi)$. Solving the above integral for one period:

$$W = \omega u_0 F_0 \int_0^{2\pi/\omega} \cos(\omega t) \sin(\omega t + \Delta\phi) dt = \omega u_0 F_0 \sin(\Delta\phi) \quad (11)$$

We see that the work is purely controlled by the phase difference $\Delta\phi$. A positive phase angle indicates that the structure is absorbing energy, an unstable system. Conversely, a negative phase angle will dampen the vibration. A way of visualizing this is the following; if the blade velocity and force is plotted together (recall the integrand in equation (10)), the areas with equal sign of the two functions will contribute to instability. This is shown in figure 1, where the forcing function lags the vibration by $\Delta\phi = -0.5$. Both the force and blade velocity are scaled to unity amplitude. As the negative area is largest, there is a net energy loss in the blade, and the vibration is damped. Damping is expected in all the simulation in this article, however a difference in phase angle may provide insight into the damping phenomena.

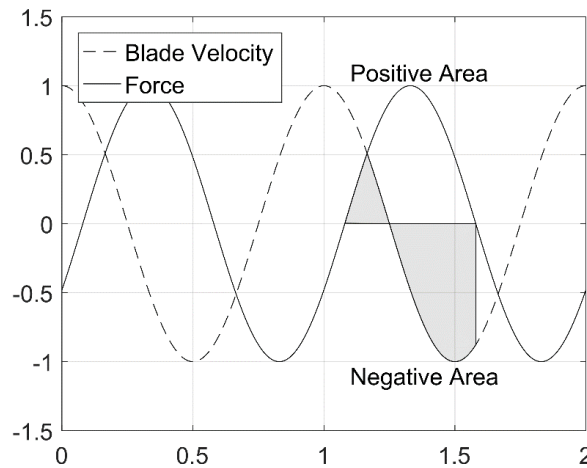


Figure 1. Illustration of phase shift between load and response.

2.2. Experimental setup

The Waterpower Laboratory at The Norwegian University of Science and Technology (NTNU) have performed experiments on both an unsymmetrical hydrofoil (to resemble a Francis turbine blade), and a symmetric hydrofoil. The experimental setup and results from the unsymmetrical test can be found in [12]. The same setup is used for the symmetric hydrofoil tested in this article, some details will be included here.

A symmetric aluminium hydrofoil was excited by electric muscles (Piezoelectric Macrofiber composite actuators from PI Cermaic) to vibrate in a harmonic motion. The hydrofoil was mounted in a stiff 150 mm x 150 mm steel test section, as a part of a longer experimental \varnothing 300 mm pipe system. Several Plexi glass windows were inserted to provide visual access to the blade. Strain gauges and Laser Doppler Vibrometry was used to measure the trailing edge motion. The frequency response was obtained for several different flow velocities and used to calculate the damping characteristics of the system.

Interested readers can find more details in reference [12]. Figure 2 shows a cross-section of the test section, including the placement of the Piezo patches on the aluminum blade. Some global blade dimensions are also included.

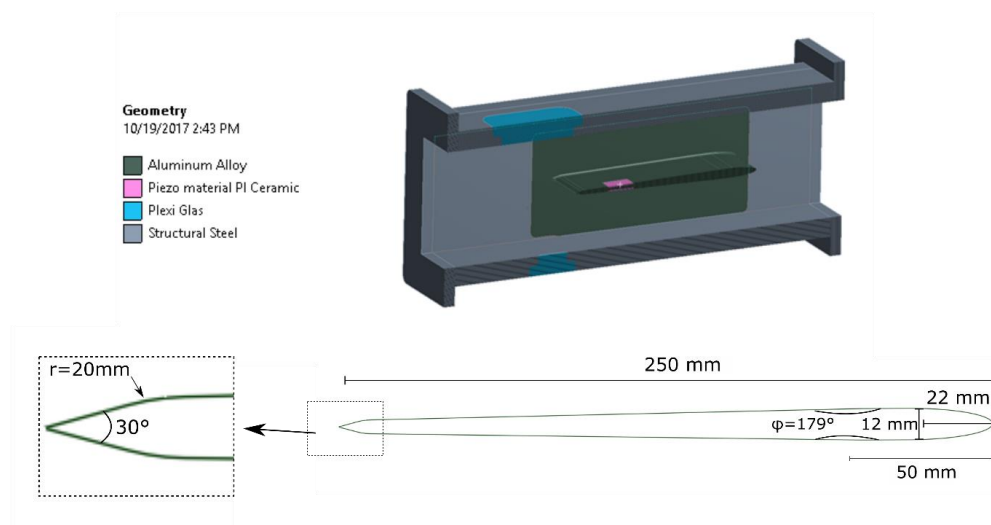


Figure 2. Test section and blade geometry.

2.3. Numerical setup

The work presented in this article tries to replicate the damping characteristics of the symmetric hydrofoil tested at NTNU. Table 1 lists a summary of the most important simulation settings used in this article. The 3 - dimensional numerical domain replicating the experimental rig is shown in figure 3. To ensure that the flow was fully developed before entering the measurement section, the inlet of the domain was extended such that a common entrance length criterion, $> 10D_h$ [16], was satisfied by a large margin. Fully developed flow was verified by testing the inlet turbulence intensity from 0 – 10%, with no difference in the levels at the blade. Similarly, the domain was extended downstream to avoid outlet conditions affecting the simulations, and to avoid backflow at the outlet, as the test section is diverging after the blade.

Table 1. Numerical setup.

Software	ANSYS CFX
Turbulence model	$k - \omega SST$
Timestep	7.75e-6 [s] (256 timesteps per period)
Mesh	$5 \cdot 10^6$ elements, all Hexahedral
Deflection amplitude	[2.5, 0.31, 0.05] [mm]
Vibrational frequency	504.37 [Hz]
Boundary conditions	Pressure inlet, mass flow outlet
Flow velocity	2.5 m/s – 45 m/s

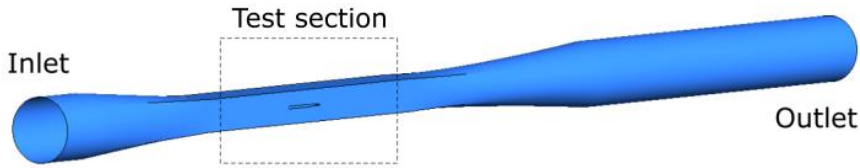


Figure 3. Numerical flow domain.

A one-way coupling was used to obtain the damping. In this case, this means that the structural mode and corresponding natural frequency is calculated in advance. The CFD simulation is then performed with a pre-determined vibrating blade. Constant deflection amplitude is not possible in the experiments, but under the assumption that the damping is primarily dependent on the flow velocity, then it is a reasonable simplification in the numerics. ANSYS CFX was used in the simulations. A specified mass flow was prescribed at the outlet, a zero relative pressure condition at the inlet. The usual no slip condition was prescribed at all walls, and mesh motion forced on the blade surface. A modal analysis was performed in ANSYS Mechanical using the same geometry, with acoustic elements to account for the added mass and stiffness of the water. The first bending mode of the blade corresponds to bending of the trailing edge, and small deflection elsewhere. In a Francis turbine, this is the blade bending mode of interest. This mode shape and corresponding natural frequency was extracted and applied to the blade in CFX. In the simulations, the maximal deflection amplitude was prescribed in advance. The amplitude ranged from 1% to 0.02% of the cord length, i.e 2.5 mm - 0.05 mm as the chord length was 250 mm. A wide range of flow velocities was used, $v = [2.5 \text{ m/s} - 45 \text{ m/s}]$ to identify any trends. The hydrodynamic damping was calculated by combining and discretizing equations (7) - (8), meaning that a normalized work was calculated for each timestep and summed over a full vibrational period, see equation (12). Every vibrational period was divided into 256 timesteps. To minimize the effect of the transient start-up on the damping, equation 12 was applied on a periodic solution.

$$\xi = \sum_{k=1}^{256} \frac{-\int_A p \cdot \dot{u}_n dA}{2\pi M \omega^2 q_0^2} \Delta t \quad (12)$$

The mesh consists of hex elements only, created in ANSYS ICEM CFD. The total number of elements was about 5 million, where the damping was found to be independent of element number. Figure 4 shows the mesh in the midplane around the blade, and the same mesh was used in all simulations. The Courant number ($C = u_{local} \Delta t \Delta x^{-1}$) and the y^+ values did therefore change as the free stream velocity was changed, however simulations at $v = 30 \text{ m/s}$ showed satisfactory values ($C_{rms} = 0.31, y_{max}^+ = 2.3$). At the trailing edge, where separation occurs, the y^+ value was well below 1, and verifies the use of the $k - \omega$ SST turbulence model [17]. In the mentioned Courant number, u_{local} denotes the local flow velocity, Δt the timestep, and Δx the mesh size. In an explicit solver, this number should be < 1 , however this is not necessary in the implicit CFX solver [18].

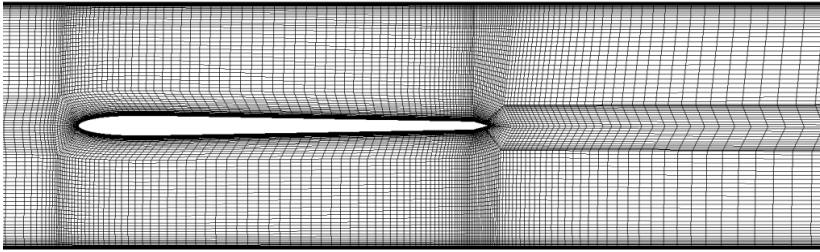


Figure 4. Cross - sectional view of mesh around blade.

3. Results

Figure 5 shows the damping ratio with respect to the flow velocity at three different, fixed amplitudes, $[A_1, A_2, A_3] = [2.5, 0.31, 0.05]$ [mm]. The amplitudes are far apart, $A_1/A_2 = 8$ and $A_2/A_3 = 6.2$, however an almost identical behaviour is seen in the simulations using A_2 and A_3 . This may indicate that there exists a range of deflections where the hydrodynamic damping factor is independent of the deflection amplitude.

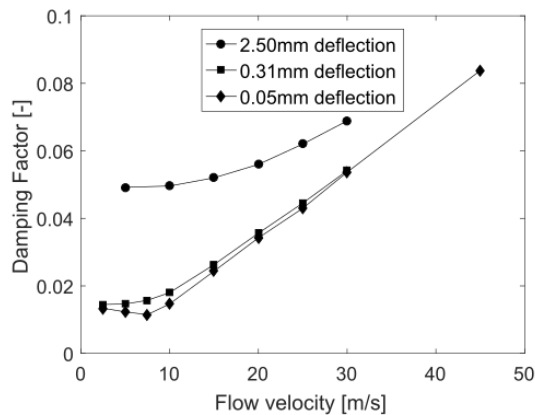


Figure 5. Effect of pre – determined deflection amplitude.

The dependency on the flow velocity however, is not constant or even linear in the whole range. There seems to exist two regions of linear behavior, with different slope. This is supported by experimental results, shown in figure 6. The experimental results are plotted along with an error bar of two standard deviations, and for flow velocities above $v = 10$ m/s, there is a great match between the experiments and simulations. The large uncertainty at $v = 28$ m/s in the experiments is due to the onset of cavitation at higher flow velocities. In the experiments, the threshold of $v \approx 6$ m/s, marked the lock-in region. Lock-in is the phenomena when the shedding frequency in the flow locks with the natural frequency of the structure over a range of flow velocities, instead of linearly increasing as is reported by i.e. Brekke [19]. A narrow band included in figure 6 for visualization of this region.

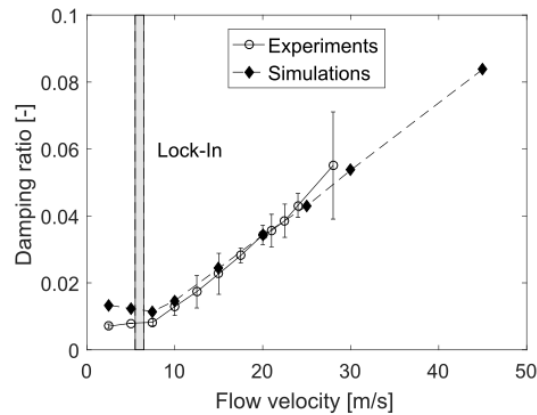


Figure 6. Numerical and experimental damping characteristics.

4. Discussion

Figure 5 indicates that there exists an amplitude range where the damping is independent of the deflection. Moreover, if this range includes the value 0.31 mm, which compared to the blade size is probably unrealistically high, then it can be assumed that the damping is deflection - independent in the whole normal operation range of the turbine. The damping is therefore only a function of the flow velocity, a massive simplification of the system. Similar experiences are seen in the gas turbine industry, however at larger deflections [20]. This result is also supporting the initial assumption of doing a one-way coupled fluid - structure simulation. The second interesting finding is the different damping regions found in figure 6. It is clear that the damping characteristics before and after the lock-in region is different. It should be noted that the simulated and experimental data may not be compared directly, as the deflection amplitude is fixed in the simulations. This is not possible in the experiments. If, however, the assumption of amplitude-independent damping is true, then a comparison could be performed without introducing much error. The phase difference between forcing and vibration, as reviewed in section 2.1.1, is extracted to investigate the damping behaviour more thoroughly by equation (9). Figure 7 (a) shows the phase difference as a function of the flow velocity. The phase difference is obtained by scaling the force on the blade (lift) to unity amplitude and comparing it with the forced vibration (sinusoidal function). The phase is then the spatial difference between the intersection with the x-axis, see small figure in figure 7 (a) or section 2.1.1.

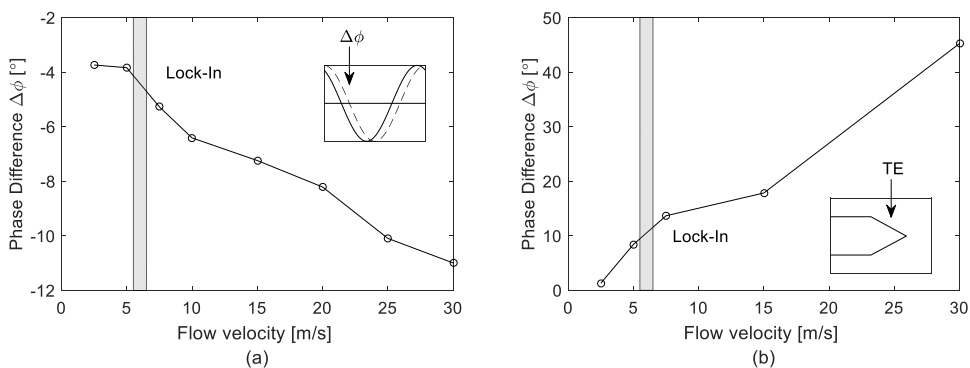


Figure 7. (a) Phase shift, lift whole blade, (b) Phase shift, lift trailing edge only.

We see a change in behaviour before and after the lock-in region here as well, however not as clear as in figure 6. Note that the phase difference is negative for all flow velocities. This indicates that the blade is damped, regardless of flow. An assumption in the derivation of equation (9), is that the velocity of the blade and the pressure on the blade is independent of the location on the hydrofoil. This assumption may not be valid for the mode shape we are studying in this article. To illustrate this, the phase difference using only the lift at the trailing edge (TE in small figure 7 (b)) is extracted and plotted in figure 7 (b). We see that the trailing edge part of the hydrofoil contributes to an unsteady (positive $\Delta\phi$) hydrofoil vibration, although the trend across lock-in is inconclusive.

Looking more closely at the two regions with different damping behaviour. The integrand in the work integral, $(p \cdot \dot{u}_n)$, is composed of two parts. The normal velocity of the blade surface is equal in all simulations, and the pressure is therefore the dimensioning quantity in the integral. The forcing at the trailing edge of the blade is primarily the shedding of vortices. Bergan et al. [12] includes an analytical derivation of the phase shift in the shedding frequency across lock - in, and explains how this may increase the damping at high flow velocities. As was seen in figure 7 (b) the forcing at the trailing edge only was unstable, which actually contradicts this theory. Figure 7 (b) does not indicate that the shedding will dampen the vibration, rather the opposite. However, the assumptions used in deriving equation (9) may be too uncertain to draw any conclusions. Additionally, other factors may dominate the trailing edge shedding, i.e. the development of the pressure field when both the frequency and amplitude is pre-determined in the simulations. A time-consuming two-way coupled simulation may provide further insight. The reason why the damping characteristics changes across the lock-in region is not yet found.

One of the objectives of this numerical and experimental work is to obtain the damping at prototype flow velocities. In a Francis turbine, the relative velocity of the water may easily exceed $v > 40$ m/s. Due to the location of the test rig and the capacity of the pump, the fluid velocity in the experiments was limited to $v \approx 28$ m/s before cavitation occurred. A simulation was therefore run at $v = 45$ m/s, seen in figure 6. We clearly see that the linear trend after the lock-in region is valid even for higher flow velocities. It is therefore reasonable to assume that one can extrapolate the experimental data to higher flow rates.

5. Conclusion

This article shows that a numerical estimation of the hydrodynamic damping of a vibrating hydrofoil is possible. The correspondence with experimental results are very good, especially above the lock-in region. Below this region, the trend is similar, however the absolute values differ somewhat. Two damping regimes are identified; roughly constant before and linearly increasing after the lock-in region. The complete explanation of this phenomena is not known. The hydrodynamic damping is fairly low, $\xi < 0.1$, even for flow velocities realistic to Francis turbines. A one way-coupled simulation was performed, and the vibration amplitude is therefore chosen in advance. This assumption is supported by the result that the damping characteristics are independent of the deflection amplitude, as long as the deflections are small. For larger deflection, a two-way coupling is probably needed.

6. Further Work

The overall goal of the research project is to understand the failure phenomenon in Francis turbines. A key difference from the present geometry and a turbine is the number of blades. In a full turbine, a phase difference in the vibration of two neighboring blades may facilitate negative damping. Therefore, the next iteration of the current study will include several blades to investigate this effect, and increase the similarity to an actual turbine.

Acknowledgments

This work is part of the HiFrancis research project, with financial support from the Research Council of Norway. This support made this work possible.

References

- [1] Kobro E 2010 *Measurement of Pressure Pulsations in Francis Turbines* Ph.D. thesis Norwegian University of Science and Technology (<http://hdl.handle.net/11250/234140>)
- [2] Liu X, Luo Y and Wang Z 2016 *Renewable and Sustainable Energy Reviews* **54** 1–14
- [3] Seidel U, Hübner B, Löfflad J and Faigle P 2012 *IOP Conf. Series: Earth and Environmental Science* **15** 052010 ISSN 1755-1315
- [4] Dorfler P, Sick M and Coutu A 2012 *Flow-induced pulsation and vibration in hydroelectric machinery* (Springer Science & Business Media)
- [5] Liang Q W, Rodriguez C G, Egusquiza E, Escaler X, Farhat M and Avellan F 2007 *Computers & Fluids* **36** 1106–1118 ISSN 0045-7930
- [6] Tanaka H 2011 *Int. J. of Fluid Machinery and Systems* **4** 289–306
- [7] Coutu A, Seeley C, Monette C, Nennemann B and Marmont H 2012 *IOP Conf. Series: Earth and Environmental Science* **15** 062060 ISSN 1755-1315
- [8] Kaminer A A and Kavitskii B M 1976 *Strength of Materials* **8** 25–27
- [9] Roth S, Calmon M, Farhat M, Mnch C, Bjoern H and Avellan F 2009 *Proc. of the 3rd IAHR Int. Meeting of the Workgroup on Cavitation and Dynamic Problems in Hydraulic Machinery and Systems* **1** 253–260
- [10] Monette C, Nennemann B, Seeley C, Coutu A and Marmont H 2014 *IOP Conf. Series: Earth and Environmental Science* **22** 032044 ISSN 1755-1315
- [11] Liaghat T, Guibault F, Allenbach L and Nennemann B 2014 *ASME 2014 Int. Mech. Eng. Congress and Exposition* pp V04AT04A073–V04AT04A073
- [12] Bergan C W, Solemslie B W, Østby P and Dahlhaug O G 2018 *Int. J. of Fluid Machinery and Systems* **11** 146–153
- [13] Craig R R and Kurdila A J 2006 *Fundamentals of structural dynamics* (John Wiley & Sons)
- [14] Seeley C 2013 *54th AIAA/ASME/ASCE/AHS/ASC Structures, Structural Dynamics, and Materials Conference* p 1910
- [15] ANSYS 2013 *CFX-solver modeling guide* (ANSYS inc)
- [16] Yunus A C and Cimbala J M 2006 *Fluid mechanics fundamentals and applications* (McGraw Hill Publication)
- [17] Menter F R 1994 *AIAA journal* **32** 1598–1605
- [18] Ferziger J H and Peric M 2012 *Computational methods for fluid dynamics* (Springer Science & Business Media)
- [19] Brekke H 1994 *Proc. of the 17th IAHR Symp., Beijing, China* pp 15–19
- [20] Giersch T, Hnisch P, Beirow B and Khhorn A 2013 *J. of Turbomachinery* **135** 031034

Paper 4

Model Order Reduction Technique Applied on Harmonic Analysis of a Submerged Vibrating Blade

Tengs, E., Charrassier, F., Holst, M., Storli, P. T.

International Journal of Applied Mechanics and Engineering, **24.1** (2019): 131-142

MODEL ORDER REDUCTION TECHNIQUE APPLIED ON HARMONIC ANALYSIS OF A SUBMERGED VIBRATING BLADE

E. TENGS*

The Waterpower Laboratory, Norwegian University of Science and Technology
7491 Trondheim, NORWAY
EDR&Medeso, Leif Tronstads Plass 4
1337 Sandvika, NORWAY
E-mail: erik.tengs@edrmedeso.com

F. CHARRASSIER and M. HOLST
EDR&Medeso, Leif Tronstads Plass 4
1337 Sandvika, NORWAY

PÅL-TORE STORLI

The Waterpower Laboratory, Norwegian University of Science and Technology
7491 Trondheim, NORWAY

As part of an ongoing study into hydropower runner failure, a submerged, vibrating blade is investigated both experimentally and numerically. The numerical simulations performed are fully coupled acoustic-structural simulations in ANSYS Mechanical. In order to speed up the simulations, a model order reduction technique based on Krylov subspaces is implemented. This paper presents a comparison between the full ANSYS harmonic response and the reduced order model, and shows excellent agreement. The speedup factor obtained by using the reduced order model is shown to be between one and two orders of magnitude. The number of dimensions in the reduced subspace needed for accurate results is investigated, and confirms what is found in other studies on similar model order reduction applications. In addition, experimental results are available for validation, and show good match when not too far from the resonance peak.

Key words: model order reduction, FSI, vibration, harmonic response.

1. Introduction

The quality and precision in the manufacturing industry have improved massively during the last couple of decades, due to automation and CNC machining. Even still, there have been several failures in new high head Francis turbines lately [1, 2]. This suggests that there is a problem in the design process. The dominating periodic load on the runner is known to be the forces due to the pressure field created by the flow passing the stationary components interacting with the pressure field following the rotating runner (known as Rotor-Stator Interaction (RSI)) [3]. When engineering a turbine, the RSI frequency is known in advance, and the design aims to have natural frequencies of components and assembly far away from the RSI frequencies to avoid any resonance issues. The runner however, is submerged in water, which is known to change its structural behavior [4]. The surrounding fluid complicates the structural calculations, as the added mass of water will lower the natural frequencies of the structure, and dampen the amplitude of the deflections. Furthermore, moving water will affect the structure differently from water standing still. It is also observed that the presence of water can change the order of the structural modes [5]. An acoustic-structural simulation will account for the presence of the surrounding fluid. Before such simulations were available, the industry

* To whom correspondence should be addressed

used empirical estimates to approximate the reduction of the natural frequency. Today however, studies show that it is not possible to obtain an all-purpose rule [4-6]. To conclude, if the goal is to investigate dynamic response of a turbine by performing a harmonic sweep of a Francis turbine with surrounding water, a coupled acoustic-structural simulation is needed.

The calculation of the coupled acoustic-structural harmonic response of a submerged structure is computationally expensive [7] and not applicable for all industries. This article will implement a Krylov-subspace based model order reduction method for rapid calculation of harmonic analyses, based on the methodology presented by Rudnyi [8]. The structure in question is a submerged vibrating hydrofoil, a geometry studied in a research project investigating Francis runner failures at the Norwegian University of Science and Technology [9]. Experimental data on the same geometry is available for validation. This data is publicly available from the Francis99 project website [10].

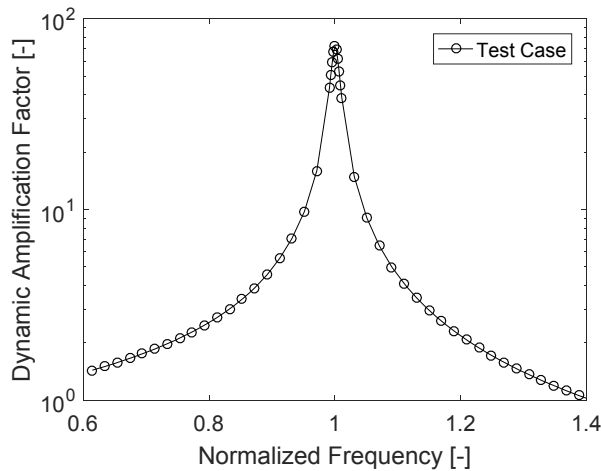


Fig.1. Dynamic amplification factor on generic blade.

2. Theory and methods

All structures have several natural frequencies and corresponding vibrational modes. If a structure is loaded at a frequency close to its natural frequency, the structural response A will be magnified compared with the static load magnitude A_0 . This is referred to as resonance and could in the worst case cause violent structural failure [11]. Figure 1 shows an example of the first mode Dynamic Amplification Factor, $DAF = A/A_0$, on a generic blade. The DAF is defined as deformation normalized by the steady response of the applied harmonic load. Equivalently, normalized with the response as the frequency goes to zero, $f \rightarrow 0$ [11].

From a design point of view, this graph is very interesting. In a design process, you will always try to avoid the natural frequencies and resonance. What Fig.1 shows is how the structure responds, not only at resonance, but at off-resonance conditions. The exact shape of the response graph is dependent of many factors; the damping; closeness to next natural frequency, etc., however let us use this figure to illustrate a design issue; If one assumes a linear material, and linear force-deflection relationship, then the amplification factor can be directly translated into a multiplication factor for the applied load. In the above figure we can see that even loading as far away as 25% from the natural frequency will be multiplied by a factor of 2, whereas loading at the natural frequency will be multiplied with about 75. The danger is the following; there will always be an uncertainty in the calculation of the natural frequency of your component. Especially submerged structures can be difficult to perfectly predict, and the response away from the natural frequency

then becomes even more important. Let us assume that you design to be 15% from resonance, but the error in natural frequency is in the order of 10%. The multiplication factor during operation will then be anywhere between 2 and 10. Clearly this is not acceptable for subsequent operation of the investigated component.

This underlines the need for the construction of harmonic response and amplification factor plots, the computational cost of removing all uncertainty in the calculation of the natural frequency is extreme, and maybe impossible. It is therefore desirable to obtain the dynamic response early in a design process, to identify risks, find sufficient safety margins, and perform design changes accordingly. To obtain this you need to solve a set of time-consuming harmonic equations. The simulation time will in this case be reduced by the use of Krylov subspaces. Model order reduction based on Krylov subspaces started in the electrical community [12, 13], and later in other industries with good results [14, 15].

The following sections will describe the governing equations of coupled structural-acoustic problems, as well as some of the theory behind a Krylov subspace model order reduction technique.

2.1. Second order, dynamic structural systems

Much of the theory in the following sections is adapted from [16], please refer here for more information. Most dynamic systems are second order. A general second order system can be modeled as follows

$$M\ddot{x}(t) + C\dot{x}(t) + Kx(t) = Fy(t) \quad (2.1)$$

where $x \in R^N$ is the state variable (typically displacement), and $y \in R^N$ is the force vector. The matrices $M, C, K \in R^{N \times N}$ are the usual mass, damping and stiffness matrices respectively, and N is the degrees of freedom. F controls the distribution of the input force. In the case of a harmonic excitation and response we have

$$Fy(t) = \{F\} e^{i\omega t}, \quad (2.2)$$

$$x(t) = x_{max} e^{i\varphi} e^{i\omega t} = \{x\} e^{i\omega t} \quad (2.3)$$

where ω denotes the angular frequency, and φ a potential phase shift. By using Eqs (2.2) and (2.3) and removing the time dependency, Eq.(2.1) can be rewritten as

$$\left[-\omega^2 M + i\omega C + K \right] \{x\} = \{F\}. \quad (2.4)$$

Equation (2.4) is the equation solved when performing a harmonic analysis, and the one implemented in most commercial codes, including ANSYS Mechanical, used in this paper. However, if solved as is, the effects of added mass of the surrounding fluid is not accounted for. The structural natural frequencies will be wrong, and useless in a design phase. Therefore, we have to expand this equation to include the acoustic domain.

2.2. Coupled acoustic-structural systems

Acoustics denotes the science of mechanical waves in fluids and structures. In terms of the fluid, no advection terms are modelled, only the pressure propagation is resolved. The pure harmonic motion of the sound pressure inside a fluid domain can be modelled by the Helmholtz equation (time-independent wave equation) [17]

$$\nabla^2 p + k^2 p = 0 \quad (2.5)$$

where p is the acoustic pressure, $k = \omega / c$ is the wave number, and c is the speed of sound in the fluid. A structure submerged in water will change characteristics due to the density of water. Especially eigenfrequencies and harmonic response are significantly altered by a surrounding heavy fluid. The above Eq.(2.5) can therefore be rewritten for harmonic motions as done in the previous section, and combined with the structural response, Eq.(2.4), to obtain a coupled acoustic-structural system, referred to as the Eulerian displacement-pressure formulation [16, 18]

$$\left(-\omega^2 \begin{bmatrix} M_s & 0 \\ M_{fs} & M_a \end{bmatrix} + i\omega \begin{bmatrix} C_s & 0 \\ 0 & C_a \end{bmatrix} + \begin{bmatrix} K_s & K_{fs} \\ 0 & K_a \end{bmatrix} \right) \begin{Bmatrix} u \\ p \end{Bmatrix} = \begin{Bmatrix} F_s \\ F_a \end{Bmatrix} \quad (2.6)$$

where u is the structural displacement, and p is the acoustic pressure. The subscripts: s , a , fs denotes structure, acoustic, and fluid-structure respectively. The cross-multiplication matrices (M_{fs} , K_{fs}) are obtained by enforcing boundary conditions on the fluid-structure interface. This way information will cross the domain interfaces in a consistent way. This second order coupled formulation allows for accurate harmonic analysis of submerged structures. A major drawback is the increased computational expense of solving the above acoustic/structural system.

2.3. Model order reduction

In engineering problems, the number of degrees of freedom could be extremely large. When considering acoustic elements as well, the coefficient matrices become unsymmetric (see Eq.(2.6)) [19, 20]. The added complexity from the acoustic-structural coupling makes the above system in many cases too expensive to solve, especially if a large frequency range is to be covered with satisfactory resolution [21]. The reasoning behind the Model Order Reduction (MOR) is to find a lower dimensional subspace $V \in R^{N \times q}$ such that

$$\begin{Bmatrix} u \\ p \end{Bmatrix} = \{x\} \approx Vz + \varepsilon \quad (2.7)$$

where $z \in R^q$ and $q \ll N$. The symbol ε denotes a small error introduced by utilizing the reduced model. If one assumes that the subspace V is available, Eq.(2.6) can be rewritten as

$$\left[-\omega^2 M_r + i\omega C_r + K_r \right] \{z\} = \{F_r\} \quad (2.8)$$

where the subscript r denotes a reduced quantity, and the reduced matrices are defined as follows

$$M_r = V^T M V ; \quad C_r = V^T C V ; \quad K_r = V^T K V ; \quad F_r = V^T F V . \quad (2.9)$$

The matrices in Eq.(2.8) are reduced to order $R^{q \times q}$, an enormous improvement from the original system in Eq.(2.6), where the coefficients were $R^{N \times N}$. For a subspace of order $q=30$ or similar, the new system is solved in seconds.

The problem is to obtain the subspace V . In this article, V is chosen to be a Krylov subspace, created using the Arnoldi algorithm. This subspace satisfies the moment-matching property to resemble the original system, see [22]. The details of the model reduction procedure will not be explained here, interested readers

can find more in [8, 16, 23, 24]. In the process of creating the reduced model, the number of dimensions, q , must be chosen. In general, the larger the q , the higher the accuracy, but at a computational cost.

2.3.1. Application of model order reduction

The application of the model order reduction process outlined in the previous sections is shown in Fig.2. The commercial software ANSYS Mechanical is used to set up the system, define loads, constraints and more, and to create the coefficient matrices used in the reduction process. Then the reduction process is performed with the main parameter being the number of dimensions of the reduced system. Finally, the reduced system is solved.

2.4. Experimental setup

This study is a part of a larger research project at the Norwegian University of Science and Technology (NTNU), where the goal is to understand why

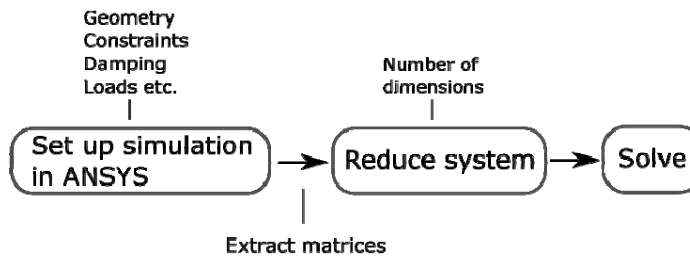


Fig.2. The process of performing the model order reduction.

high head Francis runners experience cracks [9]. Experiments have been performed on both an unsymmetrical hydrofoil (to resemble a Francis turbine runner blade), and a symmetric hydrofoil. The goal of these experiments is to study the damping characteristics of the fluid-structure system, and importantly, the relationship between the flow velocity and the damping. The experimental setup and results from the unsymmetrical hydrofoil can be found in [25], as well as on the Francis99 project homepage [10]. The same setup is used for the symmetric hydrofoil which will be studied here.

In short, an aluminum hydrofoil is excited by electric muscles (Piezoelectric Macrofiber composite actuators from PI Ceramic) to vibrate in a harmonic motion. Laser Doppler Vibrometry and strain gauges is used to measure the vibrating trailing edge motion. The frequency response is obtained for several different flow velocities, and used to calculate the damping characteristics of the system. The hydrodynamic damping ratio, ξ , obtained at $v = [2.5, 10, 20][m/s]$ in the experiments, is used in all the simulations presented here.

2.5. Numerical setup

The goal of this article is to present a model order reduction method. Experimental data is in this case strictly not needed, as a comparison with the assumed correct ANSYS solution would determine the accuracy of the MOR approximation and the speedup of the method. However, it is chosen to use the same geometry as in the aforementioned experiments as well as some of the

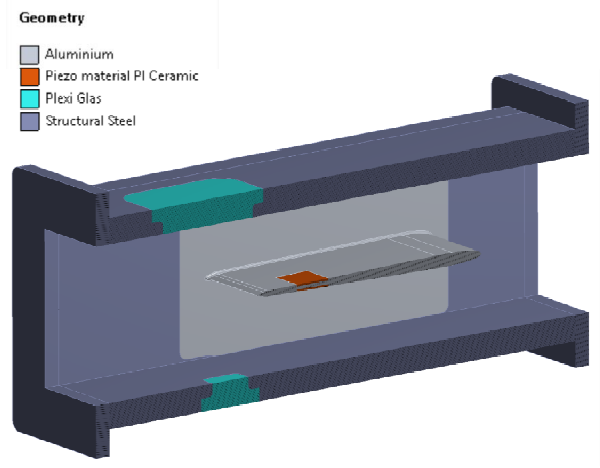


Fig.3. Numerical geometry.

results from the damping measurements, so that the current study is relevant to the overall project. The numerical domain is therefore as shown in Fig.3, and Tab.1 lists a summary of the most important simulation settings used in this article.

The simulations performed in ANSYS Mechanical will henceforth be referred to as the “full” solution. A constant load is used in all the simulations. This load was obtained from a CFD simulation on the same geometry, where the blade was vibrating at its natural frequency [27]. The fluid load (pressure) is imported to the blade in the harmonic analysis. A harmonic sweep is then performed in the range 300-750 Hz, divided into 100 equally spaced frequencies. The damping from the experiments, ξ , is used, from which the numerical damping is defined as $\beta = 2\xi/\omega_n$, [11] with ω_n being the natural frequency of the structure. There are two things to note about this procedure. First, the pressure load is extracted from a blade vibrating at a

Table 1. Numerical settings.

Parameter	Value
Software	ANSYS Mechanical
Analysis type	Full Damped, MOR
Damping	$\beta = [4.43e^{-6}, 8.16e^{-6}, 2.17e^{-5}]^*$
Frequency range	300-750 Hz
Number of frequencies	100
Mesh	500.000 nodes **
Acoustic domain	Water: $c = 1482 \text{ m/s}$, $\rho = 998 \text{ kg/m}^3$
Dimensions in MOR	$q=[10, 30, 50, 100]$

* Corresponding to flow velocity of 2.5,10 and 20m/s respectively [25]
** Discretization error estimated to be 0.2% using GCI method [26]

given mode shape. The corresponding load distribution and magnitude is therefore “locked” to the given mode. If one wants to investigate a range of frequencies where more than one bending mode is excited, more load distributions should be included. Second, note that the damping ratio is also valid for the first bending mode only. The same argument as above can be used for the damping, if more modes are to be investigated. The assumptions made in this paper are a simplification, but should be valid as the focus is on one mode at the time.

In addition to the full simulation, reduced simulations were performed. The simulation was set up as above, and the model reduction was performed on the equation system extracted from ANSYS, such that a direct comparison of the reduced versus the full solution is possible. In the reduced models, the number of dimensions were set to $q=[10, 30, 50, 100]$, to investigate both the accuracy of the reduced model, as well as the computational cost. Many papers report the use of $q=30$, however this is from different industries, and chosen somewhat arbitrary, and may not be applicable here [8].

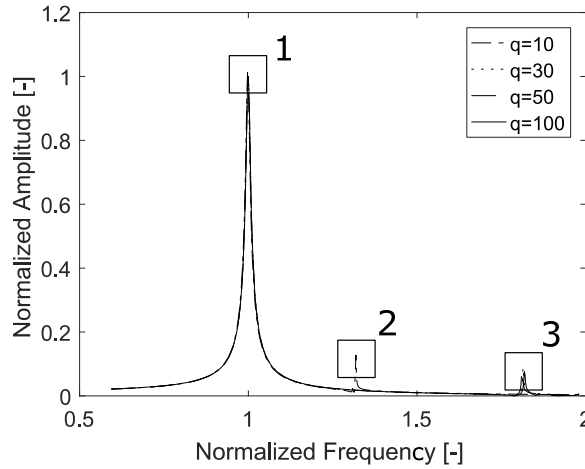


Fig.4. Comparison of the different number of dimensions in the reduced model.

3. Results

This first section will investigate the effect of changing the number of dimensions of the reduced order model, recall Eq.(2.8). The objective is to evaluate how many dimensions are needed to fully capture the behavior of the original system. The test case of $v=2.5m/s$ and corresponding damping is used. Figure 4 compares the different reduced models, with $q=[10, 30, 50, 100]$. The amplitude and frequency is normalized with the simulation using $q=100$ as it is assumed to be the most accurate. As the models perform very similarly, three boxes are marked in Fig.4, to be further investigated in Fig.5.

Figure 5 shows a zoomed view of the boxes marked in Fig.4. From Figs 5a, b it can be seen that only $q=10$ dimensions show some discrepancy compared to the rest of the simulations. In Fig.5c it is seen that the accuracy drops for $q=30$ and $q=50$ as well. Based on Fig.5 it is concluded that 30 dimensions are sufficient in terms of accuracy for this case. Therefore, all reduced order models will from this point on use $q=30$, as was reported in the literature to be sufficient.

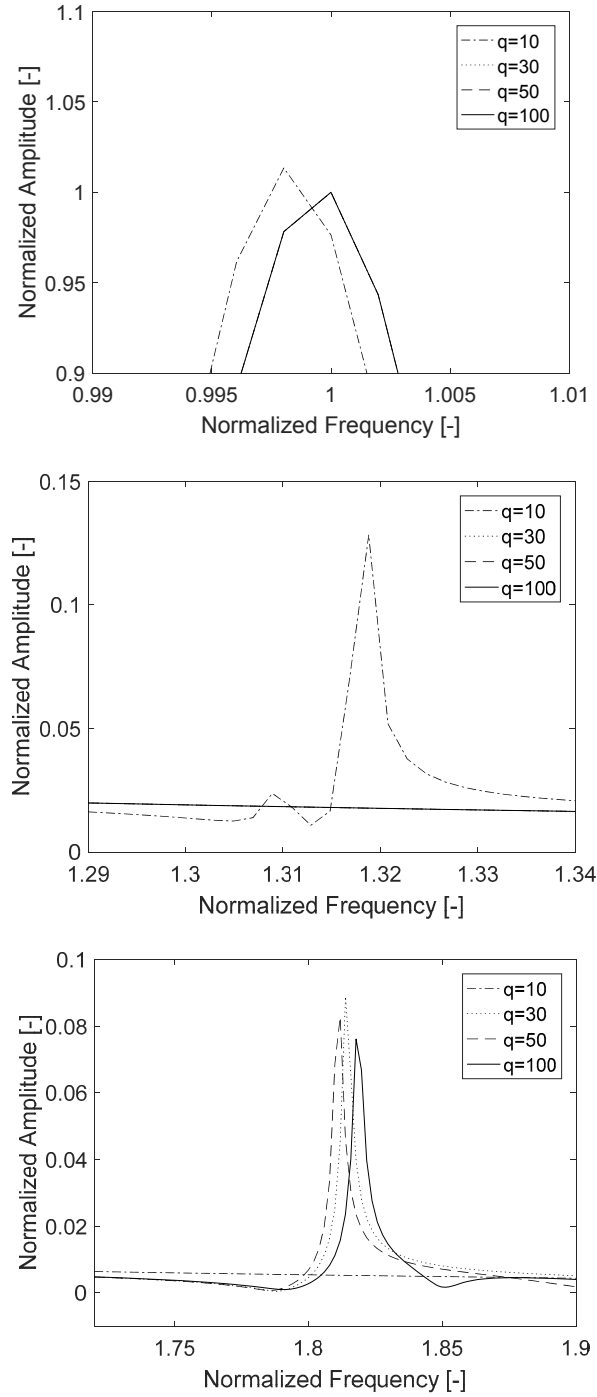


Fig.5. Detailed view of the effect of changing the number of dimensions in the MOR.

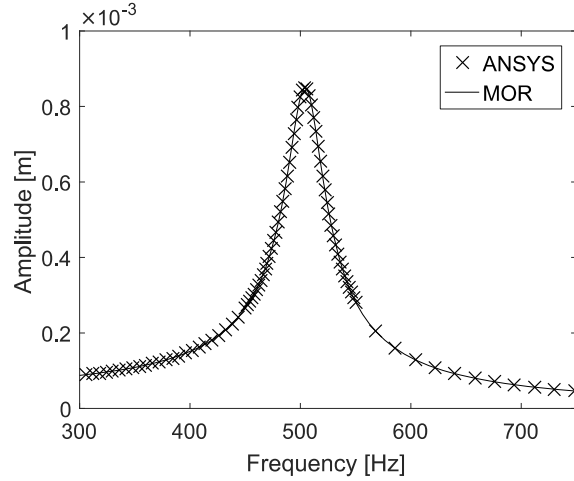


Fig.6. Comparison between full ANSYS solution and reduced order model.

3.1. Verification

In the following section, the MOR results using $q=30$ will be compared with the full ANSYS solution. Figure 6 shows a comparison using the damping corresponding to a flow velocity of $v=20\text{m/s}$ ($\beta = 2.17e^{-5}$). There is an excellent match in the complete range. Similar results are seen for the other flow velocities.

In addition to accuracy with respect to the full solution, the obtained speedup is the second crucial metric used to evaluate the MOR method. The speedup factor is calculated as follows; 100 evenly spaced frequencies were simulated with the full ANSYS solution. The MOR was performed on the same problem, and the total simulation time was compared. The results are shown in Tab.2. The speedup is case-dependent, mesh-dependent, etc., however Tab.2 will give a qualitative indication of the gain in simulation time.

It is clear that both the accuracy and simulation time are excellent. If we return to the dynamic amplification factor in Fig.1, creating such a plot is now possible in a reasonable time frame due to the speedup documented here.

Table 2. Speedup factor.

Method	Speedup*
Full ANSYS solution	1
MOR 10 dimensions	56
MOR 30 dimensions	40
MOR 50 dimensions	31
MOR 100 dimensions	18

* Per 100 frequencies

3.2. Validation

This section will compare the numerical frequency response with the experimental one. Figure 7 shows the scaled harmonic response of the vibrating blade obtained in experiments and in the simulations for flow velocities $v=20\text{m/s}$.

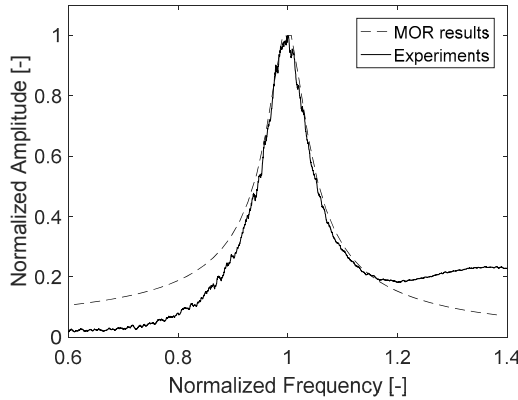


Fig.7. Comparison between experimental results and MOR solution.

It is observed that the overall match close to the response peak is very good, and that the accuracy decreases when moving further away from it.

4. Discussion

As in other studies, a reduced system of order 30 was deemed sufficient. This may be by chance, in the literature this number was chosen more or less arbitrarily [8], however it does indicate that a fairly low number of vectors/dimensions is needed to properly describe the original system. One thing that we can observe is that the method used for reducing the original system will be most accurate around a pre-determined point, i.e. the mid-point of the domain (think Taylor expansion about a point). In essence, the accuracy of the approximation will decrease in the ends of the investigated domain, this is seen in, i.e., Fig.5c, where $q=30, 50$ starts to deviate from the solution of $q=100$. This may imply that fewer dimensions are needed if the interesting frequencies are known in advance, and conversely, more dimensions are needed if a large sweep is to be performed with no prior knowledge of the location of the natural frequencies.

Observe that in the numerics, only one bending mode is excited in the frequency sweep (bottom right corner of Fig.7 indicates new mode in the experiments). This is due to the fact that the load distribution imported from CFD is linked to the first bending mode only. For resonance to occur, both the frequency and the spatial load distribution have to match with the mode in question. This is only satisfied for the first bending mode in this case. If a more generic load was applied, specifically one where the spatial distribution does not limit which bending modes are possible to obtain, a larger frequency range and more modes could be investigated.

Another factor is the damping from the experiments. The damping factor is strictly only valid at the natural frequency, not when moving away from the resonance peak. This may explain why the accuracy decreases when moving away from the peak in Fig.7. Yet another factor is the point at which the amplitude is measured in the simulations and the experiments. It is unlikely that exactly the same location is tracked, and this will therefore possibly introduce an uncertainty.

5. Conclusion

Solving complex engineering problems involving submerged structures require a coupled acoustic-structural simulation. This is computationally expensive, but this article shows that the simulation time can be reduced by an order of magnitude of one to two, without reducing the accuracy. A Krylov subspace method is used in the model order reduction process. Using this method can allow the designers to obtain dynamic amplification plots early in a design process, and can give valuable information regarding product design. The results are also compared with ongoing experiments, and show overall good results.

Acknowledgements

CADFEM Germany are the creators of the core solver, the mathematical process of reducing the original system. We thank them for allowing us access to their code, and all the help during this work. This project is funded by the Research Council of Norway, project number 254987, their contribution is greatly acknowledged.

Nomenclature

A	– amplitude of deflection
A_0	– amplitude at static load
β	– proportional/ Rayleigh damping
c	– speed of sound
DAF	– Dynamic Amplification Factor
f	– frequency
k	– wave number
MOR	– Model Order Reduction
M, C, K, F	– mass, damping, stiffness and force matrices
N	– degrees of freedom in original system
p	– pressure
q	– degrees of freedom in reduced system
RSI	– Rotor Stator Interaction
s, a, fs	– as subscripts; structure, acoustic, fluid-structure
V	– Krylov subspace
v	– flow velocity
x, \dot{x}, \ddot{x}	– deflection, velocity and acceleration
y	– force vector
ε	– error
ξ	– damping ratio
ρ	– density
ϕ	– phase shift between load and response
ω	– angular frequency
ω_n	– natural frequency

References

- [1] Kobro E. (2010): *Measurement of Pressure Pulsations in Francis Turbines*. – Ph.D. Thesis, Norwegian University of Science and Technology.
- [2] Liu X., Luo Y. and Wang Z. (2016): *A review on fatigue damage mechanism in hydro turbines*. – Renewable and Sustainable Energy Reviews, vol.54, pp.1–14.
- [3] Seidel U., Hübner B., Löfflad J. and Faigle P. (2012): *Evaluation of RSI-induced stresses in Francis runners*. – In: IOP Conference Series: Earth and Environmental Science, vol.15, IOP Publishing, pp.052010.
- [4] Dörfler P., Sick M. and Coutu A. (2012): *Flow-induced pulsation and vibration in hydroelectric machinery: engineers guidebook for planning, design and troubleshooting*. – Springer Science and Business Media.
- [5] Liang Q., Rodríguez C.G., Egusquiza E., Escaler X., Farhat M. and Avellan F. (2007): *Numerical simulation of fluid added mass effect on a francis turbine runner*. Computers and Fluids, vol.36, No.6, pp.1106–1118.
- [6] Tanaka H. (2011): *Vibration behavior and dynamic stress of runners of very high head reversible pump-turbines*. – International Journal of Fluid Machinery and Systems, vol.4, No.2, pp.289–306.

- [7] Pirk R., Desmet W., Pluymers B., Sas P. and Goes L.C. (2002): *Vibro-acoustic analysis of the brazilian vehicle satellite launcher (vls) fairing*. – In: Proceedings of the International Conference on Noise and Vibration Engineering, ISMA, Leuven, Belgium.
- [8] Rudnyi E.B. (2013): *Mor for ansys*. – System-Level Modeling of MEMS, pp.425–438.
- [9] The hifrancois research project, <https://www.ntnu.edu/web/norwegian-hydropower-center/hifrancois>, accessed: 2018-05-07.
- [10] The francis99 research project, <https://www.ntnu.edu/nvks/francis-99>, accessed: 2018-05-23.
- [11] Craig R.R. and Kurdila A.J. (2006): *Fundamentals of Structural Dynamics*. – John Wiley and Sons.
- [12] Bai Z. (2002): *Krylov subspace techniques for reduced-order modeling of largescale dynamical systems*. – Applied Numerical Mathematics, vol.43, No.1-2, pp.9–44.
- [13] Freund R.W. (2000): *Krylov-subspace methods for reduced-order modeling in circuit simulation*. – Journal of Computational and Applied Mathematics, vol.123, No.1-2, pp.395–421.
- [14] Willcox K., Peraire J. and White J. (2002): *An arnoldi approach for generation of reduced-order models for turbomachinery*. – Computers and Fluids, vol.31, No.3, pp.369–389.
- [15] Lassaux G. (2002): *High-fidelity reduced-order aerodynamic models: Application to active control of engine inlets*. – Ph.D. Thesis, Massachusetts Institute of Technology.
- [16] Puri R.S., Morrey D., Bell A.J., Durodola J.F., Rudnyi E.B. and Korvink J.G. (2009): *Reduced order fully coupled structural–acoustic analysis via implicit moment matching*. – Applied Mathematical Modelling, vol.33, No.11, pp.4097–4119.
- [17] Fahy F.J. (2000): *Foundations of Engineering Acoustics*. – Elsevier.
- [18] Everstine G. (1997): *Finite element formulations of structural acoustics problems*. – Computers and Structures, vol.65, No.3, pp.307–321.
- [19] Zienkiewicz O.C. (1969): *Coupled vibrations of a structure submerged in a compressible fluid*. – In: Proc. of Symposium on Finite Element Techniques Held at the University of Stuttgart.
- [20] Craggs A. (1971): *The transient response of a coupled plate-acoustic system using plate and acoustic finite elements*. – Journal of Sound and Vibration, vol.15, No.4, pp.509–528.
- [21] Atalla N. and Bernhard R. (1994): *Review of numerical solutions for low-frequency structural-acoustic problems*. – Applied Acoustics, vol.43, No.3, pp.271–294.
- [22] Benner P., Feng L. and Rudnyi E.B. (2008): *Using the superposition property for model reduction of linear systems with a large number of inputs*. – In: Proceedings of the 18th International Symposium on Mathematical Theory of Networks and Systems.
- [23] Rudnyi E.B. and Korvink J.G. (2004): *Model order reduction for large scale engineering models developed in ansys*. – In: International Workshop on Applied Parallel Computing, Springer, pp.349–356.
- [24] Rudnyi E.B., Lienemann J., Greiner A. and Korvink J.G. (2004): *Mor4ansys: Generating compact models directly from Ansys models*. – In: Technical Proceedings of the 2004 Nanotechnology Conference and Trade Show, Nanotech, vol.2, pp.279–282.
- [25] Bergan C., Solemslie B., Ostby P. and Dahlhaug O.G. (2018): *Hydrodynamic damping of a fluttering hydrofoil in high-speed flows*. – International Journal of Fluid Machinery and Systems, vol.11, No.2, pp.146–153.
- [26] Celik I.B., Ghia U., Roache P.J., Freitas C.J., Coleman H. and Raad P.E. (2008): *Procedure for estimation and reporting of uncertainty due to discretization in {CFD} applications*. – Journal of Fluids {Engineering-Transactions} of the {ASME}, vol.130, No.7.
- [27] Tengs E, Bergan C., Storli P.-T. and Jakobsen K.-R. (2018): *Numerical simulation of the hydrodynamic damping of a vibrating hydrofoil*. – In: Proceedings of the 29th IAHR Symposium on Hydraulic Machinery and Systems, Not yet published, 2018.

Received: June 11, 2018

Revised: November 5, 2018

Paper 5

Two-way coupled simulation of the Francis-99 hydrofoil using model order reduction

Tengs, E., Einzinger, J. , Storli, P. T.

Journal of Physics: Conference Series, **1296** 012001, 2019

Two-way coupled simulation of the Francis-99 hydrofoil using model order reduction

Erik Tengs^{1,2}, Johannes Einzinger³, Pål-Tore Storli²

¹ EDR&Medeso, Leif Tronstad Plass 3, 1337 Sandvika, Norway

² Norwegian University of Science and Technology, 7491 Trondheim, Norway

³ ANSYS Germany GmbH, Staudenfeldweg 20, 83624 Otterfing, Germany

E-mail: erik.tengs@edrmedeso.com

Abstract. The Francis-99 hydrofoil is simulated using a quasi two-way Fluid-Structure Interaction procedure. The structural domain is reduced by the use of modal decomposition, and solved for inside the commercial fluid solver ANSYS CFX. Both the first order Backward Euler and second order Crank-Nicolson time discretization scheme is used in the structural equations, with significantly different results. Several coupled fluid-structure phenomena is observed that would be unobtainable in a normal one-way approach. The most interesting is an "added stiffness" effect, where the eigenfrequency of the foil increases when the flow velocity is increased. This trend corresponds well with available experimental results. The same phenomenon is observed in the hydrodynamic damping on the foil. Self-induced vibration due to vortex shedding is also simulated with good results.

The implemented two-way approach allows the different forcing terms to be tracked individually, due to the discretization of the second order structural system. This provides insight into the underlying physics behind the different FSI phenomena seen, and helps us explain why the damping and eigenfrequency characteristics change as the flow velocity passes the lock-in region.

1. Introduction

In the last couple of decades, numerical simulation and Computational Fluid Dynamics (CFD) have become one of the pillars in fluid mechanical research, alongside experiments and analytical work. The tools are in constant development and are in need of validation and testing. In the hydropower industry, the turbine designs are usually confidential, which makes it difficult for academic institutions to do research on state-of-the-art geometries. The Francis-99 workshops aims to provide an open source geometry and experimental data for validation of numerical tools and methods [1]. The model turbine is located at the Norwegian University of Science and Technology. The third Francis-99 workshop deals with Fluid-Structure Interaction (FSI). Two test cases are available to the public, one case on resonance in turbine runner channels, and one case on a more fundamental issue, hydrodynamic damping and eigenfrequencies of submerged hydrofoils. This paper will focus on the Francis-99 hydrofoil.

As part of the validation data presented for the Francis-99 Hydrofoil, two interesting figures are included and shown below, credit to Bergan et al [1, 2]. Figure 1a shows the hydrodynamic damping as a function of flow velocity. There is a distinctly different trend before and after the lock-in region. Lock-in can be defined as the frequency range where the shedding frequency of a



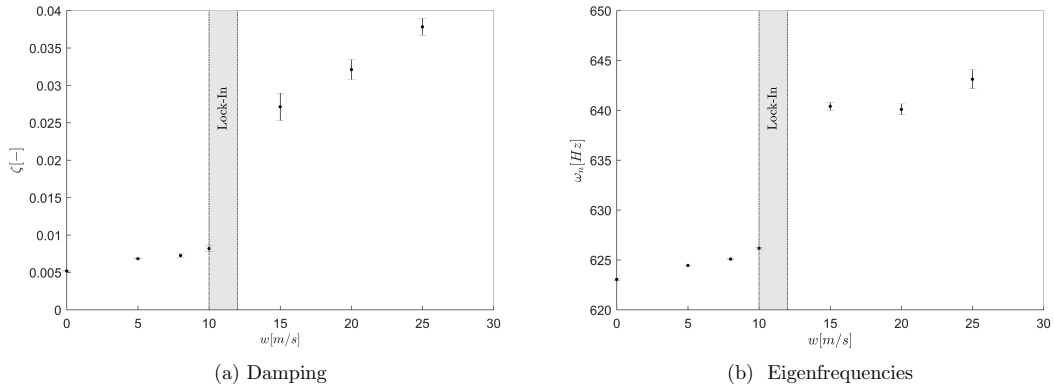


Figure 1: Validation data provided by [2]

body coincide and "locks" with the natural frequency of the object in question [3]. The damping is approximately constant before, and linearly increasing, after lock-in. This experiment has been repeated with a different hydrofoil, but with the same outcome [4], and this was numerically replicated with good results [5]. This numerical work however was utilizing a one-way coupling, and although the damping was predicted, *why* the damping is different before and after lock-in was not answered in the cited works. Performing a two-way simulation may give insight into this.

The second figure, 1b, shows the natural frequency of the foil. There is a similar shifting phenomenon before and after lock-in in this case, although a linearly increasing trend after lock-in is not seen. The increase in eigenfrequency is not big, but definitely significant. Another reason why this is interesting is the fact that in a simple oscillating system, an increase in damping would correspond to a *decrease* in the eigenfrequency, not an increase. From classical structural oscillating theory we have that the *damped* eigenfrequency, f_d , is related to the natural frequency, f_n , in the following way; $f_d = f_n \sqrt{1 - \xi^2}$, where ξ is the damping ratio [6]. Note also that the reduction in eigenfrequency should be very small, using the largest measured damping value in figure 1a, $\xi \approx 0.04$ will provide a frequency reduction of less than 1 %. From figure 1b we see a frequency *increase* of 30 times that. Therefore, it seems like there is an inconsistency between the two figures and the classical theory. Or rather, that the above description of the eigenfrequency, $f_d = f_n \sqrt{1 - \xi^2}$ is insufficient when the surrounding water is non-stationary. The two figures, and more importantly, the physical explanation to this behaviour, is the goal of this article. In order to obtain an understanding as general as possible, the focus will be on trends rather than obtaining the exact values.

This will be obtained by using a two-way FSI procedure. The structural problem will be reduced using a modal decomposition approach, and solved inside the fluid solver. This will provide a significant speedup compared with a traditional two-way approach, as well as a simplification of the setup.

2. Theory

The goal is to use a model order reduction scheme to reduce the structural motion such that it can be solved for inside a fluid solver. The model order reduction scheme is based on modal decomposition, and the fluid solver used is ANSYS CFX. The following sections will explain the

procedure. The two-way coupling will then be used to simulate the added mass and stiffness effects of flowing water over the Francis-99 hydrofoil.

2.1. Reduced structural model

The system we want to reduce is the usual, second order oscillating structural system [6],

$$M\ddot{u} + C\dot{u} + Ku = F \quad (1)$$

Where M, C, K, F is the mass, damping, stiffness and force coefficient matrix respectively. u denotes the deflection, and the over-dot notation indicates differentiation in time. To reduce the above equation, the principle of modal decomposition is used. For such a technique one needs the structural eigenmodes and eigenfrequencies, and thus, a modal analysis has to be performed on the system. The modal analysis, which is an eigenvalue problem, can be described as follows [7];

$$(-\omega^2 M + K)\Phi = 0 \quad (2)$$

As in all eigenproblems, the result will be the eigenvalues (ω^2) and the eigenvectors Φ_i . The scaling or length of the eigenvectors is arbitrary, however the direction is unique, and all eigenvectors are mutually orthogonal [7]. This property is used to create a modal basis Φ , a reduced vector-space, for the system. Using the modal basis, the structural deflection can be described as follows;

$$u^{n \times 1} = \Phi^{n \times m} q^{m \times 1} \quad (3)$$

The sizes of the matrices/vectors are included. The superscript n denotes the degrees of freedom in the original system, and m the number of modes in the modal basis. The variable q is referred to as a modal amplitude, the scaling factor that multiplied with the mode shape results in the actual, physical deflection. If the above expression is inserted in eq 1, and then pre-multiplied with the modal basis, you get the following [8]:

$$\Phi^T M \Phi \ddot{q} + \Phi^T C \Phi \dot{q} + \Phi^T K \Phi q = \Phi^T F \quad (4)$$

Where the new, reduced coefficient matrices are of the following order, $[\Phi^T]^{n \times m} M^{n \times n} \Phi^{n \times m} = M_{red}^{m \times m}$. This illustrates the model order reduction as $m \ll n$.

An advantage of using the eigenmodes to create a modal basis is that due to the orthogonality of the modes, the reduced system will be diagonal, consisting of a set of linearly independent, 1-dimensional equations. This will simplify calculations, and also let us express the structural deformation as a superposition of the different structural modes, Φ_i . Note that in eq. 2, the eigenmodes were calculated without damping. To preserve the diagonal system we assume Rayleigh/ proportional damping [6].

Let the coefficients in equation 4 still be denoted M, C, K and F for simplicity. The coefficient of \ddot{q} is usually normalized such that $\Phi^T M \Phi = 1$ [9]. The second order system can now be written as;

$$M\ddot{q} + C\dot{q} + Kq = F \quad (5)$$

Let the damping ratio ξ be defined as $\xi = C/(2M\omega)$ and the natural frequency $\omega = \sqrt{K/M}$, and we can derive the following [6] (recall that the matrices are diagonal);

$$\ddot{q}_i + 2\omega\xi\dot{q}_i + \omega^2 q_i = f_i \quad (6)$$

Note that the new second order harmonic system is now decoupled from the physical meaning of equation 1. Equation 6 solves for the modal displacement, using the modal force. The actual structural deformation is recovered by equation 7.

$$u = \sum_i^m \Phi_i q_i \quad (7)$$

The big advantage of the above representation, is that the solution to the structural motion is now reduced to solving a set of independent 1-dimensional equations for the modal amplitude, instead of solving for the deflection in the complete solution space.

2.2. Numerical discretization in CFX

The above section reduced the structural motion to equation 6 and 7. Further modification is needed for this to be solvable inside the commercial fluid solver ANSYS CFX. Specifically, a time discretization method is needed, the first order backward Euler and the second order Crank-Nicolson method will be presented here.

In both the discretization methods, the original second order system is split into two, first order systems, one for the displacement, and one for the velocity, illustrated below using the implicit, backward Euler scheme [10];

$$\begin{aligned} \frac{q_{i,k+1} - q_{i,k}}{\Delta t} &= v_{i,k+1} \\ \frac{v_{i,k+1} - v_{i,k}}{\Delta t} &= -2\omega\xi v_{i,k+1} - \omega^2 q_{i,k+1} + f_{i,k+1} \end{aligned} \quad (8)$$

where the subscript $i = 1, 2, \dots, m$ denotes the mode, and the subscript $k = 1 \rightarrow \infty$ denotes the discretization in time. The forward Euler scheme is identical, except all $(k+1)$ subscripts on the right-hand side is replaced with (k) only.

The Crank-Nicolson time discretization scheme is a linear combination of the forward and backward Euler method [10];

$$\begin{aligned} \frac{q_{i,k+1} - q_{i,k}}{\Delta t} &= 0.5(v_{i,k+1} + v_{i,k}) \\ \frac{v_{i,k+1} - v_{i,k}}{\Delta t} &= 0.5(-2\omega\xi v_{i,k+1} - \omega^2 q_{i,k+1} + f_{i,k+1} - 2\omega\xi v_{i,k} - \omega^2 q_{i,k} + f_{i,k}) \end{aligned} \quad (9)$$

The expression for velocity can be inserted in the expression for the acceleration, then rearranged to isolate the unknowns $q_{i,k+1}$, $v_{i,k+1}$ on the left hand side, to obtain the final Crank-Nicolson scheme:

$$\begin{aligned} q_{i,k+1} &= \frac{q_{i,k}(1 + \omega\xi\Delta t - \frac{1}{4}\omega^2\Delta t^2) + \Delta t v_{i,k} + \frac{1}{4}\Delta t^2(f_{i,k+1} + f_{i,k})}{1 + \omega\xi\Delta t + \frac{1}{4}\omega^2\Delta t^2} \\ v_{i,k+1} &= 2\frac{q_{i,k+1} - q_{i,k}}{\Delta t} - v_{i,k} \end{aligned} \quad (10)$$

The same procedure is done for the backward Euler scheme for a similar result. The final expression for $q_{i,k+1}$ consists only of known quantities, namely the eigenfrequency of that mode, the (structural) damping, the time step size, and the modal force calculated by the fluid solver at that time step. The old value of the modal amplitude, velocity and force needed to calculate

the expression is stored using a Fortran script, and called upon during calculation. The modal force has not been properly defined yet. From equation 5 to 6 the force matrix is divided by the diagonal mass matrix to obtain $f_i = F/M[\frac{N}{kg \cdot m^2}]$. The forcing is decoupled into the force projection onto the different modes and is implemented as

$$f_i = \frac{1}{M} \int_A p \cdot \Phi_i dA \quad (11)$$

where p is the fluid pressure. The above (eq. 10-11) can be implemented in CFX using the CEL expression language. The performance of the different discretization schemes will be presented in the results section.

2.3. Reduced velocity

In order to compare results across hydrofoil geometries, experiments, and simulations, it is desirable to use a different variable than the flow velocity. Bergan et al. [11] presents a reduced velocity, $v^* = v/f_n$, defined as the flow velocity divided by the eigenfrequency of the vibrating hydrofoil. In a way, this describes how much water that passes the foil during one vibrational period. It was found that if the damping was expressed with respect to v^* , then many different foils showed near identical behaviour, namely a change in damping characteristics around $v^* \approx 0.02$. This is also seen in figure 1a, as $v^* \approx 11.5/625 = 0.018$. The reduced velocity is similar to the inverse of the famous Strouhal number, $St = fL/v$, used to link the shedding frequency of vortices in the wake of an object to the flow velocity [12, 13], but without the characteristic length.

The simulations in this paper is 2D to speed up the process. As a consequence, the surface area of the foil changes compared with the 3D case. This will in turn reduce the surface force on the foil (see eq. 11), which affects the eigenfrequency. The result is as follows; in a 2D simulation, the added mass effect is smaller than in 3D, and the loaded eigenfrequency will therefore be closer to that of the foil vibrating in vacuum. By presenting the result using the reduced velocity v^* from above, the 2D simplification should not affect the results, as the flow velocity is normalized with the eigenfrequency.

3. Method

The focus have been the Francis-99 hydrofoil, more information about the hydrofoil can be found in the paper by Bergan et al, or the workshop website [1, 2]. For reference, the first bending mode (trailing edge motion) of the hydrofoil is shown in figure 2, with exaggerated deformation for illustration. Three test cases have been performed, a comparison of the discretization schemes, a simulation of self-induced vibration, and an attempt to replicate the damping and eigenfrequency behaviour across the lock-in region.

3.1. Discretization schemes

The first task is to assess the different discretization schemes. In this test case, a cantilever beam has been used for simplicity. The setup is as follows; the beam has been given an initial deflection ($\approx 3\%$ of the total length), then released. The structural damping has been set to zero, $\xi = 0$, and importantly, the fluid force (f_i in equation 6) have been hardcoded to be zero. This results in a system of equations for the structural deformation that purely consists of the structural mass and stiffness term. Theoretically, this system, given an initial deflection, should result in the following solution: $u = A \cdot \cos(\omega t)$. That is, a perfect sinusoid with constant amplitude and frequency.

This test case is natural to use as it will reveal if any of the discretization schemes exhibit any unwanted *numerical* damping. The simulations were performed using 100 timesteps per oscillatory period.

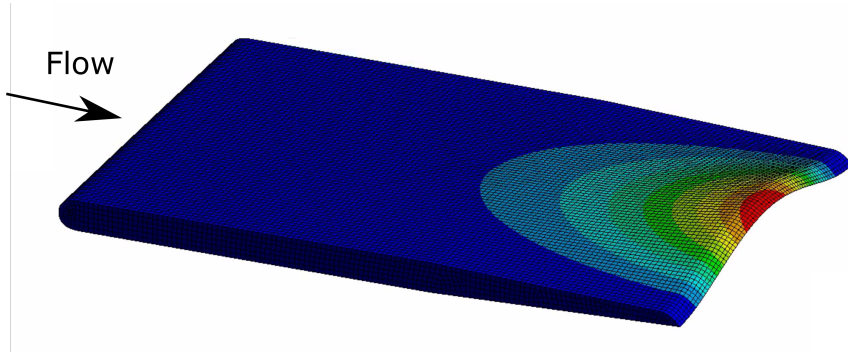


Figure 2: First bending mode of Francis-99 hydrofoil

3.2. Self-induced vibration

The coupled physics phenomenon of self-induced vibration will be simulated next. Fluid flow across an object will, at certain Reynolds numbers, induce an oscillatory pressure and velocity field. This field creates vortices trailing the body, and the body itself will experience periodic forces perpendicular to the flow direction [14]. If these periodic forces are close to the eigenfrequency of the structure, resonance can occur in the worst case. The structural vibration can also magnify the shedding of vortices and can therefore have a self-magnifying effect.

A phenomenon called "lock-in" is also something that can be observed during vortex shedding. In general, the frequency at which the vortices are shedded is linearly dependent on the flow velocity [3, 15]. If the flow velocity however, is such that the shedding frequency is close to the eigenfrequency of the structure, then the shedding frequency will "lock" to the structural frequency rather than increase linearly. For reference, Particle Image Velocimetry and CFD simulations have been used on this geometry in a previous study [16]. The simulations in that study was pure CFD, meaning no structural motion.

The hydrofoil was subjected to flow velocities in the range $v^* = [0.12 - 0.25]m$, and the SST turbulence model was used in all simulations.

3.3. Damped Vibration

The final task is to assess the added damping and stiffness effects of the flowing water. This is done by the use of damped vibration. The solution to a system of damped vibration without external forces is in the most general form the following [6];

$$x(t) = A \cdot e^{-\xi\omega t} \cdot \cos(\omega_d t + \phi) \quad (12)$$

In essence, this is a sinusoid enveloped by an exponential decay. The sinusoid contains the oscillating part of the solution, i.e. the eigenfrequency, and the exponential decay contains the damping part of the solution. This representation is used when the results are analyzed.

The analysis was set up as follows; the hydrofoils was given an initial deflection, and the *structural* damping was set to $\xi = 0$. Any damping of the foil will therefore originate in hydrodynamic forces. All simulations were performed with approximately 150 timesteps per oscillatory period, and was allowed to oscillate for at least 20 periods. This ensures that the error in estimating the damping and the submerged, loaded eigenfrequency was minimized. The error in the damping was estimated to be $\approx 1.5\%$ (using a 95% confidence interval of the exponential fit), and the error in the eigenfrequency, $\approx 0.6[Hz]$.

4. Results and discussion

4.1. Discretization schemes

Figure 3 shows the normalized structural deformation of the beam using Euler and Crank-Nicolson discretization scheme. Recall that in the test of discretization schemes, the structural damping and the fluid damping is set to zero to highlight any unwanted numerical damping.

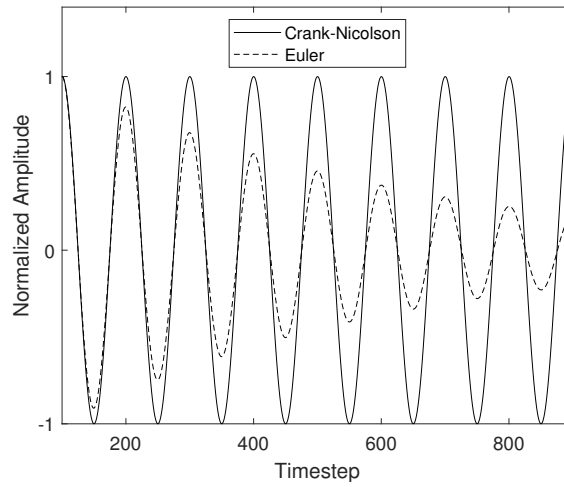


Figure 3: Comparison of the different discretization schemes

Clearly the performance of the Crank-Nicolson scheme is superior, with no numerical damping under the given conditions. The numerical damping in the Euler scheme is estimated using exponential decay to be $\approx 3\%$. This is not a large number, it is no larger than what is expected from the surrounding fluid flow [2, 17], however the effect on the displacement over time is significant. It is larger than can be accepted for subsequent simulations. The number of timesteps per period, 100, is considered sufficient and in the order of what would be used in a normal simulation. Based on the above it is therefore concluded that the Crank-Nicolson scheme should be used, especially as it carries no additional computational cost.

The Euler scheme displayed some unwanted numerical damping, compared with Crank-Nicolson. Evaluating the scheme using a Taylor expansion;

$$u_k = u_{k+1} - \Delta t \left(\frac{du}{dt} \right)_{k+1} + \frac{\Delta t^2}{2!} \left(\frac{d^2u}{dt^2} \right)_{k+1} + H.O.T. \quad (13)$$

where H.O.T denotes higher order terms. Rearranging will give the following;

$$\frac{u_{k+1} - u_k}{\Delta t} = \left(\frac{du}{dt} \right)_{k+1} - \frac{\Delta t}{2!} \left(\frac{d^2u}{dt^2} \right)_{k+1} + H.O.T. \quad (14)$$

Where we see that the scheme produces the time derivative we seek (it is *consistent*), and that the scheme is first order accurate, as predicted. Interestingly, the first order error term is related to a $\frac{d^2u}{dt^2}$ - acceleration operator. The damping seen in figure 3 is likely to originate in this term. This might indicate that structures with high eigenfrequencies, and thus high acceleration, will be more sensitive to discretization error. The structure in this case does have a fairly high eigenfrequency, however a sensitivity study on this have not been performed.

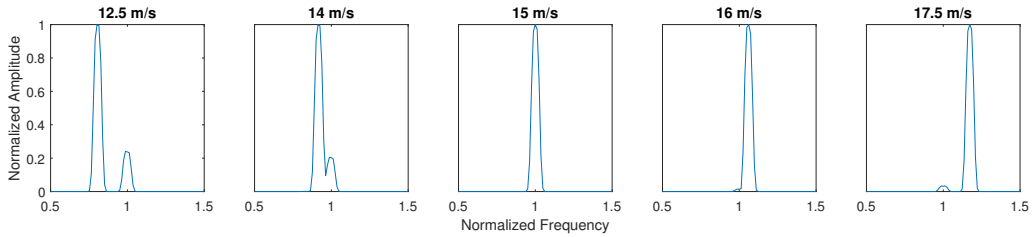


Figure 4: Frequency content during simulations of self-induced vibration

4.2. Self-induced vibration

Figure 4 shows the frequency spectrum of the vibration of the hydrofoil. The magnitude is normalized such that the different flow velocities can be compared. Interestingly, we see a component of the structural eigenfrequency ($f = 1$ in the figure) in all the simulations, along with another frequency component. The other component is the shedding frequency.

Figure 5 shows on the left axis the dominating frequency component as a function of the reduced velocity. The relation is close to linear as expected, however there is some discrepancy around the point where the eigenfrequency of the foil matches the shedding. This is signs of the lock-in phenomenon, although not as clear as was shown in other experimental works [16, 3]. On the right axis, the normalized amplitude of the self-induced vibration is plotted. It is clear that the effect of resonance is extreme.

Another finding is that the reduced velocity at which these phenomena occur is exactly where Bergan et. al [11] predicted, $v^* \approx 0.018 - 0.02$, even though this is a 2D representation of the foil, with changed eigenfrequency. This is a great justification of the use of the reduced velocity.

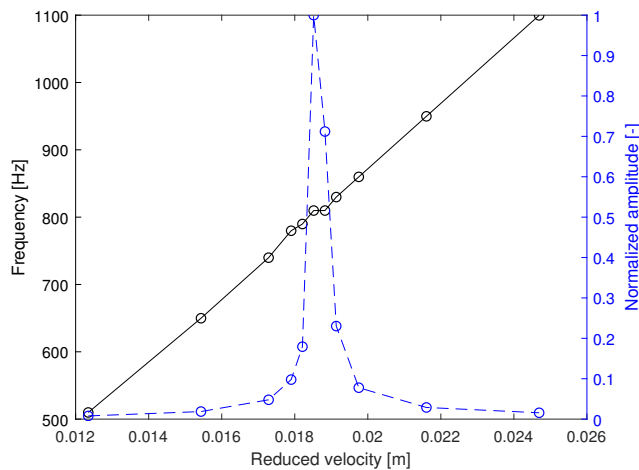


Figure 5: Shedding frequency and lock-in effect

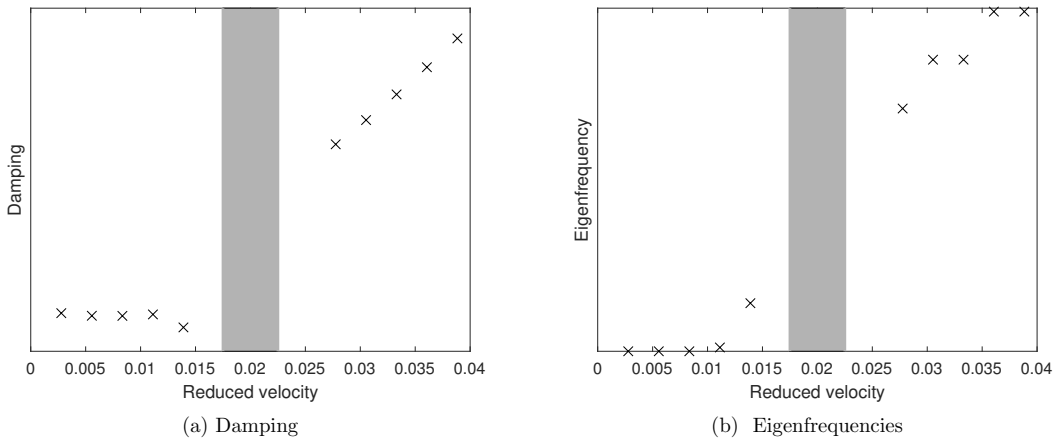


Figure 6: Numerical simulation of damping and eigenfrequency across lock-in

4.3. Damping and Eigenfrequency

Figure 6 shows the damping and natural frequency of the Francis-99 hydrofoil. The x-axis shows the reduced velocity rather than the absolute velocity, due to the 2D representation of the foil. The scale on the y-axis is purposely omitted as the changes are fairly small and should not be compared with figure 1 in terms of absolute values, again due to the 2D representation, however the relative change is clear. The shaded areas represent the "lock-in" area where the change in characteristics changed in the experiments.

Comparing figure 6 to figure 1 it is clear that similar trends are seen. The change in damping across the "lock-in" is simulated before, but the fact that it is observed here as well verifies the methods used. More interesting is the figure showing the eigenfrequencies. Similar as for the damping, a clear change is observed when crossing the "lock-in" region. Such a shift would be impossible to obtain in a one-way coupled simulation, as the vibration frequency would be an input to the simulation, see i.e. [5].

The primary goal of the paper is to be able to simulate the shift in damping and eigenfrequency seen in the experiments. This was done in this section. Equally important is to understand *why* such phenomena occur. The following section will try to use one of the inherent advantages in the presented two-way procedure, the ability to separate the different terms in the second order oscillatory system, and track them over time.

If we start with the second order equation for structural oscillating motion, eq. 1, we can label the terms as *inertial*, *damping*, *restoring* and *external forcing*.

$$\underbrace{M\ddot{u}}_{\text{inertial forces}} + \underbrace{C\dot{u}}_{\text{damping forces}} + \underbrace{Ku}_{\text{restoring forces}} = \underbrace{F}_{\text{external forces}} \quad (15)$$

An observation; the structural damping in all simulations have been set to zero, yet damping is still observed. However, if the external forcing is also set to zero, as in section 4.1 where the discretization schemes was tested, there was no damping at all. This indicates that the damping originates in the external forcing. The next question is how.

One hypothesis is that the external force can have a phase shift relative to the structural deformation. If the force has such a phase shift, it can be decomposed into the different order

derivatives of the structural motion, u, \dot{u} . An equivalent or additional damping can then be found as the \dot{u} component. This is a normal way of looking at the damping, see i.e. [5], as only the velocity-proportional term in eq. 1 is energy dissipative.

Assume that the deflection can be expressed as $u = a_1 \sin(\omega t)$ and the forcing on the blade $F = a_F \sin(\omega t + \phi)$. This means that the two are similar in shape and frequency, but separated by a phase shift. Now assume that the forcing can be decomposed into two terms;

$$a_F \sin(\omega t + \phi) = a_u \sin(\omega t) + a_{\dot{u}} \cos(\omega t) \quad (16)$$

one term following the structural motion u , and one term following its derivative \dot{u} . This decomposition was done in MATLAB by solving a set of coupled equations for different phase shifts on a generic sinusoidal force. Figure 7 shows how the amplitudes of the decomposition changes with the phase shift. On closer inspection we see that the amplitude of the u -term follows the relation $a_u = \cos(\phi)$, and the amplitude of the \dot{u} -term follows the relation $a_{\dot{u}} = \sin(\phi)$. For small values of ϕ , $\sin(\phi)$ is linear. This might explain why the damping is linearly increasing after lock-in, if the phase shift is also linearly increasing. This representation will not however, explain why the eigenfrequency increases, as figure 7a shows a strictly decreasing u -component of the force, going away from the lock-in region.

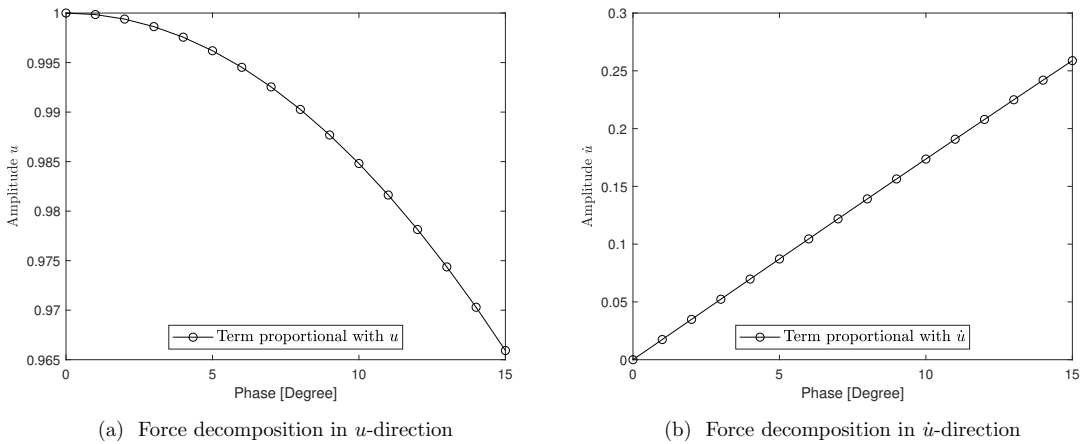


Figure 7: Force decomposition

In fact, if we insert the "damping" from figure 7b into the classical formula for damped eigenfrequency, $f_d = f_n \cdot \sqrt{1 - \xi^2}$ we get exactly figure 7a. Additional information is therefore needed to separate the eigenfrequency component of the force.

From classical vibration we have that the eigenfrequency can be defined as $\omega_n = \sqrt{k/m}$, proportional to the stiffness and inversely proportional to the mass. Note as well that the above decomposition of the force does not separate between the u and \dot{u} components, as the two are the negative of each other (180° phase). This means that the u -component above really contains information regarding both. Or in other words, even if the sum is reduced, the ratio $r = k/m$ may not do so. An increase in this ratio would in theory increase the eigenfrequency. The next section will try to split the u -component into an acceleration and stiffness component.

Here we will use the inherent advantage of the two-way approach, the possibility to track the different forcing terms. Let us again start with the second order equation for structural

oscillating motion, with damping set to zero. If one during the derivation of equation 10 keeps the different forcing terms separated, we get discretized terms representing the inertial, restoring and external forces:

$$\overbrace{2\left(\frac{v_{i,k+1} - v_{i,k}}{\Delta t}\right)}^{\text{inertial forces}} + \overbrace{\omega^2(q_{i,k+1} + q_{i,k})}^{\text{restoring forces}} = \overbrace{(f_{i,k+1} + f_{i,k})}^{\text{external forces}} \quad (17)$$

These terms, and their ratio can be tracked throughout the simulation as a way of quantifying the shift in eigenfrequency.

Figure 8a shows the approximate phase shift of the external forces with respect to the structural deformation. The phase shift is manually extracted from a time-series of the force and deflection, and will therefore be somewhat uncertain, however there seems to be an increasing trend across the lock-in region, although not as clear as in figure 6a.

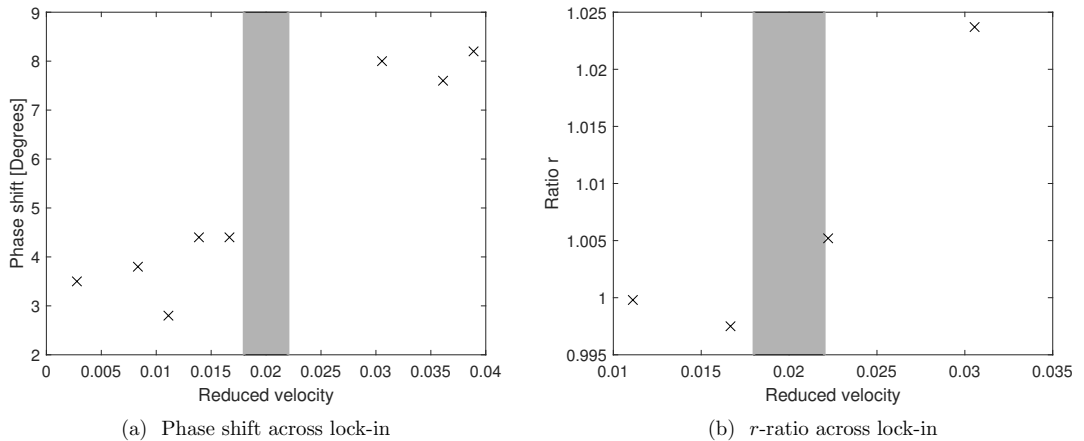


Figure 8: Analysis of phase shift between force and deflection (left), and ratio between restoring and inertial forces (right)

Figure 8b shows the approximate ratio between the restoring and inertial forces for the different flow velocities. Interestingly there is a change in this ratio across the lock-in region. It is dangerous to draw conclusions based on such a limited number of data points, however it seems like the r -ratio is about 1 before lock-in, but increases a couple of percent after. As discussed above, this change might be a reason for the added stiffness effect seen across the lock-in region.

4.4. Future work

In this paper, a modal decomposition-based model order reduction method was used. Some limitations apply, namely symmetric matrices such that a diagonal system can be created. This is then solvable inside CFX as simple expression evaluations. If a more sophisticated model order reduction technique was used, i.e. a Krylov based model, used on a similar geometry in [18], then this would allow for inclusion of phenomena such as gyroscopic effects, arbitrary damping and more. The simulation time would be the same, but as the reduced system is no longer simple evaluations, it would have to be solved by i.e. a Fortran script.

5. Conclusion

The hydrodynamic damping of a hydrofoil changes significantly across the lock-in region. The same is true for the eigenfrequency, there is actually a stiffening effect observed in experiments when the flow velocity is increased. Both effects are successfully simulated in this paper using a quasi-two-way FSI approach.

The hydrodynamic damping is approximately constant before the lock-in region and linearly increasing after, something shown numerically and experimentally earlier. This behaviour may be explained by the fact that the fluid load on the foil changes its phase relative to the foil, and thus dissipates more energy. The simulation of the added stiffness is new, and may be explained by tracking the inertial and restoring forces on the hydrofoil during the simulations. The ratio of the two is non-constant, and can be the reason for the changed behaviour.

Even though the test geometry in this case was fairly simple, the modal decomposition based two-way approach is shown to provide a great way of adding a layer of information to the simulations. Especially cases where there is a risk of significant fluid structure interaction could easily be investigated using this approach.

Acknowledgement

This work was done in the HiFrancis project, supported by the Norwegian Research Council and the Hydropower industry in Norway.

References

- [1] Francis-99 research project <https://www.ntnu.edu/nvks/francis-99> accessed: 2019-03-12
- [2] Bergan C W, Solemslie B W, Østby P and Dahlhaug O G 2018 *International Journal of Fluid Machinery and Systems* **11** 146–153
- [3] Dörfler P, Sick M and Coutu A 2012 *Flow-induced pulsation and vibration in hydroelectric machinery: engineers guidebook for planning, design and troubleshooting* (Springer Science & Business Media)
- [4] Bergan C W, Tengs E O, Solemslie B W and Dahlhaug O G 2019 *IOP Conference Series: Earth and Environmental Science* **240** 062008
- [5] Tengs E O, Bergan C W, Jakobsen K R and Storli P T 2019 *IOP Conference Series: Earth and Environmental Science* **240** 062002
- [6] Craig R R and Kurdila A J 2006 *Fundamentals of structural dynamics* (John Wiley & Sons)
- [7] Clough Ray W and Joseph P 1995 *Computers & Structures, Inc*
- [8] Zienkiewicz O C, Taylor R L and Zhu J Z 2005 *The finite element method: its basis and fundamentals* (Elsevier)
- [9] Ansys® mechanical apdl, release 19.3, command reference, exprofile, ansys, inc.
- [10] Ferziger J H and Peric M 2012 *Computational methods for fluid dynamics* (Springer Science & Business Media)
- [11] Bergan C W, Tengs E, Solemslie B W and Dahlhaug O G 2019 Damping measurements on a multi-blade cascade with multiple degrees of freedom *Journal of Physics: Conference Series* (Accepted for publication)
- [12] Kundu P K, Cohen I M and Dowling D 2008 *Fluid mechanics* 4th
- [13] Gabbai R and Benaroya H 2005 *Journal of Sound and Vibration* **282** 575–616
- [14] Bearman P W 1984 *Annual review of fluid mechanics* **16** 195–222
- [15] Brekke H 1994 A review on oscillatory problems in francis turbines and simulation of unsteady flow in conduit systems *Proceedings of the 17th IAHR Symposium, Beijing, China* pp 15–19
- [16] Sagmo K F, Tengs E O, Bergan C W and Storli P T 2019 *IOP Conference Series: Earth and Environmental Science* **240** 062006
- [17] Coutu A, Seeley C, Monette C, Nennemann B and Marmont H 2012 Damping measurements in flowing water *IOP Conference Series: Earth and Environmental Science* vol 15 (IOP Publishing) p 062060
- [18] Tengs E, Charrassier F, Holst M and Storli P T 2019 *International Journal of Applied Mechanics and Engineering* **24** 131–142

Part III

Additional Papers

Paper 6

Numerical Generation of Hill-Diagrams; Validation on the Francis99 Model Turbine

Tengs, E. , Storli, P. T. , Holst, M. A.

International Journal of Fluid Machinery and Systems, **11.3** (2018): 294-303.

Original Paper

Numerical Generation of Hill-Diagrams; Validation on the Francis99 Model Turbine

Erik Tengs^{1,2}, Pål-Tore Storli¹ and Martin Aasved Holst²

¹Department of Energy and Process Engineering, Norwegian University of Science and Technology
The Waterpower Laboratory, Alfred Getz veg 4, 7491 Trondheim, Norway

²EDR&Medeso Leif Tronstads Plass 4, 1337 Sandvika, Norway

Abstract

This article compares a numerically simulated, and an experimentally obtained Hill-Diagram. The Francis99 model turbine was used in the validation. By using steady-state simulations and passage modeling in ANSYS CFX, the simulation time is in the order of minutes for each operating point. Except for the smallest guide vane opening, the error in hydraulic efficiency is less than 2.5% for all flow configurations. The individual error in head and torque follow clear, almost identical trends. The error along a line of small incidence losses indicate less than 0.5% error in the efficiency in almost the complete simulated range. The results in this article may be used in future optimization design processes using Hill-Diagrams.

Keywords Hydro-power, Validation, CFD, Hill-Diagram, Optimization, Francis99

1. Introduction

The continuous development in the computational world enables simulations to be an integral part of the design of new products. Simulation Driven Product Development (SDPD) is the concept of introducing simulation tools early in the design process, rather than using it as a verification tool in the final stages of production [1]. If SDPD were fully utilized, it could be a significant speedup and cost-saving measure. However, for SDPD to be trusted and fully embraced by the industry, the methods have to be verified and validated with experimental results. This article will recreate an experimental Hill-Diagram by use of simulations. Moreover, the article aims to prove that the time used for the chart generation is low enough so that it can be used in an optimization design process.

The long-term goal for this work is to use an optimization routine in a turbine design phase. Optimization routines for turbines have been used earlier (see i.e. [2]–[4]), however this paper aims to prove the accuracy of a complete Hill-Diagram, rather than certain operating points [5]. This diagram is crucial if the goal is to design a variable speed turbine, as both the rotational speed of the runner and the flow rate can be varied. Variable speed operation is a technology that allow a turbine to operate at high efficiencies in a wider range of operating conditions, as well as avoiding dynamic phenomena and increasing the range of operation [6], [7]. The optimization characteristic of each turbine design will be taken from a Hill-Diagram, thus, a diagram has to be made for all turbine designs. Therefore, a validation of the accuracy of the numerically simulated Hill-Diagrams is needed.

The model turbine used in this article is the Francis99 turbine, a model turbine located at the Hydropower Laboratory at the Norwegian University of Science and Technology. The runner consists of 15 main blades, and 15 splitter blades. More information about the runner can be found in [8]. The model turbine has been the focus point of extensive research, among others, the research project Francis99 [8], which is focusing purely on numerically replicating detailed experimental results from the model, and the HiFrancis project [9]. The simulations presented in this article are in the extreme, short duration, end of the simulation spectra, where loss of accuracy is unavoidable. Quantifying this loss in accuracy is one of the main objectives of this article.

2. Theory and methods

2.1. The Hill diagram

The hydraulic efficiency in a hydro turbine is calculated as the power output divided by the available water power [10]:

$$\eta = \frac{T\omega}{\rho g H Q} \quad (1)$$

where T is torque, Q is the volume flow, ω is the angular velocity, g is the gravitational acceleration and ρ is the fluid density. H is referred to as the *head* and will be defined precisely later. It is a measure of the mechanical energy difference over the runner. The losses in the runner is to a large extent determined by how the water flow coincides with the runner geometry. Fig. 1 shows the velocity triangles on a generic blade, where u denotes the runner peripheral velocity, c the absolute water velocity, and w the relative water velocity. The guide vane angle is denoted as $\alpha_1 = \text{atan}(c_{m1}/c_{u1})$ (not explicitly shown in Fig. 1). If the combination of runner speed and guide vane angle is off-design, the angle of the relative velocity β_1 , will not coincide with the runner geometry, and losses occur.

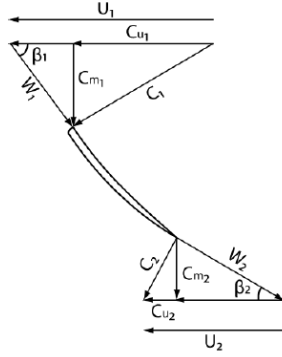


Fig. 1 Velocity components in a turbine

Several combinations of runner speed and guide vane opening can be tested, measuring the hydraulic efficiency for every flow configuration. The resulting surface will be a convex surface, or simply, a *Hill*. A Hill-Diagram is a two-dimensional visualization of this surface. Fig. 2 shows the general idea. The lines in the 2D plot are iso-lines of constant hydraulic efficiency.

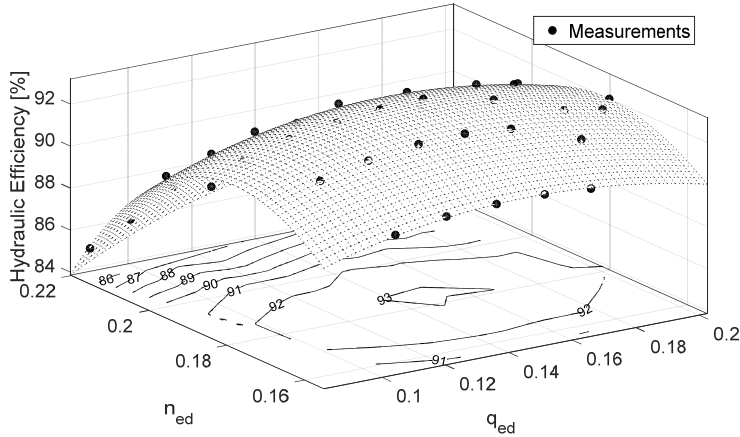


Fig. 2 Hill Diagram; a 2-dimensional projection of a 3-dimensional surface.

The axis may be defined in several ways, the most common is to use reduced quantities of flow and runner speed, q_{ed} and n_{ed} , respectively. This way, comparing different turbine runners is easier. The definitions are as follows [10];

$$q_{ed} = \frac{Q}{D_2^2 \sqrt{gH}} \quad (2)$$

$$n_{ed} = \frac{n D_2}{\sqrt{gH}} \quad (3)$$

where D_2 is the outlet diameter and n is the runner speed. H as above, is the head, defined by eq.(4) (see [11] for details), where ΔP is the pressure difference upstream and downstream the turbine, see probe $PT02$ and $PT03$ respectively, in Fig. 3.

$$H = \frac{\Delta P}{\rho g} + \frac{v_1^2 - v_2^2}{2g} + (z_1 - z_2) \quad (4)$$

Hydropower plants today are usually operated at a constant speed n , and for most cases (unless there is a large variation in head during operation) a 1 dimensional representation of the efficiency can be used. This 1-dimensional representation is the line of intersection between the 3D surface in Fig. 2 and a vertical plane at a constant speed at varying flow rate due to varying guide vane opening. This figure will typically have a parabolic shape indicating the efficiency at different flow rates. If new technologies like variable speed operation is developed, the 2-dimensional representation of a Hill Diagram will become very important. This is because both the guide vane opening (flow rate) *and* the runner speed is variable. Regarding efficiency, this could in theory allow for relative velocities that follow the geometry better in a wider range of operation, and in turn, creates smaller losses. This is the motivation for why a full Hill-Diagram can be used in an optimization process on variable speed turbines.

A note on the construction of Hill-Diagrams; The Hill Diagram is composed of lines of constant efficiency, the efficiency iso-lines. Depending on how many operating points that are tested/simulated, and what interpolation/extrapolation method is used, vastly different results can be obtained. A purely visual comparison of charts is therefore not recommended. If two Hill Diagrams are created using the same algorithm, then a visual comparison can be done with care. There is also the case of balancing overfitting and prediction. A low order surface fit will create more circular iso-lines, a method possibly suited for indicating trends in the diagram. Higher order fits, and extrapolation outside of the tested range may increase the accuracy, but also overfit the test data to the extent that the predictive quality of the chart decreases. These problems can be seen in the Hill-Diagram published in [12], where extrapolation outside the experimental range creates an unphysical result in some regions.

2.2. Experimental measurements

Experiments have been performed on the Francis99 model turbine at the Hydropower Laboratory at the Norwegian University of Science and Technology. The experimental procedure followed the guidelines set in IEC 60193 [11]. The experimental results have been used for validation of the numerical results in this article. More information about the experimental setup in the lab can be found in [12], [13], however the actual results used for validation comes from personal correspondence with the laboratory staff, and is not related to the mentioned references. The results used here was used as a reference for a model acceptance test of the runner being replaced at Tokke power plant.

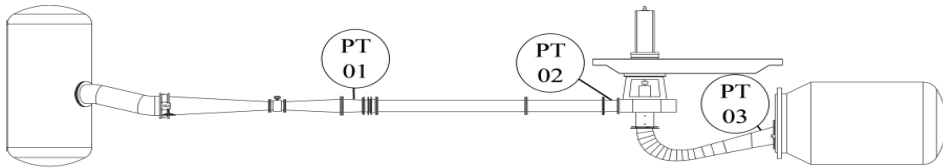


Fig. 3 Experimental Setup[5]

The laboratory consists of a closed loop and an open loop. Only the closed loop was used in the experiment, and is presented in Fig. 3. The loop consists of an upstream pressure tank, the turbine, draft tube, and a downstream pressurized tank. The pressure probes $PT02$ and $PT03$ define, as mentioned, the head over the turbine. One important thing to remember is that the efficiency calculated from the experimental results will be the efficiency of the entire length between these measurement sections, including not only the efficiency of the runner itself, but also the guide- and stay vanes, spiral casing and draft tube. As we shall see, much of this is not included in the numerical simulations.

The experimental data provided to the author consisted of almost 150 points, distributed evenly in the $n_{ed} - q_{ed}$ plane. The guide vane opening was operated on 10 levels in the range $\alpha \approx [-50\%, +40\%]$ of the assumed best efficiency point. The runner speed was operated on 15 levels in the range $n \approx \pm 20\%$. In the experiments, the head was kept approximately constant ($<0.5\%$ deviation).

2.3. Numerical simulations

A Hill-Diagram consists of many points, the simulation time have to be low for each point. One of the main goals of this article is to assess the loss of accuracy when simulation time is minimized. The excellent review paper by Trivedi et.al [14] lists, and reviews a spectra of simulation settings, and have been used as a recommended practice reference. A summary of simulation settings can be found in Table 1, a detailed explanation will follow.

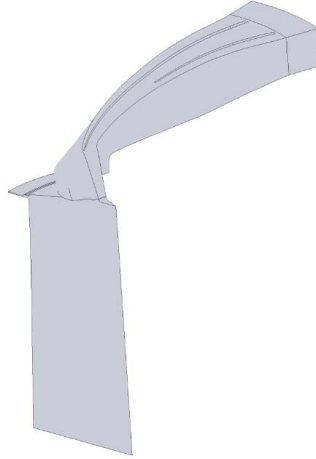
Table 1 Simulation settings

Parameters	Description
Software	ANSYS CFX
Analysis type	Steady State
Components	Inlet section, node matching to runner Runner: 1 main blade, 1 splitter blade Draft tube: Straight, shortened section, pitch ratio 1:1
Interfaces	Frozen Rotor (Inlet-Runner, Runner-Draft Tube)
Fluid properties	Incompressible water, constant properties
Boundary Conditions	Inlet: Mass flow Outlet: 0 Pa average static pressure (relative pressure) Periodic interfaces, node matching No-slip walls No leakage flow
Turbulence model	SST
Run type	Parallel MPI: 6 cores

The first, and possibly most important time-saving measure, have been to only perform steady-state simulations. Because only global parameters, Q, H, η, T is needed for creation of a Hill-Diagram, steady-state simulations have proven to be sufficient [15], [16]. This reduces the simulation time to a fraction of what could be required of transient simulations. It can however, introduce simulation inaccuracies, especially at off design operation, where transient effects are more prominent.

2.3.1. Geometry and Mesh

A second time-saving measure was to use passage modelling in all the simulations. This means that only one passage, i.e. one main and one splitter blade of the runner, was simulated. This simplification is possible due to the rotational symmetry of the runner geometry, and it is assumed that there are negligible changes in the main flow field in the different passages. This simplification is fairly standard in the industry, and have previously shown good results [17]. Additionally, as the simulations are steady state, no particular interface treatment (other than conventional periodicity) is needed at the rotationally symmetric interfaces. Fig. 4 shows the simulated geometry.

**Fig. 4:** Simulated Domain

No guide vanes were included in the simulations. The main reason for not including the guide vane domain is that the current setup only requires one mesh regardless of the operating point. The different guide vane angles will be accounted for by the boundary conditions, see next section for details. If the guide vane domain was included, different guide vanes angles would need different meshes, or mesh motion. Mesh motion could be possible if mesh quality was continuously monitored, however it does require a transient simulation. If optimization is the end goal, the setup presented here would be the easiest, and fastest, as there is no need for re-meshing of the guide vane domain.

A second argument is that the flow parameters, i.e. the pressure will, to a first approximation, assume the following form; $p = p_0 + A * \sin(k\omega t)$, where p_0 is the mean pressure, A is some amplitude of oscillation, and k indicates the number of guide vanes. If however, this is integrated over time as in a steady simulation, the sinusoid will disappear, and we are left with the mean parameter, p_0 . For global parameters like torque, efficiency and such, the approximation of using only the mean parameter can be used. If the goal of the simulations was pressure amplitudes, time-dependent fluctuations and such, the guide vane domain would have to be included (or at least be described as a sinusoidal function in time).

Using the setup presented, the same mesh could be used for all points in the Hill-Diagram. A small, stationary inlet domain is included in front of the runner to allow for development of the pressure and velocity field upstream of the blades. A cut-off draft tube cone with pitch (angular span) equal to the runner was included at the outlet. Leakage flow was not included. There exist several (usually Fourier based) methods for approximating the complete runner flow field, even if only passage modelling is used. These are all transient methods and cannot be used in the current case. However, as global parameters are integrated quantities over the whole domain, and if the assumption of negligible changes between the channels are correct, then the global quantities should not change much even if only one passage is simulated.

The runner mesh was created using ANSYS Turbogrid. The mesh is one 15th of the full runner, rotationally symmetric with node-matching periodic interfaces. The draft tube mesh was created separately using ANSYS Meshing to improve the mesh quality close to the draft tube centre. The number of elements is 636000 and 303000 in the runner and draft tube respectively. With the inlet section, the total number of elements was 1M. The Grid Convergence Index (GCI) [18] was used to verify the quality of the mesh. The GCI is an industry-recognized method for assessing mesh quality, a step-by-step explanation can be found in [19], but will not be repeated here. Table 2 list the GCI for head and torque, and indicates that the spatial discretization error on the selected mesh is small. Please note that the values used for the GCI analysis is taken from simulations with the full spiral casing, full runner (15 mode matching passages) and complete draft tube [15]. This should reduce the modelling error, and isolate the discretization error better. The mesh used in this article is one passage of the converged mesh in the reference. A stepwise refinement was performed in the near-wall region, leading to an average y^+ of 2.8 in the runner.

Table 2 Grid convergence index

Parameter	GCI
Head	0.22%
Torque	0.04%

2.3.2. Boundary Conditions

From the experimental results, all parameters were given. This includes pressure at inlet and outlet, head, mass flow and rotational speed. This allowed for a range of possible boundary condition configurations. The mass-inlet, pressure-outlet configuration is widely used, and regarded in the industry as the most stable [14]. In the laboratory however, this is not how it is done. In the laboratory, the head is fixed to a near constant value. The mass flow is developing freely, it is not controlled by the experimentalist. This configuration is harder to achieve in the simulations, as the total pressure cannot be specified at both inlet and outlet. The mass-inlet, pressure-outlet configuration was therefore used, with the experimental mass flow at the inlet, and zero relative pressure at the outlet. The head was defined as the difference in the total pressure from inlet to outlet, with an additional hydrostatic term accounting for the different pressure probe locations in the experiments and the simulations (compare Fig. 3 and Fig. 4). The torque is a built-in parameter in CFX, defined as $\int \vec{r} \times \vec{F} dA$.

Almost tangential velocity components were imposed on the inlet domain in order to replicate the effect of the guide vanes. The flow was otherwise uniform. Numerical error is more likely to occur if there is tangential flow on a domain, the default minimum allowed angle in CFX is $\alpha = 10^\circ$ [20]. An expert parameter was therefore included such that simulations could be performed down to $\alpha \approx 6^\circ$. This guide vane opening is outside of normal operating range, and the tested range covers most practical cases. Even lower angles were deemed too uncertain, and disregarded. In the results section, this assumption will be assessed. The angle imposed on the inlet domain was the same as the guide vane outlet angle. The assumption comes from $\alpha = \text{atan}(c_m/c_u)$, where $c_m \propto 1/r$ by continuity and $c_u \propto 1/r$ by free vortex theory [21]. Thus, $\alpha = \text{constant}$ in the inlet section, see Fig. 5 with $\alpha_1 = \alpha_2$. This assumption is normal practice in vaneless spaces in turbine design.

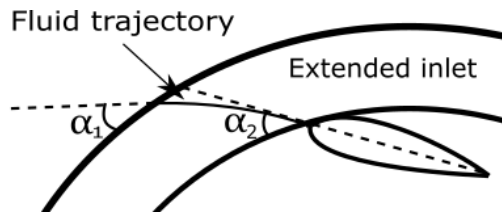


Fig. 5 Velocity components in extended inlet section

The 150 experimental points given to the author was excessive for validation of this method, every third point was therefore chosen. Additionally, no simulations were performed on the smallest guide vane openings, $\alpha \approx 5^\circ$, such that the total simulated points ended up being about 40. All simulations were initialized from a simulation at design point, making the Hill-Diagram highly parallelizable. In this article, the points were simulated sequentially on a workstation with 6 cores.

3. Results

The following section will list the results of the numerical simulations. First the Hill-Diagram will be presented in both 3-dimensional and 2-dimensional form. This first section is mostly a visual comparison, rather than detailed analysis. Then the error in the quantities head, torque and hydraulic efficiency will be regarded separately. This is to avoid that errors in head and torque

cancels, as per eq.(1). This is a common mistake, and could potentially lead to perfect results in hydraulic efficiency, even though both head and torque have errors. Each of the ≈ 40 simulated points took about 15 minutes each on 6 cores.

Fig. 6 shows the 3D (a) and 2D (b) Hill-Diagram from the experiments and the simulations. Reduced quantities n_{ed}, q_{ed} make up the axis of the charts. In the 3D comparison, we observe a good fit in almost the complete simulated space. Interestingly, the simulations underestimate the efficiency slightly ($\approx 0.5\%$) around the best efficiency point. In such a visual comparison, the trends are more interesting than the details, and a complete third order fit was deemed sufficient.

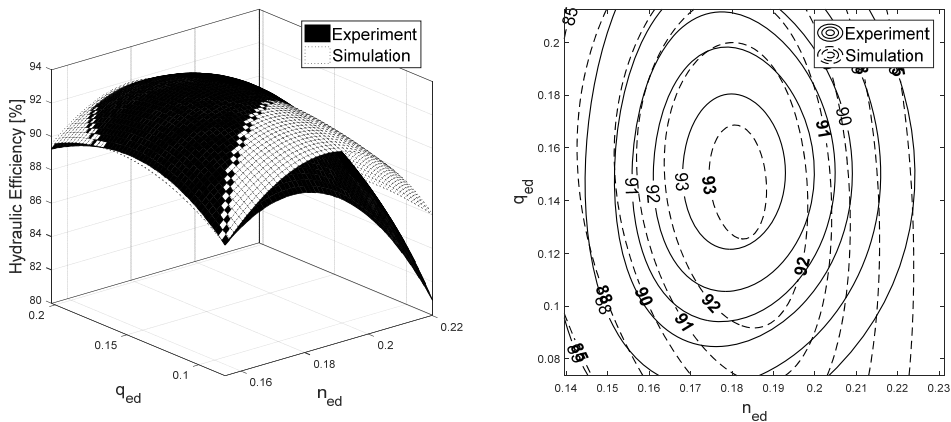


Fig. 6 Comparison of Hill-Diagrams, 3D(left), 2D(right).
In the 2D figure, bold font and dashed lines mark the simulations

In 2-dimensional Hill-Diagrams, the measured points are usually included. This is purposely left out of Fig. 6 to improve readability, as the points do not perfectly overlap. The lines marking constant guide vane opening is also omitted. The reason is that it would be two set of lines indicating the guide vane opening (because n_{ed}, q_{ed} is dependent on the simulated head), and this would be a disturbing element in the chart. Even though a 2-dimensional comparison is not visually ideal, we see a good agreement between the experiment and the simulation.

3.1. Head

In the following sections the individual quantities will be presented in more detail. Fig. 7 shows the error, in percent, in the simulated head versus the experimental head. The error is defined as $e = (simulation - experiment)/experiment$, in other words, a negative error indicates an underprediction. The axis in this, and the following plots, are not reduced values, but actual runner speed and flow. This is because the reduced values both are dependent on the simulated head, and this could introduce errors in the axis points.

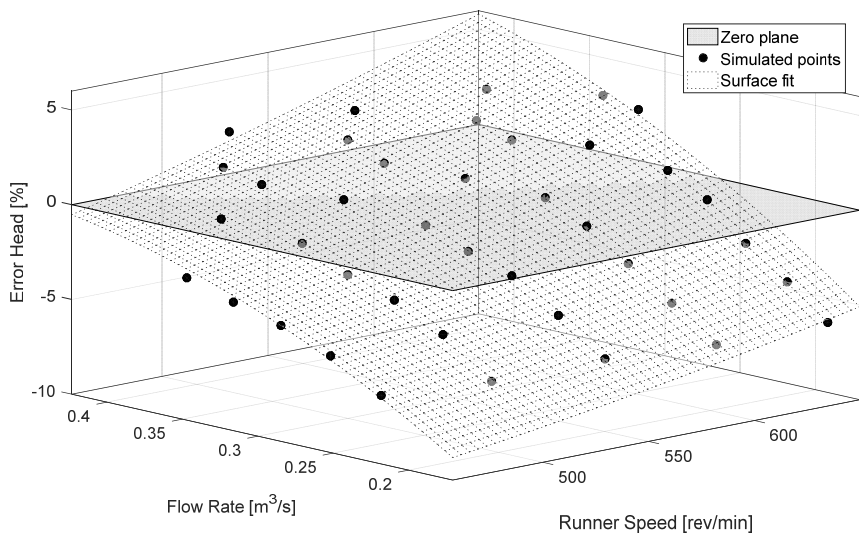


Fig. 7 Error in Head

The surface fit in the figure is a complete second order polynomial, ($z = a_0 + a_1x + a_2y + a_3xy + a_4x^2 + a_5y^2$), but a distinct planar trend is observed. The error is clearly not normally distributed about the zero plane, but rather about a defined, tilted plane. If the flow and runner speed is normalized to be in the range [0,1], and a plane fit is performed on the error, the following relation is obtained.

$$Error_{head}[\%] = -8.7 + 4.8 * RPM + 9.7 * Flow, \quad RPM, Flow \in [0,1] \quad (5)$$

If the simulation perfectly matched the experiments, all the coefficients in eq.(5) would be zero. In this case we see that the error is close to twice as sensitive to changes in flowrate as changes in rotational speed. Please note that this is within the simulation ranges explored in this article. From section 2.2 we remember that the guide vane angle was tested in a wider percentage range than the runner speed, and larger error may therefore be expected.

3.2. Torque

Fig. 8 shows the error, in percent, in the simulated torque versus the experimental torque. We see almost the same conceptual behavior as for the head in Fig. 7, where higher values of runner speed and flow rate tends to overestimate the torque. The opposite is true for lower values.

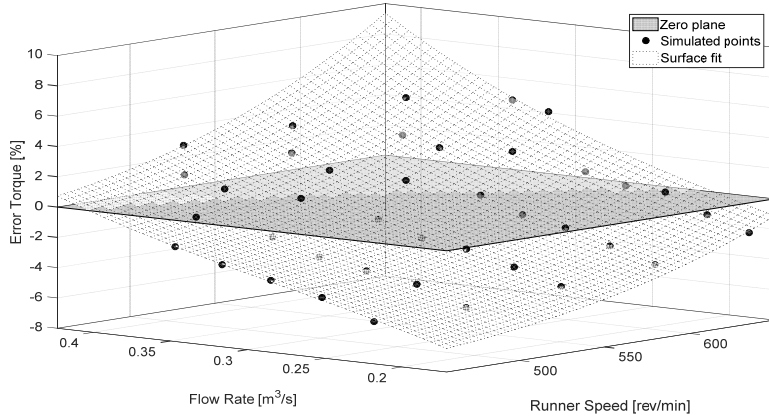


Fig. 8 Error in torque

As above, the polynomial fit is second order, and as above, a distinct planar trend is observed. The same normalization exercise was performed on the torque, which resulted in the following plane fit:

$$Error_{torque}[\%] = -7.5 + 5.9 * RPM + 7.9 * Flow, \quad RPM, Flow \in [0,1] \quad (6)$$

The error is still more sensitive to changes in flow rate than changes in rotational speed, however not as much as for the head (eq.(5)).

3.3. Hydraulic Efficiency

The hydraulic efficiency is calculated as per eq. (1). Fig. 9 shows the error, in percent, in the simulated efficiency versus the experimental hydraulic efficiency.

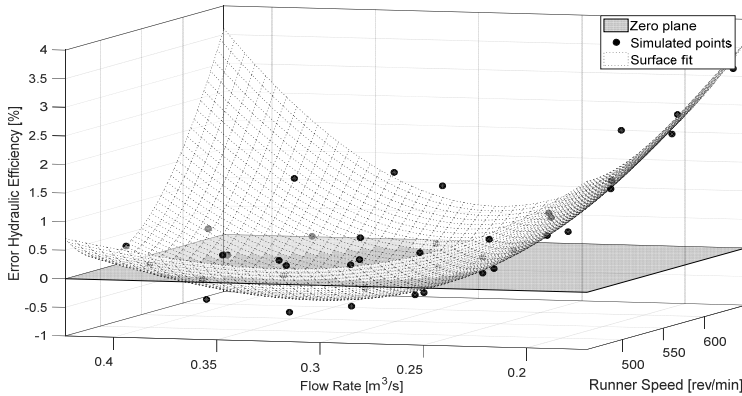


Fig. 9 Error in Hydraulic efficiency

As the individual error in torque and head is similar, the error in efficiency is expected to be lower than both. This is observed here. In fact, the error is within $[-0.5\%, 2.5\%]$ in almost the complete simulated range. Observe also the “tails” of the error, the efficiency is overestimated at off-design operation. Furthermore, the error is by far largest in the region with low flow rate, i.e. small guide vane angle and small tangential velocity angles. This validates the assumption made in section 2.3 regarding minimal tangential vector, and at the same time sets a limit for what is possible using this setup.

4. Discussion

In Fig. 6 it is shown that the efficiency is underestimated slightly around the best efficiency point. This is somewhat counter-intuitive, and contrary to what is seen in many other studies [14]. Consider the location of PT02 and PT03 in Fig. 3, compared with the size of the domain in Fig. 4. The simulated geometry does not extend to where the pressure measurements are taken in the experimental domain, and thus, larger frictional losses should be expected in the experiments. The absence of leakage flow and corresponding viscous losses should also indicate a larger efficiency in the simulations. One way of explaining this is to look into the components of the efficiency, the torque and the head, $\eta \propto T/H$. In this case, at BEP, both quantities are slightly underestimated, $\approx -1\%$, however torque is obviously underpredicted most as the efficiency is underpredicted. Because of the small errors however, small variations will heavily affect their ratio, i.e. the efficiency. A small change (a tenth of a percent) in the torque would actually cause an overestimation of the efficiency. This may explain why the efficiency is underpredicted, as it is a ratio of two simulated components. It should also be noted that the uncertainty in the experimental results are approximated to be $\approx 0.2\%$.

The way the different variables are extracted in the laboratory and in the simulation, may also be a source of error. In the lab, the torque is calculated using a load cell and a lever arm on the generator casing in accordance with IEC60193. The exact definition, $T = \int \vec{r} \times \vec{F} dA$, is used in CFX. This definition is sensitive to the mesh resolution. A second possible way of calculating the torque would be from the Euler equations, where it can be showed that $T \approx \Delta(u c_u)$ [22]. This is not done in the current study, but the two methods have been shown to converge to the same solution for satisfactory mesh resolution [15]. As for the uncertainties in the simulated head; the locations where the pressure difference is defined, is different in the simulations and experiments. This is unavoidable as the geometrical domain in the simulation is restricted to save computational cost, but accounted for manually.

The simulated head, torque and efficiency was all well within an acceptable error range, especially considering the short simulation time. This could open for new possibilities within SDPD and optimization. Interestingly, the error seems to be clearly defined. Both the error in head and torque is distributed in virtually the same way, not randomly. This could potentially help in the understanding of simulation of hydro turbines, or at least be used as a possible post-processing tool. However, one should be careful in deriving any universal rules based on a sample of one.

5. Further work

The present work will be used as the foundation for future optimization routines involving a Hill-Diagram as key characteristic. The goal is to use a Francis-runner design tool, create Hill-Diagrams at different designs, analyze the Hill-Diagrams, and couple it all together in an optimization loop. The basic idea is presented in Fig. 10.

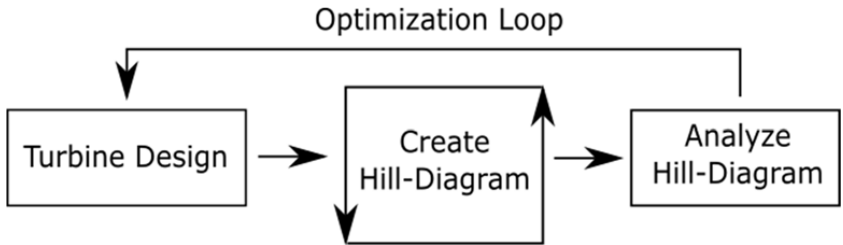


Fig. 10 Optimization loop based on Hill-Diagrams

Standard response surface algorithms require in the order of $n = 2^k$ runs, where k is the number of optimization parameters. Therefore, keeping the simulation time per Hill-Diagram low is of absolute necessity, if this is to be used in an optimization procedure. The simulations in this article were performed on a workstation using 6 cores in parallel. Each simulated point took approximately 15 minutes, 40 points are thus simulated in 10 hours. This is by no means powerful hardware, and most companies have access to parallel computing frameworks orders of magnitudes as fast. This means that a Hill Diagram could be created in the order of an hour or less. Parallelization is also very easy using the setup presented, and will reduce the simulation time drastically.

Another way of speeding up the process is the following. From Fig. 1 we get the angle of the relative velocity entering the runner, $\beta_1 = \text{atan}(c_{m1}/(u_1 - c_{u1}))$. At the best efficiency point (BEP), the incidence losses should be small. All the variables in β_1 are inputs (at least implicitly) to a simulation, and the condition $\beta_1 = \beta_{BEP}$ is fulfilled several places in the $n_{ed} - q_{ed}$ plane. This concept is shown in Fig. 11. Moving along such a line may be a direction of interest when designing turbines for variable speed. Also shown in Fig. 11 is the 10 simulated points closest to $\beta_1 = \beta_{BEP}$. Fig. 12 shows the efficiency at these points in order of increasing flow rate.

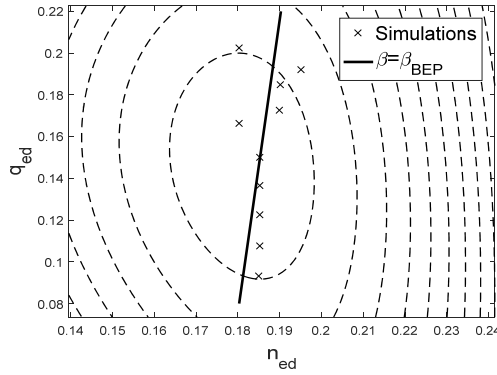


Fig. 11 Possible line where $\beta = \beta_{BEP}$

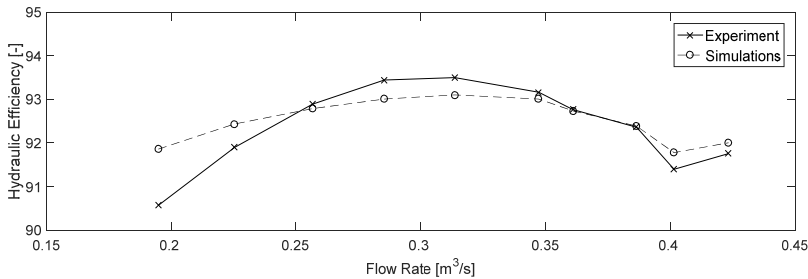


Fig. 12 Hydraulic efficiency in points close to $\beta = \beta_{BEP}$

The error is smaller than 0.55% for all points except the first, where the guide vane opening is 6° . If a variable speed runner is to be designed using an optimization scheme and Hill-Diagrams as characteristic, points along such a line may be sufficient, and will reduce the number of simulations needed drastically.

6. Conclusions

As this article shows, it is possible to create a Hill-Diagram with good accuracy, fast enough that it may be used in a design process. This allows for new possibilities within simulation driven product development, where an optimization algorithm can search for the best possible turbine design. Moreover, it is shown that the simulation error follows distinct trends, which can be used to post-process simulation results.

The biggest sources of error are thought to be steady state simulation, and passage modeling with no Fourier methods. The errors are primarily at off-design conditions, where there are transient flow phenomena not captured by the steady simulations. If simulations are performed without a guide vane domain, and tangential velocity components are imposed on an inlet domain, care should be taken when simulating angles below $\alpha \approx 6^\circ$. It is shown that simulations at part-load gives larger errors than full load. For flow configurations where the incidence losses are small, $\beta_1 \approx \beta_{BEP}$, the error is 0.55% or less. This may be used in further work using optimization routines.

Acknowledgments

This research was carried out as a part of a High Head Francis research program sponsored by the Norwegian Research Council, The Norwegian Hydropower industry, and the Norwegian Center for Hydropower. This support made this experiment possible.

Nomenclature

BEP	Best Efficiency Point	T	Torque [Nm]
c	Absolute water velocity [m/s]	u	Runner peripheral velocity [m/s]
D_2	Outlet diameter [m]	w	Relative water velocity [m/s]
H	Head [m]	α	Guide vane angle [$^\circ$]
n	Runner speed [rev/min]	β	Angle of relative velocity [$^\circ$]
n_{ed}	Reduced runner speed [-]	η	Hydraulic efficiency [%]
Q	Flow rate [m³/s]	ρ	Water density [kg/m³]
q_{ed}	Reduced flow rate [-]	ω	Angular velocity [rad/s]
$SDPD$	Simulation Driven Product Development		

References

- [1] U. Sellgren, "Simulation-driven design: motives, means, and opportunities," PhD Thesis, KTH, 1999.
- [2] J.-H. Kim and K.-Y. Kim, "Optimization of vane diffuser in a mixed-flow pump for high efficiency design," *International Journal of Fluid Machinery and Systems*, vol. 4, no. 1, pp. 172–178, 2011.
- [3] A. E. Lyutov, D. V. Chirkov, V. A. Skorospelov, P. A. Turuk, and S. G. Cherny, "Coupled multipoint shape optimization of runner and draft tube of hydraulic turbines," *Journal of Fluids Engineering*, vol. 137, no. 11, p. 111302, 2015.
- [4] K. Nakamura and S. Kurosawa, "Design optimization of a high specific speed Francis turbine using multi-objective genetic algorithm," *International Journal of Fluid Machinery and Systems*, vol. 2, no. 2, pp. 102–109, 2009.
- [5] T. Vu, M. Koller, M. Gauthier, and C. Deschênes, "Flow simulation and efficiency hill chart prediction for a Propeller turbine," *International Journal of Fluid Machinery and Systems*, vol. 4, no. 2, pp. 243–254, 2011.
- [6] J. Fraile-Ardanuy, J. R. Wilhelmi, J. J. Fraile-Mora, and J. I. Pérez, "Variable-speed hydro generation: operational aspects and control," *IEEE Transactions on energy conversion*, vol. 21, no. 2, pp. 569–574, 2006.
- [7] K. Krüger and J. Koutnik, "Dynamic Simulation of Pump-Storage Power Plants with different variable speed configurations using the Simsen Tool," *International Journal of Fluid Machinery and Systems*, vol. 2, no. 4, pp. 334–345, 2009.
- [8] "The Francis-99 Research Project." [Online]. Available: <https://www.ntnu.edu/nvks/francis-99>. [Accessed: 23-Dec-2016].
- [9] "The HiFrancis Research Project." [Online]. Available: <https://www.ntnu.edu/nvks/hifrancis>. [Accessed: 22-Dec-2016].
- [10] P. Dörfler, M. Sick, and A. Coutu, *Flow-Induced Pulsation and Vibration in Hydroelectric Machinery: Engineer's Guidebook for Planning, Design and Troubleshooting*. Springer Science & Business Media, 2012.
- [11] International Electrotechnical Commission, "IEC 60193: 1999, Hydraulic turbines, storage pumps and pump-turbines - Model acceptance tests," Geneva, Switzerland, 1999.
- [12] C. Trivedi, M. J. Cervantes, B. K. Gandhi, and O. G. Dahlhaug, "Experimental and Numerical Studies for a High Head Francis Turbine at Several Operating Points," *J. Fluids Eng*, vol. 135, no. 11, pp. 111102–111102, Aug. 2013.
- [13] K. Kloster, "Trykkpulsasjoner inne i et Francis løpehjul," Master Thesis, NTNU, 2016.
- [14] C. Trivedi, M. J. Cervantes, and O. Gunnar Dahlhaug, "Numerical Techniques Applied to Hydraulic Turbines: A Perspective Review," *Appl. Mech. Rev*, vol. 68, no. 1, pp. 010802–010802, Feb. 2016.
- [15] K.-R. G. Jakobsen and M. A. Holst, "CFD simulations of transient load change on a high head Francis turbine," in *Journal of Physics: Conference Series*, 2017, vol. 782, p. 012002.
- [16] L. Stoessel and H. akan Nilsson, "Steady and unsteady numerical simulations of the flow in the Tokke Francis turbine model, at three operating conditions," in *Journal of Physics: Conference Series*, 2015, vol. 579, p. 012011.
- [17] R. Gong, C. Trivedi, O. G. Dahlhaug, and T. K. Nielsen, "Blade passage modeling strategy for hydraulic turbine," *International Journal of Fluid Machinery and Systems*, vol. 10, no. 4, pp. 345–354, 2017.
- [18] P. J. Roache, "Perspective: a method for uniform reporting of grid refinement studies," *Journal of Fluids Engineering*, vol. 116, no. 3, pp. 405–413, 1994.
- [19] I. Celik, "Procedure for Estimation and Reporting of Uncertainty Due to Discretization in CFD Applications," *J. Fluids Eng*, vol. 130, no. 7, pp. 078001–078001–4, Jul. 2008.
- [20] C. F. X. Ansys, *ANSYS CFX-Solver Modeling Guide*. Release, 2013.
- [21] P. K. Kundu and L. M. Cohen, "Fluid mechanics, 638 pp," Academic, Calif, 1990.
- [22] K. Subramanya, *Hydraulic Machines*. Tata McGraw-Hill Education, 2013.

Paper 7

Optimization procedure for variable speed turbine design

Tengs, E., Storli, P. T. , Holst, M. A.

Engineering Applications of Computational Fluid Mechanics, **12.1** (2018): 652-661

Optimization procedure for variable speed turbine design

Erik Tengs ^{a,b}, Pål-Tore Storli^a and Martin Holst^b

^aDepartment of Energy and Process Engineering, Norwegian University of Science and Technology, Trondheim, Norway; ^bEDR&Medeso AS, Sandvika, Norway

ABSTRACT

This article outlines a design procedure for variable speed Francis turbines using optimization software. A fully parameterized turbine design procedure is implemented in MATLAB[®]. ANSYS[®] CFX[®] is used to create hill diagrams for each turbine design. An operation mode of no incidence losses is chosen, and the mean efficiency in the range $\pm 20\%$ of the best efficiency point is used as optimization criterion. This characteristic is extracted for each design, and optiSLang[®] is used for system coupling and optimization. In the global optimization loop, the downhill simplex method is used to maximize the turbine performance. For this article, the bounding geometry of the runner is kept as in the original configuration. This way, the performance of the different variable speed turbines can be compared directly. Two optimization parameters describing the blade leading-edge geometry have been used in the optimization procedure. The resulting design was an almost circular leading edge, and shows an increase in mean efficiency of 0.25% compared to the reference case. There was a significant change in the turbine performance, with close to no change at the best efficiency point, and an increase in efficiency of almost 1% at low rotational speed. The outlined procedure is parallelizable and can be performed within an industrial timeframe.

ARTICLE HISTORY

Received 2 May 2018
Accepted 30 July 2018

KEYWORDS

Numerical simulations;
optimization; hydraulic
turbines; design; CFD

1. Introduction

Modern computational resources allow Computational Fluid Dynamics (CFD) to be an integral part of turbine design. A vast amount of research has been done on numerical simulation of hydraulic turbines. A state-of-the-art review can be found in Trivedi, Cervantes, and Gunnar Dahlhaug (2016). The main take-away is that the different flow phenomena require very different modeling strategies; tip vortices require more advanced turbulence models than other phenomena, pressure pulsations need transient simulations, but simulation time can be drastically reduced by Fourier-series-based passage modeling, and importantly, global parameters can easily be obtained with steady simulations due to the periodic-in-time nature of the flow field. Within numerical simulations on hydropower, the most advanced numerical simulations include all components, use hundreds of millions of mesh elements, model water as a compressible fluid, and use sophisticated turbulence models like large eddy simulations. The accuracy of the simulations has reached excellent levels, shown e.g. by the research project Francis99 (Norwegian Hydropower Centre, 2018). Research also shows that, for global parameters such as hydraulic efficiency and head, simpler

modeling assumptions give good results (Tengs, Storli, & Holst, 2018). When simulations are trusted, the natural extension of traditional design involves optimization techniques.

Optimization of hydraulic turbines is not new. Several examples of Francis turbine runner optimization exist (Enomoto, Kurosawa, & Kawajiri, 2012; Nakamura & Kurosawa, 2009; Pilev et al., 2012), some even optimizing the runner and draft tube simultaneously (Lyutov, Chirkov, Skorospelov, Turuk, & Cherny, 2015). Most of these attempts deal with medium-to-high specific speed Francis turbines, but other turbine types have also been optimized using similar techniques (Ezhilsabareesh, Rhee, & Samad, 2018; Semenova et al., 2014). The peak efficiency of hydro turbines has not increased much in the last decades, as noted in Electric Power Research Institute (1999) and Lyutov et al. (2015). Instead, optimization attempts usually aim to increase the efficiency away from the best operating point. Typically, one point at part load and one point at high load are chosen.

Recent changes in the international power market and the introduction of intermittent power sources have led to increased demand from hydro turbines. The operation of turbines has changed to more off-design operation,

CONTACT Erik Tengs  erik.tengs@edrmeso.com

This article has been republished with minor changes. These changes do not impact the academic content of the article.

© 2018 The Author(s). Published by Informa UK Limited, trading as Taylor & Francis Group.
This is an Open Access article distributed under the terms of the Creative Commons Attribution License (<http://creativecommons.org/licenses/by/4.0/>), which permits unrestricted use, distribution, and reproduction in any medium, provided the original work is properly cited.

which results in lower efficiencies and higher wear. One solution to this problem is to make variable speed turbines, a technology that allows a turbine to operate in a larger operating range without increased fatigue wear. The idea of using variable speed is not new. Back in 1987, several turbine types were tested to investigate if variable speed could increase performance (Farell & Gulliver, 1987). More recent investigations into variable speed utilize computational tools and show the possibility of increasing the efficiency at off-design conditions (Abubakirov et al., 2013). Power plants with large variations in head will also gain from variable speed operation, as seen in Pérez, Wilhelmi, and Maroto (2008). Today, most variable speed units are reversible pump–turbines (Energy Storage Association, 2018). This article introduces a simulation and optimization framework for the design of variable speed turbines. The optimization procedure is based on the two-dimensional hill diagram of a variable speed Francis turbine. The optimization objective is taken from a number of operating points along a line in the operating space with small incidence losses. Structural performance, draft tube phenomena, etc. will not be covered in this article.

2. Theory and methods

2.1. Conventional and variable speed operation of Francis turbines

An hydraulic turbine converts the available static pressure energy in a water body into torque and rotational energy in the runner. The static pressure in pascals is given by

$$p_{\text{stat}} = \rho g H, \quad (1)$$

where $\rho \text{ kg/m}^3$ is the water density and H metres is the height of the water column above the turbine. The potential power, P watts, in the water body can then be expressed as $P = Q \cdot p_{\text{stat}}$, where $Q \text{ m}^3/\text{s}$ is the volume flow. The rotational output power in the runner can be expressed as the torque, T newton-metres, multiplied by the rotational speed, ω hertz, and as it is impossible to extract all the potential energy from the water, an hydraulic efficiency can be defined as follows:

$$\eta = \frac{T\omega}{\rho g H Q}. \quad (2)$$

The hydraulic efficiency of a modern Francis turbine can exceed 96% at the best operating point (Andritz Hydro, 2018). At off-design conditions, however, the efficiency will be lower due to incidence losses at the inlet, spin losses at the outlet, etc. The hill diagram is used as a visual representation of how the efficiency changes. Assuming a test plant where both the flow rate and the

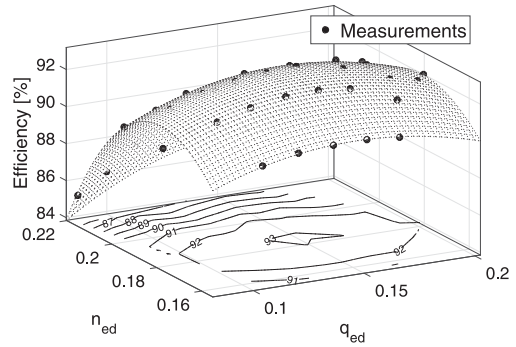


Figure 1. Example hill diagram: a 2D projection of a 3D surface.

runner speed are adjustable, if the hydraulic efficiency is measured at various points in the operational space and plotted, the resulting surface will form a convex hill, with the best operation point (ideally) at the top. A hill diagram is a two-dimensional projection of such a surface. The general idea is presented in Figure 1. The axes are normalized versions of the flow rate, Q , and rotational speed, n , see Equations (3) and (4), where D meters is the runner diameter (Dörfler et al., 2012). This formulation allows for easier comparison between different turbines.

$$n_{\text{ed}} = \frac{nD}{\sqrt{gH}} \quad (3)$$

$$q_{\text{ed}} = \frac{Q}{D^2 \sqrt{gH}}. \quad (4)$$

Conventional hydro turbines operate at a fixed speed controlled by the frequency of the power grid. The guide vanes allow for adjustment of the mass flow through the runner, and the hydraulic efficiency can be displayed as a function of the flow rate or guide vane opening only. In a variable speed turbine, however, both the runner speed and the flow rate are adjustable. This allows the turbine operator to match the runner speed and guide vane opening such that the water entering the runner perfectly coincides with the runner geometry. This could reduce the aforementioned incidence losses at off-design operation. In terms of bounding geometry, there is no difference between a runner installed in a variable speed turbine and one installed in a conventional hydro turbine. However, from an optimization point of view, it is obvious that the desired characteristics from a hill diagram are different. In a conventional runner, the efficiency need only be optimized in one dimension (the flow rate), whereas a two-dimensional representation is required for a variable speed turbine.

2.2. The optimization procedure

The idea is to design turbines using a Francis-runner design tool, create hill diagrams for the different designs, analyse the hill diagrams, and couple them all together in an optimization loop. The goal is to end up with a variable speed turbine design. The optimization procedure is presented in Figure 2. The procedure is similar to that presented in Ezhilsabareesh et al. (2018) and Jiang et al. (2018), although applied on a different turbine type. The following sections will describe the different blocks presented in Figure 2 in some detail, and how they interact.

2.2.1. Block A – turbine design

Traditional turbine design is a combination of using the Euler turbine equations and empirical knowledge. The procedure outlined here is adapted from the works of Brekke (2003). In order to describe the design steps of a Francis turbine, we need to define some nomenclature. The rated water head, H , and flow rate, Q , are known in advance. The velocity components entering and exiting a typical blade are shown in Figure 3. The letter \mathbf{u} (m/s) denotes the runner velocity, \mathbf{c} (m/s) denotes the

water absolute velocity, and \mathbf{w} (m/s) denotes the water velocity relative to the runner. The guide vane angle, α° , is controlling the angle of the water entering the runner, and thus implicitly also β° , the angle of the water in the rotating frame of reference. The subscripts \mathbf{u} and \mathbf{m} denote the tangential and meridional directions, respectively, and the subscripts 1, 2 denote the inlet and outlet. The meridional velocity component is the component in the flow direction, i.e. $Q = c_m A$.

Before defining the main dimensions of the turbine, we use the Euler turbine equation (Subramanya, 2013) to derive an important relation:

$$\eta = (u_1 c_{u1} - u_2 c_{u2}) / gH. \quad (5)$$

The second term in Equation (5) will contribute purely negatively to the efficiency, therefore this term is set to zero at optimum design. As u_2 is the runner velocity, and strictly non-zero, this equates to setting

$$c_{u2} = 0. \quad (6)$$

Physically, this condition means is that there should be no spin in the water body at the outlet. The turbine should transfer all the rotational energy in the water over to the runner. This condition will be used throughout the following derivation. It is customary to start designing a turbine from the outlet. Two parameters are chosen in advance, β_2 and u_2 . Based on empirical knowledge, these parameters are taken from the following range (Gogstad, 2012):

$$15^\circ \leq \beta_2 \leq 22^\circ \quad (7)$$

$$35 \text{ m/s} \leq u_2 \leq 42 \text{ m/s}, \quad (8)$$

with higher values corresponding to higher head. Once the above parameters are chosen, the meridional outlet velocity can be calculated (keeping in mind Equation 6):

$$c_{m2} = \tan(\beta_2) \cdot u_2. \quad (9)$$

The outlet radius is then easily derived:

$$r_2 = \sqrt{\frac{A_2}{\pi}} = \sqrt{\frac{Q}{\pi c_{m2}}}, \quad (10)$$

where $A_2 \text{ m}^2$ is the outlet area. Once the outlet dimension is set, the rotational speed of the turbine is calculated as follows:

$$\omega = \frac{u_2}{r_2}, \quad n = \frac{30\omega}{\pi}, \quad (11)$$

where ω and n is the rotational speed in hertz and r.p.m. In general, n will not be the synchronous speed, which is a requirement in conventional turbines. To change this,

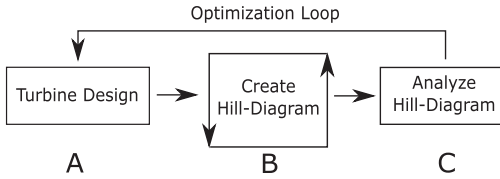


Figure 2. Optimization loop based on hill diagrams.

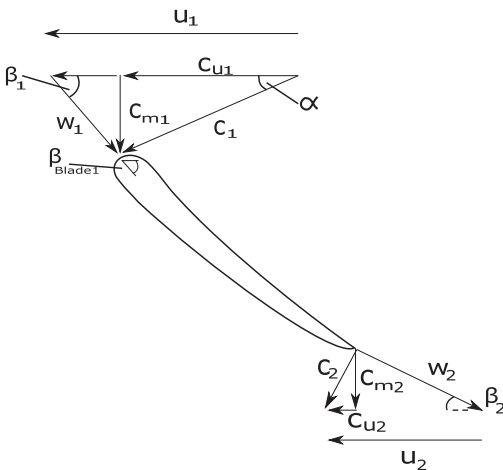


Figure 3. Velocity components on runner blade.

the closest synchronous speed is chosen, and the design process of Equations (9)–(11) is repeated in reverse order. This is strictly not necessary for variable speed turbines. Once the outlet dimensions are set, the inlet is designed. As for the outlet, an empirical range is used, this time for the runner inlet velocity:

$$0.7 \leq \bar{u}_1 \leq 0.75, \quad (12)$$

where the overbar notation denotes a reduced parameter:

$$\bar{x} = \frac{x}{\sqrt{2gH}}. \quad (13)$$

The inlet radius is now given directly by the runner speed, and the inlet runner velocity:

$$r_1 = \frac{u_1}{\omega}. \quad (14)$$

The meridional velocity can be found by demanding that the velocity through the runner is increasing. This will reduce the chance for flow separation, backflow, and other phenomena in the runner. A typical acceleration is 10%, i.e.

$$c_{m2} = 1.1c_{m1}. \quad (15)$$

The height of the inlet channel, B metres, is then found by

$$B = \frac{Q}{2\pi r_1 c_{m1}}. \quad (16)$$

Finally, the inlet blade angle, β_1 , needs to be calculated. From Figure 3 we see that the inlet tangential water velocity is needed. Returning to the Euler turbine equation,

$$\eta = (u_1 c_{u1} - u_2 c_{u2})/gH. \quad (17)$$

With $c_{u2} = 0$, Equation (5) reduces to $\eta = (u_1 c_{u1})/gH$, and as the runner speed u_1 is set, this allows for calculation of the tangential water velocity component:

$$c_{u1} = \frac{\eta}{u_1} gH, \quad (18)$$

with $\eta = 0.96$ being a typical value (Brekke, 2003). This is because 100% efficiency is impossible due to hydraulic friction, bearing losses, etc. As the final main parameter, β_1 can be calculated as

$$\beta_1 = a \tan \left(\frac{c_{m1}}{u_1 - c_{m1}} \right). \quad (19)$$

When the main parameters are set, further details need to be determined. From the Euler turbine equation, Equation (5), we see that the quantity $u_i c_{ui}$ is a measure of energy. From Equation (6) we also see that this quantity is zero at the outlet ($u_2 c_{u2} = 0$). How the distribution

changes through the runner is free for the designer to choose. Typically, the $u_i c_{ui}$ distribution is chosen such that most of the energy is transferred to the runner in the beginning of the runner. This is due to runner blades generally being thinner and more prone to fractures at the outlet. The blades will also be given a thickness distribution, and leading and trailing edge profiles. These modifications will change the flow area in the runner channels, and in general one should revert back to Equations (10) and (16) to account for this. The design procedure outlined here is implemented in a MATLAB® code. The program writes the turbine geometry into text files that are compatible with the ANSYS® software.

In terms of optimization, there exist tens of free optimization parameters: number of blades, energy distributions, thickness distributions, leading and trailing edge shape, etc. In this article, only two parameters, as listed in Table 1 and shown in Figure 4, have been chosen. The parameters define the leading-edge geometry of the blade. Both the pressure and suction sides of the leading edge are expressed as ellipses, and the parameters a_{ps} , a_{ss} control the free axis in the ellipses, as the blade leading edge thickness in this case is held constant at $t = 30$ mm. Changing the parameters changes the curvature of the leading edge, and presumably also the turbine performance at different operating conditions, i.e. different inlet flow angles.

The reason only these parameters are chosen is twofold: the main goal of this article is to prove that the optimization framework works. This is best shown using few parameters so that the simulation time is in a reasonable range. Secondly, it is desired to use parameters where the bounding runner geometry is unchanged. This way, the different designs can be compared directly. For reference, the main dimensions in all the runners in this article are the following: $H = 350$ m, $Q = 25$ m³/s, $\bar{u}_1 = 0.72$, $D_2 = 1.71$ m and $B_1 = 0.205$ m. The specific

Table 1. Optimization parameters.

Parameters	Type	Range (mm)
a_{ps} , pressure side geometry	Continuous	10–40
a_{ss} , suction side geometry	Continuous	10–40

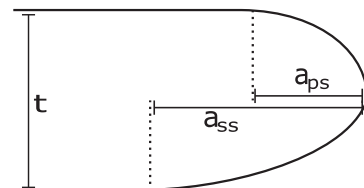


Figure 4. Definition of leading edge geometry.

speed is $n_s = \omega \cdot \sqrt{Q}/(2gH)^{0.75} = 0.26$, classifying this as a high-head Francis turbine. The uc_u -distribution through the runner follows the relation $uc_u = x^2$, where $x = 1$ marks the inlet and $x = 0$ the outlet.

2.2.2. Block B – simulation

Block B contains an ANSYS® Workbench™ project, where the geometry is meshed in TurboGrid™, and simulated in CFX®. The present authors have previously published an article on the accuracy and time-consumption of a numerically simulated hill diagram (Tengs et al., 2018). Some of the results will be repeated here. The Norwegian University of Science and Technology provided an experimentally obtained hill diagram along with a model geometry. About 40 operating points were simulated, and the experimental data were used as validation. The guide vane opening and the runner speed were operated in the range $\alpha \approx [-50\%, +40\%]$ and $n \approx \pm 20\%$, respectively, of the assumed best efficiency point. ANSYS CFX was used for simulation, as this is the leading simulation software with regards to rotating machinery. Only the runner domain and a cut-off draft tube were simulated, this ensured that only one mesh was needed for the whole hill diagram. In the runner domain, one passage was simulated, utilizing the rotational symmetry of the geometry. The different operating points were tested by changing the direction of the velocity components on the inlet, the mass flow, and the runner speed. The simulation strategy of no re-meshing allowed for parallel simulation of all operating points. Steady state, passage modeling, and incompressible flow were assumed to reduce the simulation time where possible. The SST turbulence model was used, and the average y^+ in the runner was 2.8. Mesh convergence was confirmed using the GCI method due to Celik, Ghia, Roache, and Christopher (2008). The boundary condition at the inlet was the mass flow taken from the experiment; at the outlet, zero relative pressure was used. The results were highly encouraging. If one disregards operating points with extremely low guide vane opening, the error in hydraulic efficiency was found to be less than 2.5% in the whole simulated range. Around the best efficiency point, the deviation was in the order of 0.5%, see Figure 5. The error was also not randomly distributed, but followed a clear pattern. The simulations were performed on a workstation using 6 cores in parallel, and each simulated point took approximately 15 minutes. Using more powerful hardware, or utilizing the parallelization properties of the method, could decrease the simulation time drastically.

Based on the above, a numerically obtained hill diagram is assumed to be trusted, especially for identifying

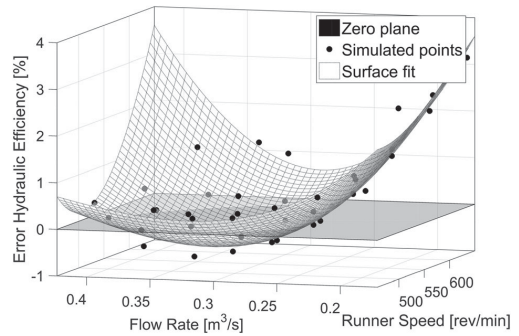


Figure 5. Error in hydraulic efficiency, taken from Tengs et al. (2018).

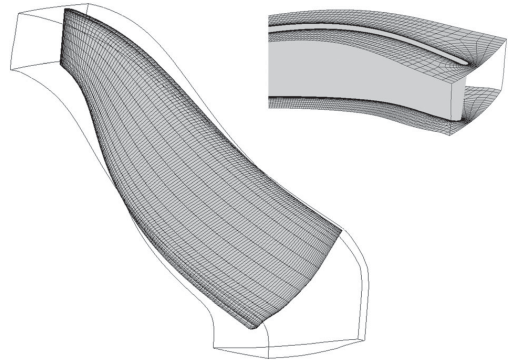


Figure 6. Typical mesh used in the simulations.

behavioural trends. This is based on the non-random error distribution of the simulated head and torque (Tengs et al., 2018). Far away from the best efficiency point, simulation error is inevitable; however, the error is assumed to behave equally in all designs, making a relative comparison valid. Similar simulation settings as in the reference are used in this article, however expanded to include automatic meshing of the new runner geometry as well as the draft tube. Another necessary change is to use total pressure inlet conditions, as the mass flow is not given a priori in the simulations. The outputs of the simulation are thus the hydraulic efficiency and mass flow. The mesh was automatically generated with TurboGrid for each design; a typical blade surface mesh and inlet are shown in Figure 6. Note that the extended inlet section and draft tube is omitted for clarity. The total number of mesh elements was $\approx 2 \times 10^5$ per passage, equivalent to 4.2 million elements if the whole turbine had been simulated rather than using passage modeling.

2.2.3. Block C – analysis

Block C defines the optimization objectives in the loop. There are many ways of analyzing the simulation output; the goal could be a high peak hydraulic efficiency, or conversely a ‘flatter’ curve, albeit with a lower peak performance. In terms of variable speed turbines, it might be clever to synchronize the flow and runner speed such that the direction of the water entering the runner matches the runner geometry. This equates to $\beta = \beta_{\text{blade}}$ in Figure 3. This should in general result in smaller incidence losses, fewer transient effects, and better turbine operation. A high mean efficiency along this ‘line of operation’ could be an optimization criterion. Figure 7 illustrates such an approach. In this single-objective function, all operating points are given the same importance/weight; if this were a real optimization case for a customer, a weight function based on actual turbine operation should be provided. More advanced objective functions including curvature of the hill diagram, etc., is just as easily implemented; however, the mean is chosen here.

If it were possible to input $\beta = \beta_{\text{blade}}$ to the simulations, there would be no need to simulate the complete hill diagram. Some flow/speed combinations will not be used, and are therefore not of interest. This would in turn result in fewer simulations, and faster optimization. The problem with this approach is that it is difficult to input $\beta = \beta_{\text{blade}}$ in the simulations. β is defined as $\beta = a \tan\{c_m/(u - c_m)\}$, and since $c_m = Q/A$ and the flowrate is not specified in the simulations, beta cannot be precisely determined in advance. Optimization along a line $\beta = \beta_{\text{blade}}$ is still possible; however, a more ‘complete’ hill diagram is needed, assuming several operating points have been simulated. The flow rate can now be plotted with respect to guide vane opening and runner speed. By using a surface fitting procedure, one can obtain a mathematical description of this relation, $Q(\omega, \alpha)$. Thus, the inlet angle can be reduced to a function of the inlet

parameters only:

$$\beta = \tan^{-1} \left(\frac{Q(\omega, \alpha)/A}{\omega r - \frac{Q(\omega, \alpha)}{A \cdot \tan(\alpha)}} \right). \quad (20)$$

Such an approach was implemented in MATLAB. The runner speed and guide vane angle were simulated in a 3×3 matrix for each design. The limits were set to $\pm 30\%$ of the assumed optimal configuration for both input values. A complete second order fit was performed on the resulting mass flow versus speed and α ; β was then calculated from Equation 20, and the hydraulic efficiency was extracted at five points along a line where $\beta = \beta_{\text{blade}}$. Finally, the mean efficiency of the five points was used as optimization characteristic. The above algorithm was tested on the experimental data from the hill diagram validation case mentioned in Section 2.2.2. The guide vane angle/runner speed combinations with β equal to that of the best operating point was found and plotted together with the hill diagram in Figure 8. A line indicating the conventional fixed-speed operation is also included to illustrate the difference in the two operation schemes. In this example, the optimization characteristic, the mean of the five points, is $\eta = 92.8\%$.

2.3. Optimization

Optimization is a scientific field of its own, with a vast amount of research. Surrogate models are very popular, the most known being the classical Response Surface Method (RSM) (Box & Wilson, 1992). In the RSM, the variable space is properly sampled, using Box–Behnken, Central Composite Design or similar, then the outcomes are evaluated and a surrogate model is created based on the results. This allows for the possibility of creating meta-models/reduced order models of a process

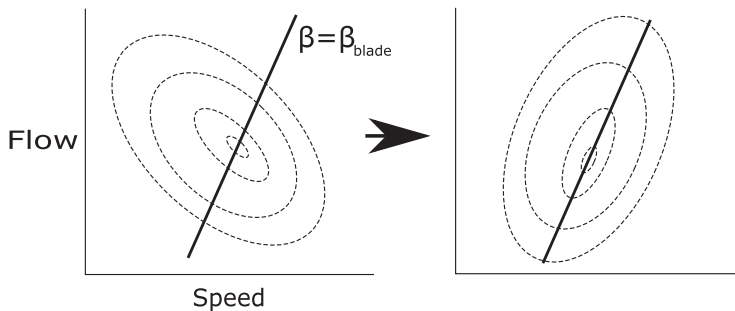


Figure 7. Optimize efficiency along line of small incidence losses.

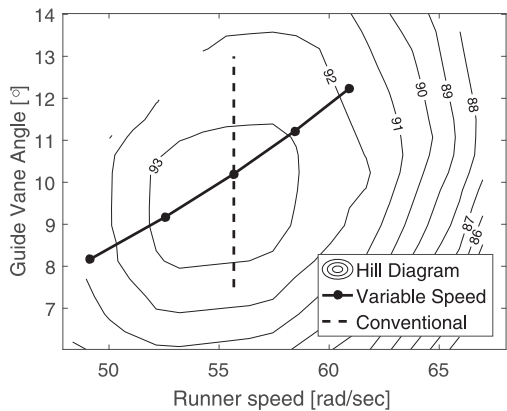


Figure 8. Difference in operating schemes.

response, and makes the method very popular. Similar methods have also been used in the turbine industry (Enomoto et al., 2012; Ezhilsabareesh et al., 2018). Another, newer, optimization strategy is the evolutionary algorithm. The method mimics biological populations; a randomly sampled parameter set evolves in a fashion similar to how populations evolve through generations (Jiang et al., 2018; Vikhar, 2016). Recently, artificial/computational intelligence (CI) or machine learning methods have received much attention; e.g. in Kazemi et al. (2018) and Ardabili et al. (2018), 21 articles from the present decade regarding the usage of CI in the hydrogen production industry alone are reviewed. The mentioned methods are global methods, and fairly computationally expensive. A more classical approach employs gradient based methods, e.g. the conjugate gradient method (Hestenes & Stiefel, 1952). In essence, these methods find the gradient of the response and ‘move’ in the desired direction (i.e. maximize a function). These methods are not a global methods, meaning the final solution may be a local optimum rather than the global one. However, such methods will find an approximate optimum fairly fast. Finally, there is a branch of optimization techniques called local search, including the hill-climbing method and the simplex method (Nelder & Mead, 1965). Common to these methods is making small local changes in the variables, and a direct evaluation of the new response. As with gradient based methods, these methods are not global.

The commercial software optiSLang® has been used to couple all the blocks presented in Figure 2 together. optiSLang is an optimization software based on graphical programming, where external programs can be used as modules in a system. In this case, MATLAB and ANSYS have been the different modules. The program

can automatically select the appropriate optimization algorithm from among gradient methods, evolutionary strategies, adaptive response surface method (ARSM), etc. Which methodology is used is very much dependent on the problem at hand, and the time needed for the evaluation of each outcome. In this article, the simplex method will be used, owing to its simplicity.

2.3.1. Downhill simplex method

The downhill simplex method is a non-gradient-based method. It is, however, not a global method, and the solution does therefore in general risk getting caught in a local optimum. For a small number of optimization parameters, the convergence is fast. For a larger number, other algorithms may be preferred. The method is chosen here owing to its simplicity. The simplex method starts of by creating a geometrical figure (a simplex) of $N+1$ vertices, with N being the number of optimization parameters. The vertex values are evaluated, before simple transformations (reflection, expansion, contraction) are applied to the simplex, to obtain new design points to be evaluated. In this way, the solution progresses towards the optimum. A thorough explanation can be found in the original article by Nelder and Mead (1965). In summary, the downhill simplex method will be used to optimize the leading-edge geometry of a Francis turbine runner. The optimization goal is to maximize the mean hydraulic efficiency along a line of small incidence losses, as presented in Section 2.2.3.

3. Results

The results from the optimization procedure are presented in Table 2. We observe that the converged solution is well within the given parameter range. Throughout the results section, designs 5 and 24 will be used as representatives for designs early and late in the optimization process, respectively. The first few designs are avoided because the initial guess was chosen arbitrarily. Figure 9 shows the change in the leading edge geometry (please refer to Figure 4 for definitions).

The optimization algorithm was manually terminated after 28 iterations following a visual inspection of the convergence. Figure 10(a) shows the convergence of the simplex algorithm. The y-axis shows the mean efficiency relative to the maximum mean efficiency. We see a difference of $\approx 0.25\%$ in the mean efficiency in the different

Table 2. Optimization results.

Method	Result [a_{ps} , a_{ss}]
Downhill simplex	[14.06, 16.15]

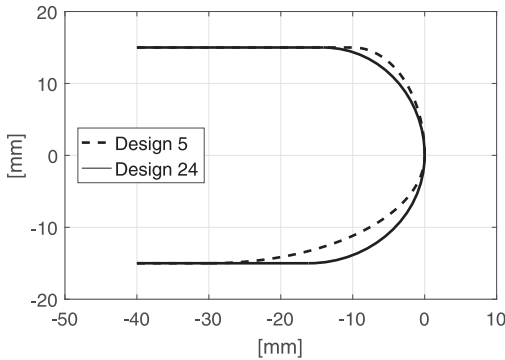


Figure 9. Comparison between one of the earlier and one of the final designs, i.e. 5 and 24, respectively.

designs. The increase is significant when such a limited parameter set is considered.

The objective function in this article is the mean, and no information is thus provided as to how the hill-diagram shape changes. Figure 10(b) is therefore included to show the hill diagram of designs 5 and 24, with the z -axis being the efficiency relative to the best efficiency. We see that, around the best operating point, there are no significant variations; however, at low runner speed and small guide vane opening, the performance differs by more than 0.5%.

It should be noted that the assumption that the best operation mode is along $\beta = \beta_{\text{blade}}$ is not necessarily valid, at least not for the designs tested here. By operating the new design as a conventional runner (constant speed), the mean efficiency will be larger than if $\beta = \beta_{\text{blade}}$ is satisfied. The optimized design performs better than the start design in both operation modes. See Figure 11 for comparison of designs 5 and 24 (variable speed is denoted by dashed lines). The different operation modes are shown in Figure 8. The reason

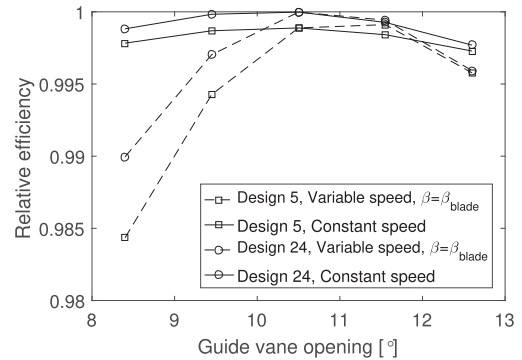
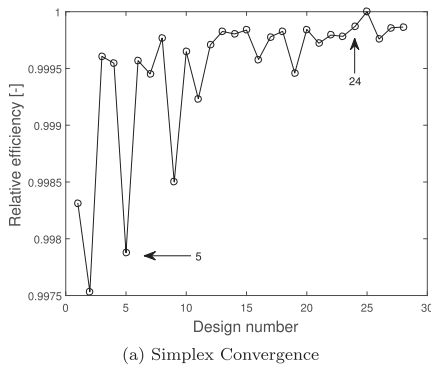


Figure 11. Efficiency along different lines of operation.

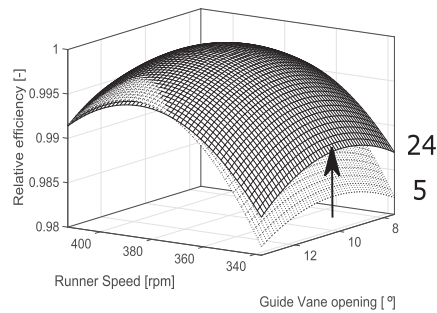
why conventional operation is superior is that, when only the leading edge geometry is changed, the different turbines will still be very similar. The design from Section 2.2.1 is unchanged, the thickness of the blades is the same, etc. Keeping in mind that the original turbine was designed for constant speed, then conventional operation is therefore more efficient. There are a number of other design parameters that could trigger larger changes in the hydraulic efficiency and be more interesting from a design point of view. In essence, to get a proper, optimized, variable speed turbine, more parameters have to be included in the optimization loop.

4. Discussion and further work

The simulations in this article were performed on a laptop using four cores in parallel. The simulation of each hill diagram took about two hours. The time used on design and post-processing was negligible, meshing and simulation in ANSYS accounting for all time consumption. By using hardware with more cores, the



(a) Simplex Convergence



(b) Effect of design change

Figure 10. Change in performance as the simplex method is converging to the final design.

simulation time per hill diagram could be significantly reduced. ANSYS reports scaling properties of >80% efficiency for additional cores (ANSYS, 2018), a close-to-linear reduction of simulation time. Another way of drastically speeding up the simulation would be to simulate the different points in the hill diagram in parallel, as the mesh is the same. This will give a linear reduction factor equal to the number of simultaneously simulated operating points, and coupled with more powerful hardware this will reduce the simulation time to the order of minutes per hill diagram.

The simplex algorithm was terminated after a visual inspection. The reasoning is that the underlying uncertainty in the simulation of the hill diagrams, and the second order approximation when calculating the relative flow angle β , makes further optimization excessive. The absolute change from iteration to iteration reached the order of 0.01% in mean efficiency before termination. Further work should verify the simplex method by using another, preferably global, optimization method, such as the ARSM due to Gary Wang, Dong, and Aitchison (2001), to see if the same leading edge geometry is obtained.

The resulting ellipse axes are $a_{ps} = 14.1$ mm, $a_{ss} = 16.2$ mm, see Figure 9, which means that the final leading-edge geometry is close to a circular shape, as the blade thickness is 30 mm. It is interesting, though somewhat intuitive, that a circular edge is better at dealing with velocity entering from different angles. Any definite recommendation with respect to leading edge geometry should however not be taken from these results, as this article is a test to prove the optimization concept. As a reference, a high-fidelity simulation could be performed to reveal the actual hydraulic performance. If we do, however, assume that the result is correct, then another conclusion is that the efficiency is not very dependent on the leading-edge geometry at the best operating point. At low runner speed, however, the changes are dramatic – close to 1% increase in efficiency and a visually flatter curve. This is exactly the desired change, and indicates that the method works. The choice of using the mean as objective function, however, might not be optimal, as a flat curve is not explicitly looked for. An alternative could include, for example, the standard deviation of the points, to force a flatter curve. In future work using this framework, a more advanced analysis will be implemented.

5. Conclusions

This article presents an optimization procedure for variable speed turbines and shows that the idea of using hill diagrams as the optimization characteristic is feasible. A parametric test of the leading edge shows a mean

efficiency improvement of 0.25% along a certain line of operation. At lower rotational speeds, the differences in the designs becomes more prominent, in some cases with a close to 1% efficiency increase. The actual hydraulic performance should be verified with a high-fidelity simulation. As of now, each hill diagram was created in the order of hours. The procedure is however highly parallelizable and, by utilizing this fact, the simulation time could be reduced to the order of minutes. If this is done, several parameters could be added to the optimization and the procedure still be performed within an industrial timeframe.

Disclosure statement

No potential conflict of interest was reported by the authors.

Funding

This work was supported by Norges Forskningsråd [grant number 254987].

ORCID

Erik Tengs  <http://orcid.org/0000-0001-8873-724X>

References

- Abubakirov, S. I., Lunatsi, M., Plotnikova, T., Sokur, P., Tuzov, P. Y., Shavarin, V., ... Shchur, V. (2013). Performance optimization of hydraulic turbine by use of variable rotating speed. *Power Technology and Engineering*, 47 (2), 102–107.
- Andritz Hydro. (2018). *Turbines for hydropower plants*. Retrieved from <http://energystorage.org/energy-storage/technologies/variable-speed-pumped-hydroelectric-storage>
- ANSYS. (2018). *HPC for uids*. Retrieved from <https://www.ansys.com/products/fluids/hpc-for-fluids>
- Ardabili, S. F., Naja, B., Shamshirband, S., Minaei Bidgoli, B., Deo, R. C., & Chau, K.-w. (2018). Computational intelligence approach for modeling hydrogen production: A review. *Engineering Applications of Computational Fluid Mechanics*, 12 (1), 438–458.
- Box, G. E., & Wilson, K. B. (1992). On the experimental attainment of optimum conditions. In *Breakthroughs in statistics: Foundations and basic theory* (pp. 270–310). New York: Springer.
- Brekke, H. (2003). *Pumper & turbiner*. Vannkraftlaboratoriet, Norges Teknisk-Naturvitenskapelige Universitet (NTNU).
- Celik, I., Ghia, U., Roache, P., & Christopher. (2008). Procedure for estimation and reporting of uncertainty due to discretization in CFD applications. *Journal of Fluids Engineering*, 130 (7), Article ID 078001. doi:10.1115/1.2960953
- Dörer, P., Sick, M., & Coutu, A. (2012). *Flow-induced pulsation and vibration in hydro-electric machinery: Engineer's guidebook for planning, design and troubleshooting*. London: Springer-Verlag. doi:10.1007/978-1-4471-4252-2
- Electric Power Research Institute (EPRI). (1999). *EPRI Hydro life extension modernization guide*, Vol. 2 – Hydromechanical equipment.

- Energy Storage Association (ESA). (2018). *Variable speed pumped hydroelectric storage*. Retrieved from <http://energy-storage.org/energy-storage/technologies/variable-speed-pumped-hydroelectric-storage>
- Enomoto, Y., Kurosawa, S., & Kawajiri, H. (2012). Design optimization of a high specific speed Francis turbine runner. *IOP Conference Series: Earth and Environmental Science*, 15 (3), Article ID 032010. doi:10.1088/1755-1315/15/3/032010
- Ezhilsabareesh, K., Rhee, S. H., & Samad, A. (2018). Shape optimization of a bidirectional impulse turbine via surrogate models. *Engineering Applications of Computational Fluid Mechanics*, 12 (1), 1–12.
- Farrell, C., & Gulliver, J. (1987). Hydromechanics of variable speed turbines. *Journal of Energy Engineering*, 113 (1), 1–13. 25
- Gary Wang, G., Dong, Z., & Aitchison, P. (2001). Adaptive response surface method – a global optimization scheme for approximation-based design problems. *Engineering Optimization*, 33 (6), 707–733.
- Gogstad, P. J. (2012). *Hydraulic design of Francis turbine exposed to sediment erosion* (Master's thesis). Norwegian University of Science and Technology (NTNU).
- Hestenes, M. R., & Stiefel, E. (1952). Methods of conjugate gradients for solving linear systems. *Journal of Research of the National Bureau of Standards*, 49 (6), 409–436.
- Jiang, J., Cai, H., Ma, C., Qian, Z., Chen, K., & Wu, P. (2018). A ship propeller design methodology of multi-objective optimization considering uid–structure interaction. *Engineering Applications of Computational Fluid Mechanics*, 12 (1), 28–40.
- Kazemi, S., Minaei Bidgoli, B., Shamshirband, S., Karimi, S. M., Ghorbani, M. A., Chau, K.-w., & Kazem Pour, R. (2018). Novel genetic-based negative correlation learning for estimating soil temperature. *Engineering Applications of Computational Fluid Mechanics*, 12 (1), 506–516.
- Lyutov, A. E., Chirkov, D. V., Skorospelov, V. A., Turuk, P. A., & Cherny, S. G. (2015). Coupled multipoint shape optimization of runner and draft tube of hydraulic turbines. *Journal of Fluids Engineering*, 137 (11), Article ID 111302. doi:10.1115/1.4030678
- Nakamura, K., & Kurosawa, S. (2009). Design optimization of a high specific speed Francis turbine using multi-objective genetic algorithm. *International Journal of Fluid Machinery and Systems*, 2 (2), 102–109.
- Nelder, J. A., & Mead, R. (1965). A simplex method for function minimization. *The Computer Journal*, 7 (4), 308–313.
- Norwegian Hydropower Centre (NVKS). (2018). *The Francis99 research project*. Retrieved from <https://www.ntnu.edu/nvks/francis-99>
- Pérez, J. I., Wilhelmi, J. R., & Maroto, L. (2008). Adjustable speed operation of a hydropower plant associated to an irrigation reservoir. *Energy Conversion and Management*, 49 (11), 2973–2978.
- Pilev, I. M., Sotnikov, A. A., Rigin, V. E., Semenova, A. V., Cherny, S. G., Chirkov, D. V., . . . Skorospelov, V. A. (2012). Multiobjective optimal design of runner blade using efficiency and draft tube pulsation criteria. *IOP Conference Series: Earth and Environmental Science*, 15 (3), Article ID 032003. doi:10.1088/1755-1315/15/3/032003
- Semenova, A., Chirkov, D., Lyutov, A., Cherny, S., Skorospelov, V., & Pylev, I. (2014). Multi-objective shape optimization of runner blade for Kaplan turbine. *IOP Conference Series: Earth and Environmental Science*, 22 (3), Article ID 012025. doi:10.1088/1755-1315/22/1/012025
- Subramanya, K. (2013). *Hydraulic machines*. New Delhi: Tata McGraw-Hill Education.
- Tengs, E., Storli, P.-T., & Holst, M. A. (2018). Numerical generation of hill-diagrams; validation on the francis99 model turbine. *International Journal of Fluid Machinery and Systems*, 11(3), 294–303.
- Trivedi, C., Cervantes, M. J., & Gunnar Dahlhaug, O. (2016). Numerical techniques applied to hydraulic turbines: A perspective review. *Applied Mechanics Reviews*, 68 (1), Article ID 010802. doi:10.1115/1.4032681
- Vikhar, P. A. (2016, December). Evolutionary algorithms: A critical review and its future prospects. *ICGTSPICC. 2016 International Conference on Global trends in Signal Processing, Information Computing and Communication*, Jalgaon, Maharashtra, India (pp. 261–265).

Paper 8

Reducing computational effort of high head Francis turbines

Jakobsen, KR., Tengs, E., Holst, M. A.

IOP Conference Series: Earth and Environmental Science, **240** 072001, 2019

Reducing computational effort of high head Francis turbines

Ken-Robert G. Jakobsen, Erik Tengs, Martin Aa. Holst

EDRMedeso AS, Leif Tronstads plass 4, 1337 Sandvika, Norway

ken-robert.g.jakobsen@edrmedeso.com

Abstract. The present work shows how a complete full-wheel model of a high head Francis turbine can be reduced directly by leaving out parts of the computational domain, but without losing accuracy in the RSI pressure that is of primary interest. Instead great savings in mesh size and consequently computational time is gained. Two main modifications have been performed: 1) Reducing the draft tube and 2) Excluding the distributor except for the guide vanes. This is performed both on separate models as well as combining them obtaining an ultimate mesh reduction of about 60%. From this process it is shown that the volute could be replaced by a very simple set of inlet boundary conditions without affecting the results as well as simplifying the meshing procedure. A close to linear speed-up with mesh size is obtained. For comparison, simulations performed on passage models have also been included and all results are validated against full-wheel transient simulations as well as experimental data. The work has been performed as part of the HiFrancis project at the Norwegian University of Science and Technology and the Norwegian Hydropower Centre.

1. Introduction

Computational Fluid Dynamics (CFD) is a powerful tool when designing and investigating hydraulic turbines. However, using CFD puts a high demand on computational resources. Acknowledging the fact that an industrial design loop must be completed within a practical time frame, typically 6-12 hours, it is crucial to reduce the computational effort. Today this is usually achieved by utilizing very simplified numerical models of the turbines, compromising on accuracy and the available information that can be retrieved from the simulation results. For high head Francis turbines, the latter is commonly justified by the need to only focus on Rotor-Stator-Interaction (RSI) to avoid resonance effects between the pressure pulsations and natural frequencies of the turbine as these are main sources for blade cracking [1]. A thorough overview of existing numerical techniques applied to high head Francis turbines can be found in [2].

Aiming to achieve more time efficient simulation procedures that are of industry relevance, the present work shows how a complete 360° model (also referred to as full-wheel model) of a high head Francis turbine can be reduced directly by leaving out parts of the computational domain, but without losing accuracy in the RSI pressure that is of primary interest. Instead great savings in mesh size and consequently computational time is gained. Two main modifications have been performed: 1) Reducing the draft tube 2) Excluding the distributor except for the guide vanes. This is performed both on separate models as well as combining them. In general, reducing the draft tube will lead to the greatest reduction in computational mesh due to the vast number of elements being contained there, but modifying the distributor will also simplify the meshing procedure and consequently reduce the time needed for mesh generation. The present investigation also includes simulations performed on



some of the much faster passage models available in ANSYS CFX, utilizing the periodic symmetry of the turbine.

Existing experimental data together with CFD simulations on the same geometry and operating points are used for data validation. The latter include three-dimensional transient simulation of a full-wheel turbine model with spiral casing (also referenced as volute or distributor), guide vanes, runner, and draft tube. This mesh consists of about 42 million nodes leading to extensive simulation times before reaching a periodic state.

The work has been performed as part of the HiFrancis project at the Norwegian University of Science and Technology and the Norwegian Hydropower Centre.

2. Reference data

In the following section, reference data used to validate the reduced models will be presented. This includes both experimental and numerical assessments.

2.1. Experimental validation data

As presented in [3], an overview of the experimental setup is shown in Figure 1. The runner is a modified model of the turbine previously installed at the Tokke power plant in Norway and is used at Norwegian University of Science and Technology (NTNU) for research on pressure pulsations inside high head Francis turbines. Moreover, the runner is a so-called splitter design and consists of 15+15 blades and the distribution unit of 28 guide vanes and 14 stay vanes. To perform the measurements and capture the propagation of the pressure pulses, five pressure sensors were positioned in the middle of two of the runner channels. This is shown in Figure 2.

With the present setup combined with a runner speed of 5.54Hz, the predominant frequencies seen in this test rig become the guide vane passing at 155Hz and the blade passing at 166Hz. In addition to the RSI frequencies the system will be subjected to additional phenomena such as draft tube pulsations (Rheingans frequency), vortex shedding and elastic fluctuations in the waterway when going outside of BEP. These are included in the experimental results but are not part of the scope.

The operating point of primary interest in the present study is BEP performed at a head of 11.94m and flow rate equal 0.2m³/s. It is referred [3] for further details on this and other load conditions.

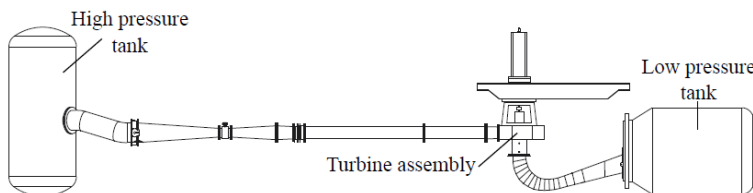


Figure 1. Overview of measurement setup.

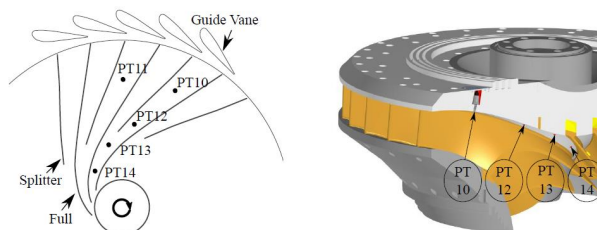


Figure 2. Position of hub mounted pressure sensors in runner channels.

2.2. Numerical validation data

Mimicking the setup of the model measurements, CFD simulations of the full-wheel model have been presented in [4] and [5]. Referred to as Base Case in the present paper, the results from these analyses are used as numerical validation data for the reduced models, both in terms of accuracy and computational speed. The simulations are transient utilizing a sliding mesh interface between the runner and volute (rotor/stator).

A mesh independent solution consisting of approx. 42 million nodes has been utilized, where the volute consists of mesh with tetrahedral elements (size), while the runner and draft tube are generated with hexahedral elements (size). The industry standard k-w SST turbulence model has been applied for all simulations with the boundary conditions as shown in Figure 3. Performed in ANSYS CFX, the simulations were run for three revolutions after steady periodic flow behaviour had been achieved. Three distinct operating points were considered, however, only BEP will be presented here.

In general, the full-wheel results agree very well with the experimental data discussed in the previous section. For BEP, this is exemplified through global parameters in Table 1 and the corresponding pressure signal in PT10 in Figure 4. The second harmonic is clearly underpredicted, which in recent studies has been shown to be due to resonance effects occurring at the double RSI frequency in the experiments.

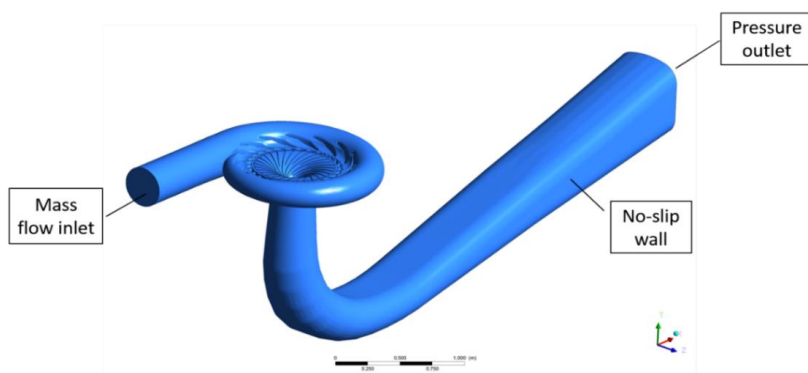


Figure 3. Computational domain for full-wheel simulations [5].

Table 1: Global parameters for full-wheel simulation and experiments at BEP [5].

Case	Net head [m]	Torque to generator [Nm]	Inlet pressure [kPa]	Outlet pressure [kPa]	Hydraulic efficiency [%]
Experiment	11.94	620.7	215.6	111.1	92.2
CFD transient	12.08	640.8	218.4	111.8	94.1
Deviation	1.17%	3.24%	1.30%	0.63%	2.06%

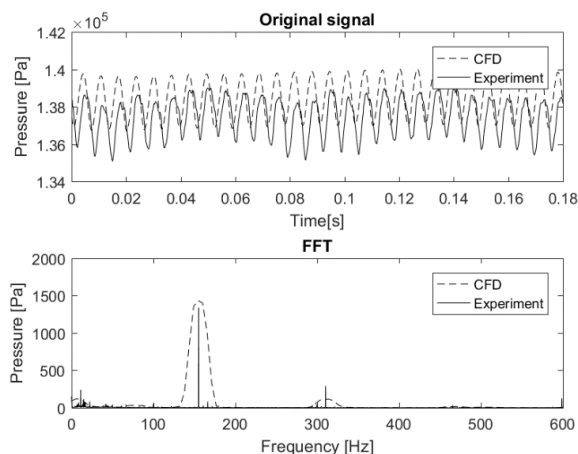


Figure 4. Pressure signal in PT10 at BEP for full-wheel simulation and experiments [5].

3. Reduced models

This section will compare different approaches to reduce the overall computational time on the high head Francis turbine. Two main methods will be discussed:

- 1) Reducing the total number of elements in the full-wheel model directly by leaving out parts of the volute or the draft tube domain.
- 2) Utilizing the rotational symmetry of the Francis turbine through different passage models available in ANSYS CFX.

The experimental and numerical investigations presented in the previous two subsections are used as validation data.

3.1. Reducing full-wheel model

The effects of removing the volute or draft tube have been investigated in the following, including one case combining both. Figure 5 shows the resulting computational domains. Same boundary conditions as for the Base Case have been used for all cases, except for the no volute/combined inlet for which velocity vectors have been specified at the slightly extended guide vane passage (see Figure 6). The velocity direction was determined from the stay vane angle, which is independent of the operating point.

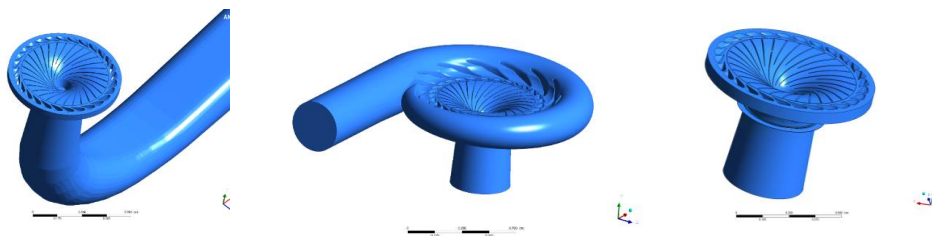


Figure 5. Computational domain of reduced full-wheel models. Left: No volute, middle: Short Draft Tube, right: Combined.

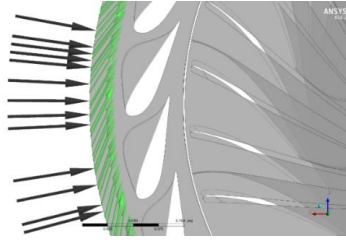


Figure 6. Constant velocity profile at inlet.

Figure 7 shows streamlines for all three cases and Figure 8 and Figure 9 give the pressure signals and corresponding FFT plots from the PT10 probe onboard the runner (see definition of sensor location in Figure 2). Clearly, none of the separate full-wheel model reductions affect the results to any significant degree relative to Base Case as both the pressure amplitudes and the pulsation frequencies match well. This is also true for the combined case. Although insignificant, it is interesting to note that the No Volute case produce a slightly higher pressure amplitude and the Short Draft Tube case sees a somewhat higher average pressure signal. These effects can be explained by the strictly uniform velocity profile substituting an otherwise periodic inlet condition and the outlet pressure condition being much closer to the measurement locations for the respective cases, respectively. The Combined case sees both effects accordingly. The small differences seen can easily be reduced further by adjusting the outlet condition at that location due to the shorter draft tube giving a lower pressure reduction from the runner to the outlet. Furthermore, a more accurate inlet condition can be obtained by for instance assuming a sinusoidal periodic velocity profile. This is expected to reduce the pressure amplitude at the measurement location. Noticeably, this is also information that can be gained prior to performing any simulations.

It is referred to section 2.2. and [5] for validation of the full-wheel simulations.

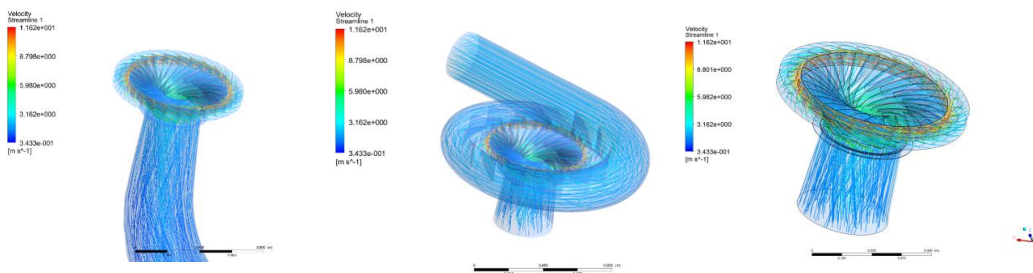


Figure 7. Streamlines on reduced model. Left: No volute, middle: Short Draft Tube, right: Combined.

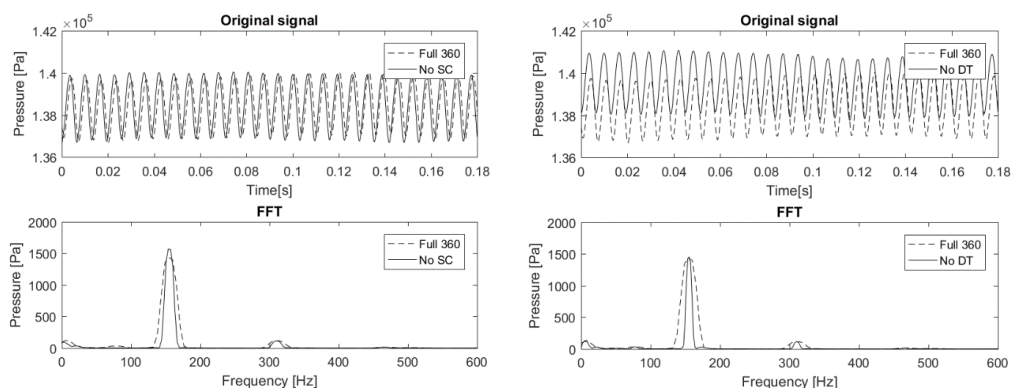


Figure 8. PT10 pressure signal. Left: No Volute, right: Short Draft Tube.

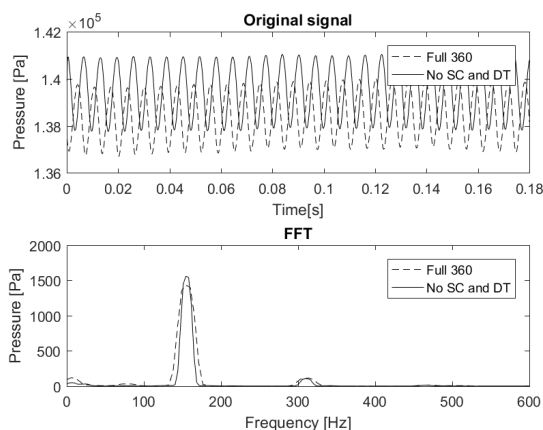


Figure 9. PT10 pressure signal for Combined at BEP.

3.2. Passage modelling

Parts of the following section is adapted from [6] with permission from author.

The turbine runner is rotationally symmetric and significant speed-up can be achieved by simulating only a section of the geometry. Challenges arise, however, when the number of stator (S) and rotor (R) components are not equal. First, periodic interfaces must be prescribed. Conventional periodic interfaces require the assumption that fluxes on one interface equals that of the other. This is not the case in a hydro turbine if $S \neq R$. Instead, phase-shifted periodic boundaries will be present, meaning that one periodic interface will equal the other at an earlier or later instance in time. This will have to be addressed by the methods used. Furthermore, pitch change also occurs when $S \neq R$ as illustrated in the passage model in Figure 9 ($S=19$ and $R=24$). If the pitch is different from unity, some modification will be performed on the information crossing the frame change interface

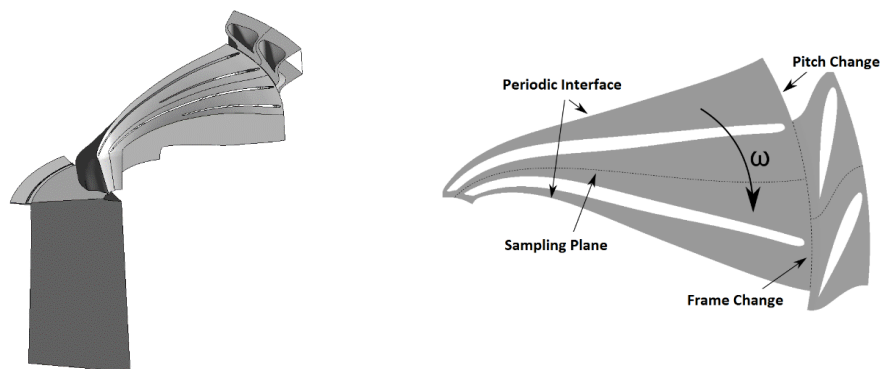


Figure 10. Computational domain of passage models. Right: definition of boundary conditions and pitch change [6].

The present investigation includes simulations on three of the passage methods available in ANSYS CFX:

1. Profile Transformation (PT)
2. Fourier Transformation (FT)
3. Frozen Gust (FG).

In all passage models, the inlet boundary conditions have been defined as total pressure and velocity directions taken from a steady simulation. The settings were otherwise as for the full-wheel simulation discussed in chapter 2.2. The direction of the velocity components imposed on the inlet to replicate the effect of the guide vane/stay vanes, was the same as the guide vane/stay vane outlet angle. This work was first published in [6]

Whereas the PT method simply scales the flow from the stator domain to match the size of the runner domain conserving mass and momentum, the FT utilizes the periodic nature of the flow through Fourier series decomposition. In the latter method, the trigonometric functions are applied directly at the rotor/stator interface resulting in a close to pitch independent methodology. Frozen Gust is an alternative to FT where only the runner passage is included in the simulation and the inlet conditions are applied directly upstream of the runner. Obviously, this results in great reduction in mesh size, but the results will depend significantly on the accuracy of the inlet conditions. Detailed descriptions of the respective methods can be found in [7].

Figure 11 shows the spectral content at pressure probe PT10 with the PT and FG methods together with the experimental measurements and full-wheel simulations presented previously. Manual Fourier coefficient sampling was implemented in the full-wheel simulation to extract the true periodic nature at the RSI interface. The profile was then reconstructed at the inlet of the Frozen Gust simulation as a periodic inlet boundary condition (FG Fourier Inlet). Clearly, the blade passing frequency is very well predicted. However, in accordance with the full-wheel and reduced model simulations, the second harmonic is consistently underpredicted by approx. 50%. Only the results from the PT and FG have been included as the FT simulation diverged after two runner revolutions and were deemed too uncertain to be included in this section.

In order to address the sensitivity of the choice of inlet condition, additional simulations were performed by applying a constant velocity profile as illustrated in Figure 6 (FG Original) as well as a sinusoidal periodicity (FG Sine Inlet). Figure 12 shows the spectral content of these simulations. Both alternatives match the blade passing frequency, but significantly overpredict the pressure amplitude of the first harmonic, especially FG Original.

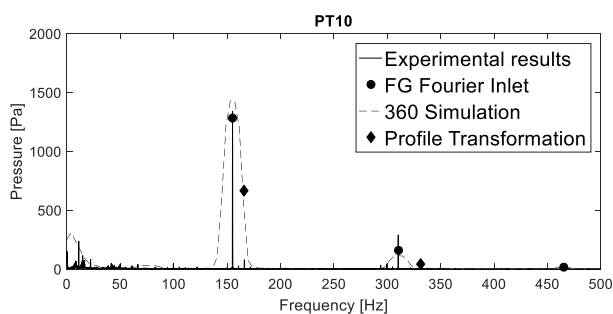


Figure 11. PT10 spectral content for Profile Transformation and Frozen Gust [6].

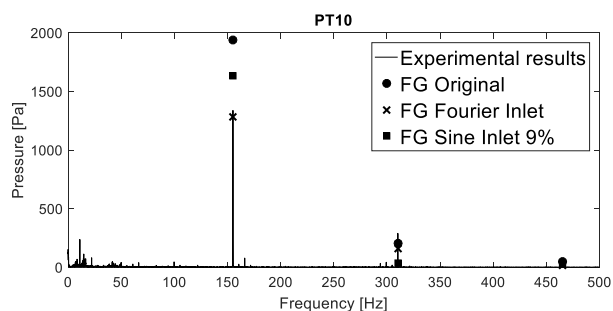


Figure 12. PT10 spectral content for Frozen Gust with different inlet conditions [6].

4. Speed up

The main purpose of this investigation has been to reduce computational time without compromising on accuracy to any significant degree. The present section will thus address the speed-up gained by the various methods presented.

Table 2 summarizes the node count for the reference case (Base Case) and the three modified cases for the full-wheel reductions together with relative speed up for each case normalized by number of time steps and compute cores. Comparing the No Volute and Short Draft Tube cases, most is gained by excluding the draft tube leading to a node reduction of 44%. And obviously, combining both effects results in the highest speed up of all cases. Nevertheless, all reductions show a close to linear speed-up with respect to mesh size and as discussed in section 3.1 only minor effects on the results were experienced by performing these simplifications. A more time efficient meshing procedure can also be expected, especially for the No Volute and Combined cases for which the meshing of the spiral casing has now been made redundant.

Table 2 also shows the relative speed-up gained by utilizing the various passage models. Here, the FT method has been included for comparison. Normalized by the number of runner revolutions, time steps and compute cores, clearly higher speed-up is achieved than for the full-wheel reductions, but only the FG Fourier Inlet method proved to give results at an acceptable level of accuracy. Remembering also that the results were obtained using information from an existing full-wheel simulation, this highlights the main advantage of the full-wheel reduction method. That is, despite the lower speed-up, no extra information is needed to achieve the level of accuracy presented and the full frequency content of the flow field is retained when moving from the Base Case to the simplified solutions.

Table 2. Speed-up of reduced models.

	Global Number of Nodes	Mesh size factor	Relative speedup [-]
Base Case	42476565	1	1
No Volute	36021993	1.18	1.2
Short Draft Tube	23822372	1.78	1.7
Combined	17367800	2.45	2.2
FT	-	-	3.7
FG	-	-	5.5
PT	-	-	8.3

5. Concluding remarks

Aiming to adopt to an industry time frame, the present work shows how a complete 360° simulation model of a high head Francis turbine can be reduced directly without losing accuracy in the RSI pressure that is of primary interest. The reduction is achieved by: 1) Reducing the draft tube and 2) Excluding the distributor except for the guide vanes. Consequently, great savings in mesh size and computational time is gained. This has been applied both on separate models as well as combining them, obtaining an ultimate mesh reduction of about 60% and a relative speed-up factor equal 2.2. A nearly linear speed-up with mesh size was achieved for all cases.

In general, reducing the draft tube will lead to the greatest reduction in computational mesh due to the vast number of elements being contained there, but modifying the distributor will also simplify the meshing procedure and consequently reduce the time needed for mesh generation. Despite a moderate speed-up compared to the passage models, the reduction of the full-wheel model does not lose any of the frequency content in the flow during this process. This is an essential aspect in describing the high level of accuracy that has been achieved. It is also shown that the entire volute could be replaced by a very simple set of inlet boundary conditions without affecting the results to any significant degree.

References

- [1] Seidel U, Hübner B, Löfflad J and Faigle P 2012 *Evaluation of RSI-induced stresses in Francis runners* 26th IAHR Symp. Hydr. Machinery and Systems (Beijing)
- [2] Trivedi C, Cervantes M J and Dahlhaug O G 2016 *Numerical techniques applied to hydraulic turbines: A perspective review* Applied Mechanics Reviews **68**
- [3] Agnalt E 2016 *Pressure measurements inside a Francis turbine runner* Master thesis (NTNU)
- [4] Jakobsen K-R G and Holst M 2017 *CFD simulations of transient load change on a high head Francis turbine* J. Physics: Conference Series **782**
- [5] EDRMedeso AS 2018 *Recommended Practice HiFrancis WP3.1* (HiFrancis project)
- [6] Tengs E, Storli P-T and Holst M 2017 *Effects of passage modelling in high head Francis turbines* Int. J. Hydropower & Dams (Hydro 2017 conference)
- [7] ANSYS INC 2017 *ANSYS CFX Reference Guide Release 18*

Paper 9

High Efficiency CFD Simulations of High Head Francis Turbines

Jakobsen, KR., Tengs, E., Holst, M. A.

International Journal of Fluid Machinery and Systems, Accepted for publication,
2019

Original Paper

High Efficiency CFD Simulations of High Head Francis Turbines

Ken-Robert G. Jakobsen, Erik Tengs and Martin Aa. Holst

¹EDR&Medeso As,

Leif Tronstads plass 4, 1337 Sandvika, Norway, ken-robert.g.jakobsen@edrmedeso.com,
erik.tengs@edrmedeso.com, martin.holst@edrmedeso.com

Abstract

Traditionally, there has been one main method for improving computational speed of hydraulic machines such as high head Francis Turbines. Namely, utilizing the periodicity in the flow field through so-called passage models. These are time marching schemes, but considers only a small section of the turbine, for instance one or two runner blades. Now, however, ANSYS CFX offers a method for solving in the frequency plane instead, called Harmonic Analysis. Theoretically, this method is set to improve speed up by about 100 times considering targeted frequencies only such as the RSI. The present work shows how the Harmonic Analysis method applied to a high head Francis turbine (Tokke runner) is converging within 5 hours of wall clock time. Retaining all flow features, however, a different method is presented aiming at reducing the full-wheel domain directly, i.e. leaving out parts of the volute and draft tube and working on the complete runner geometry. The work shows that not nearly the same speed up is achieved by this method, nor was it expected to be, but the solution space is kept in accordance with the full-wheel system and at equally high accuracy in the RSI pressure. Following the latter method, an ultimate mesh reduction of about 60% is obtained with a close to linear speed-up with mesh size. However, simulation time is still a matter of days at the given compute cluster, so by targeting the RSI pressure pulsation and solving in the frequency domain the Harmonic Analysis gives accurate results at an unprecedented solution time.

The work has been performed as part of the HiFrancis project at the Norwegian University of Science and Technology and the Norwegian Hydropower Centre.

Keywords: High Head Francis, Reduced Models, Harmonic Analysis.

1. Introduction

Part of the work presented in the paper has been presented and discussed at the 29th IAHR Symposium on Hydraulic Machinery and Systems in Kyoto [1], and as such a couple of text passages not concerning the actual work have been left unmodified. The paper presents new results giving a more in-depth understanding of the work, together with a completely new set of passage modelling simulations, including a theory section.

Computational Fluid Dynamics (CFD) is a powerful tool when designing and investigating hydraulic turbines. However, using CFD puts a high demand on computational resources. Acknowledging the fact that an industrial design loop must be completed within a practical time frame, typically 6-12 hours, it is crucial to reduce the computational effort. Today this is usually achieved by utilizing very simplified numerical models of the turbines, compromising on accuracy and the available information that can be retrieved from the simulation results. For high head Francis turbines, the latter is commonly justified by the need to only focus on Rotor-Stator-Interaction (RSI) to avoid resonance effects between the pressure pulsations and natural frequencies of the turbine as these are main sources for blade cracking [2]. A thorough overview of existing numerical techniques applied to high head Francis turbines can be found in [3].

Aiming to achieve more time efficient simulation procedures that are of industry relevance, the present work shows how a complete 360° model (also referred to as full-wheel model) of a high head Francis turbine can be reduced directly by leaving out parts of the computational domain, but without losing accuracy in the RSI pressure that is of primary interest. Instead great savings in mesh size and consequently computational time is gained. Two main modifications have been performed: 1) Reducing the draft tube 2) Excluding the distributor except for the guide vanes. This is performed both on separate models as well as combining them. In general, reducing the draft tube will lead to the greatest reduction in computational mesh due to the vast number of elements being contained there, but modifying the distributor will also simplify the meshing procedure and consequently reduce the time needed for mesh generation. The present investigation also includes simulations performed on a new and much faster passage model available in ANSYS CFX Release R2019, utilizing the periodic symmetry of the turbine and solving in the frequency plane. This model has been available since Release 18, but at the time only applicable for blade flutter simulations. It has since seen continuous improvement.

Existing experimental data together with CFD simulations on the same geometry and operating points are used for data validation. The latter include three-dimensional transient simulations of a full-wheel turbine model with spiral casing (also called volute or distributor), guide vanes, runner, and draft tube. The mesh consists of about 42 million nodes leading to extensive simulation times before reaching a periodic state. This simulation is referenced as Base Case.

2. Reference Data

In the following section, reference data used to validate the reduced models will be presented. This includes both experimental and numerical assessments and has been taken from existing investigations.

2.1 Experimental Validation Data

As presented in [4], an overview of the experimental setup is shown in Fig. 1. The runner is a modified model of the turbine previously installed at the Tokke power plant in Norway and is used at Norwegian University of Science and Technology (NTNU) for research on pressure pulsations inside high head Francis turbines. Moreover, the runner is a so-called splitter design and consists of 15+15 blades and the distribution unit of 28 guide vanes and 14 stay vanes. To perform the measurements and capture the propagation of the pressure pulses, five pressure sensors were positioned in the middle of two of the runner channels. This is shown in Fig. 2.

With the present setup combined with a runner speed of 5.54Hz, the predominant frequencies seen in this test rig become the guide vane passing at 155Hz and the blade passing at 166Hz. In addition to the RSI frequencies the system will be subjected to additional phenomena such as draft tube pulsations (Rheingans frequency), vortex shedding and elastic fluctuations in the waterway when going outside of BEP. These are included in the experimental results but are not part of the scope.

The operating point of primary interest in the present study is BEP performed at a head of 11.94m and flow rate equal 0.2m³/s. It is referred [4] for further details on this and other load conditions.

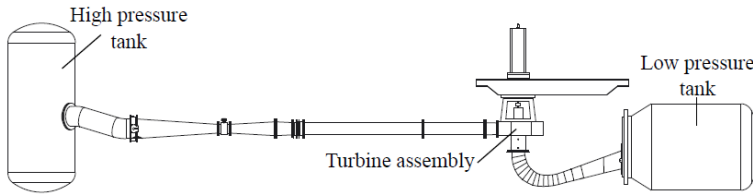


Fig. 1 Overview of measurement setup

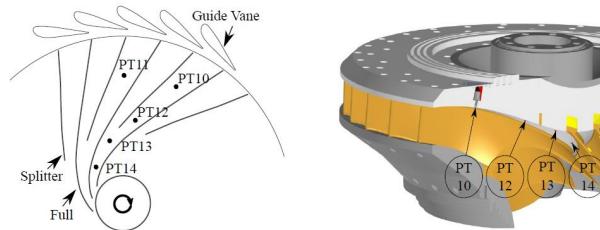


Fig. 2 Position of hub mounted pressure sensors in runner channels

2.2 Numerical Validation Data

Mimicking the setup of the model measurements, CFD simulations of the full-wheel model have been presented in [5] and [6]. Referred to as Base Case in the present paper, the results from these analyses are used as numerical validation data for the reduced models, both in terms of accuracy and computational speed. The simulations are transient utilizing a sliding mesh interface between the runner and volute (rotor/stator). However, extensive CPU requirements from the size of the mesh in combination with small time steps lead to simulation times that are totally unrealistic in terms in an industry time frame.

A mesh independent solution consisting of approx. 42 million nodes has been utilized, where the volute consists of mesh with tetrahedral elements (size), while the runner and draft tube are generated with hexahedral elements (size). The industry standard k- ω SST turbulence model has been applied for all simulations with the boundary conditions as shown in Fig. 3. Performed in ANSYS CFX, the simulations were run for three revolutions after steady periodic flow behavior had been achieved. Three distinct operating points were considered, however, only BEP will be presented here.

In general, the full-wheel results agree very well with the experimental data discussed in the previous section. For BEP, this is exemplified through global parameters in Table 1 and the corresponding pressure signal in PT10 in Fig. 4. The second harmonic is

clearly underpredicted, which in recent studies has been shown to be due to resonance effects occurring at the double RSI frequency in the experiments [7]. Obviously, a very interesting topic in itself, but outside the scope of the present report.

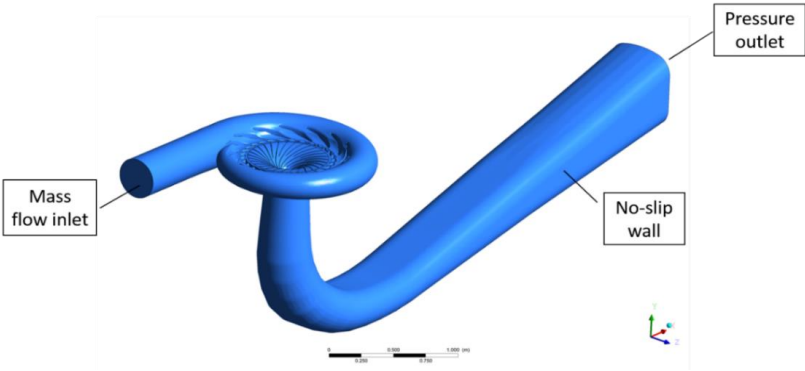


Fig. 3 Position of hub mounted pressure sensors in runner channels (Base Case)

Table 1 Global parameters for full-wheel simulation (Base Case) and experiments at BEP [5].

Case	Net head [m]	Torque to generator [Nm]	Inlet pressure [kPa]	Outlet pressure [kPa]	Hydraulic efficiency [%]
Experiment	11.94	620.7	215.6	111.1	92.2
CFD transient	12.08	640.8	218.4	111.8	94.1
Deviation	1.17%	3.24%	1.30%	0.63%	2.06%

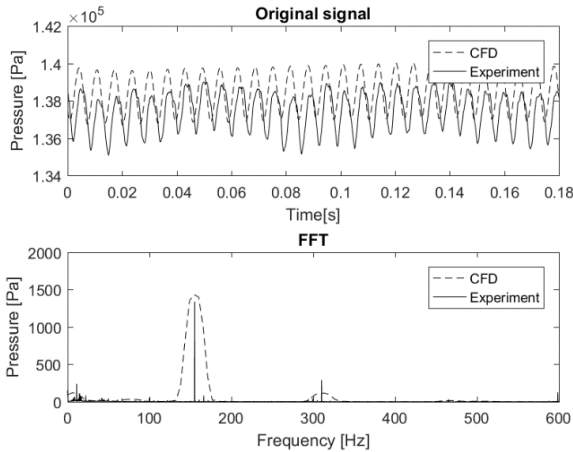


Fig. 4. Pressure signal in PT10 at BEP for full-wheel simulation and experiments [5].

3. Reduced Models

When specific features such as RSI is the primary focus, this section compares different approaches to reduce the overall computational time on the high head Francis turbine. Two main procedures will be discussed:

- 1) Reducing the total number of elements in the full-wheel model directly by leaving out parts of the volute or the draft tube domain. Note that this will also retain a solution space outside the RSI pressure pulsations.
- 2) Utilizing the rotational symmetry of the Francis turbine through different passage models available in ANSYS CFX. Only the Harmonic Analysis (HA) method is included here, while [1] also discusses the Profile Transformation (PT) and Fourier Transformation (FT) methods.

The experimental and numerical investigations presented in the previous two subsections are used as validation data.

3.1 Reducing Full-Wheel Model

The effects of removing the volute or draft tube have been investigated in the following, including one case combining both (ref. Combined). Fig. 1 shows the resulting computational domains. Same boundary conditions as for the Base Case have been used for all cases, except for the no volute/combined inlet condition for which velocity vectors have been specified at the slightly extended guide vane passage (see Fig. 2). The velocity direction was determined from the stay vane angle, which is independent of the operating point.

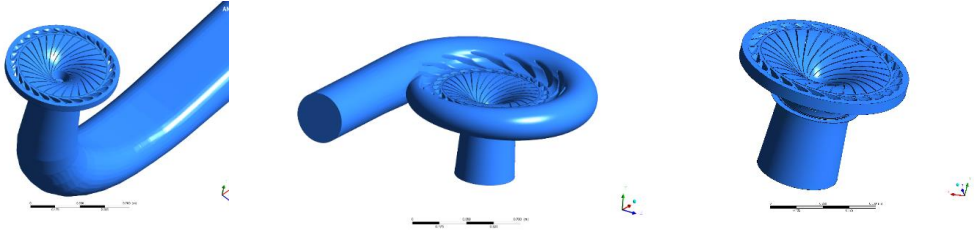


Fig. 1 Computational domain of reduced full-wheel models. Left: No volute, middle: Short Draft Tube, right: Combined

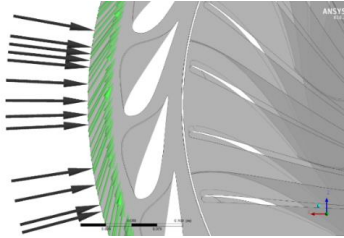


Fig. 2 Constant velocity profile at inlet

Fig. 3 shows streamlines for all three cases and Fig. 4 and Fig. 5 give the pressure signals and corresponding FFT plots from the PT10 probe onboard the runner (see definition of sensor location in [4]). Clearly, none of the separate full-wheel model reductions affect the results to any significant degree relative to Base Case as both the pressure amplitudes and the pulsation frequencies match well. This is also true for the combined case. Although insignificant, it is interesting to note that the No Volute case produce a slightly higher pressure amplitude and the Short Draft Tube case sees a somewhat higher average pressure signal. These effects can be explained by the strictly uniform velocity profile substituting an otherwise periodic inlet condition and the outlet pressure condition being much closer to the measurement locations for the respective cases. The Combined case sees both effects accordingly. If desired, the small differences seen can easily be reduced further by for instance adjusting the outlet condition at that location due to the shorter draft tube giving a lower pressure reduction from the runner to the outlet. This is demonstrated in the error plot in Fig. 6 where a step-wise adjusted outlet pressure reduces the average pressure measured in P10 towards the values obtained in the full-wheel Base Case. From estimates using the Bernoulli equation, the pressure reduction in Combined DP3 corresponds roughly to the pressure drop in the section of the draft tube that was cut away. This is calculated from only knowing the mass flow and areas at the respective boundaries. Hydrostatic pressure difference has not been accounted for.

By following the above procedure, one will obtain very accurate results compared to a full-wheel case (0.04% from Base Case) and at a much lower cost, but without the need of prior knowledge to the flow behavior, e.g. no interpolation at inlet boundary of existing pressure field. All the flow frequencies in the runner domain have also been retained. A more accurate inlet condition can be obtained by for instance assuming a sinusoidal periodic velocity profile with number of periods depending on the stay vane configuration. This is expected to reduce the pressure amplitude at the measurement location (see No Volute in Fig. 4). Noticeably,

this is also information that can be gained prior to performing any simulations. Testing of the latter has been left for future work.

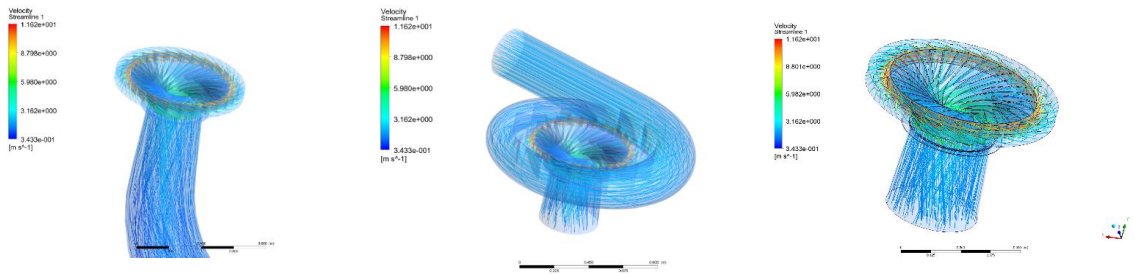


Fig. 3 Streamlines on reduced model. Left: No volute, middle: Short Draft Tube, right: Combined

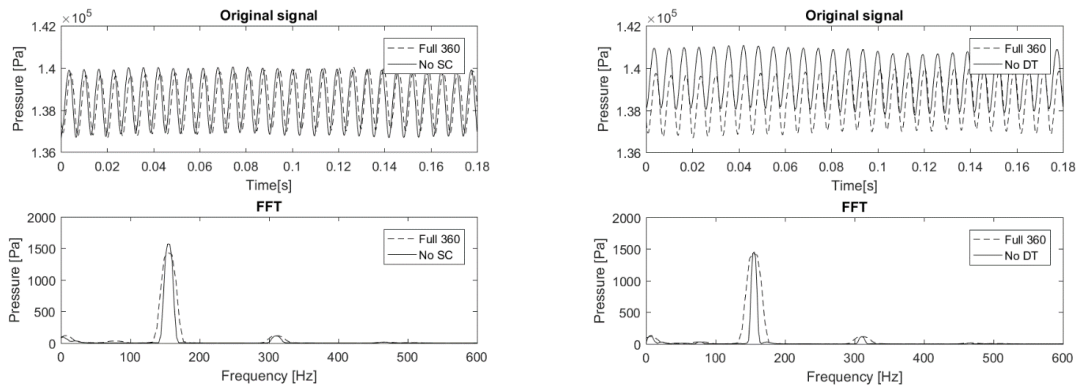


Fig. 4 PT10 pressure signal. Left: No Volute, right: Short Draft Tube

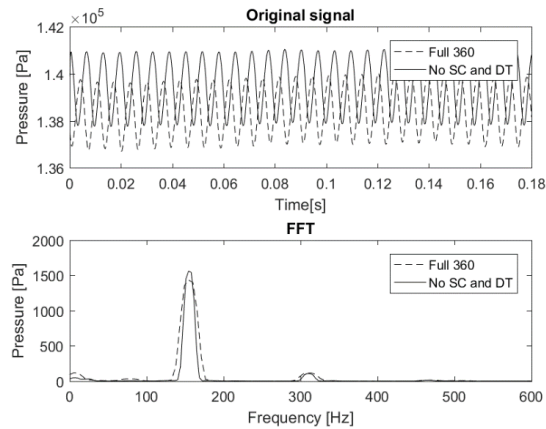


Fig. 5 PT10 pressure signal for Combined at BEP

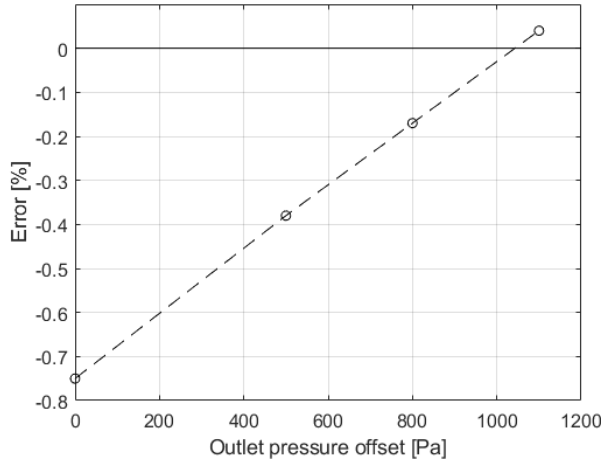


Fig. 6 Absolute pressure in probe P10 with outlet reduction

Speed up

Table 2 summarizes the node count for the Base Case and the three modified cases for the full-wheel reductions together with relative speed up for each case normalized by number of time steps and compute cores. Comparing the No Volute and Short Draft Tube cases, most is gained by excluding the draft tube leading to a node reduction of 44%. And obviously, combining both effects results in the highest speed up of all cases. Nevertheless, all reductions show a close to linear speed-up with respect to mesh size and as discussed in section 3.1 only minor effects on the results were experienced by performing these simplifications. A more time efficient meshing procedure can also be expected, especially for the No Volute and Combined cases for which the meshing of the spiral casing has now been made redundant.

Despite the lower speed-up than would be achieved using a transient blade row method [1], no initial conditions are required to meet the same level of accuracy, and the full frequency content of the flow field is retained when moving from the Base Case to the simplified solutions.

Table 2 Speed-up of reduced models

	Global Number of Nodes	Mesh size factor	Relative speedup [-]
Base Case	42476565	1	1
No Volute	36021993	1.18	1.2
Short Draft Tube	23822372	1.78	1.7
Combined	17367800	2.45	2.2

3.2 Harmonic Analysis

The turbine runner is rotationally symmetric and significant speed-up can be achieved by simulating only a section of the geometry when utilizing the periodic nature of the flow, so-called passage modelling (see Fig. 7). Challenges arise, however, when the number of stator and rotor components are not equal. [1] discusses some of the general theory behind passage modelling and presents results for the PT and FT methods applied to the same high head Francis turbine as used here. Results for the Frozen Gust (FG) approach has been replicated in Fig. 8. The latter is an alternative to FT where only the runner passage is included in the simulation and the inlet conditions are applied directly upstream of the runner. While these are time marching schemes, however, the Harmonic Analysis (HA) method solves the system in the frequency domain converging on a steady state solution.

A brief introduction to the HA theory is presented below followed by a review of the simulation results.

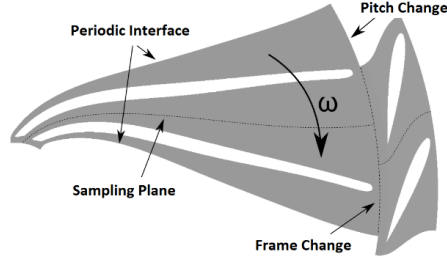


Fig. 7 Definition of boundary conditions and pitch change [1]

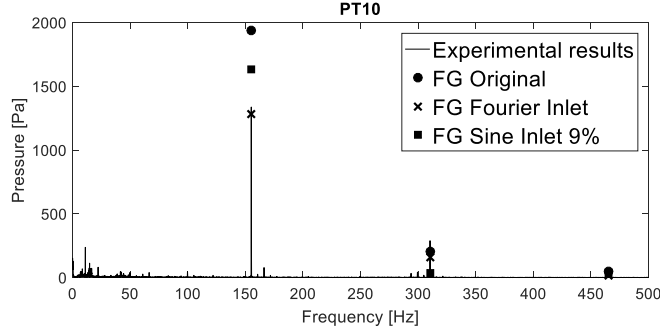


Fig. 8 PT10 spectral content for Frozen Gust with different inlet conditions [1]

General theory

In cases where the solution to the Navier-Stokes equations are assumed to be transient and periodic, solving in time can be a very inefficient method. Temporal periodicity can be described as:

$$Q(x; y; z; t) = Q(x; y; z; t + T) \quad (1)$$

where Q is some conserved variable (momentum in the incompressible NS), and T is the period of oscillation, $T = 1/f$. With the presence of a spatial periodicity as well, such as a cascading runner blade, this can be expressed as:

$$Q(x; y + \rho; z; t) = Q(x; y; z; t + T) \quad (2)$$

where ρ is a spatial shift, and only variation in y -direction is considered for simplicity. In cases where the above is valid, a harmonic solution method can be applied to converge the flow solution to a steady-periodic state faster than for a true time marching scheme. The reason is easily seen from eq. (1), where it is clear that the only time interval of interest is $t = T$. If a solution is given for the interval T , this solution will by equation 1 repeat itself in infinitum. If a solution is sought using a time stepping manner, however, reaching this periodic state might take a very long time, as initial transient effects often require several oscillatory periods to dissipate. Looking at the simplest harmonic solution, $Q = A \cdot \sin(\omega t)$, we see that the two parameters of interest is the amplitude, A , and the frequency, ω . Extracting this will require a long time series to reach sufficient accuracy, and the matter will be even more complicated if the solution assumes the form of a more general harmonic solution, such as $Q = \sum_n a_n \cos(\omega n t) + b_n \sin(\omega n t)$, for which the time step has to be small enough to resolve all frequencies present. A remedy against costly simulations is then to solve the system of equations in the frequency plane.

A review of different implementations of the idea presented above in [8]. In short, the conservation variables in the Navier-Stokes equation are expressed as a Fourier series, and then substituted into the governing equations. The Fourier coefficients are balanced, and the result is a set of algebraic equations that are solved using a steady solver, driving a pseudo time derivative term to zero. A time-spectral form of the harmonic balance method, where the solution is stored at a number of time instances during one time period, is the method used in ANSYS [9]. This is called Harmonic Analysis, where M harmonics are retained in the Fourier series and the unsteady period is divided into $N = (2M + 1)$ time levels. A pseudo-time marching approach is used to solve the N time level coupled equations.

More complex transient flow features require a greater number of harmonics to be specified. Obviously, this comes at the cost of reduced efficiency compared to a true transient simulation. Also, for fast simulations the pseudo time steps per period must be kept as low as possible, although within limits of convergence. The main drawback of using Harmonic Analyses, however, is that the solution contains only the frequency associated with targeted fundamental frequencies, such as the blade passing frequency and retained harmonics. The rest is filtered out. In a time-marching method, on the other hand, the flow solution typically sees a large frequency content and captures most of the flow characteristics.

In this work, manual Fourier coefficient sampling was implemented in the full-wheel simulation to extract the true periodic nature at the RSI interface. The profile was then reconstructed at the inlet of the Frozen Gust simulation as a periodic inlet boundary condition (FG Fourier Inlet).

Results

In the following section, results obtained from simulations with the Harmonic Analysis method available in ANSYS CFX Release R2019 are presented. Today, HA is not compatible with using mixing plane interface between runner and draft tube as applied in [1]. Therefore, the present geometry sees an elongated runner forming a passage of the draft tube. In that way, no draft tube/runner interface is required. The runner and boundary conditions are the same as previously discussed, except for the inlet condition as seen (see Fig. 9). Here, a pressure field has been mapped on to the RSI interface on the new geometry through Fourier coefficients sampled from Base Case (full-wheel). This ensures the true periodic nature of the flow to be represented at the interface and allows for leaving out the guide vanes as well for further mesh reduction. But it does indeed require results from a previous simulation.

The mesh has been acquired through the Francis-99 project [10] and consists of approximately 2 million nodes. The main goal of these simulations is to document how well the HA method handles a high head Francis case in terms of accuracy and increased computational speed. In general, passage models, including Harmonic Analysis, performs better for machines with a high number of blades/passages and multiple stages, such as for an axial compressor.

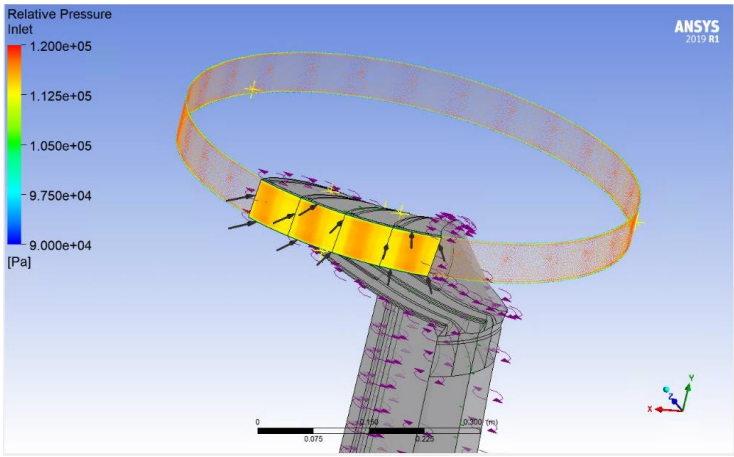


Fig. 9 Pressure interpolation through Fourier coefficients

An overview of the simulation cases investigated is presented in Table 3, where M is the number of retained harmonics and TSPP is the pseudo-time steps discussed in the theory section. The physical timescale applied in the simulations then becomes:

$$dt = \frac{1}{TSPP \cdot TF} \text{ [s]}$$

where TF is the targeted fundamental frequency in the system, in this case the blade passing frequency equal to 155 [Hz]. In theory, the relatively simple flow case requires only few retained harmonics, but the results also reveal that the solutions actually become unstable for M higher than one (see Fig. 10). And as indicated in Table 3, the same is true for TSPP less than 90. Comparing the average absolute pressure in P10 for HA2 and HA3, however, close agreement with the Base Case is seen. Fig. 11 presents the convergence behavior for the two cases.

The above simulations were started from scratch, i.e. with no initial results file, and the solutions converged after approximately 1800 iterations, equaling about 5 hours wall clock time on 72 CPUs.

Table 3 HA simulations cases with P10 results

Case	M	TSPP	P10 [Pa]
Base Case	-	-	13845
HA1	1	60	<i>Not converged</i>
HA2	1	90	13987
HA3	1	120	13984
HA4	3	90	<i>Not converged</i>
HA5	5	90	<i>Not converged</i>

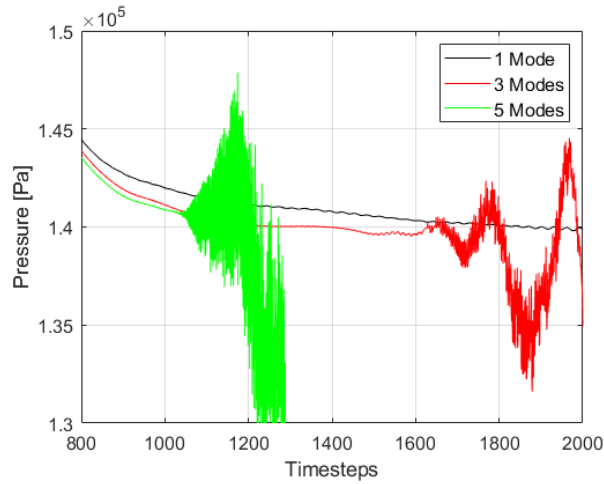


Fig. 10 HA diverging for higher modes

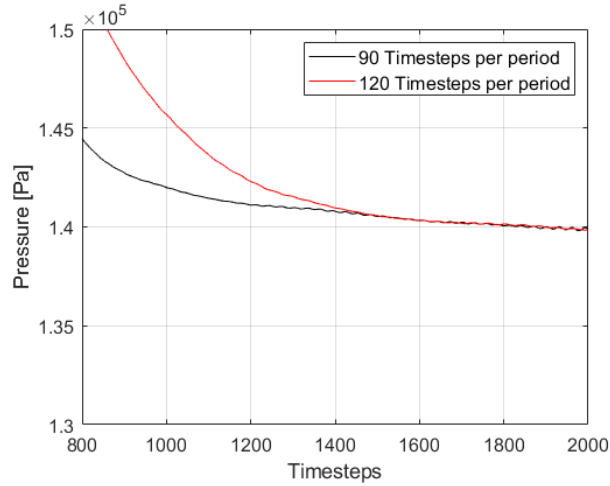


Fig. 11 Convergence for the P10 pressure probe

4. Conclusion

The main purpose of this investigation has been to reduce computational time without compromising on accuracy. Thus, adapting to an industry time frame when designing high head Francis turbines. The focus of the work has been on the RSI pressure in specific locations of the Tokke runner as defined by an experimental setup performed at NTNU.

The paper shows how a full-wheel simulation model of a high head Francis turbine can be reduced directly without losing accuracy in the RSI pressure that is of primary interest. The reduction is achieved by: 1) Reducing the draft tube and 2) Excluding the distributor except for the guide vanes. Consequently, great savings in mesh size and computational time is gained. This has been applied both on separate models as well as combining them, obtaining an ultimate mesh reduction of about 60% and a relative speed-up factor equal 2.2. A nearly linear speed-up with mesh size was achieved for all cases. Noticeably, with this method all flow frequencies in the runner are retained.

Simulations performed with the passage model called Harmonic Analysis are also included, solving in the frequency plane rather than utilizing a traditional time-stepping procedure. Although somewhat unstable for increasing number of retained harmonics, convergence was obtained in the matter of hours compared to days for the previous method. However, only results for the targeted flow frequency (RSI) is then available.

In general, reducing the draft tube will lead to the greatest reduction in computational mesh due to the vast number of elements being contained there, but modifying the distributor will also simplify the meshing procedure and consequently reduce the time needed for mesh generation. Despite a moderate speed-up compared to the passage models, the reduction of the full-wheel model does not lose any of the frequency content in the flow during this process. This is an essential aspect in describing the high level of accuracy that has been achieved. It is also shown that the entire volute could be replaced by a very simple set of inlet boundary conditions without affecting the results to any significant degree.

Acknowledgments

Our acknowledgements go to NTNU, the Norwegian Hydropower Centre and the rest of the staff working at the HiFrancis project.

Nomenclature

<i>BEP</i>	Best Efficiency Point	<i>CFD</i>	Computational Fluid Dynamics
<i>TF</i>	Targeted Frequency [Hz]	<i>HA</i>	Harmonic Analysis
<i>M</i>	Retained Harmonics [-]	<i>TSSP</i>	Pseudo time-step [-]
<i>NTNU</i>	Norwegian University of Science and Technology		

References

- [1] Jakobsen, K. R. G., Tengs, E., and Holst, M. Aa., 2018, "Reducing Computational Effort of High Head Francis Turbines," 29th IAHR Symposium on Hydraulic Machinery and Systems, Kyoto.
- [2] Seidel, U., Hübner, B., Löfflad, J., and Faigle, P., 2012, "Evaluation of RSI-induced stresses in Francis runners," 26th IAHR Symposium on Hydraulic Machinery and Systems, Beijing.
- [3] Trivedi, C., Cervantes, M. J., and Dahlhaug, O. G., 2016, "Numerical techniques applied to hydraulic turbines: A perspective review," *Applied Mechanics Reviews*, Vol. 68, 010802-010802-18.
- [4] Agnalt, E., 2016, "Pressure measurements inside a Francis turbine runner," Master's thesis, Department of Energy and Process Engineering, Norwegian University of Science and Technology, Trondheim, Norway.
- [5] Jakobsen, K. R. G., and Holst, M. Aa., 2017, "CFD simulations of transient load change on a high head Francis turbine," *J. Physics: Conference Series*, Vol. 782.
- [6] Jakobsen, K. R. G., 2018, "EDR&Medeso AS Recommended Practice HiFrancis WP3.1," HiFrancis Project.
- [7] Agnalt, E., Østby, P., Solemslie, B. W., and Dahlhaug, O. G., 2018, "Experimental Study of a Low-Specific Speed Francis Model Runner during Resonance," *Shock and Vibration*, Vol. 2018, Article ID 5796875, 12 pages.
- [8] Hall, K. C., 2013, "Harmonic balance methods applied to computational fluid dynamics problems," *International Journal of Computational Dynamics*, pp. 52-67.
- [9] Hall, K. C., Thomas, J. P., and Clark, W. S., 2002, "Computation of unsteady nonlinear flows in cascades using a harmonic balance technique," *AIAA journal*, pp. 879-886.
- [10] Norwegian Hydropower Centre, 2019, "Francis-99", <https://www.ntnu.edu/nvks/francis-99>.

Paper 10

An Experimental Investigation of the Hydrodynamic Damping of Vibrating Hydrofoils

Bergan, C. W., Tengs, E. O., Solemslie, B. W., Dahlhaug, O. G.

IOP Conference Series: Earth and Environmental Science, **240** 062008, 2019

An experimental investigation of the hydrodynamic damping of vibrating hydrofoils

C W Bergan¹, E O Tengs^{1,2}, B W Solemslie¹, and O G Dahlhaug¹

¹ NTNU Vannkraftlaboratoriet, 7491 Trondheim

² EDR & Medeso AS, NO-1337 Sandvika

E-mail: carl.w.bergan@ntnu.no

Abstract. As Francis turbines are chasing a higher efficiency, while trying to accommodate a wider load region, turbine blade fatigue is becoming a more pronounced problem. Details of the Fluid-Structure Interaction (FSI) between the turbine blades and the passing water is necessary to accurately predict the dynamic behavior of a runner in the design phase. The dynamic behavior of the turbine blades is characterized by three properties: The added mass of the surrounding water, the increased stiffness due to passing water, and the hydrodynamic damping provided by the surrounding water. Of the aforementioned properties, the hydrodynamic damping is not yet fully understood. When the turbine blades are excited close to resonance, the damping of the vibrating system determines the vibrational amplitude, and is therefore important in order to estimate the lifetime of a runner. The hydrodynamic damping of passing water has been investigated in a simplified setup, where the turbine blades are represented by a 2D hydrofoil. Two separate hydrofoil geometries have been tested. The hydrofoils were mounted in a “fixed-beam” configuration, meaning that both the deflection and the angle at the fastening point is zero. This setup was chosen, since it is the way that turbine blades are fastened in a Francis runner, and should therefore give applicable results when performing modal testing. The hydrofoils were mounted without any angle of attack, and exposed to water velocities up to 28 m/s. Modal tests in the entire velocity regime indicates that the damping factor increases linearly with water velocity, but at different rates below an above lock-in. The damping factor is rapidly increasing when the velocity goes beyond that of lock-in. This behavior is observed for both hydrofoils, even if the magnitude of the vortex shedding is of different magnitude for the two. A slight increase in natural frequency was also observed with increasing velocity, due to a combination of a stiffening effect of the water passing over the deflected blade, and a reduced added mass effect, in that the amount of water that vibrates with the hydrofoil is diminished when the water velocity is sufficiently high, i.e. it is blown away. The measurements have been compared with CFD simulations, indicating that the observed trend does indeed continue up to at least 45 m/s, indicating that the results are applicable to the velocity regimes occurring in a prototype Francis runner

1. Introduction

In the current energy market, Francis turbines are expected to deliver power at high efficiency while accommodating a large range of operation [1, 2]. This has caused several high head Francis runners to fail due to blade cracking, caused by Rotor-Stator Interaction (RSI) [3]. Fatigue damage due to vibration is a complex phenomena, with several factors: The static (mean) stress, the amplitude of the vibration, and the frequency of vibration. Within this, the amplitude of vibration, and hence the amplitude of the stress, can determine whether a turbine will withstand



the load, or if it will fail during operation. It is therefore important to understand the underlying mechanics that determine the vibrational amplitudes in the RSI-caused vibrations.

A classic damped vibrating system with a single degree of freedom can be characterized by three key parameters: stiffness, mass and damping. If one considered the oscillating turbine blade as a classic damped vibrating system, these characteristics will be slightly modified, as the presence of flowing water adds to stiffness, mass and damping. These parameters have been extensively investigated, and the impact of water on the stiffness and mass is well understood [4, 5, 6, 7]. The effect on damping has received less attention in the past, but recent studies have been conducted, indicating that the damping is indeed affected by the moving water. The damping is a critical quantity to understand, as the vibration amplitude is sensitive to damping at resonance. Some investigations of this have been performed in recent years, but they are limited in the velocity range investigated. In addition, the behavior of fluid damping in the velocity range where the blade's natural frequency coincides with the shedding frequency, known as lock-in, has not been a point of focus.

This paper presents experimental results on two separate hydrofoils, and a comparison is made between the results and simulation efforts.

2. Materials and Methods

The experimental setup and data analysis methods are described in the following section. The numerical setup is briefly explained, for an in-depth description, see [8].

2.1. Experimental Setup

The experiments were conducted at the Waterpower Laboratory at the Norwegian University of Science and Technology (NTNU). The test set-up consisted of a 150 mm by 150 mm square channel, containing the hydrofoil in a fixed-beam configuration, i.e. fastened in both ends. An image of the test rig is shown in Figure 1



Figure 1. Image of the test rig.

The hydrofoils tested are illustrated in Figure 2. They are of the same width and cord length, but F0 has an asymmetric trailing edge, and a more blunt leading edge than F1 .

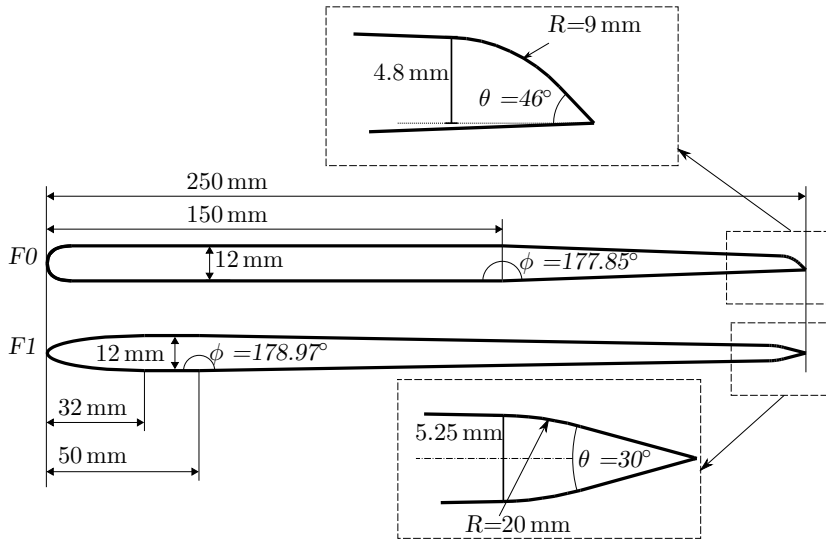


Figure 2. Hydrofoil geometries tested. Note that the tapering is much longer for F1 than for F0, allowing for a much smoother tapering angle, ϕ . In addition, F0 has an asymmetric trailing edge, while F1 has a symmetric trailing edge. The leading edge of F0 closely resembles a semicircle with diameter equal to the foil thickness, whereas the leading edge of F1 is elliptic with major and minor diameter of 62 mm and 12 mm respectively.

The excitation was performed using Piezoelectric Macrofiber Composites (MFCs), which have the ability to provide excitation at specific frequencies, enabling measurements when the damping is quite large. This procedure is based on the approach previously employed by Coutu et al, Yao et al, and Roth et al [4, 9, 10, 5, 6], and the MFCs are similarly excited 180° out of phase, in order to obtain the maximum excitation force. For a more in-depth explanation on the application of MFCs in conjunction with modal testing of hydrofoils, the reader is referred to the work of Seely et al [10]. The response was measured with a combination of Laser Doppler Vibrometry (LDV) and semiconductor strain gauges from Kulite. A schematic of the test setup is shown in Figure 3. The tests were performed in cavitation-free conditions.

2.1.1. Testing procedure In order to avoid transient effects, a stepped-sine excitation pattern was chosen, as recommended by Ewins [11]. The testing therefore consisted of

- (i) performing a continuous sweep, to identify the natural frequency
- (ii) generating discrete sine waves around the resonant region
- (iii) testing the response of each frequency

This process was repeated approx. 30 times for each velocity in order to estimate the uncertainty in both natural frequency and damping.

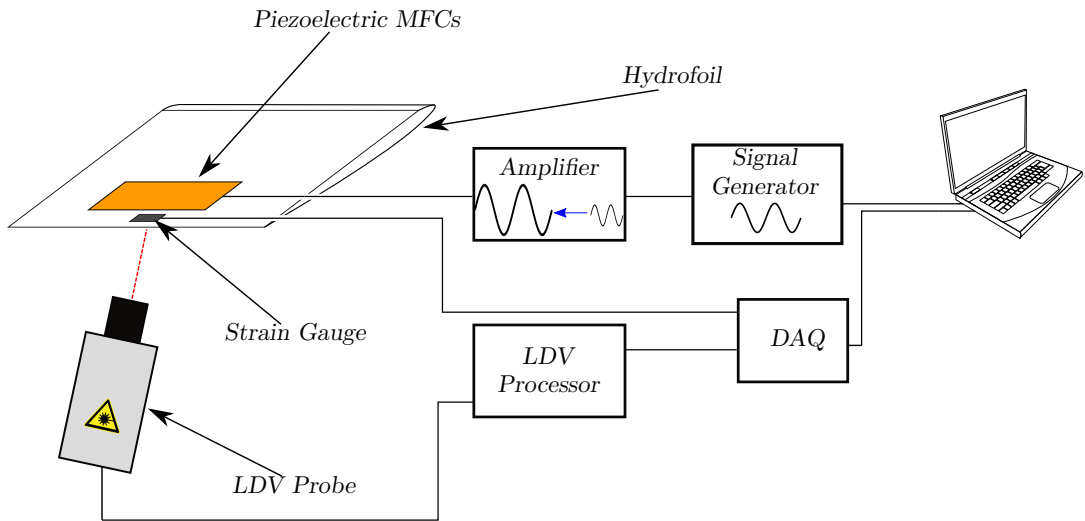


Figure 3. Schematic view of the measurement setup.

2.1.2. Analysis The amplitudes of both the excitation and response were calculated using the Welch method as implemented by MATLAB. The Welch method is an estimate of the power spectrum, which reduces the noise by reducing the frequency resolution through overlapping windows. For the amplitude estimates, the flattop window was chosen. Since the Welch method in MATLAB does not yield phase data, the phase difference between the excitation and response was estimated by calculating the cross-power spectral density. The magnitude ratio between the excitation and response, along with the phase difference was used to recreate the complex Frequency Response Function (FRF), which was used to calculate damping and natural frequency, using the nyquist diagram. By plotting the real part vs. the imaginary part of the FRF, a resonant region will appear as a circle. By curve fitting the data to a circle, geometric properties of the curve fit can be used to accurately estimate modal properties. This method was chosen, since it does not rely on data far away from the resonant region, and is therefore less sensitive to neighbouring modes of vibration. For a detailed explanation of the circle-fit method and the Nyquist diagram, the reader is referred to Ewins [11], and Bergan et al [12].

2.2. Numerical setup

The damping of F1 has been tested numerically using ANSYS CFX. To ensure fully developed flow conditions in the test section, the inlet of the test domain was extended in order to satisfy a common entrance length criterion of $L > 10 \cdot D_h$. Similarly, the test domain was extended downstream to avoid outlet conditions affecting the simulation results. The damping was found using a one-way coupling, but investigating the structural response in advance, and performing CFD on the blade with pre-determined vibration. For a more in-depth explanation of the numerical setup and results, the reader is referred to [8].

3. Results

In Figure 4, the damping factor ζ is shown with respect to the water velocity w . Figure 6 shows the evolution of the natural frequency ω_n of the hydrofoils with respect to w . The slope estimates for the evolution of the damping are summarized in Table 1

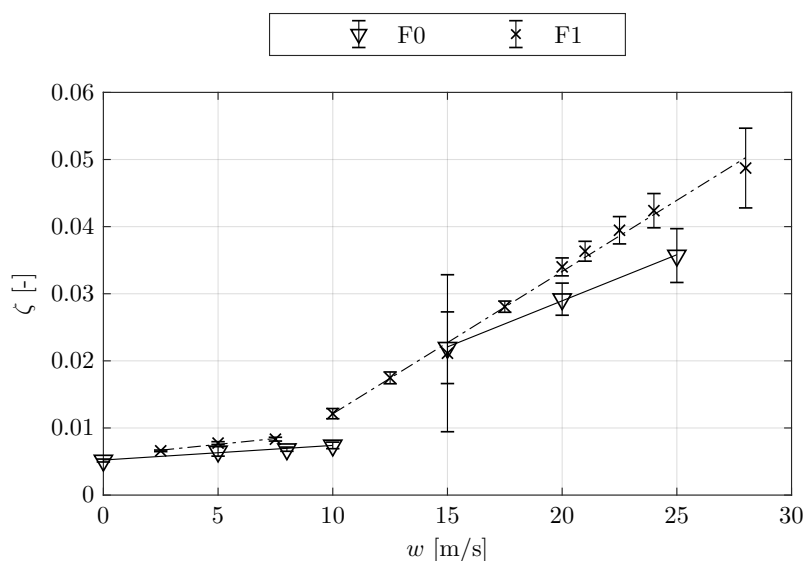


Figure 4. Damping vs velocity. Note that both hydrofoils exhibit a discontinuity in the slope around lock-in, at approx. 11 m/s for F0 , and at approx. 8 m/s for F1 .

Table 1. Slope of damping change vs. velocity

ζ/w	F0	F1
below lock-in	2.18×10^{-4}	3.48×10^{-4}
above lock-in	1.37×10^{-3}	2.12×10^{-3}

To give an idea of the numbers provided in table 1, the *Half-Amplitude* method is a useful tool [13]: A damping factor, ζ , of 0.01 (or 1%), means that oscillations will half in amplitude after 11 cycles, which for a hydrofoil with a natural frequency of 500 Hz is approx. 0.02 s.

The measurements are closely matched by the numeric simulations, shown in figure 5.

The experiments were limited to 28 m/s due to the onset of cavitation upstream the test section, even with a gauge pressure of 9 bar in the test section. Simulations were therefore conducted at 45 m/s, indicating that the trend obtained above lock-in continues.

As seen in Figure 4, the damping is nearly constant up to lock-in, but with a slightly positive slope. There is a distinct discontinuity, at approx. 11 m/s for F0 and at approx. 8 m/s for F1 . This is the lock-in region for each hydrofoil, the velocity at which the vortex shedding frequency coincides with the hydrofoil's natural frequency. This is detailed in table 2, where the maximum vibrational amplitudes are shown with and without MFC excitation. Vibration measured without MFC excitation is solely due to vortex shedding.

The natural frequency of the hydrofoils, as seen in Figure 6, seem to be relatively unaffected, but a closer investigation reveals a trend, see Figure 7.

Figure 7 shows that the natural frequency is not constant with velocity, it does in fact increase slightly with water velocity. F0 shows a sudden jump in natural frequency around lock-in, a

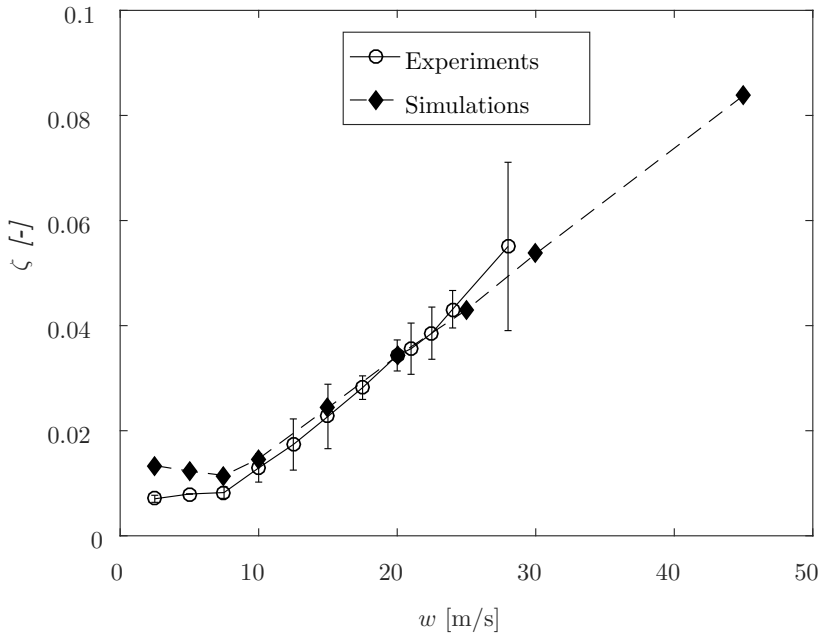


Figure 5. Experimental and numeric results for F1 . Note that both the experimental and numerical results indicate a change around the lock-in region (at 8 m/s), but they differ in the results below lock-in.

Table 2. Maximum Vibrational Amplitudes

Excitation Source	F0	F1
MFC	0.085 mm	0.125 mm
Vortex Shedding	0.013 42 mm	1.4×10^{-9} mm

behaviour that is not reflected in F1 . The order of increase seems to be quite similar as well, around a 0.1% increase for each m/s

The maximum vibrational amplitudes for F0 and F1 are shown in table 2. As the results indicate, the effect of vortex shedding is virtually non-existent for F1 , whereas the shedding-related vibrational amplitude for F0 is at approx. 16% of the maximum excited amplitude.

4. Discussion

The measurements were limited to 28 m/s due to cavitation, but the numerical analysis indicates that the trend is likely to continue at least up to 45 m/s, see figure 5. Given the similarities between the numerical and experimental results at velocities up to 28 m/s, there simulations performed at 45 m/s are most likely accurate.

At this stage, it is relevant to make comparison to other similar measurements, mainly those of Coutu et al [4], where a hydrofoil has been mounted in a fixed-beam configuration, and modal testing was done for velocities up to 25 m/s; and those of Yao et al [6], where the effect of the trailing edge shape was tested on a cantilever beam.

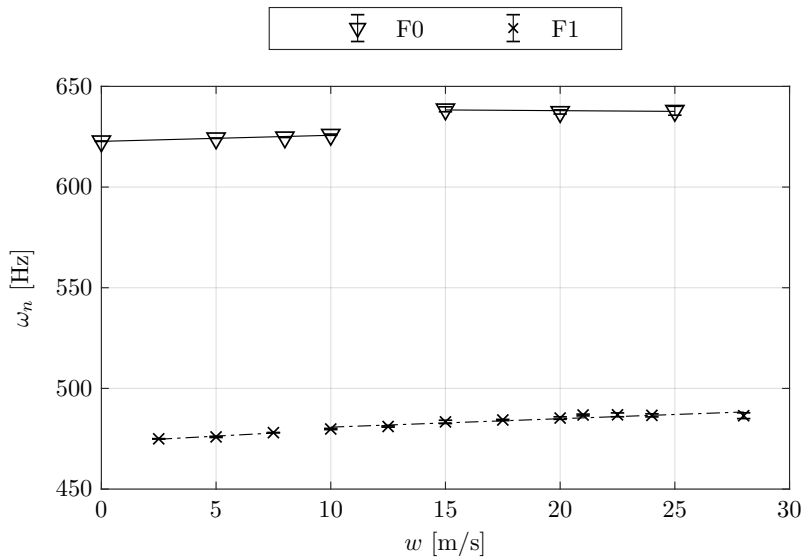


Figure 6. Natural Frequency. Note that there is a slight increase in natural frequency for both F0 and F1 .

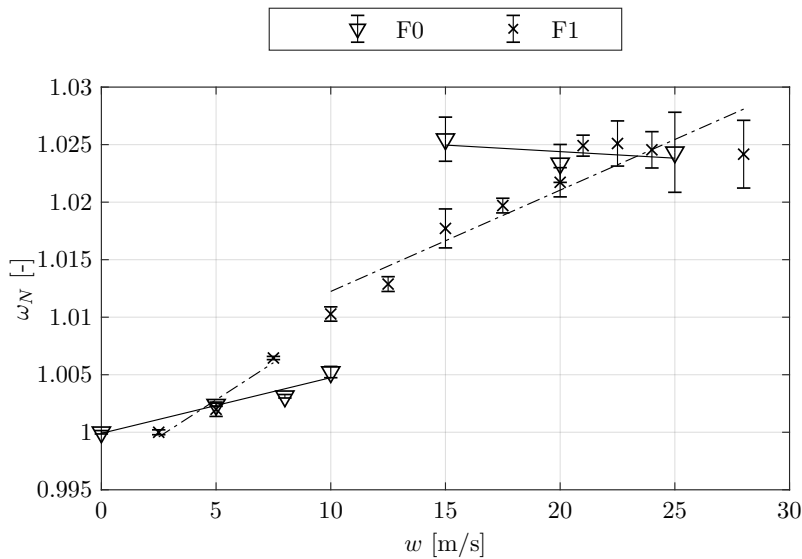


Figure 7. Normalized natural frequency. Note that both F1 and F0 appear to approach a constant value at 1.025.

Coutu et al found that the damping factor was consistently increasing with water velocity, without any discontinuities, but only above lock-in velocity. Comparing with Yao et al, a discontinuity in damping slope was observed at lock-in for the torsional bending mode, which for a cantilever beam is quite similar to the bending mode of a fixed-beam foil. Said discontinuity was observed at lock-in, which agrees very well with the trends observed in the present work.

In order to make a quantitative comparison to the results obtained by Yao et al, consider figure 8. Here, the damping is presented as a function of the *reduced velocity*, C^* , defined by Equation 1.

$$C^* = \frac{w}{L \cdot \omega_n} \quad (1)$$

As Figure 8 shows, the slope of the damping factor change is nearly identical for F0 and F1 when plotted against their reduced velocities. Compared with figure 9, it is clear that the observed damping behavior is similar in scale.

The slope of the damping change measured in the present work agree adequately with the measurements conducted by Yao et al, in which the slope of the damping was approx. 3.9×10^{-3} (when the velocity is expressed in absolute terms), as compared to approx. 2×10^{-3} obtained in this work. In the work of Coutu et al, the damping factor slope was found to be 1.07×10^{-2} to 1.23×10^{-2} , approx. 5 times higher than the results from this work. This result was fairly consistent for all the geometries tested by Coutu. Even if the geometry of the hydrofoils differ within each experiment, the dimensions for the test section remains.

Another key feature in the work of Yao is the apparent jump in natural frequency observed at lock-in, something that was also seen in the present measurements. Coutu et al found that the natural frequency remains constant, but CFD simulations performed by Nenneman et al [14] indicate that the natural frequency does indeed increase with velocity. The present results, and those of Yao, found that the natural frequency does change through the lock-in region, but there is no conclusive experimental evidence of further trends above lock-in. It could very well be the case that it is constant above lock-in.

Previous results have indicated that the phase shift in vortex shedding is the main contributor to the observed discontinuity in the evolution of the damping factor[12], but the present results contradict this. It is difficult to argue that the vortex shedding is the main contributor to the increase in damping when the same behavior is observed for both F0 and F1, even if the magnitude of the vortex shedding is quite different for the two test specimens.

The divergence in the present results, along with those of Coutu and Yao, raises the question of dimensionlessness: To what degree do we expect the damping factor to be dependent on the geometry and/or scale? Since the geometries in question differ, the proportion between the added mass and the blade stiffness is varying, which could cause different hydrodynamic behavior. It is also interesting to address the validity of the assumption of linearity in the vibrating system. Most theory regarding vibrating structures assume linearity, ie. spring force linearly proportional with displacement, damping force linearly proportional with velocity [13]. This may not be the case when the effects of FSI are prevailing[11]. There is lacking documentation on the effect of non-linearities in turbine blades, but the difference in scale between the prevailing experiments in this field suggest that the relative scale of the hydrofoil could be crucial to the expected rise in damping factor.

5. Conclusion

The present measurements show that the damping factor of a hydrofoil behaves differently above and below lock-in conditions, and the natural frequency is also affected by this. The two different test geometries indicate that a more slender blade might produce a lower natural frequency, having a reduced stiffness with the same oscillating mass, due to the larger relative

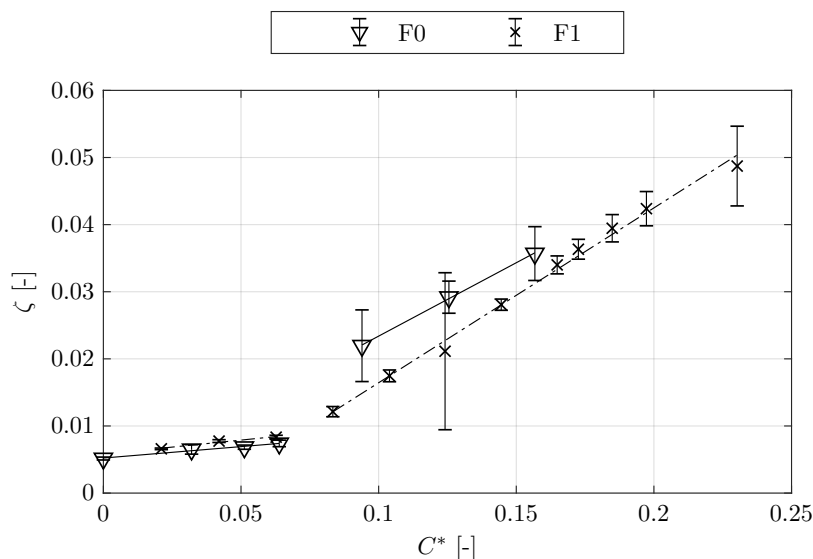


Figure 8. Damping vs reduced velocity.

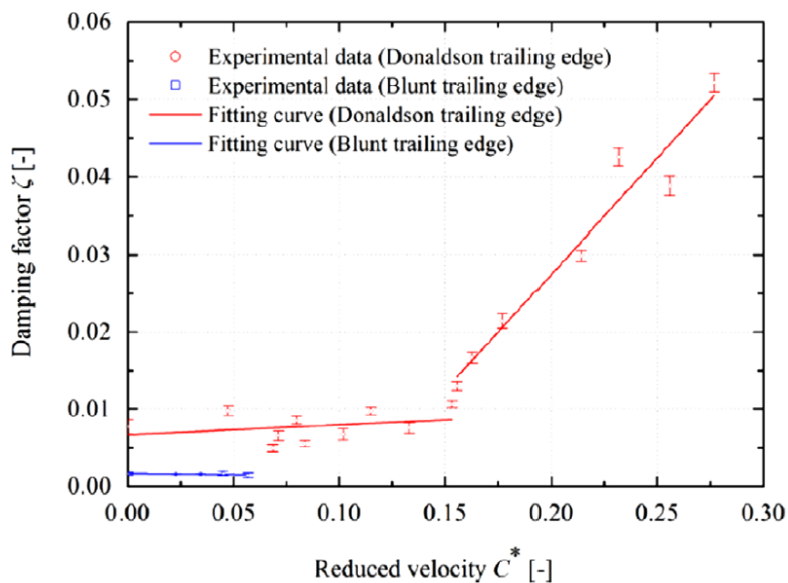


Figure 9. Measurements performed by Yao et al [6].

contribution from the water. Comparisons with similar experiments indicate that the increase in damping factor will be smaller for a stiffer hydrofoil, due to the reduced relative influence

of the fluid and the inherent non-linearities in a fluid-structure vibration. This could arguably be extended to encompass similar geometries of different scale, meaning that different types of turbines, with different relative blade thickness might have very different damping evolution with respect to the changing water velocities.

6. Further Work

Further investigations of damping behavior in submerged hydrofoils should include a thorough assessment of the linearity of the vibrating system. In addition, focus should be placed upon understanding the behavior of the natural frequency above lock-in, as the present measurements are inconclusive. Additionally, all the work performed on vibrating hydrofoils has focused on a single blade in vibration. Further measurements will encompass a multi-blade cascade, in order to capture influence from neighbouring blades.

7. Acknowledgements

The research was carried out as a part of HiFrancis, a high-head Francis turbine research program supported by the Norwegian Research Council, The Norwegian Hydropower industry, and the Norwegian Center for Hydropower.

References

- [1] Gagnon M and Thibault D 2015 *Proc. 6th IAHR International Meeting of the Workgroup on Cavitation and Dynamic Problems in Hydraulic Machinery and Systems*
- [2] Flores M, Urquiza G and Rodríguez J M 2012 *World J. Mech.* **2** 28–34
- [3] Trivedi C 2017 *Eng. Fail. Anal.* **77** 1 – 22
- [4] Coutu A, Seeley C, Monette C, Nennemann B and Marmont H 2012 *IOP Conf. Ser.: Earth Environ. Sci.* **15** 062060
- [5] Roth S, Calmon M, Farhat M, Münch C, Bjoern H and Avellan F 2009 *Proc. 3rd IAHR International Meeting of the Workgroup on Cavitation and Dynamic Problems in Hydraulic Machinery and Systems* **1** 253–260
- [6] Yao Z, Wang F, Dreyer M and Farhat M 2014 *J. Fluids Struct.* **51** 10. 189–198
- [7] Reese M C 2010 *Vibration and Damping of Hydrofoils in Uniform Flows* Master's thesis Pennsylvania State University
- [8] Tengs E O, Bergan C W, Jakobsen K R and Storli P T 2018 *Proc. 29th IAHR Symp. on Hydraulic Machinery and Systems (Kyoto) IAHR2018-033* (to be presented)
- [9] Monette C, Nennemann B, Seeley C, Coutu A and Marmont H 2014 *IOP Conf. Ser.: Earth Environ. Sci.* **22** 032044
- [10] Seeley C, Coutu A, Monette C, Nennemann B and Marmont H 2012 *Smart Mater. Struct.* **21** 035027
- [11] Ewins D J 2000 *Modal Testing: Theory, Practice, and Application* 2nd ed (*Mechanical engineering research studies* no 10) (Research Studies Press)
- [12] Bergan C W, Solemslie B W, Østby P and Dahlhaug O G 2018 *Int. J. Fluids Mach. Syst.* **11** 146–153
- [13] Craig R R, Kurdila A and Craig R R 2006 *Fundamentals of Structural Dynamics* 2nd ed (John Wiley)
- [14] Nennemann B, Monette C and Chamberland-Lauzon J 2016 *IOP Conf. Ser.: Earth Environ. Sci.* **49** 072006

Paper 11

Damping Measurements on a Multi-Blade Cascade with Multiple Degrees of Freedom

Bergan, C. W., Tengs, E. O., Østby, P.T., Solemslie, B. W., Dahlhaug, O. G.

Journal of Physics: Conference Series, **1296** 012003, 2019

Damping Measurements on a Multi-Blade Cascade with Multiple Degrees of Freedom: A Francis-99 Test Case

C W Bergan¹, E O Tengs^{1,2}, B W Solemslie¹, P Østby^{1,3}, and O G Dahlhaug¹

¹ NTNU Vannkraftlaboratoriet, 7491 Trondheim

² EDR & Medeso AS, NO-1337 Sandvika

³ Rainpower AS, NO-2027 Kjeller

E-mail: carl.w.bergan@ntnu.no

Abstract. Due to thinner blades and higher demands for flexibility, the high-head Francis runners designed today face considerable challenges that severely affect the runners' expected lifetime. For many high-head Francis runners, the leading cause of fatigue is blade cracking due to Rotor-Stator Interaction, which cause vibrations in the runner blades.

Accurate prediction of the vibration magnitudes in a turbine is paramount in designing a reliable Francis runner. The understanding of the interaction between the hydrodynamic forces and the internal stresses in the runner is not yet sufficient to make this prediction. Previous investigations have identified some key parameters that affect dynamic behaviour in water, such as added mass, as well as added stiffness and damping from moving water. These parameters affect the natural frequency and damping of a structure, which in the end will affect what vibrations magnitudes the runner will be subjected to for a given frequency of excitation. The behavior of these parameters have recently been investigated by several researchers, but the effect of neighboring blades is yet not understood.

A multi-blade cascade has been tested for four of its different modes of vibration. The results indicate that the slope of the damping with respect to the inverse Strouhal number is constant. This slope was found to be the same as for several single-blade tested performed, both in the same rig and in other works. The implication is that the product of added mass and mode shape does not change significantly.

1. Introduction

Evaluating the dynamic response of a Francis runner is becoming increasingly important, in order to avoid resonance with pressure pulsations induced by Rotor-Stator Interactions (RSI). In fact, resonance with RSI has been the cause of failure in several high head Francis runners in the past 15 years [1]. At the design stage, turbine designers need to analyze the levels of vibration a runner is expected to experience during operation, and in order to achieve this, a better understanding of the vibrating system that the runner and water comprises is needed.

A classic damped vibrating system with a single degree of freedom can be characterized by three key parameters: stiffness, mass and damping. If one considered the oscillating turbine blade as a such a system, these characteristics will be slightly modified, as the presence of flowing water adds to stiffness, mass and damping. These parameters have been extensively investigated, and the impact of added mass is well understood [2–5]. The effect on damping has received less attention in the past, but recent studies have been conducted, indicating that the damping is



indeed affected by the moving water. The damping is a critical quantity to understand, as the vibration amplitude is sensitive to damping at resonance. Recent papers have investigated the effect of water velocity on damping, and the general conclusion is that the damping increases with increasing water velocity. [2–4, 6] There is some indication that the damping and natural frequency undergo a change in the lock-in region [4, 6], and Computational Fluid Dynamics (CFD) results indicate that the damping increases linearly up to at least 45 m/s [7]. There are two key limitations with the investigations performed up to this point: They do not evaluate the effect of adjacent blades, and they only investigate a single mode of vibration. The aim of this paper is therefore to investigate the effect of the neighbouring blades, and to state whether or not it is sufficient to examine a single blade. Multiple modes of vibration of a multi-blade cascade will be evaluated, and comparisons will be made to similar works in the field.

2. Materials and Methods

The experimental setup and data analysis methods are described in the following section.

2.1. Experimental Setup

The experiments were conducted at the Waterpower Laboratory at the Norwegian University of Science and Technology (NTNU). The test set-up consisted of a 150 mm by 150 mm square channel, containing the hydrofoil in a fixed-beam configuration, i.e. fastened in both ends. The test rig itself is rigid, with steel walls of 25 mm thickness. This was done to minimize simulation errors resulting from the assumption of stiff walls.

The hydrofoil geometry is presented in Figure 1. The three hydrofoils are identical, and their centerlines are spaced 39 mm apart.

Blade 1 and 3 were excited to vibration using Piezoelectric Macrofiber Composites (MFCs). MFCs were chosen for their ability to excite vibration with direct frequency- and phase control, making them ideal for this test case. The use of MFCs in hydrofoil testing has been documented previously by Presas et al [9], and they have been successfully employed for hydrofoil experiments by multiple researchers [2–4, 6, 10, 11]. The response was measured with semiconductor strain gauges from Kulite at both the leading edge and the trailing edge, in order to be able to separate the vibration modes of a single blade. The tests were performed in cavitation-free conditions, for velocities up to 20 m/s.

2.2. Testing procedure

2.2.1. Mode shapes, damping and natural frequencies Preliminary simulations indicated that the system contains modes with blade 2 as a node. In order to be able to investigate modes, both with blade 2 moving and with blade 2 as a node, a preliminary measurement was performed with excitation at blade 3 only, in stationary water. The Frequency Response Functions (FRFs) from that sweep are shown in Figure 2.

The relative phase delay between the trailing edges and leading edges, along with the natural frequency, are used to identify the modes. The modes chosen for further investigation are shown in Figure 3, and outlined in Figure 2 as vertical dash-dot lines.

In order to get a more powerful response from the system, excitation was applied at both blade 1 and 3 simultaneously. M1, M2 and M3 are achieved by exciting blade 1 and 3 in phase, while M4 is achieved by exciting blade 1 and blade 3 with a phase delay of 180°.

For each water velocity, a preliminary continuous sweep was conducted to roughly locate the frequencies of the modes of interest. The modes were then further investigated using a classical *stepped-sine excitation*, as recommended by Ewins [12]. Each stepped-sine excitation was repeated 30 times to get statistical data to accurately calculate the damping and natural frequency for each mode.

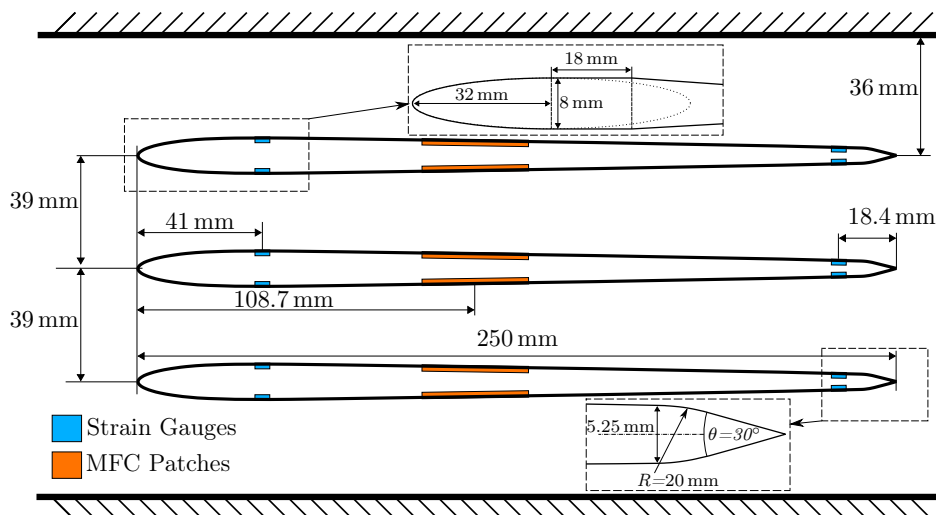


Figure 1: Blade cascade geometry. Note that the trailing edge is symmetric, and that there is a tapering of the hydrofoil, indicated in the detailed image of the leading edge. The choice in leading edge and trailing edge geometries is based on the setup previously employed in the same rig, with a single-blade configuration. [8]. The blade thickness has been reduced to 18mm, to counterbalance the increased "blocked area" imposed by multiple blades. The strain gauges were placed as close to the leading and trailing edges as possible while being situated in a flat area of the geometry, for practical reasons. The MFC placement was dictated by a minimum distance to the hydrofoil's center-line

2.2.2. Analysis The amplitudes of both the excitation and response were calculated using the Welch method as implemented by MATLAB. The Welch method is an estimate of the power spectrum, which reduces the noise by reducing the frequency resolution through overlapping windows. For the amplitude estimates, the flattop window was chosen, with 30 windows overlapping by 50%. The sample rate was 5120 S/s, and the measurement length was 14 000 samples. Since the Welch method in MATLAB does not yield phase data, the phase difference between the excitation and response was estimated by calculating the cross-power spectral density. The magnitude ratio between the excitation and response, along with the phase difference was used to recreate the complex FRF, which was used to calculate damping and natural frequency, using the Nyquist diagram. By plotting the real part vs. the imaginary part of the FRF, a resonant region will appear as a circle. By curve fitting the data to a circle, geometric properties of the curve fit can be used to accurately estimate modal properties. This method was chosen, since it does not rely on data far away from the resonant region, and is therefore less sensitive to neighbouring modes of vibration. For a detailed explanation of the circle-fit method and the Nyquist diagram, the reader is referred to Ewins [12], Craig and Kurdila [13], and Bergan et al [6].

3. Results and discussion

The resulting variations in damping are shown in Figure 4

Due to the low amplitude of vortex shedding, measurements without external excitation were unable to determine the velocity for lock-in. However, since the hydrofoil geometry is quite

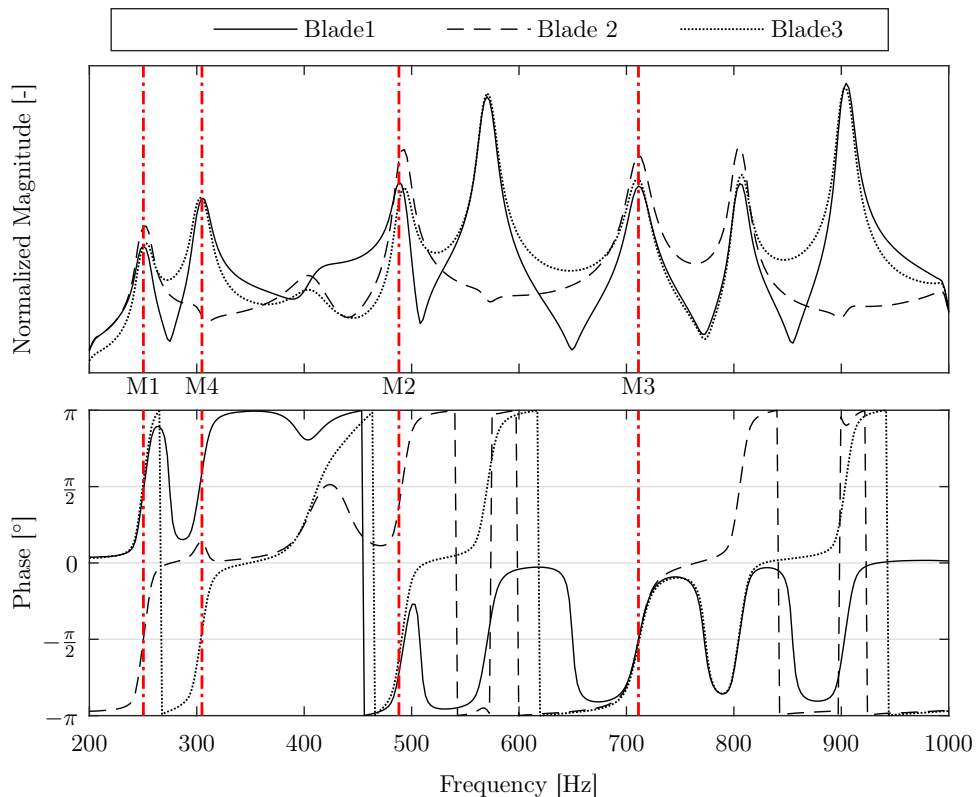


Figure 2: Bode plot for excitation at a single blade. The vertical dash-dot lines indicate the frequency of the modes investigated. Note that this is a preliminary and transient measurement, as such, the exact amplitudes of each mode is not accurate. This can be seen in particular for the amplitude of blade 2 around 310 Hz, 575 Hz, and 900 Hz. These are frequencies where blade 2 is a node, but in this transient measurement, the anti-resonance is swept through before blade 2 reaches zero amplitude. The bottom plot shows the phase delay between each blade and the excitation signal. Note that only trailing edge measurements are shown here.

similar to previous investigations in the same rig [8], the lock-in velocity is expected to be found at more or less the same velocity. Referring to Figure 4, it is evident that a change in the slope of the damping factor occurs at around 5 to 10 m/s, depending on which mode is investigated. This is due to the difference in natural frequency for the different vibrational modes, causing lock-in to occur at different velocities. According to Figure 4, we expect lock-in to occur in the order M1, M4, M2, M3. This corresponds to increasing natural frequency, see Figure 3.

Another interesting feature of Figure 4, is that M3 appears to have a much flatter slope than all the other modes. In order to make comparisons between the different modes, the reduced velocity is suggested as a dimensionless term. The reduced velocity is defined as the ratio between the time for a single vibration cycle, and the time for a particle to travel from the leading edge to the trailing edge. The formula is given in Equation (1)

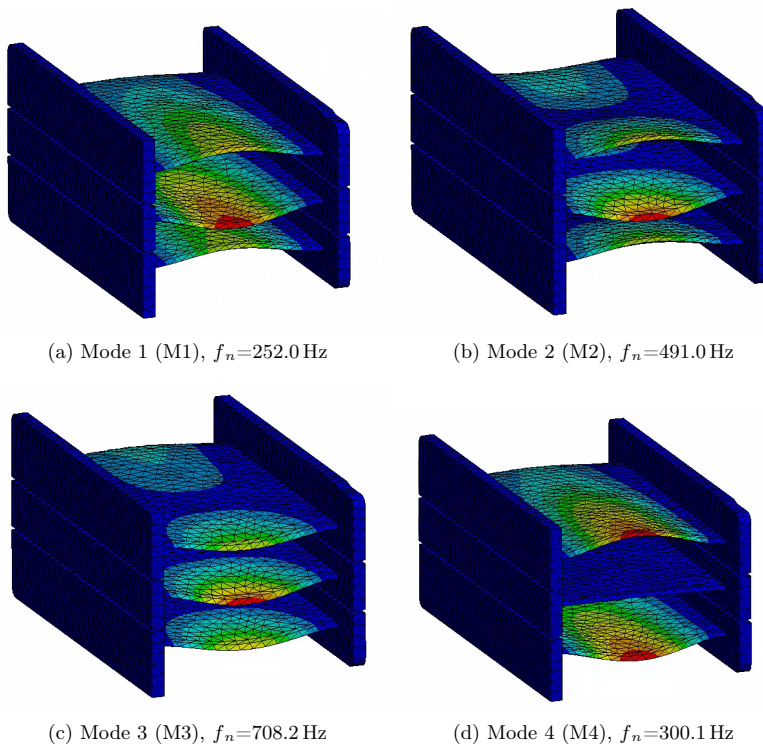


Figure 3: The four modes investigated. Note that the main difference between M1 and M2 is the phase between the leading and trailing edge. Also note that for M4, the middle blade is stationary.

$$v^* = \frac{v}{L \cdot f_n} \quad (1)$$

The reduced velocity is, in fact, the inverse of the Strouhal number, defined in Equation (2), but with the chord length in stead of the trailing edge thickness as the characteristic length.

$$St = \frac{fL}{v} \quad (2)$$

in Equation (2), St is the Strouhal number, f is the frequency, L is the "characteristic length", and v is the velocity.

If the results from Figure 4 are plotted against the inverse Strouhal number, the behavior of the different modes is much more similar, see Figure 5

Figure 5 shows that, for this particular test rig, the damping factor evolution is more or less the same for all the tested modes of vibration, when plotted against the inverse Strouhal number. This is an interesting result, indicating that some generalizations can be made. For comparison purposes, the experimental data of Coutu et al [2] has been manually read from the plot shown in Figure 6. Lacking information about the physical scales, the unit length has been omitted in the modified reduced velocity used in the comparison. This does not affect the internal similitude

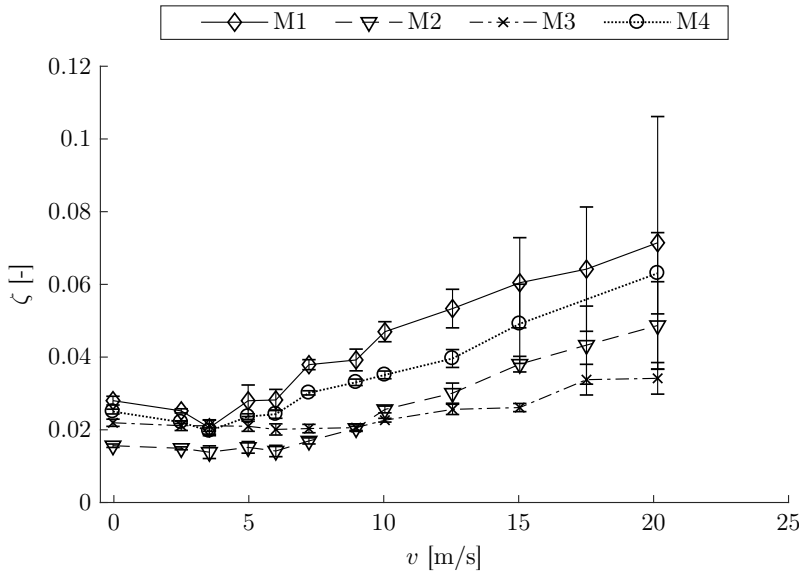


Figure 4: Damping vs velocity for the four modes investigated. Note that M3 deviates from the common pattern of the other modes, maintaining a nearly constant damping.

between the modes investigated in this paper, as the geometry, and hence the unit length, is unchanged throughout the experiment.

Figure 7 shows the damping plotted against the modified reduced velocity, defined by Equation (3)

$$v^{**} = \frac{v}{f_n} \quad (3)$$

As Figure 7 shows, the slopes for H0, H1 and H3 share the same similarity as before, but in the lower left corner of the graph, it is evident that the data obtained in this paper, combined with previous measurements in the same test rig [6–8], approximate the same slope. This is clearer when considering Figure 8, where the data for $v^{**} < 0.08$ is displayed.

The similarity in slope means that the actual damping of low-frequency vibrations increases at a higher rate than those of high-frequency vibration. However, this assertion is based on measurements performed at a limited selection of natural frequencies, and more data is needed for making an empirical generalization. In addition, this limitation in v^{**} investigated leaves some uncertainty to the slope, as Figure 8 shows, where the markers for F0 and M2 apparently follow a steeper curve. Nonetheless, not only do similar hydrofoil in the same rig approximate the same slope, different modes of a multi-bladed cascade approximate the same slope, as well as experiments performed in an entirely different test rig, with natural frequency an order of magnitude lower. As a simple test of this concept, CFD simulations were performed on one of the hydrofoils previously investigated in this test rig, denoted F1 in Figure 7. For details about the CFD setup, see Tengs et al [7]. The modified reduced velocity was altered by manually altering the hydrofoil's natural frequency in the numerical setup. The results of this simulation are shown in Figure 7.

If one were to interpret the physical meaning of the modified reduced velocity, $\frac{1}{f_n}$ is a measure

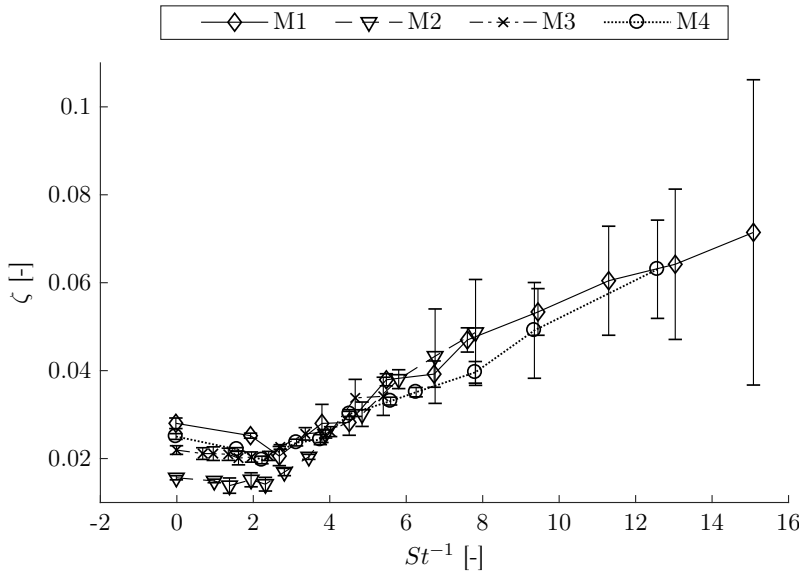


Figure 5: Damping plotted against the inverse Strouhal number. Note that all modes of vibration show a change in behavior around $St^{-1} = 2.5$. This is the lock-in region as discussed in Figure 4, meaning that the vortex shedding frequency is equal to the natural frequency. The relatively high value for St at lock-in indicates that the trailing edge thickness is not representative for the wake thickness for this geometry.

of time, namely the time per cycle of vibration, and v is a measure of how much water passes the blade per unit time. In that regard, v^{**} is a measure of how much water passes the trailing edge per cycle of vibration, and could very well be a relevant quantity in determining the effect of the water's momentum on the trailing edge's vibration. Going back to the reduced velocity, or the inverse Strouhal number, the selection of the characteristic length is not straightforward. For simple geometries, there are conventions, such as for the cylinder, the diameter is the characteristic length. For a hydrofoil, the chord length is a viable candidate, and it has been used by Yao [4]. The blade thickness is also a possibility, which in combination with trailing edge geometry is widely used for estimating vortex shedding frequencies [14]. Looking back at the damping comparisons, Figures 7 and 8, it is evident that for the vibrations investigated, it doesn't really matter. The slope is more or less the same, but that is not surprising. Although the test rigs, natural frequencies, number of blades, and physical scales are different, the mode shape of each single blade is not that different in each case. For a broader investigation on how damping behaves in submerged structures, with different boundary conditions and other modes of vibration, there is a need to assess geometric parameters. This is where the use of characteristic length is a drawback: it does not factor in how much of the structure is vibrating.

At this point, it is appropriate to take a step back, and consider the theoretical work performed by Monette et al [10]. The damping ratio for a submerged vibrating structure can be calculated as follows:

$$\zeta = \frac{v}{f_n} \left[1 - \left(\frac{f_n}{f_v} \right)^2 \right] \frac{\iint \Phi(x, y) \frac{\partial \Phi(x, y)}{\partial x} dx dy}{\iint \Phi^2(x, y) dx dy} \quad (4)$$

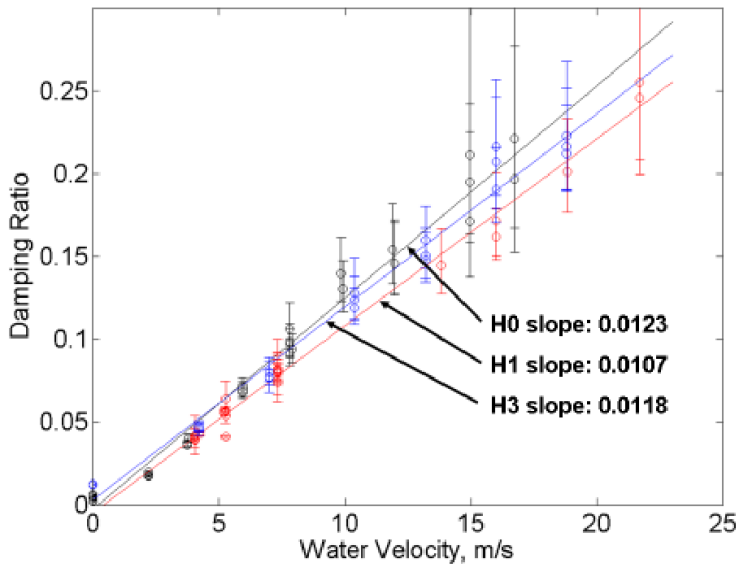


Figure 6: Damping measurements obtained by Coutu et al [2]

In Equation (4), f_n denotes the structure's natural frequency in the fluid, f_v the natural frequency in vacuum, while Φ denotes the mode shape, an integral of the structure's deflection.

By considering the equation, it is clear that it contains three main parts:

- (i) the "modified reduced velocity", as defined in Equation (3)
- (ii) a measure of the added mass, or the thickness of fluid affected by the motion, defined by

$$\widehat{M} = \left[1 - \left(\frac{f_n}{f_v} \right)^2 \right] \quad (5)$$

- (iii) a measure of the "amount of movement" of the structure, namely the mode shape.

$$\widehat{\Phi} = \frac{\iint \Phi(x, y) \frac{\partial \Phi(x, y)}{\partial x} dx dy}{\iint \Phi^2(x, y) dx dy} \quad (6)$$

If only the results measured in this experimental campaign are considered, the slope of damping ratio is constant above lock-in velocities, meaning that the second and third term in Equation (4) must either cancel each other out, or individually remain constant for the different mode shapes.

$$\widehat{M}\widehat{\Phi} = \text{const} \quad (7)$$

It is not unreasonable to expect the mode shape integral to yield the same result for different hydrofoils, given that the boundary conditions are similar, ie. fixed beam, single blade. Given that the vibration deflections are not too large, the relative added mass is not expected to change, and as such, Equation (7) still holds: the product is constant, and hence the damping slope is

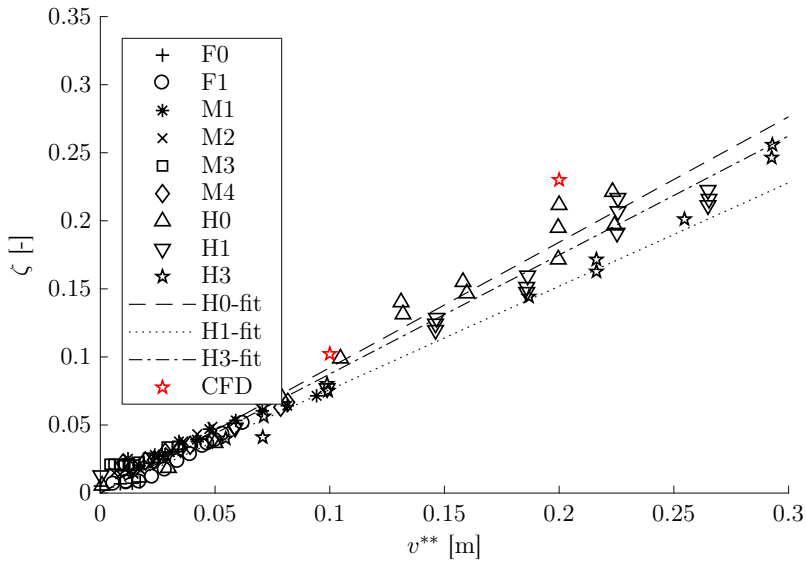


Figure 7: Damping comparison. The lines indicate the linear curve fits from Figure 6, when corrected for their natural frequencies. The mean slope of all the plots was found to be $\zeta/v^{**} = 0.873$

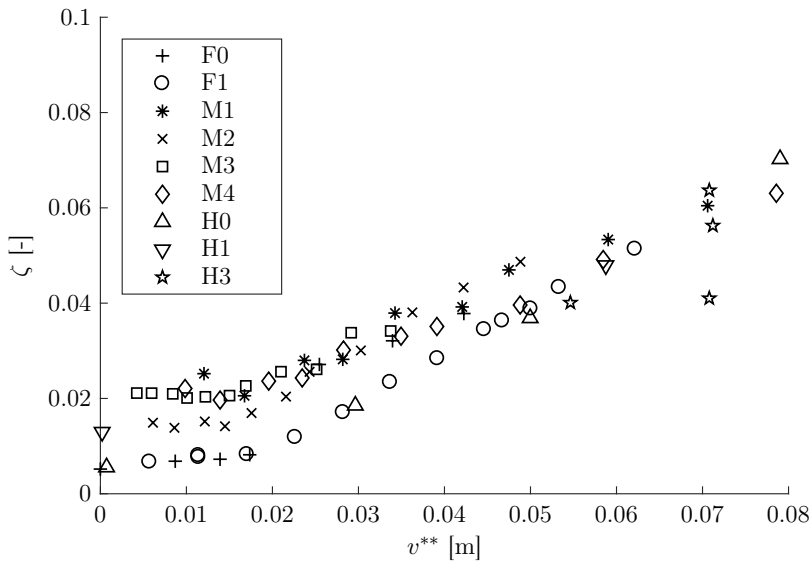


Figure 8: Damping comparison zoomed.

constant. In fact, small variations in the added mass, \widehat{M} , could explain the difference in the slope in Coutu's measurements, see Figure 6.

Even for the three-bladed cascade, although the blade movement is coupled through the water, their deflections can still be integrated in Equation (6), yielding a similar value as for their single-blade counterpart. The value of \widehat{M} is a bit more tricky to estimate for the three bladed cascade case. This is because the response of the water does more than just add mass and damping, it couples the structural movement, producing modes that were not there in air. As such, the assumption of unchanged modes does not hold in a strict sense, but one could speculate that the relatively large spacing of the hydrofoils, combined with the relatively high frequency of vibration, means that the relative added mass of each blade is not affected by the proximity of neighbouring blades. As such, the damping should still adhere to Equation (4), with some substitutions for the estimate for added mass.

This raises an interesting possibility: Even with a multi-blade cascade, with blades coupled through the fluid, we still expect the damping to be described by Equation (4), as long as the appropriate term is found to describe the amount of added mass. If this is indeed true for larger and more complex structures, a runner may be analyzed by considering it as a collection of blades with individually known modes of vibration. However, there are still some unknown parameters to this: Although this experiment shows that three blades behave similarly as one, it is not known for certain if that behavior will translate to a cascade of more blades. Additionally, the question of complex modes and rotational symmetry is not assessed in this experiment, and it is therefore not known if the damping estimates for such a vibration will be different.

4. Conclusion

This experiment indicates that the modes of vibration in a blade cascade show the same behavior in damping when plotted against the reduced velocity. Further comparisons with other experiments indicate that the damping slope can be determined if the natural frequency of the hydrofoil is known, for blades with the same boundary conditions. This can be described by theory developed by Monette et al, and the present investigations show that the product of the added mass and the mode shape integral remain fairly constant for fixed-beam hydrofoils. Moreover, it has also been shown that this product is unchanged when higher modes of multi-blade cascades are considered. This indicates that damping estimates for the blades of a turbine runner can be performed in the same way as for a single blade. However, this has only been demonstrated on a structure exhibiting real modes of vibration. Four modes of vibration were tested, including one where the center blade was stationary. The observed behavior is that the damping factor is unchanged up to $St^{-1} = 2.5$, beyond which the change is linear with respect to reduced velocity. The slope was the same for all modes of vibration, when plotted as reduced values, $\zeta/v^{**} = 0.873$.

5. Further Work

The main focus of further investigations should be to systematically vary different geometric parameters, in order to provide data for the added mass and the mode shape integral for typical geometries. In addition, further work on such a multi-blade cascade should aim to investigate the effect of complex modes. Complex modes are not necessarily going to behave similarly to real vibration modes, and this investigation is of particular relevance for turbines, as they are prone to complex modes due to their rotational symmetry. In addition, although several modes of vibration have been investigated in this work, they are quite similar in their shape. For further investigations on the turbine blade behaviour in high-velocity flows, a twisted blade is suggested, as it is expected to produce less symmetric vibrational modes. Finally, the effects of vibration amplitude have not been investigated in this work. At large amplitudes, the added mass might begin to change, altering the slope of the damping.

6. Acknowledgements

The research was carried out as a part of HiFrancis, a high-head Francis turbine research program supported by the Norwegian Research Council, The Norwegian Hydropower industry, and the Norwegian Center for Hydropower.

Nomenclature

Greek Symbols

Φ	Mode shape
ϕ	Taper angle
θ	Trailing edge angle
$\hat{\Phi}$	Measure of mode shape movement
ζ	Damping

Latin Symbols

\widehat{M}	Measure of added mass
f	Frequency
L	Cord Length
St	Strouhal number
v	Water velocity
F0	Old Hydrofoil
F1	New Hydrofoil

Indices, superscripts

**	Reduced Modified
*	Reduced

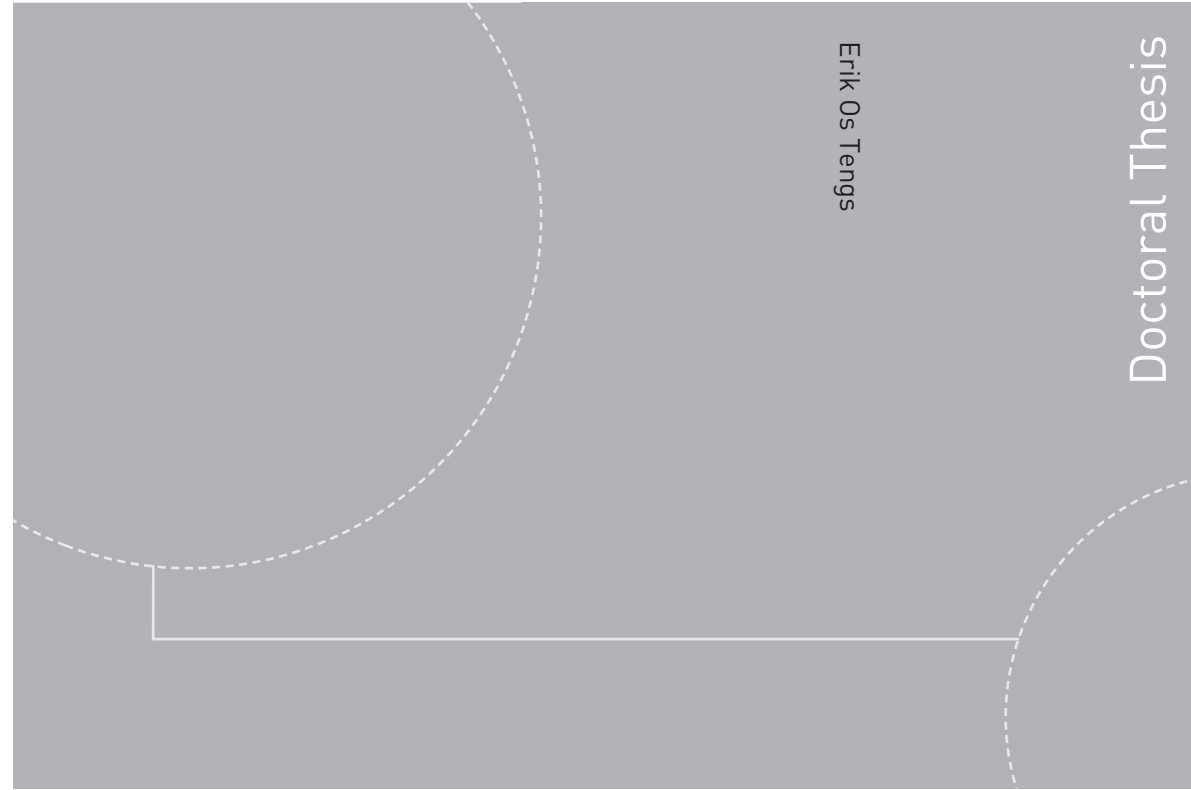
Indices, subscripts

n	Natural
v	In vacuum

References

- [1] Østby P T K, Billdal J T, Sivertsen K, Haugen B and Dahlhaug O G 2016 *International journal on hydropower and dams*
- [2] Coutu A, Seeley C, Monette C, Nennemann B and Marmont H 2012 *IOP Conference Series: Earth and Environmental Science*
- [3] Roth S, Calmon M, Farhat M, Münch C, Bjoern H and Avellan F 2009 *Proceedings of the 3rd IAHR International Meeting of the Workgroup on Cavitation and Dynamic Problems in Hydraulic Machinery and Systems* vol 1 (Brno, Czech Republic: Brno University of Technology)
- [4] Yao Z, Wang F, Dreyer M and Farhat M 2014 *Journal of Fluids and Structures*
- [5] Reese M C 2010 *Vibration and Damping of Hydrofoils in Uniform Flow* Master's thesis
- [6] Bergan C W, Solemslie B W, Østby P and Dahlhaug O G 2018 *International Journal of Fluid Machinery and Systems*
- [7] Tengs E O, Bergan C W, Jakobsen K R and Storli P T 2018 *IOP Conference Series: Earth and Environmental Science*
- [8] Bergan C W, Tengs E O, Solemslie B W and Dahlhaug O G 2018 *IOP Conference Series: Earth and Environmental Science*
- [9] Presas A, Valentin D, Egusquiza E, Valero C, Egusquiza M and Bossio M 2016 *Proceedings*
- [10] Monette C, Nennemann B, Seeley C, Coutu A and Marmont H 2014 *IOP Conference Series: Earth and Environmental Science*
- [11] Seeley C, Coutu A, Monette C, Nennemann B and Marmont H 2012 *Smart Materials and Structures*
- [12] Ewins D J 2000 *Modal Testing: Theory, Practice, and Application* 2nd ed (*Mechanical engineering research studies* no 10) (Baldock, Hertfordshire, England ; Philadelphia, PA: Research Studies Press)
- [13] Craig R R, Kurdila A and Craig R R 2006 *Fundamentals of Structural Dynamics* 2nd ed (Hoboken, N.J.: John Wiley)
- [14] Heskestad G and Olberts D R 1960 *Journal of Engineering for Power*

ISBN 978-82-326-4054-6 (printed version)
ISBN 978-82-326-4055-3 (electronic version)
ISSN 1503-8181



Doctoral theses at NTNU, 2019:229

Erik Os Tengs

Numerical simulation of Fluid- Structure Interaction in high head Francis turbines

 **NTNU**
Norwegian University of
Science and Technology

Doctoral theses at NTNU, 2019:229

 **NTNU**

NTNU
Norwegian University of
Science and Technology
Faculty of Engineering
Department of Energy and Process Engineering

 **NTNU**
Norwegian University of
Science and Technology